Dark Matter Production after Inflation and Constraints

Saleh Sadaka O. Qutub

Master of Science (King Abdulaziz University)

Physics

Department of Physics

Lancaster University

July 2017

A thesis submitted to Lancaster University for the degree of Doctor of Philosophy in the Faculty of Science and Technology

Abstract

A multitude of evidence has accumulated in support of the existence of dark matter in our Universe. There are already plenty of dark matter candidates. However, we do not know yet whether any of these candidates constitutes the whole or a part of the dark matter population despite the tremendous experimental efforts. In this thesis, we study several possible dark matter production mechanisms and the corresponding observational and theoretical constraints in the context of inflationary cosmology. Adopting a model-independent approach, we explore the parameter space for dark matter with a mass of order MeV and above showing that only small regions of the parameter space for the popular freeze-out mechanism are still viable. Nevertheless, the regions of the parameter space corresponding to the freeze-in and non-thermal dark matter scenarios are mostly unexplored. We, therefore, zoom into these regions and show that a connection to the inflationary observables can be established, which can help constrain these scenarios. We then consider the parameter space of a sub-eV dark matter candidate, the axion. We show that using the Cosmic Microwave Background radiation constraint on the effective number of relativistic species, an interesting constraint can be placed. This bound arises from the fact that the field whose angular excitations are the axions can be displaced from its minimum during inflation and later decays dominantly into ultra-relativistic, axions which contribute to the effective number of relativistic species. We finally consider the possible production of axion-like particle via non-perturbative effects due to their coupling to inflatons or moduli. We show that this mechanism is efficient only if the amplitude of inflaton/moduli oscillations is initially much larger than the mass scale associated with the axion-like

particles. In this case, bounds can be placed on the corresponding parameter spaces.

To the memory of my mother

Acknowledgements

I would like to take this opportunity to acknowledge some of those who have guided and supported me throughout my studies.

First and foremost, I would like to thank my supervisors, Dr John McDonald and Dr Ian Bailey, for their support and sincere advice. I would also like to thank my collaborators, Dr Bhupal Dev and Dr Ken'ichi Saikawa, for the many fruitful discussions we had.

I am very grateful to my colleagues, Aindriú Conroy, James Edholm, Ernestas Pukartas, Arron Rumsey, Spyridon Talaganis, Ilia Teimouri and Lingfei Wang. Especial thanks to my dear friend, Spyridon Talaganis, for his continuous support. I would like to extend my gratitude to the King Abdulaziz University for funding me throughout my studies.

Last, but certainly not least, I would like to express my unreserved thanks to my family members whose constant support and encouragement made even the toughest days bearable.

Declaration

This thesis is my own work and no portion of the work referred to in this thesis has been submitted in support of an application for another degree or qualification at this or any other institute of learning.

Contents

List of Figures

List of abbreviations

BAO :	Baryon Acoustic Oscillations
BBN :	Big Bang Nucleosynthesis
CM :	Centre-of-Mass
CL :	Confidence Level
CP :	Charge conjugation-Parity transformation
DD :	Direct Detection
DE :	Dark Energy
DM :	Dark Matter
d.o.f. :	degrees of freedom
EDM:	Electric dipole moment
EOM :	Equation of Motion
EW :	Electro-weak
FIMP :	Feebly Interacting Massive Particle
FLRW :	Friedmann-Lemaître-Robertson-Walker
GR :	General Theory of Relativity
GUT :	Grand Unified Theories
ID :	Indirect Detection
JLA :	Joint-Light-Curve Analysis
MACHOs :	Massive Astrophysical Compact Halo Objects
MD :	Matter Domination
Mpc :	Mega parsecs
PQ :	Peccei-Quinn
PBH :	Primordial Black Holes
QCD :	Quantum Chromodynamics
RD :	Radiation Domination
SCM (ΛCDM) :	Standard Cosmological Model
SDSS :	Sloan Digital Sky Survey
SM :	Standard Model of particle physics
SUSY :	Supersymmetry
VEV :	Vacuum Expectation Value
WIMP :	Weakly Interacting Massive Particle
WISP :	Weakly Interacting Sub-eV (Slim) Particle

Chapter 1

Introduction

The field of cosmology has come a long way since Albert Einstein formulated his theory of General Relativity (GR) [1] due to the rapid development of observational techniques. We now have a simple model, the Standard Cosmological Model (SCM or ΛCDM), which successfully describes most of the evolutionary history of our Universe. According to the SCM, the observable Universe started with a Big Bang roughly fourteen billion years ago [1] and since then, it has been expanding. It is assumed (and has also been verified by observations [2, 3, 4, 5, 6, 7]) that our Universe is homogeneous and isotropic on large scales. In the SCM framework, the dynamics of the Universe is driven by gravity described by GR which relates the geometry of the space to its energy content [8, 9, 10, 11, 12]. The latter includes the ordinary (baryonic) matter (and energy) [2] and non-luminous (dark) matter. It also contains dark energy which effectively acts as a cosmological constant.

It is astonishing that ordinary matter (and energy) constitutes only a small fraction of the total energy budget of the Universe today (4.9% [13]), and that

[1] More precisely, the Big Bang took place around 13.807 ± 0.026 (at 68% CL) billion years ago according to the recent measurement of the Cosmic Microwave Background radiation (CMB) by the Planck satellite [2].

[2] Radiation (i.e. relativistic species including photons) does not contribute significantly to the total energy budget of the Universe today as it dilutes with expansion faster than the other components. Also, the leptonic contribution to the total energy density is much smaller than that of baryons.

the rather unfamiliar forms of matter and energy, dark matter (26.6% [13]) and dark energy (68.5% [13]), dominate the energy density of the Universe. Dark energy (DE), the less understood of the two, was only discovered recently [14, 15] whereas hints for the existence of dark matter (DM) started showing up much earlier [16, 17, 18, 19, 20, 21, 22, 23, 24].

Nevertheless, the nature and origin of both DM and DE remain among the fundamental mysteries in physics. Furthermore, many other puzzles lack satisfactory explanations within the SCM framework, such as the observed large-scale homogeneity, isotropy and spatial flatness of the Universe. The latter issues can be explained by an early epoch of accelerated expansion, dubbed "inflation" [25, 26, 27]. Inflation also provides a simple mechanism for the production of primordial perturbations which, in the presence of DM, have grown into the observed structure (for a review see e.g. [28, 29, 30]). However, inflation dilutes all the possibly pre-existing relics, and hence to match observations the Standard Model (SM) degrees of freedom (d.o.f.) have to be excited after the end of inflation. Similarly, DM has to be produced directly and/or indirectly after inflation.

This thesis is dedicated to the study of DM. In particular, we investigate some of the DM production mechanisms and the corresponding theoretical and observational constraints on DM in the context of inflationary cosmology. We begin in this chapter by briefly reviewing the elements of the SCM, some of its shortcomings, and how they can be solved by an epoch of inflation. We also discuss the observational evidence for DM, its known properties, and some of the famous DM candidates and alternatives. In Chapter 2, we present a model-independent scan of the parameter space for DM production after inflation and identify the regions of the parameter space corresponding to thermal and non-thermal DM. For the thermal case (both freeze-out and freeze-in scenarios), we show the current observational and theoretical bounds and highlight the allowed regions of the parameter space in both scenarios. For the non-thermal case, we identify the regions of the parameter space corresponding to cold, warm and hot DM. In Chapter 3, we focus on the freeze-in and non-thermal DM scenarios whose parameter space is mostly unexplored territory. We show that for the case of DM interactions with the SM particles being mediated by a heavy particle, which naturally leads

to a freeze-in scenario, the DM abundance can be connected to the inflationary observables. We show that this is also the case for the non-thermal DM scenario. The established connection between the inflationary observables and DM abundance for the non-thermal and frozen-in (via heavy mediator) DM could provide a useful way to constrain the corresponding DM parameter spaces. We also scan the parameter space for the DM production via this ultra-violet freeze-in mechanism and show that the observed DM abundance can be fulfilled in a wide range of the frozen-in DM masses. In Chapter 4, we turn our attention to a famous DM candidate, the axion, which belongs to the low mass spectrum. We show that large amounts of ultra-relativistic axions can be non-thermally produced, increasing the effective number of the relativistic d.o.f. in our Universe which is constrained by various astrophysical observations. This, in turn, places an interesting constraint on the axion parameter space and the reheating temperature. Further for completeness, we briefly review the other observational constraints. In Chapter 5, we consider the non-perturbative production of axion-like particles (ALPs) via their non-renormalisable derivative coupling to a scalar condensate of inflatons or moduli. We first ignore the effect of the cosmic expansion and show that the excitation of ALPs with a very wide range of masses can take place via tachyonic and parametric instabilities that happen for two short periods of time during each oscillation of the condensate. We repeat the calculation including the effect expansion and show that the non-perturbative excitation of ALPs is rendered completely inefficient unless the initial amplitude of oscillations is much larger than the associated mass scale. In this case, the energy of the scalar condensate can be drained as excitations of the axion-like field within a few oscillations. This analysis can be used to constrain the parameter space of many ALP DM candidates. We present our conclusions in Chapter 6.

1.1 Standard Cosmological Model (SCM)

According to the SCM, our Universe is homogeneous and isotropic on large scales. Such a Universe can be described by the Friedmann-Lemaître-Robertson-Walker (FLRW) metric [9, 10, 11, 12], which in spherical-polar coordinates (r, θ, ϕ) takes

the form

$$\mathrm{d}s^2 = \mathrm{d}t^2 - a(t)^2 \left[\frac{\mathrm{d}r^2}{1-\kappa r^2} + r^2 \left(\mathrm{d}\theta^2 + \sin^2\theta \mathrm{d}\phi^2 \right) \right], \tag{1.1}$$

where $a(t)$ denotes the time-dependent scale factor which parameterises the size of the Universe and κ parameterises its spatial curvature. κ has the units of length^{-2}; with a proper re-scaling of the coordinates, κ can be made dimensionless with $\kappa = 0$ corresponding to a flat Universe (Euclidean spatial geometry), and $\kappa = +1, -1$ corresponding to a closed (3-sphere) and open (3-hyperboloid) Universe, respectively. Using the Einstein field equations and the FLRW metric, Eq. (1.1), one obtains the Friedmann equations describing the time evolution of our homogeneous and isotropic Universe [1]:

$$H^2 = \frac{\dot{a}^2}{a^2} = \frac{\rho}{3M_{\rm P}^2} - \frac{\kappa}{a^2}\,, \tag{1.2}$$

$$\dot{H} + H^2 = \frac{\ddot{a}}{a} = -\frac{1}{6M_{\rm P}^2}(\rho + 3\mathcal{P})\,, \tag{1.3}$$

where

$$H \equiv \frac{\dot{a}}{a} = \frac{\mathrm{d}\ln a}{\mathrm{d}t}\,, \tag{1.4}$$

is the Hubble expansion parameter, 'dot' denotes derivative with respect to (w.r.t.) physical time t and $M_{\rm P} \equiv [8\pi G_{\rm N}]^{-1/2} \simeq 2.43 \times 10^{18}$ GeV is the reduced Planck mass with $G_{\rm N}$ being the Newton's gravitational constant. Here $\rho = \sum_i \rho_i$ and $\mathcal{P} = \sum_i \mathcal{P}_i$ are respectively the total energy and pressure of the cosmic fluid, where the sum runs over all the components of the fluid. Further, using Eqs. (1.2) and (1.3), energy conservation can be expressed by the following continuity equation:

$$\dot{\rho} + 3H(\rho + \mathcal{P}) = 0\,. \tag{1.5}$$

Note that the continuity equation holds for each component of the fluid separately if there is no energy transfer between the different components. For a perfect fluid,

[1] In this thesis, we mostly use natural units, i.e. we set the speed of light, the reduced Planck constant and the Boltzmann constant to one, $c = \hbar = k_{\rm B} = 1$, respectively.

the pressure is related to the energy density via the equation of state

$$\mathcal{P}_i = \omega_i \rho_i \,, \tag{1.6}$$

where the dimensionless parameter, ω_i, is constant in time. The equation of state parameter $\omega_i = 0$, $1/3$ and -1 for matter, radiation and dark energy, respectively. Substituting for $\mathcal{P}$ into Eq. (1.5), one obtains

$$\rho_i = \rho_{i,0} \left(\frac{a_0}{a}\right)^{3(1+\omega_i)}, \tag{1.7}$$

where '0' refers to the today's values. Thus, as the Universe expands, the different energy components dilute with different rates leading to three epochs of a single energy component domination, starting with a radiation [$\rho_{\rm rad} \propto a(t)^{-4}$] domination (RD) epoch followed by a matter [$\rho_m \propto a(t)^{-3}$] domination (MD) epoch, where the observed structures started to grow linearly, and finally an epoch of accelerated expansion dominated by DE [$\rho_\Lambda = $constant].

It is convenient to define the critical density $\rho_c \equiv 3H^2 M_{\rm P}^2$ corresponding to a spatially-flat Universe and the density parameter $\Omega_i \equiv \rho_i/\rho_c$. One can then re-write Eq. (1.2) as

$$H^2 = H_0^2 \left[\Omega_{m,0} \left(\frac{a_0}{a}\right)^3 + \Omega_{\rm rad,0} \left(\frac{a_0}{a}\right)^4 + \Omega_{\kappa,0} \left(\frac{a_0}{a}\right)^2 + \Omega_{\Lambda,0}\right], \tag{1.8}$$

where the curvature term $\Omega_{\kappa,0} \equiv -\kappa/(a_0 H_0)^2$, and $\Omega_{m,0}$ contains the contributions of both dark and ordinary matter. According to the recent measurement of CMB by the Planck mission $H_0 = 67.27 \pm 1.32$ km Mpc^{-1} s^{-1}, $\Omega_{m,0} = 0.3156 \pm 0.0182$, $\Omega_{\rm rad,0} = 9.17^{+0.37}_{-0.35} \times 10^{-5}$ (assuming three relativistic species of neutrino), $\Omega_{\Lambda,0} = 0.6879 \pm 0.0174$ and $|\Omega_{\kappa,0}| < 0.005$ (at 95% CL) [13]. Given the current abundance of the different energy components, one can see easily from Eq. (1.8) that the curvature contribution to the total energy density has always been sub-dominant, and hence it can be safely ignored while discussing the history of the Universe. Integrating Eq. (1.8) for each energy component separately while ignoring the

curvature term, one obtains

$$a(t) \propto \begin{cases} t^{2/[3(1+\omega_i)]} & (\text{MD\&RD}) \quad \Rightarrow \quad H \simeq \frac{2}{3(1+\omega_i)\,t} \\ e^{Ht} & (\text{DE domination}) \quad \Rightarrow \quad H \simeq \text{constant}\,. \end{cases} \tag{1.9}$$

With the help of Eqs. (1.2) and (1.7) while setting $\kappa = 0$, the comoving Hubble radius $(aH)^{-1}$, which is the maximum comoving distance that can be travelled by a particle during one expansion (Hubble) time H^{-1}, can be expressed as

$$(aH)^{-1} \propto a^{\frac{1}{2}(1+3\omega)}. \tag{1.10}$$

It is clear from Eq. (1.10) that the comoving Hubble sphere always expands unless the Universe is dominated by a fluid with $\omega < -1/3$. For a Universe dominated with a fluid with $\omega > -1/3$, the comoving particle horizon, which is the maximum comoving distance from which light could have travelled to the observer,

$$\frac{d_{\rm hor}(t)}{a(t)} = \int_0^t \frac{\mathrm{d}\tilde{t}}{a(\tilde{t})} = \frac{3(1+\omega)}{C_1(1+3\omega)}\, t^{\frac{1+3\omega}{3(1+\omega)}}\,, \tag{1.11}$$

roughly coincides with the comoving Hubble radius $(aH)^{-1} = \frac{3(1+\omega)}{2C}\, t^{\frac{1+3\omega}{3(1+\omega)}}$, where C is a constant. In such a Universe, regions separated by comoving distances much larger than $(aH)^{-1}$ were never in causal contact.

Another important concept in cosmology is redshift z, which is often used as a proxy of time inferred from the measurement of the spectra of different astronomical and cosmological light sources,

$$z = \frac{\lambda_0 - \lambda}{\lambda} = \frac{a(t_0)}{a(t)} - 1\,, \tag{1.12}$$

where λ denotes the wavelength of a spectral line characterising the source as measured in laboratories (i.e that of the photon at the time of emission from the source) and λ_0 is the wavelength of the redshifted photon as measured from Earth. For close objects, $z \simeq H_0 d$ with d being the distance to the object. For later convenience, let us define the conformal time τ, which is related to the

cosmic (physical) time, t, via the relation

$$\mathrm{d}\tau \equiv \frac{\mathrm{d}t}{a(t)} = \frac{\mathrm{d}a}{a^2 H}\,. \tag{1.13}$$

1.2 Shortcomings of the SCM

Let us briefly review some of the most widely-discussed puzzles of the SCM in relation to the initial condition of the Universe.

1.2.1 Flatness problem

The recent measurement of the CMB has indicated that our Universe is spatially flat to a very good accuracy, i.e. the energy density of the Universe today is very close to the critical density ($\Omega_0 = \rho_0/\rho_c$ is very close to unity) [13]. By re-writing Eq. (1.2) in the form

$$\Omega - 1 = \kappa\,(aH)^{-2}\,, \tag{1.14}$$

one can see that in our Universe, which has been dominated by radiation [$H^2 \propto \rho_{\rm rad} \propto a^{-4} \Rightarrow (\Omega - 1) \propto a^2$] or matter [$H^2 \propto \rho_m \propto a^{-3} \Rightarrow (\Omega - 1) \propto a$] for most of its history, Ω should have been extremely close to unity at early times. Put in other words, a tiny deviation from the critical density at early times could have caused the Universe to collapse very soon after the Big Bang or expand too fast such that no structure could form. This is a serious fine tuning problem.

1.2.2 Horizon problem

According to the SCM, the CMB sky we observe today was initiated around 380,000 years after the Big Bang when photons decoupled from electrons and baryons. Amazingly, the CMB is very isotropic with an almost perfect black body spectrum [31] at temperature $T_0 = 2.7255 \pm 0.01$ K [32]. The temperature anisotropies in the CMB are smaller than 10^{-4} [33]. This indicates that the CMB photons we detect today must have been in causal contact. On the other hand, in the SCM, regions separated by distances larger than the particle horizon, $d_{\rm hor,dec}$,

were not in causal contact with each other at the era of decoupling $t_{\rm dec}$, and hence there is no reason for such regions to share the same temperature. Assuming for the sake of estimation that the Universe has always been dominated by non-relativistic matter, the horizon size at photon decoupling is [see Eq. (1.11)]

$$d_{\rm hor,dec} \sim 3\, t_{\rm dec} \sim 0.3 \text{ Mpc}\,, \tag{1.15}$$

whereas the present horizon size redshifted back to the era of decoupling is given by

$$d_{\rm hor,0}(t_{\rm dec}) \sim d_{\rm hor,0}(1+z_{\rm dec})^{-1} \sim 10 \text{ Mpc}\,. \tag{1.16}$$

Thus, there were about $[d_{\rm hor,0}(t_{\rm dec})/d_{\rm hor}]^3 \sim 10^4$ disconnected patches of space within the volume that corresponds to our present horizon. So, how is it that these causally-disconnected regions of space have the same properties? This is known as the horizon problem which has no solution within the SCM framework.

1.2.3 The origin of large-scale structure

The CMB sky we observe today indicates that at early times the Universe was remarkably homogeneous and isotropic with tiny density perturbations (at the level 10^{-5}) whose power spectrum is nearly scale-invariant on large scales [13]. These small fluctuations have grown under the influence of gravity into the structure we observe today, such as galaxies and galactic clusters. So from where have these perturbations arisen? The SCM does not explain the origin of these primordial perturbations, which were outside the Hubble sphere (super-Hubble) in the early universe. Within the SCM framework, these initial perturbations have to be put in by hand. This is known as the primordial perturbations problem.

1.2.4 Unwanted relics

According to the SCM, the Universe started up with a very high temperature. As the temperature decreased due to expansion, several phase transitions may have taken place giving rise to topological defects and exotic particles (see [34] for a review). For instance, many grand unified theories (GUT) predict the existence

of magnetic monopoles which are stable, very massive ($m \sim T_{\rm GUT} \sim 10^{15}$ GeV), point-like, topological defects. Other topological defects such as cosmic strings and domain walls can be produced, for example in a GUT or Peccei-Quinn phase transition. Furthermore, heavy exotic particles such as gravitinos (the supersymmetric partner of the graviton), Kaluza-Klein particles and weakly-coupled moduli fields predicted by theories of extra-dimensions [1], can be abundantly produced at high temperatures. These exotic relics if stable (or sufficiently long-lived) can come to dominate the energy density of the Universe because they dilute slower than radiation does as the Universe expands. Obviously, such relics are ruled out by observations.

1.3 Cosmic inflation

The initial condition problems of the SCM discussed in the previous section can be elegantly solved by an early epoch of accelerated expansion (inflation). In this section, we briefly discuss the basic idea of inflation and how it solves the initial condition puzzles of the SCM.

1.3.1 The basic idea

In the SCM framework, the comoving Hubble radius, $(aH)^{-1}$, is a monotonically increasing function of time [see Eq. (1.10)]. Going back in time, fewer and fewer regions of space were in causal contact, which contradicts many cosmological observations [4, 5, 6, 13]. Hence, an early epoch with a shrinking Hubble sphere is needed to bring more regions of space into causal contact at early times. This is exactly the idea of inflation (for a review see e.g. [34, 40, 41]). To see whether

[1] The moduli fields are natural consequence of any low energy string theory, which appear in four dimensions with almost flat potential [35]. Typically, the moduli could be made heavy by stringy non-perturbative effects [36], but still there could be one light moduli with a mass around the scale of low supersymmetry (SUSY) breaking. If the low scale SUSY breaking is at $\mathcal{O}$(TeV), then the moduli would typically take a mass of that order. Light moduli could be displaced during inflation by virtue of quantum fluctuations of order the Hubble expansion rate during inflation (see [34, 37, 38, 39]). In which case, the moduli lighter than the Hubble expansion rate during inflation could be settled with a large VEV, i.e. $\mathcal{O}(M_{\rm P})$.

this is possible, let us consider the time evolution of the comoving Hubble radius,

$$-\frac{\mathrm{d}}{\mathrm{d}t}(aH)^{-1}=\frac{1}{a}(1-\epsilon)=-\frac{\mathrm{d}}{\mathrm{d}t}(\dot{a})^{-1}=\frac{\ddot{a}}{\dot{a}^2}>0\,. \tag{1.17}$$

It is clear from Eq. (1.17) that a shrinking Hubble sphere corresponds to accelerated expansion of the Universe and can be achieved if

$$\epsilon\equiv-\frac{\dot{H}}{H^2}=-\frac{\mathrm{d}\ln H}{\mathrm{d}\ln a}=-\frac{\mathrm{d}\ln H}{\mathrm{d}N}=1-\frac{(\ddot{a}/a)}{H^2}=\frac{3}{2}(1+\omega)<1\,, \tag{1.18}$$

where we have used Eqs. (1.2) and (1.3), and defined $\mathrm{d}N\equiv\mathrm{d}\ln a=H\mathrm{d}t$ with N being the number of e-folds of cosmic expansion [alternatively $a(N)=a(N_i)\exp(N-N_i)$]. Eq. (1.18) is satisfied if $\omega=\mathcal{P}/\rho<-1/3$, i.e. $(\rho+3\mathcal{P})<0$. For a perfect de Sitter Universe, $H\propto\rho^{1/2}=\text{constant}$ ($\omega=-1$) which implies that $\epsilon=0$, in which case inflation would last for ever. However, in our Universe inflation has to end which requires ϵ to increase with time. Nevertheless, for inflation to solve the horizon problem it has to last for sufficiently long time (i.e. for a large number of Hubble expansion times) which requires ϵ to be a slowly-varying function of time, i.e.

$$\eta\equiv\frac{\dot{\epsilon}}{H\epsilon}=\frac{\mathrm{d}\ln\epsilon}{\mathrm{d}N}\,,\qquad|\eta|<1\,. \tag{1.19}$$

Thus, inflation takes place if $\epsilon,|\eta|\ll1$ and ends when ϵ reaches unity.

1.3.2 Inflation and the SCM problems

Let us see how an early epoch of inflation can solve the initial condition problems of the SCM. During inflation the Hubble parameter, $H\propto\rho^{1/2}$, is roughly constant; as a result, the Universe expands quasi-exponentially,

$$a(t)\simeq a(t_{\rm I})\,e^{\int_{t_{\rm I}}^{t}H d\tilde{t}}\sim a(t_{\rm I})\,e^{H(t-t_{\rm I})}\,. \tag{1.20}$$

Thus, if inflation lasts long enough, any unwanted relic can be inflated away. Requiring that the decay of the field(s) driving inflation do not reheat the Universe to a very high temperature, one can make sure that these unwanted relics do not

get produced after inflation. The SM d.o.f. needed for the success of Big Bang Nucleosynthesis (BBN) can then be excited after inflation.

Moreover during inflation, the comoving Hubble volume decreases monotonically [see Eq. (1.17)] allowing more regions of the Universe to be in causal contact at early times. In other words, a given physical scale $\lambda = a(t)\tilde{\lambda}$ grows much faster than the Hubble radius does, $H^{-1} \simeq$ constant, which means that physical scales that are outside the Hubble volume (super-Hubble) at a given time were inside the Hubble volume (sub-Hubble) at earlier times (during inflation). Consequently, the horizon problem is solved provided that inflation lasts long enough. This also solves the primordial perturbations problem as the perturbations responsible for the observed structures, which were super-Hubble before the BBN era, are exponentially reduced in size going back in time. Therefore, these perturbations can be made sub-Hubble during inflation where micro-physics can act. We show in Section 1.4.1.1 below that these perturbations were actually quantum fluctuations that have been stretched to cosmological scales during inflation.

The shrinking comoving Hubble volume during inflation also solves the flatness problem, which can easily be seen from Eq. (1.14). During inflation the density parameter, $\Omega = \rho/\rho_c$, is driven toward unity. Hence, Ω can be made very close to unity as required by observations provided that inflation lasts for a long enough time.

Let us estimate how much inflation is needed in order to solve the SCM initial condition issues. Focusing on the horizon problem, it is clear that the resolution of the horizon problem at the very minimum requires that the largest observable scale must fit in the comoving Hubble volume at the beginning of inflation, i.e.

$$\frac{(a_{\rm I}H_{\rm I})^{-1}}{(a_0H_0)^{-1}} = \frac{(a_{\rm I}H_{\rm I})^{-1}}{(a_{\rm end}H_{\rm end})^{-1}} \frac{(a_{\rm end}H_{\rm end})^{-1}}{(a_0H_0)^{-1}} \gtrsim 1 \quad \Rightarrow \quad \frac{a_{\rm end}}{a_{\rm I}} \gtrsim \frac{a_0}{a_{\rm end}} \sim \frac{T_{\rm end}}{T_0}\,, \quad (1.21)$$

where the indices 'I' and 'end' refer to values at the beginning and end of inflation, respectively. Here for simplicity, we assumed that the Universe has been dominated by radiation since the end of inflation till today ($H \propto t^{-1} \propto T^2 \propto a^{-2}$). From Eq. (1.21), one can easily see that the amount of expansion during inflation should be at least equal to that after inflation in order for the horizon prob-

lem to be solved. Plugging in the current temperature $T_0 \simeq 2.37 \times 10^{-4}$ eV and substituting $T_{\rm end} \sim 10^{15}$ GeV (for high scale inflation models $\rho^{1/4} \sim 10^{16}$ GeV), one sees that the Hubble volume has to shrink roughly by a factor $\gtrsim 10^{27}$ [or $N = \ln(a_{\rm end}/a_{\rm I}) \gtrsim 63$] during inflation in order to solve the horizon problem. A more accurate estimation of the number of e-folds during inflation for high scale inflation models holds $N = 50$–60 depending on the details of the reheating period after inflation [1]. One can also show that a similar amount of inflation solves the flatness problem and the other initial condition problems of the SCM.

1.3.3 Single-field slow-roll inflation

The earliest successful and perhaps the simplest implementation of the above idea is realised via what is known as "single-field slow-roll inflation" in which the accelerated expansion of the Universe is driven by the potential energy of a slowly rolling scalar field (see e.g. [42]). To see this, let us consider the following generic action of a scalar field, ϕ, dubbed as "inflaton", with a canonical kinetic term:

$$\mathcal{S}_\phi = \int \sqrt{-g}\, \mathrm{d}^4x\, \mathcal{L}_\phi = \int \sqrt{-g}\, \mathrm{d}^4x \left[\frac{1}{2} g^{\mu\nu} \partial_\mu \phi \partial_\nu \phi - V(\phi) \right], \tag{1.22}$$

where $g \equiv \det(g_{\mu\nu})$ [2]. The stress-energy tensor for the inflaton field can be expressed as

$$T_{\mu\nu} = \partial_\mu \phi \partial_\nu \phi - g_{\mu\nu} \left[\frac{1}{2} g^{\alpha\beta} \partial_\alpha \phi \partial_\beta \phi - V(\phi) \right]. \tag{1.23}$$

In general, both the inflaton field and the metric are functions of space and time. For sufficiently homogeneous initial condition, both the inflaton field and the metric can be expanded as

$$\phi(x^\alpha) = \bar{\phi}(t) + \delta\phi(x^\alpha)\,, \tag{1.24}$$

$$g_{\mu\nu}(x^\alpha) = \bar{g}_{\mu\nu}(t) + \delta g_{\mu\nu}(x^\alpha)\,, \tag{1.25}$$

[1] For many other models of inflation such as low scale models, the amount of required (observable) inflation can be significantly smaller.

[2] Here and throughout this thesis, the Greek indices denote the four-vector components and take on values $0, 1, 2, 3$.

where the bars on top indicate the homogeneous background part and the δ's in front indicate the perturbations in the corresponding quantities [1]. Here, the background FLRW metric is given by Eq. (1.1). The dynamics of the homogeneous part of the inflaton field is governed by the following equation of motion (EOM) which can be easily obtained by varying the inflaton action, Eq. (1.22), w.r.t. ϕ keeping only the zeroth order terms:

$$\ddot{\phi} + 3H\dot{\phi} + \partial_\phi V = 0\,. \tag{1.26}$$

Moreover, the 00 component of the stress-energy tensor, Eq. (1.23), gives the energy density of the inflaton field, while the spatial components give its pressure. These can respectively be expressed as

$$\rho_\phi \simeq \frac{1}{2}\dot{\phi}^2 + V\,, \tag{1.27}$$

$$\mathcal{P}_\phi \simeq \frac{1}{2}\dot{\phi}^2 - V\,. \tag{1.28}$$

With the help of (1.2), (1.3), (1.26), (1.27) and (1.28) while ignoring the curvature term (i.e. setting $\kappa = 0$) one can show that the conditions for inflation, Eqs. (1.18) and (1.19), now read

$$\epsilon = -\frac{\dot{H}}{H^2} \simeq \frac{3}{2}\frac{\dot{\phi}^2}{\rho_\phi} \simeq \frac{M_{\rm P}^2}{2}\left(\frac{\partial_\phi V}{V}\right)^2 \equiv \epsilon_\phi < 1\,, \tag{1.29}$$

and

$$\eta \simeq -2\frac{\dot{H}}{H^2} + 2\frac{\ddot{\phi}}{\dot{\phi}H} = 2\epsilon - 2\zeta\,, \qquad |\eta_\phi| \equiv |\epsilon + \zeta| \simeq M_{\rm P}^2\left|\frac{\partial_\phi^2 V}{V}\right| < 1\,. \tag{1.30}$$

The above conditions, which are usually called the "slow-roll" conditions, ensure that the inflaton is a slowly rolling field. The first slow-roll parameter, ϵ_ϕ, measures the slope of the potential. Having $\epsilon_\phi \ll 1$ initially ensures that the potential energy is slowly varying and is dominant over the kinetic energy ($\dot{\phi}^2 \ll V$). As a result, the energy of the inflaton (or equivalently the Hubble parameter) is

[1] In what follows, we will usually drop the over bar when it does not cause confusion.

roughly constant which is required in order for the Universe to expand quasi-exponentially [see Eq. (1.9)] [1]. Since $\epsilon_\phi \ll 1$ increases with time [see Eq. (1.30)], the first slow-roll condition will eventually break down, i.e. ϵ_ϕ reaches unity, and inflation will come to an end. Therefore, for inflation to last long enough such that it solves the initial condition issues of the SCM, the change in the slope of the potential (or equivalently ϵ_ϕ) has to be sufficiently small which requires that the second slow-roll parameter, η_ϕ, to be $\ll 1$ initially. The second slow-roll condition ensures that initially $|\ddot{\phi}| \ll 3H|\dot{\phi}| \simeq |\partial_\phi V|$. Therefore, when the slow-roll approximation holds, Eqs. (1.2) and (1.26) can be respectively re-written as [2]

$$H^2 \simeq \frac{V}{3M_{\rm P}^2}\,, \tag{1.31}$$

and

$$3H\dot{\phi} \simeq -\partial_\phi V. \tag{1.32}$$

The number of the cosmic e-folds during inflation is then given by

$$N = \ln\left[\frac{a(t_{\rm end})}{a(t_{\rm I})}\right] = \int_{t_{\rm I}}^{t_{\rm end}} H{\rm d}t \simeq -\frac{1}{M_{\rm P}^2}\int_{\phi_{\rm I}}^{\phi_{\rm end}} \frac{V}{\partial_\phi V}{\rm d}\phi = -\frac{1}{M_{\rm P}}\int_{\phi_{\rm I}}^{\phi_{\rm end}} \frac{{\rm d}\phi}{\sqrt{2\epsilon_\phi}}\,. \tag{1.33}$$

1.4 Initial perturbations and the evolution of structure

We now turn our attention to the subject of cosmological inhomogeneities, their origin and their evolution into the observed structure (for a detailed discussion see e.g. [28, 29, 30, 43, 44]). Since the measurement of the CMB indicates that these perturbations were very tiny in the early Universe (see e.g. [3]), it is sufficient to consider only first order in the perturbed quantities for a great part of the history of the Universe. Further, since the background is invariant under spatial

[1] This also leads to a negative equation of state [see Eqs. (1.6), (1.27) and (1.28)] which is a condition for inflation [see Eq. (1.18)].

[2] Here, we ignore the curvature contribution to energy density, which actually could be large initially due to a stage of decelerated expansion prior to inflation. However, once inflation begins, the curvature contribution rapidly dilutes away and can be safely ignored.

rotations [i.e. under SO(3)], the linear perturbations of the metric, $\delta g_{\mu\nu}$, can be classified according to the way they transform under spatial rotation into scalar, vector and tensor modes. Among these only the scalar and tensor perturbation exhibit non-decaying solutions whereas the vector perturbations redshift away quickly with the expansion of the Universe and hence can be ignored. At linear order, different perturbation modes are decoupled from each other and evolve independently.

Clearly, apart from tensor modes, which are automatically gauge invariant, the perturbation modes are not uniquely defined [1]. This issue can be circumvented by either fixing the gauge (in which case the gauge invariance can be restored at the end of the calculation by combining the gauge dependent quantities) or using the transformation properties of the metric fluctuations to construct gauge invariant combinations and limit the calculation to those quantities.

1.4.1 Origin of the cosmic fluctuations

As mentioned earlier the SCM lacks a natural mechanism for the production of primordial cosmic fluctuations which are responsible for the structure in the Universe. We show below how these density perturbations arise as quantum fluctuations on microscopic scales which get stretched by inflation into cosmological scales. These scalar perturbations leave their imprints on the CMB sky in the form of temperature fluctuations, which agree quite well with the observations. We also show how tensor fluctuations originate during inflation, which might be detected in the near future as polarisation fluctuations in the CMB sky.

[1] To see this, consider for example the perturbation in the energy density $\rho(x^\alpha)$. Obviously, $\rho(x^\alpha)$ is a physical quantity and does not change if one changes the coordinates (changes the gauge); instead, it gets re-mapped to the new coordinates. This is not the case, however, for the density perturbation, $\delta\rho(x^\alpha) = \rho(x^\alpha) - \rho(t)$ where $\rho(t)$ denotes the spatial average of $\rho(x^\alpha)$ at time t, since a specific choice of time slicing was made [i.e.,the average of $\rho(x^\alpha)$ is performed along the constant-time hypersurface]. Any change of coordinates, $x^\alpha \to \tilde{x}^\alpha$, which affects the constant-time hypersurfaces will also change the density perturbation [$\delta\rho(\tilde{x}^\alpha)$ in the new coordinates] as $\delta\rho(\tilde{x}^\alpha)$ will be computed by comparing the local value of $\rho(\tilde{x}^\alpha)$ with different physical points on a different constant-time hypersurface.

1.4.1.1 Scalar perturbations

Let us first consider the scalar perturbations which can be easily studied in the spatially-flat gauge. In this gauge, the spatial part of the metric contains only tensor modes; this allows the spatial perturbations of the inflaton field, $\delta\phi$, to decouple from the metric perturbations at leading order. Expanding the inflaton action, Eq. (1.22), to second order (as the first order vanished by its equation of motion at background level), one obtains

$$\begin{aligned}\delta\mathcal{S}_\phi &= \frac{1}{2}\int a^3(t)\mathrm{d}^4x\left[\partial^\mu\delta\phi\partial_\mu\delta\phi - \partial^2_{\bar\phi}V|_{\bar\phi}\delta\phi^2\right]\\ &= \frac{1}{2}\int \mathrm{d}\tau\mathrm{d}^3x\left[\psi'^2 - 2\mathcal{H}\psi'\psi - (\nabla\psi)^2 + (\mathcal{H}^2 - a^2\partial^2_{\bar\phi}V|_{\bar\phi})\psi^2\right]\\ &= \frac{1}{2}\int \mathrm{d}\tau\mathrm{d}^3x\left[\psi'^2 - (\nabla\psi)^2 + \mathcal{H}^2\left(1 + \frac{\mathcal{H}'}{\mathcal{H}^2} - \frac{a^2\partial^2_{\bar\phi}V|_{\bar\phi}}{\mathcal{H}^2}\right)\psi^2\right], \quad (1.34)\end{aligned}$$

where 'prime' denotes derivative w.r.t. conformal time [as defined by Eq. (1.13)] and $\mathcal{H}\equiv a'/a = aH$. Here, we defined $\psi\equiv a\,\delta\phi$ and integrated the $2\mathcal{H}\psi'\psi$ term in the second line by parts. Using Eqs. (1.2), (1.29) and (1.30), one can re-write Eq. (1.34) as

$$\delta\mathcal{S}_\phi = \frac{1}{2}\int \mathrm{d}\tau\mathrm{d}^3x\left[\psi'^2 - (\nabla\psi)^2 + \mathcal{H}^2\left(2 - \epsilon_\phi - 3\eta_\phi\right)\psi^2\right], \quad (1.35)$$

where we substituted $\mathcal{H}^2 = (aH)^2 \simeq V^2/(3M_\mathrm{P}^2)$ which holds true during inflation. Upon the variation of the action, Eq. (1.35), w.r.t. ψ one obtains the equation of motion for ψ,

$$\psi'' - \nabla^2\psi - \mathcal{H}^2\left(2 - \epsilon_\phi - 3\eta_\phi\right)\psi = 0\,. \quad (1.36)$$

The slow-roll parameters, ϵ_ϕ and η_ϕ, are negligibly small during inflation and can be ignored. Now expanding ψ in momentum space,

$$\psi(\tau,\mathbf{x}) = \int\frac{\mathrm{d}^3k}{(2\pi)^3}e^{i\mathbf{k}\cdot\mathbf{x}}\psi_\mathbf{k}(\tau)\,, \quad (1.37)$$

we obtain the equation of motion for each momentum mode

$$\psi_{\mathbf{k}}'' + [k^2 - 2\mathcal{H}^2]\psi_{\mathbf{k}} \simeq 0\,, \tag{1.38}$$

where $k \equiv |\mathbf{k}|$ is the comoving momentum which remains constant with expansion, while the term $2\mathcal{H}^2 = 2(aH)^2 \simeq 2/\tau^2$ (with τ being fixed to zero at the end of inflation) increases exponentially during inflation. As a consequence, each perturbation mode with momentum $\mathbf{k}$ may go through two regimes. At the early stages of inflation the comoving wavelength, $\tilde{\lambda} = 2\pi/k$, of a certain mode can be sub-Hubble (i.e. $\tilde{\lambda} \ll \mathcal{H}^{-1} = (aH)^{-1}$ or equivalently $k \gg \mathcal{H}$) in which case the equation of motion for that mode, Eq. (1.38), reduces to that of a simple quantum harmonic oscillator,

$$\psi_{\mathbf{k}}'' + k^2\psi_{\mathbf{k}} \simeq 0\,, \tag{1.39}$$

with frequency $\omega_k = k$. As the Universe inflates, the comoving Hubble volume shrinks and hence perturbation modes which are initially inside the comoving Hubble volume becomes super-Hubble, i.e. $k \ll \mathcal{H} = aH$ [see Eq. (1.38)]. In this regime, the perturbation mode, $\psi_{\mathbf{k}}$, acquires a tachyonic mass and ceases being quantum. Instead, its subsequent evolution becomes classical with initial conditions set by the preceding quantum sub-Hubble phase. The zero-point fluctuations of these quantum oscillators in the sub-Hubble regime provide the origin for the structure in the Universe. To quantise these oscillators (for more details, see e.g. [45]), we expand $\psi_{\mathbf{k}}$ in terms of the creation and annihilation operators $a_{\mathbf{k}}$ and $a_{\mathbf{k}}^\dagger$:

$$\psi_{\mathbf{k}}(\tau) = v_{\mathbf{k}}(\tau)a_{\mathbf{k}} + v_{-\mathbf{k}}^*(\tau)a_{-\mathbf{k}}^\dagger\,, \tag{1.40}$$

where $\hat{a}_{\mathbf{k}}$ and $\hat{a}_{\mathbf{k}'}^\dagger$ satisfy the commutation relation,

$$[a_{\mathbf{k}}, \hat{a}_{\mathbf{k}'}^\dagger] = (2\pi)^3\delta^3(\mathbf{k} - \mathbf{k}')\,. \tag{1.41}$$

Substituting Eq. (1.40) into Eq. (1.38) and noticing that $\mathcal{H} = -\tau^{-1}$, we obtain

$$v_{\mathbf{k}}''(\tau) + \left(k^2 - \frac{2}{\tau^2}\right) v_{\mathbf{k}}(\tau) = 0\,. \tag{1.42}$$

Eq. (1.42) has the exact solution (see e.g. [40, 41, 44, 46])

$$v_{\mathbf{k}}(\tau) = C_k^{(1)} \frac{e^{-ik\tau}}{\sqrt{2k}} \left(1 - \frac{i}{k\tau}\right) + C_k^{(2)} \frac{e^{ik\tau}}{\sqrt{2k}} \left(1 + \frac{i}{k\tau}\right). \tag{1.43}$$

At early time $t \to 0$ (or equivalently $\tau \to -\infty$), all the cosmologically interesting modes were deep inside the Hubble patch with equations of motion of a simple harmonic oscillator [see Eq. (1.39)] which exhibits two independent solutions, $v_{\mathbf{k}} \propto e^{\pm ik\tau}$. We define the vacuum such that it corresponds to the minimal excitation state (i.e. $\langle 0|\mathrm{H}|0\rangle$ is minimised, where H is the Hamiltonian of the oscillator) which picks the positive frequency mode, $e^{-ik\tau}$. This is known as the "Bunch-Davies vacuum" [47] and is satisfied if $C_k^{(1)} = 1$ and $C_k^{(2)} = 0$ in Eq. (1.43). In the limit $t \to 0$ ($\tau \to -\infty$), it reduces to the following Minkowski vacuum:

$$\lim_{\tau \to -\infty} v_{\mathbf{k}} = \frac{e^{-ik\tau}}{\sqrt{2k}}\,. \tag{1.44}$$

The zero-point fluctuations are usually quantified by the power spectrum, $\mathscr{P}$, defined as follows [1]:

$$\langle 0|\psi_{\mathbf{k}}\psi^{\dagger}_{\mathbf{k}'}|0\rangle = (2\pi)^3 \delta^3(\mathbf{k} - \mathbf{k}')\mathscr{P}_{\psi}(k)\,. \tag{1.45}$$

For later convenience, let us re-define the power spectrum as [2] .

$$\Delta^2_{\psi}(k) \equiv \frac{k^3}{2\pi^2}\mathscr{P}_{\psi}(k)\,. \tag{1.46}$$

[1] The fluctuations produced during single-field inflation are expected to be Gaussian due to the fact that deep inside the Hubble patch the action of ψ, Eq. (1.35), is quadratic and consequently the odd order correlation functions vanish whereas the even order correlation functions can be expressed in terms of two-point ones via Wick's theorem (see e.g. [45, 48]). This has been verified by the measurement of CMB which places strong constraints on the non-Gaussianity of primordial density perturbations [49]. Thus, the power spectrum defined above is sufficient to characterise the inflationary perturbations.

[2] In what follows, we will use $\Delta^2_i(k)$ as the power spectrum.

Now using Eqs. (1.40), (1.41) and (1.43), it is easy to show that

$$\Delta^2_{\psi}(k) = \frac{k^3}{2\pi^2}|v_{\mathbf{k}}|^2 = \frac{k^2}{4\pi^2}\left(1+\frac{1}{k^2\tau^2}\right). \tag{1.47}$$

In terms of $\delta\phi = \psi/a$, the power spectrum of scalar perturbations can be written as

$$\Delta^2_{\delta\phi}(k) = \frac{H^2}{4\pi^2}\left[\left(\frac{k}{aH}\right)^2+1\right], \tag{1.48}$$

where we substituted $\tau = -\mathcal{H}^{-1} = -(aH)^{-1}$. It is clear from Eq. (1.48) that on super-Hubble scales ($k \ll \mathcal{H} = aH$), i.e. several e-folds after the perturbations of cosmological interest leaves the Hubble patch, the power spectrum of the inflaton perturbations,

$$\Delta^2_{\delta\phi}(k) \simeq \frac{H^2}{4\pi^2}\,, \tag{1.49}$$

is constant provided that H is time-independent. The power spectrum of scalar perturbation is usually expressed in terms of the gauge-invariant "curvature perturbation" ($\mathscr{R}$) which in the spatially-flat gauge is related to inflaton perturbation through the relation,

$$\mathscr{R} \equiv -\frac{\mathcal{H}}{\bar{\phi}'}\delta\phi = -\frac{H}{\dot{\bar{\phi}}}\delta\phi = -\frac{\delta\phi}{\sqrt{2\epsilon_\phi}M_{\rm P}} = -\frac{\delta\phi}{M^2_{\rm P}}\left|\frac{V}{\partial_\phi V}\right|_{\bar{\phi}}, \tag{1.50}$$

where we used Eqs. (1.2) and (1.29). Now using Eqs. (1.49) and (1.50), the power spectrum of curvature perturbations on super-Hubble scales can be expressed as

$$\Delta^2_{\mathscr{R}}(k) \equiv \frac{k^3}{2\pi^2}\mathscr{P}_{\mathscr{R}}(k) \simeq \frac{1}{8\pi^2\epsilon_\phi}\frac{H^2}{M^2_{\rm P}} \simeq \frac{1}{12\pi^2}\frac{V^3}{M^6_{\rm P}(\partial_\phi V)^2}\bigg|_{\bar{\phi}}. \tag{1.51}$$

For exact de Sitter Universe, the power spectrum of curvature perturbations, $\Delta^2_{\mathscr{R}}$, is scale-invariant. This is not actually the case; $\Delta^2_{\mathscr{R}}$ exhibits a slight k-dependence due the slow time variation of both H and ϵ_ϕ while different momentum modes successively exit the Hubble patch. This scale-dependence is usually parameterised as (see e.g. [50])

$$\Delta^2_{\mathscr{R}}(k) = A_s \left(\frac{k}{k_\star}\right)^{n_s - 1 + \frac{1}{2}\frac{\mathrm{d}n_s}{\mathrm{d}\ln k}\ln\left(\frac{k}{k_\star}\right) + \text{higher orders}} , \tag{1.52}$$

where $k_\star \equiv 0.05$ Mpc^{-1} is the reference scale chosen by the Planck collaboration [13]. At this pivot scale, the amplitude of scalar perturbations is measured to be $A_s \equiv \Delta^2_{\mathscr{R}}(k_\star) = (2.142 \pm 0.049) \times 10^{-9}$ at 68% CL [13]. In Eq. (1.52), the parameter n_s, known as the "spectral index of scalar perturbations", is measured to be $n_s = 0.9667 \pm 0.0040$ at 68% CL and the factor $\frac{\mathrm{d}n_s}{\mathrm{d}\ln k}$ in Eq. (1.52) denotes the "running of the spectral index" [1]. The running of the spectral index and the higher order terms in the exponent of Eq. (1.52) are compatible with zero ($\frac{\mathrm{d}n_s}{\mathrm{d}\ln k}|_{k_\star} = -0.0065 \pm 0.0076$ at 68% CL) [13]. The spectral index of scalar perturbations can be expressed in terms of the slow-roll parameters as follows:

$$\begin{aligned} n_s - 1 &\simeq \frac{\mathrm{d}\ln\Delta^2_{\mathscr{R}}}{\mathrm{d}\ln k} = \frac{\mathrm{d}\ln\Delta^2_{\mathscr{R}}}{\mathrm{d}N}\frac{\mathrm{d}N}{\mathrm{d}\ln k} \simeq \left[2\frac{\mathrm{d}\ln H}{\mathrm{d}N} - \frac{\mathrm{d}\ln\epsilon_\phi}{\mathrm{d}N}\right]\left[\frac{\mathrm{d}(N+\ln H)}{\mathrm{d}N}\right]^{-1} \\ &\simeq -6\epsilon_\phi + 2\eta_\phi \,, \end{aligned} \tag{1.53}$$

where we have used Eqs. (1.2),(1.29) and (1.30), and evaluated the expression at Hubble exit ($k = aH$).

1.4.1.2 Tensor perturbations

Let us now consider the tensor perturbations. Unlike the primordial scalar perturbations responsible for the CMB fluctuations and the observed large scale structure, tensor perturbations do not play a role in the formation of structure. Nevertheless if present, they can cause polarisation fluctuations in the CMB sky. Expanding the Einstein-Hilbert (gravity) action to second order (the first non-trivial order), one obtains [28, 29, 30, 43, 44, 53]

$$\delta\mathcal{S}_{\mathrm{EH}} = \frac{M_{\mathrm{P}}^2}{8}\int \mathrm{d}\tau \mathrm{d}^3x\, a^2 \left[(\hat{E}'_{ij})^2 - (\nabla\hat{E}_{ij})^2\right] , \tag{1.54}$$

[1] If n_s were equal to one, we would have had a scale-invariant spectrum which is also known as "Harrison-Zel'dovich spectrum" [51, 52]. Instead, observation indicates a red-tilted spectrum ($n_s < 1$) [13].

where $\hat{E}_{ij}$ is a symmetric, transverse, traceless tensor which has only two d.o.f. [1]. $\hat{E}_{ij}$ is usually decomposed as $\hat{E}_{ij} = \varepsilon_l e_{ij}^{(l)}$ $(l = +, \times)$ where $e_{ij}^{(+)} = \frac{1}{\sqrt{2}}(e_i^{(1)} e_j^{(1)} - e_i^{(2)} e_j^{(2)})$ and $e_{ij}^{(\times)} = \frac{1}{\sqrt{2}}(e_i^{(1)} e_j^{(2)} + e_i^{(2)} e_j^{(1)})$ with $\mathbf{e}^{(1)}$ and $\mathbf{e}^{(2)}$ being two orthonormal vectors lying in the plane perpendicular to the direction of propagation. Further, it is convenient to define $\psi_l \equiv a M_{\rm P} \varepsilon_l / 2$ $(l = +, \times)$. Hence Eq. (1.54) can be re-written as

$$\begin{aligned} \delta \mathcal{S}_{\rm EH} &= \frac{1}{2} \int \mathrm{d}\tau \, \mathrm{d}^3 x \sum_{l=+,\times} \left[(\psi_l')^2 - (\nabla \hat{\psi}_l)^2 + \mathcal{H}^2 \left(1 + \frac{\mathcal{H}'}{\mathcal{H}^2} \right) \psi_l^2 \right] \\ &= \frac{1}{2} \int \mathrm{d}\tau \, \mathrm{d}^3 x \sum_{l=+,\times} \left[(\psi_l')^2 - (\nabla \hat{\psi}_l)^2 + \mathcal{H}^2 (1 - \epsilon_\phi) \psi_l^2 \right] , \end{aligned} \tag{1.55}$$

where we used Eq. (1.29). This is the same action as that for the scalar perturbations, Eq. (1.35), except that tensor perturbations have two polarisation modes. From Eq. (1.49), one can then write down the power spectrum for tensor perturbations on super-Hubble scales

$$\Delta_t^2(k) = 2 \times \Delta_\varepsilon^2(k) \simeq 2 \times \left(\frac{2}{M_{\rm P}} \right)^2 \times \frac{H^2}{(2\pi)^2} = \frac{2}{\pi^2} \frac{H^2}{M_{\rm P}^2} \, . \tag{1.56}$$

Similar to the case of scalar perturbations, the power spectrum of tensor perturbations exhibits a slight scale-dependence due to the slow variation of H in time during inflation. This k-dependence of the power spectrum of tensor perturbations can be parameterised in a similar fashion to the scalar perturbations case,

$$\Delta_t^2(k) = A_t \left(\frac{k}{k_\star} \right)^{n_t + \frac{1}{2} \frac{\mathrm{d}n_t}{\mathrm{d}\ln k} \ln\left(\frac{k}{k_\star}\right) + \text{higher orders}} , \tag{1.57}$$

where $A_t \equiv \Delta_t^2(k_\star)$, n_t denotes the spectral index of tensor perturbations and $\frac{\mathrm{d}n_t}{\mathrm{d}\ln k}$ is the running of the spectral index ($n_t = 0$ corresponds to a scale-invariant spectrum). For slow-roll inflation, it is easy to show that $n_t \simeq -2\epsilon_\phi$.

It is clear from Eq. (1.56) that the power spectrum of the tensor perturbations is directly connected to the energy scale of inflation, $H^2 \propto \rho$. Therefore, the measurement of the amplitude of tensor perturbations would fix the scale of inflation (i.e. how early in the history of the cosmos inflation occurred) [54].

[1] $\hat{E}_{ij}$ is the (transverse traceless) tensorial part of the metric fluctuations.

The amplitude of scalar perturbations is usually normalised to that of scalar perturbations,

$$r \equiv \left.\frac{\Delta_t^2}{\Delta_{\mathscr{R}}^2}\right|_{k=k_\star} = \frac{A_t}{A_s}\,, \tag{1.58}$$

where r is know as the "tensor-to-scalar ratio". For slow-roll inflation $r \simeq 16\epsilon_\phi$ [see Eqs. (1.51) and (1.56)]. The non-observation of tensor modes in the CMB sky places an upper bound on the tensor-to-scalar ratio, $r_{0.05} < 0.07$ at 95% CL [55] which constrains the energy scale of (slow-roll) inflation (e.g. [54, 56]),

$$\begin{aligned} \rho^{1/4} &\simeq 7.4 \times 10^{-3} \left(\frac{r}{0.07}\right)^{1/4} M_{\rm P} \lesssim 1.8 \times 10^{16}\,{\rm GeV}\,, \\ H &\simeq 3.1 \times 10^{-5} \left(\frac{r}{0.07}\right)^{1/2} M_{\rm P} \lesssim 7.6 \times 10^{13}\,{\rm GeV}\,. \end{aligned} \tag{1.59}$$

1.4.2 Growth of density perturbations

The scalar perturbations produced during inflation are pushed outside the Hubble patch due to the quasi-exponential expansion. After inflation, the comoving Hubble patch starts to expand and consequently the perturbations modes which are frozen on super-Hubble scales successively re-enter the Hubble patch. Once a perturbation mode is inside the comoving Hubble patch, it starts evolving.

Let us now consider the evolution of the perturbation modes governed by the Einstein field equations which relate the scalar metric perturbations to density and pressure fluctuations in the cosmic fluid. This is most conveniently done in the conformal Newtonian gauge. In this gauge, there are only two scalar modes (Φ and Ψ) which are actually equal in the absence of anisotropic stresses (perfect fluid approximation) [1]. On sub-Hubble scales, Φ acts as a Newtonian potential. For the purpose of analytical estimation, a single component domination is assumed [2].

[1] This is true provided that Φ and Ψ are Gaussian, random fields which is actually the case according to the measurement of CMB [49]. Note that, some components of the cosmic fluid such as neutrinos which decouple from the plasma when the temperature drops to a few MeV, do not behave as ideal fluids and can give rise to small anisotropic stresses. However, this effect becomes negligible once matter comes to dominate the Universe. We do not discuss this issue here.

[2] For detailed discussion see e.g. [28, 29, 30, 43, 44]. Here we just quote the relevant results.

The cosmic fluid is made of multiple components such as non-relativistic matter dominated by DM and plasma which consists of photons, baryons and leptons [1]. On super-Hubble scales, the scalar perturbations are constant and related to the gauge-invariant curvature perturbations through the relation:

$$\Phi_k \simeq -\frac{3+3\omega}{5+3\omega}\mathscr{R}_k\,, \tag{1.60}$$

which provides the initial condition for the subsequent sub-Hubble evolution. Here, the curvature perturbation, $\mathscr{R}_k$, is given by Eq. (1.50). The density perturbation of the dominant fluid component is

$$\delta_k \equiv \frac{\delta\rho_k}{\bar{\rho}} = -\frac{2}{3}\frac{k^2}{\mathcal{H}^2}\Phi_k - 2\Phi_k - \frac{2}{\mathcal{H}}\Phi_k'\,, \tag{1.61}$$

where $\delta \equiv \delta\rho/\bar{\rho}$ denotes the density contrast. On super-Hubble scales ($k \ll \mathcal{H}$), $\delta_k \simeq -2\Phi_k \simeq$ constant. For modes that re-enter the Hubble patch during RD, $\Phi_k \simeq -\frac{2}{3}\mathscr{R}_k$ on super-Hubble scales, whereas deep inside the Hubble patch

$$\Phi_k(\tau) = 6\mathscr{R}_k\left[\frac{(k\tau)\cos(k\tau/\sqrt{3}) - \sqrt{3}\sin(k\tau/\sqrt{3})}{(k\tau)^3}\right], \tag{1.62}$$

i.e. the gravitational potential exhibits an oscillatory behaviour with a decaying amplitude and a well-defined phase. Using Eq. (1.61), one then obtains the sub-Hubble radiation density contrast

$$\delta_{\mathrm{rad},k}(\tau) \simeq 6\,\Phi_k^{(i)}\cos(k\tau/\sqrt{3}) \simeq -4\,\mathscr{R}_k\cos(k\tau/\sqrt{3})\,. \tag{1.63}$$

Clearly, the radiation density fluctuations do not grow during RD; instead, they oscillate around $\delta_{\mathrm{rad},k} = 0$ with a constant amplitude (acoustic oscillations). They continue to oscillate even after matter comes to dominate the energy density of the Universe, albeit with a shifted equilibrium point $\delta_{\mathrm{rad},k} \simeq -4\Phi_{\mathrm{DM},k}$ because of the potential due to the fluctuation in DM (and baryons) density. The acoustic

[1] Baryons, leptons and photons remain coupled until the temperature drops to roughly 1 eV.

oscillations in the radiation density show up in the CMB temperature angular power spectrum as peaks and troughs.

On the other hand, the perturbations in the sub-dominant DM fluid, which are constant on super-Hubble scales, $\delta_{\rm DM,}{}_k = \mathscr{R}_k$ [1], start growing once they re-enter the Hubble patch. DM density perturbation modes that re-enter the Hubble patch during RD grow only logarithmically till the end of RD,

$$\delta_{{\rm DM},k}(\tau) \simeq -9\,\Phi_k^{(i)}\left[\ln(k\tau/\sqrt{3}) + \gamma_{\rm E} - \frac{1}{2}\right] \simeq 6\mathscr{R}_k\left[\ln(k\tau/\sqrt{3}) + \gamma_{\rm E} - \frac{1}{2}\right], \quad (1.64)$$

where $\gamma_{\rm E} = 0.577$ is the Euler constant. This is due to the fact that during RD the gravitational potential is mostly dominated by the rapidly-decaying density fluctuation in the relativistic fluid [see Eq. (1.62)] [2]. However, as it is clear from Eq. (1.64), besides their logarithmic growth during RD, the DM density perturbations are enhanced by a significant numerical factor over the initial value, $\delta^{(i)}_{{\rm DM},k} = \mathscr{R}_k$.

Let us now consider the evolution of DM perturbation during MD. On super-Hubble scales ($k \ll \mathcal{H}$), $\delta_{{\rm DM},k} \simeq -2\Phi_k^{(i)} \simeq \frac{6}{5}\mathscr{R}_k \simeq$ constant [see Eq. (1.60)]. It can be shown that the Newtonian potential, Φ_k, is also constant on sub-Hubble scales (see e.g. [29, 30]). Thus, using Eq. (1.61), the DM density contrast on sub-Hubble scales ($k \gg \mathcal{H}$) is given by

$$\delta_{{\rm DM},k}(\tau) \simeq -\frac{2}{3}\frac{k^2}{\mathcal{H}^2}\Phi_k^{(i)} \simeq -\frac{2}{3}\Phi_k^{(i)}\frac{a(\tau)}{a(\tau_\times)} \simeq -\frac{2}{5}\mathscr{R}_k\frac{a(\tau)}{a(\tau_\times)} = \frac{1}{3}\delta^{(i)}_{{\rm DM},k}\frac{a(\tau)}{a(\tau_\times)}\,, \quad (1.65)$$

where we substituted $k = \mathcal{H}_\times$ with the subscript '$\times$' referring to the second Hubble crossing (i.e. the time at which a particular perturbation mode re-enters the Hubble sphere), and $\mathcal{H} = \mathcal{H}_\times[a(\tau_\times)/a(\tau)]^{1/2}$ during MD. Further, for DM density perturbation modes that re-enter the Hubble patch during RD, these keep growing during MD but now linearly instead of logarithmically as they do during RD,

[1] Here, we assume adiabatic initial condition $\delta^{(i)}_{{\rm DM},k} = \frac{3}{4}\delta^{(i)}_{{\rm rad},k}$, see Section 1.4.3 below.

[2] The gravitational potential also receives a contribution from the perturbations in the DM fluid $\Phi_{{\rm DM},k} = -(a/k)^2(\bar{\rho}_{\rm DM}/2M_{\rm P}^2)\,\delta_{\rm DM}$ which is small compared to Eq. (1.62) deep inside RD as $\bar{\rho}_{\rm DM}$ is relatively small.

$$\delta_{\mathrm{DM},k}(\tau) \simeq -\frac{27}{2}\frac{a(\tau)}{a(\tau_{\mathrm{eq}})}\Phi_k^{(i)}\ln(0.15k\tau_{\mathrm{eq}}) \simeq 9\mathscr{R}_k\frac{a(\tau)}{a(\tau_{\mathrm{eq}})}\ln(0.15k\tau_{\mathrm{eq}})\,. \tag{1.66}$$

It is worth noting here that baryons, which are already non-relativistic during MD, contribute to both the total energy density and matter perturbations which gives rise to a contribution to the DM density perturbations growth equations, albeit relatively small (see e.g. [30]). Let us further consider the evolution of matter deep inside the era of DE domination in which case $a\propto|\tau|^{-1}$, i.e. $\mathcal{H}=|\tau|^{-1}$. Assuming that DE is constant in space and time, $\delta\rho_{_\Lambda}=\delta\mathcal{P}_{_\Lambda}=0$,

$$\Phi_k \propto \begin{cases} \tau \propto a^{-1} \\ \tau^3 \propto a^{-3}\,, \end{cases} \tag{1.67}$$

and since $\delta\rho_{_\Lambda}=0$, i.e. $\delta\rho=\delta\rho_{\mathrm{m}}$, the matter density contrast is given by

$$\delta_{\mathrm{m}} \simeq -\frac{2M_{\mathrm{P}}^2}{\bar{\rho}_{\mathrm{m}}}\frac{k^2}{a^2}\Phi \propto \begin{cases} a^3\frac{k^2}{a^2}a^{-1} = \text{constant} \\ a^3\frac{k^2}{a^2}a^{-3} \propto a^{-2}\,, \end{cases} \tag{1.68}$$

i.e. the density fluctuations stop growing once the Universe starts expanding quasi-exponentially. However, in reality the present DE domination in the Universe is not sufficient to cause it to expand quasi-exponentially. Instead the scale factor still increases with a power law. Thus, DM density perturbation modes that re-enter the Hubble patch today can still grow.

To sum up this section, all perturbations modes are constant on super-Hubble scales and start evolving once they re-enter the Hubble patch. The radiation density perturbations oscillate with a decaying amplitude whereas the perturbations in DM density grow logarithmically in the scale factor during RD and linearly during MD. Note that baryons, which are already non-relativistic when the perturbation modes of cosmological interest re-enter the Hubble patch, are coupled to photons through Compton scattering and hence their perturbations do not grow until they decouple from photons, which occurs at redshift $z_{\mathrm{dec}}\simeq 1190$ [13]. By that time, $\delta_{\mathrm{DM}} \gg \delta_{\mathrm{b}}$, where δ_{b} denotes the baryons' density contrast. As a result, baryons fall into the DM potential wells.

Many of the matter perturbation modes have already become non-linear a

long time ago and have grown into the structure we observe today. However, matter perturbations with longer wavelengths which re-enter the Hubble patch during MD (or shortly before radiation-matter equality) are still in the linear regime. Therefore, the Universe on these scales and larger ($\gtrsim 100\,\mathrm{Mpc}$) is still mostly homogeneous. In other words, there are no gravitationally bound systems with masses $\gtrsim 10^{16} M_\odot$, where $M_\odot \simeq 1.988 \times 10^{33}$ g is the solar mass (see e.g. [30]). Matter perturbations with shorter wavelengths grow according to Eq. (1.66), which upon using Eq. (1.12) can be re-written as

$$\delta_{\mathrm{DM},k}(z) \simeq 9\,\mathscr{R}_k \frac{1+z_{\mathrm{eq}}}{1+z} \ln\left(0.15 k \tau_{\mathrm{eq}}\right) . \tag{1.69}$$

Using the measured values provided by the Planck collaboration: $\Delta^2_{\mathscr{R}} \simeq 2 \times 10^{-9}$ and $z_{\mathrm{eq}} \simeq 3393$ [13], one can see that for $\delta_{\mathrm{DM},k}$ to become $\gtrsim \mathcal{O}(1)$, $\ln(0.15 k \tau_{\mathrm{eq}})$ has to be $\gtrsim 1$ which implies that modes with $k/a(t_0) \gtrsim (10\,\mathrm{Mpc})^{-1}$ have already become non-linear. This corresponds to length scales $\lesssim 30\,\mathrm{Mpc}$ and masses $\lesssim 10^{15} M_\odot$. Of particular interest is the formation of galaxies, mass $\sim (10^{11}$–$10^{12}) M_\odot$, which starts at $z \sim 4$ (see e.g. [30]). Figure 1.1 shows a sketch of the time evolution of density perturbations of the different components of the cosmic fluid that re-enter the Hubble patch during RD along with the Newtonian potential.

1.4.3 Adiabatic vs isocurvature initial conditions

As shown in Section 1.4.2, there are fluctuations in the different components of the cosmic fluid such as that in radiation (photons and baryons) and DM. In principle the initial values for these perturbations can be either independent or correlated. The latter case is referred to as "adiabatic" initial conditions. Heuristically in the conformal Newtonian gauge, the adiabatic mode can be viewed as a time shift, i.e. the local perturbations in the quantities characterising the state of the cosmic fluid at a spacetime point, $(\tau, \mathbf{x})$, are the same as in the unperturbed Universe at some slightly different time $\tau + \delta\tau(\mathbf{x})$ where $\delta\tau(\mathbf{x})$ is common for all the constituents of the cosmic fluid,

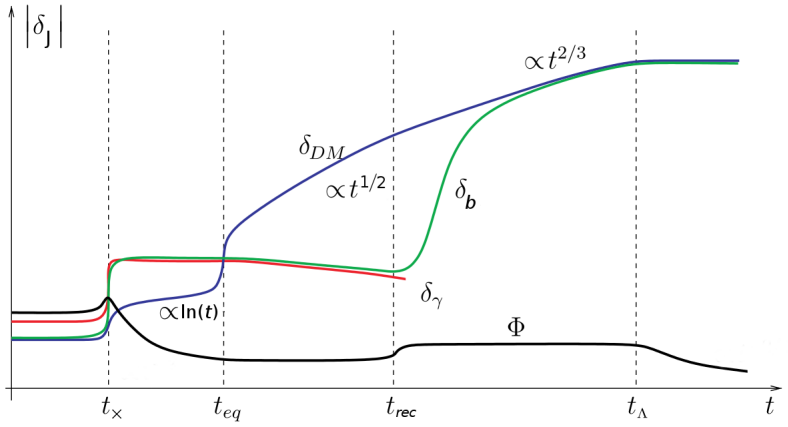

Figure 1.1: A sketch of the time evolution of the density perturbations of different components of the cosmic fluid, $\delta_{\rm DM}$, $\delta_{\rm b}$ and δ_γ, and the gravitational potential, Φ, in the linear regime; adapted from reference [57]. Here, $t_\times$ denotes the time at which a perturbation mode re-enters the Hubble patch, $t_{\rm eq}$ is the time of radiation-matter equality, $t_{\rm rec}$ is the time at which recombination takes place, and t_Λ is the time at which DE comes to dominate the energy density of the Universe.

$$\delta\rho_i(\tau,\mathbf{x}) \equiv \bar{\rho}_i(\tau+\delta\tau(\mathbf{x})) - \bar{\rho}_i(\tau) = \bar{\rho}_i'\delta\tau(\mathbf{x})\,, \tag{1.70}$$

$$\delta\mathcal{P}_i(\tau,\mathbf{x}) \equiv \bar{\mathcal{P}}_i(\tau+\delta\tau(\mathbf{x})) - \bar{\mathcal{P}}_i(\tau) = \bar{\mathcal{P}}_i'\delta\tau(\mathbf{x})\,. \tag{1.71}$$

Making use of the continuity equation [Eq. (1.5)], Eq. (1.6), and Eq. (1.70), one can write

$$\frac{\delta_i}{1+\omega_i} = \frac{\delta_j}{1+\omega_j}\,, \tag{1.72}$$

for all species i and j. Thus, for adiabatic initial conditions $\delta_{\rm DM} = \frac{3}{4}\delta_{\rm rad}$. Further, since the density contrast of different components of the cosmic fluid are of comparable size, the total density perturbation of the fluid, $\delta\rho = \bar{\rho}\,\delta_{\rm tot} = \sum_i \delta\rho_i = \sum_i \bar{\rho}_i\delta_i$, is dominated by the component that dominates its energy density. It is timely to note that single field inflation models predict completely adiabatic initial perturbations.

The adiabaticity of the Universe can get violated if the equation of state of the cosmic fluid is not just a function of density but also entropy, in which case there would be perturbations between the different components of the cosmic fluid. Such perturbations are referred to as "isocurvature perturbations". Together with the adiabatic perturbation, they form a complete orthogonal basis for general

density perturbations. Using Eq. (1.72), the isocurvature perturbations can be defined as

$$\delta S_{ij} \equiv \frac{\delta_i}{1+\omega_i} - \frac{\delta_j}{1+\omega_j} \,. \tag{1.73}$$

Isocurvature perturbations can be generated if there is more than one degree of freedom present during inflation such as the case of multiple fields driving inflation or the case where a light DM (e.g. axion) field is present during inflation. However, the measurement of CMB restricts the non-adiabatic perturbations – if they exist – to a few percent [13].

1.4.4 Free-streaming effect

As mentioned earlier, the density perturbations, in particular that in DM, which are responsible for the structure in our Universe were pushed out of the Hubble patch during inflation and re-entered the Hubble patch during RD. In the SCM, DM particles are assumed to have negligible velocities (cold DM) and hence cannot stream out from the over-dense regions to the underdense regions of sub-Hubble DM density perturbations in a Hubble time. Thus, matter perturbations on all cosmological scales can grow once they are within the Hubble patch. However, if the DM particles have non-negligible velocities, they can stream from the over-dense regions to the under-dense regions, washing out all perturbations in the DM fluid within their reach in a Hubble time. This is known as the "free-streaming effect" and the distance that DM particles can travel in a Hubble time is roughly the "free-streaming length".

In particular hot DM, which remains relativistic till the era of radiation-matter equality, washes out all DM perturbations that re-enter the Hubble patch before equality and even many of those that re-enter the Hubble patch after equality. Thus, the abundance of hot DM species is severely constrained, otherwise, density fluctuations of galaxy size and larger would have been erased, in which case superclusters would form first and later galaxies via the fragmentation of superclusters; however, this scenario does not lead to the observed Universe (see e.g. [46, 56]).

An interesting class of DM, known as "warm DM", is characterised by a non-negligible particle velocity during MD. These DM particles were relativistic deep

inside RD and hence suppress the amplitude of all DM perturbations that re-enter while the DM particles are still relativistic, $\delta_{\rm DM} \propto (k\tau)^{-1}$ [1]. However, the warm DM particles become non-relativistic much before radiation-matter equality (roughly at the time perturbations of galaxy size re-enter the Hubble patch which takes place at $T \sim 1$ keV). Nevertheless, they can still affect the evolution of DM density perturbations during MD. In particular, all DM perturbations within the reach of DM particles in a Hubble time get suppressed, which is usually quantified via the free-streaming length, $\lambda_{fs}(t) = a(t)\tilde{\lambda}_{fs} = 2\pi a(t)/k_{fs}$ where

$$k_{fs} \simeq \left(\frac{\bar{\rho}_{\rm DM} a^2}{2M_{\rm P}^2}\right) \left\langle \frac{1}{u^2} \right\rangle^{1/2} = \sqrt{\frac{3}{2}} aH \left\langle \frac{1}{u^2} \right\rangle^{1/2} \tag{1.74}$$

with u being the velocity of particles. In other words, perturbations whose current size is $\ll \lambda_{fs}(t_0) = (1+z(t))\lambda_{fs}(t)$ are suppressed by the free-streaming of warm DM particles.

1.5 Dark matter

The idea of DM existence in the form of obscure celestial objects goes well back in history (for a historical review see e.g. [58]). Nevertheless, the observational hints for the presence of such non-luminous matter started showing up only about eighty years ago. By now there is a wide variety of evidence supporting the existence of DM on all cosmological scales. However, its nature remains unknown. In this section, we briefly review the observational indications for the existence of DM, discuss its known properties, and survey some of the famous candidates with emphasis on the particle DM candidates. Further, we briefly review some of the DM search techniques.

[1] More explicitly, the amplitude of perturbation modes with $k\tau_{\rm nr} \ln(\tau_{\rm eq}/\tau_\times) \gg 1$ (where $\tau_{\rm nr}$ denotes the conformal time at which DM particles start becoming non-relativistic) which re-enter the Hubble patch before equality gets suppressed.

1.5.1 The evidence for dark matter

So far DM has demonstrated its presence only via gravitational interactions with its surroundings. A wide variety of evidence of this kind has been accumulated. In this section, let us review some of these gravitational clues.

1.5.1.1 Galactic rotation curves and dynamics of clusters

Perhaps the first observational hint, which later became the first widely-accepted evidence for the existence of large amounts of DM, was the discrepancy between the measured rotational velocities of the stars of disk galaxies (or hydrogen and helium rich clouds of gas surrounding hot stars as a proxy measurement of the motion of the stars themselves) and the corresponding theoretical prediction [16, 17, 59, 60] [1]. The observed flat rotation curves of spiral galaxies (see Figure 1.2) suggests the existence of large amounts of non-luminous (dark) matter (see e.g.[21, 22, 23, 61]).

From Newtonian dynamics, one would expect that the rotational velocities of stars beyond the galactic disk of a galaxy (which contains most of the luminous matter of the galaxy in the form of gas and stars) will fall as $v(r) \propto r^{-1/2}$. However, the observed approximately-flat galactic rotation curves, as can be seen from Figure 1.2, require that beyond the central bulge and up to a certain extent the total mass within radius r, $M(r) = \int \mathrm{d}^3 r \rho(r)$, increases roughly as r. This indicates the existence of additional, non-luminous matter. Numerical simulations show that DM is isotropically distributed in galaxies in the form of halos that extend much beyond the visible galactic disks and that the DM distribution exhibits a universal form (see e.g. [62, 63, 64]) which can be modelled for example by the Navarro-Frenk-White (NFW) [65], the Einasto [66] or the Burkert profiles [67].

Other hints for the presence of non-luminous matter on larger scales also exist. For instance, a study of the Coma Cluster showed that the dynamical mass of the cluster, obtained by measuring the velocity dispersion of roughly 1000 nebulae

[1] This discrepancy was first observed in the 1920s. However, besides the existence of DM other explanations such as the absorption of light by dust and other matter within galaxies were also invoked [17, 59]. It was not until the 1970s when the galactic rotation curves were measured to large radial extents that the DM explanation became widely accepted [21, 22, 23, 61].

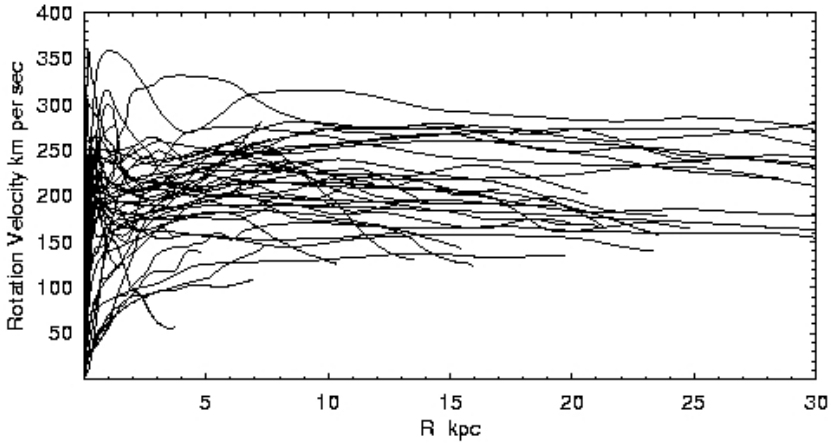

Figure 1.2: Rotation curves of a set of spiral galaxies; taken from reference [68].

in the cluster and then applying the virial theorem to obtain the total mass of the cluster, is much larger than the one obtained using the standard mass-to-light ratio for nebulae. This discrepancy indicated the existence of a significant amount of non-luminous matter in the cluster [18, 19] [1].

1.5.1.2 Gravitational lensing

Another piece of evidence for the existence of large amounts of DM comes from gravitational lensing analyses [70, 71, 72, 73, 74]. According to GR the presence of matter (or energy) in a region of space curves its geometry resulting in a deflection of the light beams propagating through or close to that region. As a result, the images of distant galaxies get distorted if their light goes through or passes by a foreground dense matter field [2]. From the distortions pattern, one can deduce the density of matter along the line of sight. The observation of many lensing clusters such as Abell 370, Bergmann, Petrosian, and Lynds show that the masses of these clusters, calculated based on their lensing effect, are much larger than the ones deduced from their luminosities, indicating the existence of large amounts of DM in these clusters (see [75] and references therein).

[1] Dwarf spheroidal galaxies also exhibit relatively large velocity dispersions suggesting the existence of large amounts of DM. In some of these galaxies the ratio of the dynamical to luminous mass is an order of magnitude higher than that for spiral galaxies [69].

[2] The distorted galaxies' images usually appear as arclets or partial Einstein rings.

Figure 1.3: The Bullet Cluster: the bluish haze shows the DM inferred from the lensing map [76] whereas the reddish haze shows the gas cloud containing most of the baryons in the Bullet cluster inferred from the X-ray observations [77]. Taken from reference [78].

The same technique can be used to reconstruct the mass distribution within the foreground object. A significant example of the application of the gravitational lensing technique to deduce the mass distribution is the Bullet cluster, which is, in fact, the merger of two clusters [77], see Figure 1.3 [1]. The X-ray data of the merger shows that the gaseous halos, containing most of the baryonic matter in the Bullet cluster (shown in Figure 1.3 by the reddish haze), are lagging behind [77] whereas the less interactive mass, which is mostly in DM (shown in Figure 1.3 by the bluish haze), lies well ahead of the baryonic gas clouds dragging along most of the galaxies as revealed by the lensing data [76, 80]. The galaxies within the two clusters, being almost point-like objects on galaxy cluster scales, go through almost unaffected. Other galaxy cluster mergers such as the MACS J0025.4-1222 cluster [81] and the Cl0024+17 cluster [82] have been observed. The gravitational lensing data show that the (dark) matter distribution in the MACS J0025.4-1222 cluster is remarkably similar to that of the Bullet cluster [83] whereas in the Cl0024+17 cluster the DM is concentrated in the centre of the cluster and in a ring around the centre [84]. Again both clusters seem to be dominated by DM.

[1]The Bullet cluster is the result of a sub-cluster, referred to as the "bullet", colliding with the larger cluster 1E 0657-56 [77, 79].

1.5.1.3 Cosmic Microwave Background radiation

Yet more evidence for DM comes from the measurement of the CMB [13]. The observed tiny fluctuations in the CMB temperature, $\delta T/T \simeq 10^{-4}$–$10^{-5}$ [33], which correspond to density fluctuations of the same order of magnitude, indicates the existence of large amounts of DM. Since baryons are coupled to the photon bath roughly till redshift $z_{\rm dec} \simeq 1090$ [13] and the matter fluctuations grow as $\delta\rho_m/\bar{\rho}_m \propto a$ during MD [see Eq. (1.65)], i.e. $|\delta\rho_b/\bar{\rho}_b|_0 \sim [a(t_0)/a(t_{\rm dec})] \times 10^{-4} \sim z_{\rm dec} \times 10^{-4} \sim 10^{-1}$, the observed structure would have not been formed if bayrons were the only form of matter in the Universe [85, 86]. This is because the photon pressure prevents the growth of the density fluctuations of baryons till they decouple from each other. Thus, another form of cold (or at most warm) matter that decouples from the thermal bath much before radiation-matter equality (i.e. a form of matter that is weakly coupled to the cosmic plasma) is needed such that the initial density fluctuations have enough time to evolve non-linearly into the observed structure.

Fitting the CMB angular power spectrum (see Figure 1.4) with the best currently available cosmological model, the SCM, indicates that matter constitutes roughly 30% of the total energy budget in the Universe ($\Omega_{m,0} = 0.3156 \pm 0.0182$) of which roughly 83% is DM ($\Omega_{\rm DM,0} \simeq 0.2608^{+0.0131}_{-0.0125}$ which corresponds to average DM density $\rho_{\rm DM,0} \simeq 1.264\,{\rm keV/cm^3} \simeq 2.254 \times 10^{-30}\,{\rm g/cm^3}$) [13] [1]. Moreover, the evolved matter power spectrum has been obtained by mapping around one million galaxies in the sky (see the Sloan Digital Sky Survey (SDSS) [5, 6]) yielding a very similar result for the DM abundance in the Universe (see e.g. [88, 89, 90]) [2]. Furthermore, N-body simulations of the large scale structure in the Universe have shown the need for DM to reproduce the observed structure (see e.g. [62, 63, 64]).

[1] The overall height of the peaks in the CMB power spectrum is sensitive to DM abundance whereas the relative height of the odd and even peaks determines the abundance of baryons, see Figure 1.4.

[2] Besides the study of the CMB and large scale structure, other measurements such as that of the abundance of light chemical elements synthesized in BBN [91, 92, 93, 94, 95] and absorption lines of the light of distant Quasars [96] show that the abundance of baryons constitutes less than 5% of the total energy content of the Universe.

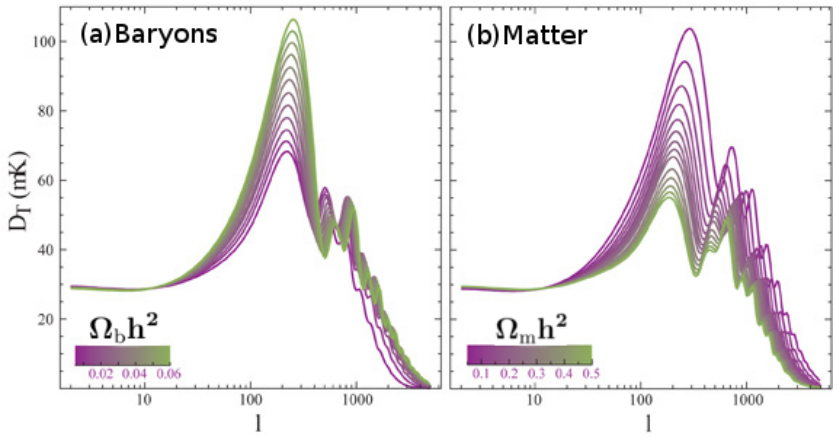

Figure 1.4: Sensitivity of the CMB angular power spectrum to (a) the abundance of baryons (b) the abundance of matter (in particular DM) where $\Omega_{\rm tot}$ is fixed to unity. Adapted from reference [87]. Here the horizontal axis shows the different multipole moments (which correspond to different angular scales), whereas the vertical axis shows the power per each multipole.

1.5.2 Dark matter properties

Here, we briefly review the properties of DM which have been deduced from a wide variety of observations.

We begin with the abundance of DM which (assuming ΛCDM) is known to a high precision from the measurement of the CMB: $\Omega_{\rm DM}h^2 = 0.1198 \pm 0.0030$ at 95% CL, where $h = 0.6726 \pm 0.0098$ denotes the reduced Hubble parameter [13]. However, we know very little about the DM mass; the allowed masses for the dominant DM species roughly range from 10^{-22} eV to several orders of magnitude of the mass of the sun. The lower limit is for bosonic DM [1] and arises from the requirement that the average de Broglie wavelengths of DM particles has to be less than the typical size of Milky Way satellites (few kpcs) [100, 101, 102]. Such light DM species are known as "Fuzzy DM" [100]. On the other hand, the upper bound arises from the possibility that DM is made of Primordial Black Holes (PBHs) [103] which can be several orders of magnitude as massive as the sun (see Section 1.5.4.1 below).

[1] If DM is of fermionic nature instead, its mass is constrained to be $\lesssim 70$ eV from the observation of the absorption lines in the spectra of distant quasars due to the Lyman-α clouds [97, 98, 99].

Moreover, from the observation of large scale structures such as galaxies and galaxy clusters, we know that DM must either be stable or has a mean lifetime larger than the age of the Universe, which rules out all the unstable particles except those with extremely long lifetimes. These observations also tell us that DM has attractive gravitational interactions. Apart from possible hints for self-interaction from the observation of the Abell 3827 cluster (see e.g. [104, 105]) and numerical simulations [106, 107, 108], we have no evidence that DM has any other interactions besides gravity. For instance assuming that DM has a particle nature, the DM-photon elastic scattering cross-section is constrained by CMB and N-body simulations to be $\lesssim 10^{-34}(m_{\rm DM}/\text{GeV})\text{cm}^2$ [109, 110]. Further, the current upper bound on the DM self-interaction obtained by analysing many cluster mergers is $\sigma/m_{\rm DM} \lesssim 1\text{cm}^2\,\text{g}^{-1} \sim 2\times10^{-24}\,\text{cm}^2\,\text{GeV}^{-1}$ [80, 111, 112], which is much weaker than the bound suggested by N-body simulations. In particular, DM with a short-range self-interaction cross-section close to the observational upper bound, known as "self-interacting DM" (SIDM) can solve the discrepancies observed in simulations with cold DM such as the very dense galactic cores [113], excessive number of satellite galaxies for the Milky Way [114] and the large amount of substructure [115, 116] (see e.g [106]). DM has not been observed to interact with any other particle species.

Further, the DM particles are believed to be neutral; however, it could have a small electric charge ("Milli-charged DM" [117]), albeit severely constrained $Q_{\rm DM} \lesssim 10^{-14}\,|e|\,(m_{\rm DM}/\text{GeV})$ where e is the electronic charge [118, 119, 120, 121]. The DM particles may also have a small electric or magnetic dipole moment [122, 123, 124, 125], a quadrupole or anapole moment [122, 126].

Furthermore, from the analysis of the CMB power spectrum, we know that the dominant component of the DM has to be cold (non-relativistic) or at most warm [62, 85, 86, 127], otherwise our Universe would have been vastly different (see Section 1.4.4). The warm DM scenario is similar to the cold DM case in the way the structures form; in both cases, the smaller structures form first. However, in the warm DM scenario, the DM particles can initially stream reducing the amount of substructure and dwarf galaxies, and also solving the dense galactic cores problem [128, 129, 130, 131, 132].

In addition, the majority of DM has to be nearly dissipationless, so the DM particles do not lose much energy which would lead to them forming disks on the galactic scale (as baryons do) instead of extended halos as expected. In fact, a slightly dissipative dark sector (which also incorporates self-interactions) can solve the problems observed in cold DM simulations [133, 134, 135, 136]. Further, DM with a small dissipative fraction (5-10%) works quite as well as dissipationless DM; however, in this case "dark disks" can form [137, 138] [1].

1.5.3 Dark matter alternative: modified gravity

Since all the pieces of evidence in support of DM are of a gravitational nature, many authors have considered modifying gravity to account for the observed gravitational discrepancies on cosmological scales. The most famous example is the "Modified Newtonian Dynamics" (MOND) model which was first introduced to explain the non-Keplerian behaviour of the galactic rotation curves without resorting to DM [140, 141, 142]. According to MOND, the gravitational force acting on an object of mass m behaves non-linearly for very small values of acceleration, $\mathrm{F} = ma\,\zeta(a)$ where $\zeta(a \gg a_0) = 1$ and $\zeta(a \ll a_0) = a/a_0$ with $a_0 \simeq 1.2 \times 10^{-8} \mathrm{cm\,s^{-2}}$ which is known as the acceleration constant [141]. For an object of mass m rotating under the influence of a central gravitational force, $\mathrm{F} = G_\mathrm{N}\, mM(r)/r^2$ [2] where $M(r)$ is the total mass enclosed by the orbit of the object in which case $a = v^2/r = G_\mathrm{N} M(r)/r^2$ for $a \gg a_0$ (i.e for small r, $r \ll r_0 = [G_\mathrm{N} M(r)/a_0]^{1/2}$) and $a = [G_\mathrm{N} M(r) a_0]^{1/2}/r$ for $a \ll a_0$ (i.e. for large r, $r \gg r_0$). Hence, the rotational velocity is $v = [G_\mathrm{N} M(r)/r]^{1/2}$ for $r \ll r_0$ and $v = [G_\mathrm{N} M(r) a_0]^{1/4}$ for $r \gg r_0$.

Clearly, for $r \gg r_0$, the rotational velocity of the object is constant if M is constant which is the case for stars rotating beyond the galactic disk of a galaxy. This is how MOND explains the flat galactic rotation curves [140, 141]. Indeed, this simple phenomenological modification to Newtonian dynamics presents a good fit for the flat rotation curves and dynamics of hundreds of high surface brightness galaxies and surprisingly also for many low surface brightness galaxies

[1] Some dark disks can also arise in simulations of galaxy formation if baryons are included [139]; however, in the case of partially dissipative DM, dark galactic disks should be a general feature.

[2] For simplicity, a circular orbit is assumed.

(see e.g. [143, 144, 145, 146, 147]). Moreover, MOND explains the empirical Tully-Fisher relationship [148], which relates the intrinsic luminosities (or masses) of spiral galaxies to their rotational velocities (see e.g. [144]) [1]. The MOND idea was successfully implemented in a general relativistic theory known as "TeVeS" which stands for "Tensor-Vector-Scalar gravity" [151]. There are several similar proposals such as Moffat's modified gravity [152] (see [153] for a review).

Despite the success of MOND on the scale of galaxies, it does not apply to motions of clusters [154] without resorting to some sort of DM such as massive active neutrinos with mass ~ 2 eV [155, 156], a sterile neutrino species with an even larger mass ~ 11 eV (and abundance $\Omega_{\nu_s} = 0.218$) [157] or cold baryonic DM in the form of dense gas clouds [158]. Moreover, recent numerical simulations have shown that MOND in addition to sterile neutrinos does not reproduce the observed cluster mass function [159, 160]. Further, MOND fails at explaining the merger events such as the Bullet Cluster [73] unless some form of DM such as active neutrinos with mass ~ 2 eV [161] or a sterile neutrino species [162] is included. Further, MOND or its relativistic variants such as TeVeS cannot match the CMB angular power spectrum (in particular peaks beyond the second one [163]) even with the inclusion of a significant abundance of massive neutrinos [163] or sterile neutrinos [164]. Furthermore, laboratory experiments show that Newton's second law holds for accelerations as small as $5 \times 10^{-13}\,\mathrm{cm\,s^{-2}}$ which is way below the MOND acceleration constant a_0 [165, 166, 167]. All these issues render the MOND idea an unappealing alternative to DM.

There are other relativistic modified gravity alternatives to DM such as Mannheim's conformal gravity [168], the "mimetic DM" model [169, 170, 171] and the infrared limit of Hořava-Lifshitz gravity [172], in which gravity mimics the effect of cold DM. However, these models are much less studied compared to MOND. Moreover, many of these models contain extra d.o.f. which secretly act as DM (see e.g. [173]). Recently, a new DM alternative based on the idea of emergent gravity [174] was put forward [175]. However, it has been criticised for the lack of rigor [176]. Furthermore, comparisons of the predictions of emergent gravity against observational data has already shown inconsistencies [177, 178].

[1] MOND also explains the baryonic Tully-Fisher relationship [149, 150].

1.5.4 Dark matter candidates

There are plenty of (composite) baryonic candidates. Each of these candidates – if it constitutes a significant part of the observed DM abundance – has to be a relic produced during the uncertain pre-BBN era. However, to most of the scientific community DM is assumed to be of particle nature and requires physics beyond the SM. In this section, we review some of the famous DM candidates and scenarios.

1.5.4.1 MACHOs

The most economical assumption is that the observed gravitational effects in galaxies and galaxy clusters are actually due to astrophysical objects whose emission is below the detection threshold (Massive Astrophysical Compact Halo Objects or "MACHOs" as coined by Griest [179]) [1]. There are many such candidates such as neutron stars, brown dwarfs and black holes. However, the analysis of the microlensing [2] data of millions of stars suggested that MACHOs can only account for a very small percentage of the missing mass in our galaxy [195, 196, 197, 198, 199, 200, 201, 202, 203, 204, 205, 206, 207].

Moreover, the measurement of CMB [88, 89, 90] and the study of the synthesis of the abundance of light chemical elements during BBN [91, 92, 93, 95, 208] including the abundance of deuterium [209, 210, 211, 212] besides several other observations such as the detection of absorption lines of the light of distant Quasars [96] and the opacity of the Lyman-α cloud [213] sets an upper bound of roughly 5% on the total abundance of baryons of the total energy budget in the

[1] There are other less popular baryonic alternatives to DM such as neutral hydrogen and molecular clouds [180, 181, 182, 183]. However, such possibilities are ruled out by the bound on the total abundance of baryons in the Universe (see e.g. [88, 95]). Furthermore, there are several composite DM candidates within the SM of particle physics (see e.g. [184, 185, 186, 187, 188]) There are also several similar composite DM candidates in many beyond SM proposals (see e.g. [189]). These candidates are generically called "Macro DM", and they are subject to several constraints (see e.g. [190, 191, 192]). Nevertheless, macro DM is still a viable candidate. However, it could be hard to produce enough of them to account for the observed DM abundance [193].

[2] Microlensing is a gravitational lensing effect in which the brightness of a distant object temporary get amplified due to the interference of a nearby object if an object in the Milky Way halo such as a MACHO passes near the line of sight to the distant object [194].

Universe (less than 20% of the matter density); see also [214]. This rules out the possibility that MACHOs make up a significant fraction of DM.

However, a particular MACHO candidate, black holes, can avoid the CMB and BBN bounds if they were produced before BBN. Such black holes are known as primordial black holes (PBHs) [103, 215]. They can form via a variety of mechanisms during or after inflation (see e.g. [216, 217, 218, 219, 220, 221, 222]). Nevertheless, many observations and theoretical studies show that PBHs with monochromatic mass function – if they at all exist – can only account for a small fraction of the non-luminous matter (see e.g. [223, 224] and references therein). Figure 1.5 shows some of the current bounds on monochromatic mass PBHs. However, these constraints (see Figure 1.5) as such may not apply to PBHs with

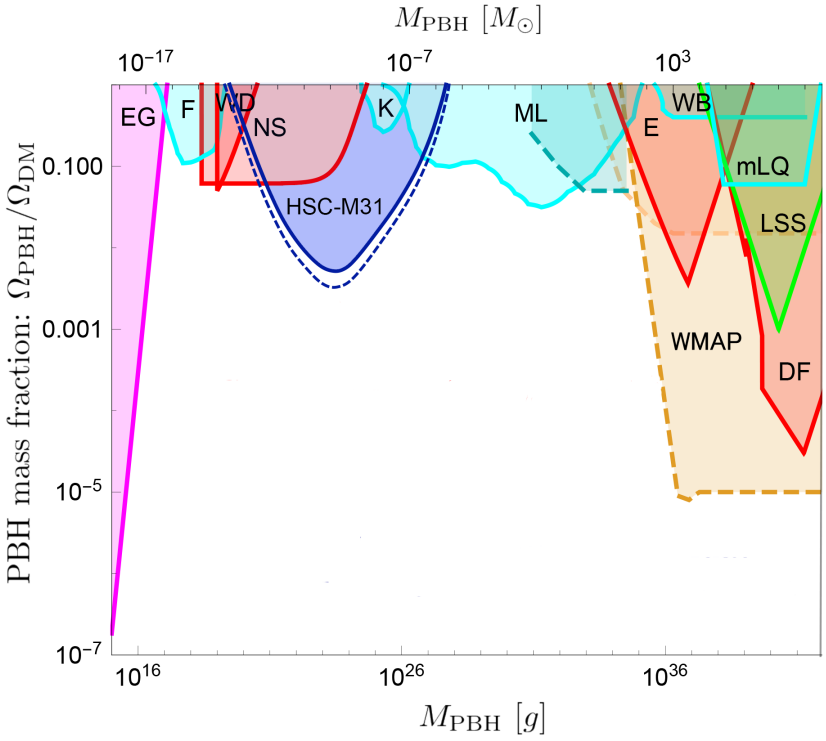

Figure 1.5: Observational bounds on PBHs with monochromatic mass function, adapted from reference [223]. The shaded regions are ruled out by various astrophysical and cosmological observations.

extended mass function [224, 225, 226]. Indeed, PBHs with extended mass func-

tion, which for instance can form due to the collapse of large density perturbations during inflation (see e.g. [227, 228]), might constitute the entirety of DM while being consistent with the current bounds [224]. Recently, some effort towards the mapping of the above bounds to the case of PBHs with extended mass function has been made [224, 225]. For the mass range $(1\text{–}10^3)M_\odot$, which encompasses the LIGO [1] sensitivity window [229], it was shown that a typical log-normal mass distribution, which accurately reproduces the mass spectrum of PBHs forming during inflation, is actually excluded [225].

1.5.4.2 Particle dark matter candidates

Given the amazing success of particle physics in describing the early Universe and the capability of particle candidates to make the right DM abundance, there is reasonable motivation to make the assumption that DM is of a particle nature. Within the SM the only possible particles that might meet the DM candidacy criteria are neutrinos because they are weakly coupled to all the other SM particles. Further, they decouple from the plasma with a thermal distribution much before radiation-matter equality [at temperature $\sim \mathcal{O}(\text{MeV})$]. However, given the current bounds on the masses of neutrinos ($m_\nu < 2.05$ eV at 95% CL from laboratory experiment [230] and $\sum m_\nu < 0.12$ eV at 95% CL from cosmological measurement [231]), it is clear that the SM neutrinos cannot make the observed DM abundance [$\Omega_{\nu,0}h^2 \simeq \sum m_\nu/(93\text{ eV}) \lesssim 0.066$ and $\Omega_{\nu,0}h^2 \lesssim 0.0013$, respectively] [46, 56]. Furthermore, the SM neutrinos are very light, and therefore they are relativistic throughout the RD era which renders them a hot DM candidate. As a result, the SM neutrinos cannot be the dominant DM species (see Section 1.4.4). Therefore, to accommodate DM within the framework of particle physics, an extension of the SM is needed. It is sensible that such an extension also addresses other problems in particle physics which lack explanations within the SM framework. In this section, we review some of the popular DM candidates.

Weakly Interacting Massive Particles (WIMPs): WIMP is a category of non-baryonic particle DM species with masses ranging from $\mathcal{O}(\text{GeV})$ to $\mathcal{O}(\text{TeV})$

[1] LIGO stands for Laser Interferometer Gravitational-wave Observatory.

and interaction strength with the SM particles of order of the weak interactions [232]. As a result, a particle species of this kind – if it exists – was in thermal (both kinetic and chemical) equilibrium with the SM particles (which constitute a thermal bath) in the early Universe and decoupled from the cosmic bath when its interaction rate with the thermal bath became smaller than the expansion rate (freeze-out), see Section 2.2.

WIMPs are compelling for several reasons. First, WIMPs can naturally satisfy the observed DM abundance for a wide range of masses almost independent of the mass [$\Omega_{\rm DM,0}h^2 \sim x_F(10^{-28}{\rm cm}^2\,{\rm s}^{-1}/\langle\sigma v\rangle)$ where $\langle\sigma v\rangle$ is the thermal average of the total interaction cross-section multiplied by the relative velocity of the colliding particles, see Eq. (2.19)]. Second, particles with this characteristics exist in many theories aiming to address the "hierarchy problem" (i.e. why the electro-weak (EW) scale is much smaller than the Planck scale) and in which new physics is expected at the TeV scale such as the "Lightest Supersymmetric Particle" (LSP) in the "Minimal Supersymmetric Standard Model" (MSSM) (for a review see e.g. [233]) and the "Lightest Kaluza-Klein particle" in the "Universal Extra Dimensions" models (see e.g. [234]). Third, WIMPs freeze-out at relatively low temperature, $T \sim m_{\rm DM}/20$ (see e.g. [235, 236]), and hence avoid the uncertain ultraviolet regime. Finally, from the detection point of view, WIMPs are within the reach of the current or near future experimental techniques (see e.g. [237, 238]).

Nevertheless, WIMP DM (or the freeze-out DM scenario in general) is already subjected to a plethora of theoretical and experimental constraints, the latter of which are becoming more stringent with time. Thus, one would expect that WIMPs will get either discovered or ruled out in the next few years [1].

Weakly Interacting Slim Particles (WISPs): This is a category of DM candidates with sub-eV masses which are weakly coupled to the SM particles; for a review see e.g. [240, 241]. Perhaps the most famous example of such light DM particles is the axion, which is a pseudo-Goldstone boson [242] arising in a solution to

[1] We note however that the reach of DD experiments could be ultimately limited by what is known as the "neutrino floor" which is caused by the scattering of neutrinos from the Sun or the cosmic-ray collisions in the Earth's atmosphere off the detectors' nuclei [239]. This is in general not the case for the ID experiments.

the strong CP [1] problem [the fact that quantum chromodynamics (QCD) is apparently CP invariant] known as the Peccei-Quinn (PQ) mechanism in which a new U(1) symmetry with a colour anomaly [2] is added to the SM [243, 244, 245, 246], see also Section 4.1. Laboratory experiments and astrophysical observations constrain the axion mass to be $\mathcal{O}(\mu\text{eV})$ or smaller [247, 248, 249].

Cold axionic DM is produced via what is known as the misalignment mechanism [250]. The main idea behind the misalignment mechanism is that the axion field does not have a potential before the QCD phase transition (i.e. the axion is massless above the QCD scale) and hence it takes on random values (between 0 and $2\pi v_{\text{PQ}}/N_{\text{DW}}$ where v_{PQ} is the scale of PQ symmetry breaking and N_{DW} is the number of domain walls, see Section 4.2) once the PQ symmetry gets broken. The axion field can get homogenised in our Hubble patch if the PQ symmetry breaking occurs before or during the early stages of inflation. In both cases the root-mean-square (rms) value of the axion field can be $\mathcal{O}(v_{\text{PQ}}/N_{\text{DW}})$. Around the QCD scale, axions acquire a potential (and consequently a mass) due to the QCD instantons [251, 252]. Consequently, the axion field starts oscillating once the Hubble parameter becomes of order of the axion mass. These oscillations effectively behave as cold DM. For a recent review see e.g. [253, 254].

Besides axions, many Axion-Like Particles (ALPs) emerge naturally in many beyond SM physics, such as familons [255] and Majorons [256, 257] which respectively arise in the spontaneous breaking of the global family and lepton number symmetries (for a review see e.g. [241] and references therein). ALPs also arise naturally in string theory, for instance from the compactification of extra dimensions (for a review see [241, 258]). We note here that ALPs can have masses much larger than eV.

Feebly Interacting Massive Particles (FIMPs): FIMP is used to denote a category of massive DM species [their masses are $\mathcal{O}$(GeV) and heavier] that were never in thermal equilibrium with the cosmic bath [259, 260]. Their coupling to the cosmic bath particles is very weak, although, it is sufficient to populate enough

[1] Here CP stands for charge conjugation and parity transformations.

[2] In quantum physics, an anomaly refers to an apparent symmetry of the classical theory which is absent at the quantum level.

DM. This mechanism of DM production was dubbed "freeze-in" [259]. Unlike the freeze-out mechanism, in the freeze-in scenario the final DM abundance is directly proportional to the interaction rate, $\Omega_{\mathrm{DM},0}h^2 \propto \langle \sigma v \rangle$ (see Section 2.3). FIMPs are usually non-relativistic (cold); however, warm DM can also be produced via the freeze-in mechanism [261]. There are many FIMP candidates such as moduli or modulino in weak-scale supersymmetry [259], axino (the supersymmetric partner of the axion) [262, 263] and gravitino (the supersymmetric partner of the graviton) [264, 265].

Sterile neutrinos: The SM (active) neutrinos were observed to oscillate (change flavour) [266, 267] which suggests that they have non-zero mass (at least two of the three active species have masses). Theoretically, the SM neutrinos can be given masses by extending the SM to include right-handed neutrinos (for a review see [268] and references therein). The right-handed neutrinos interact with the SM particles only via mixing with active neutrinos which themselves interact with the SM particles through EW interactions. As a result, the right-handed neutrinos are said to be "sterile". Moreover, sterile neutrinos are massive, and the lightest species is stable. Therefore, the lightest sterile neutrino can make a perfect DM candidate. In fact, keV-scale sterile neutrinos can have the right DM abundance [269] and further they can be warm [270, 271] which is desirable from the point of view of structure formation in our Universe as discussed in Section 1.5.2. Nevertheless, keV-sterile neutrinos are subjected to a plethora of theoretical and experimental constraints (see e.g. [272] and references therein).

1.5.5 Dark matter searches

In this section, we briefly review some of the DM searching techniques, in particular, experiments looking for WIMP-like and WISPy DM.

1.5.5.1 Heavy (WIMPy-like) dark matter

Direct detection: Since the Milky Way galaxy (like other spiral galaxies) contains a substantial amount of DM (see Section 1.5.1) in the form of a halo (as

suggested by DM simulations), there is a good chance that DM particles could be detected on Earth. With this in mind, Direct Detection (DD) experiments were built to detect the scattering of galactic DM particles off atomic nuclei (DM-SM scattering) [1]. WIMP-like DM-nucleus scattering results in the recoil of the nucleus with energies typically in the keV range. Clearly, the probability of the DM scattering off the target nuclei increases as the volume of the target increases. It also depends on the local DM density. There are already many DD experiments looking for DM such as CoGeNT [276], DAMA/LIBRA [277], CRESST-II [278], Xenon100 [279], LUX [280], CDMSlite [281] and PandaX-II [282]. See [283, 284] for a detailed review of the direct DM detection experiments.

So far DM has not been observed at DD experiments, and hence the expected sensitivity of the DD experiments are translated into upper bounds on the DM-nucleon interaction strength. Nevertheless, some of these experiments, CoGeNT [285, 286], DAMA/LIBRA [287, 288], CRESST (first phase run) [289] and CDMS [290, 291], claimed to have observed DM signals. However, these measurements are not consistent with each other. Furthermore, the regions of the parameter space favoured by these experiments are in tension with other experiments (they lie in the exclusion regions of other experiments); see Figure 1.6.

Indirect detection: Besides the DD experiments, DM particles may also be indirectly observed by searching for their decay or annihilation products. DM Indirect Detection (ID) experiments are designed to detect the fluxes of SM particles such as charged particles, photons (x-ray and gamma-ray) and neutrinos produced in DM decay or annihilation processes (for a review of indirect DM searches see e.g. [292, 293, 294]). Clearly, such signals will depend on the DM density in the region being observed. Thus, regions with large DM density such as the galactic centre, galactic halo and dwarf spheroidal galaxies are the best targets for observation. However, the analysis of the collected data is subjected to many uncertainties due to astrophysical backgrounds, especially if the DM decay or annihilation products are charged particles as they can be deflected

[1] This idea was first proposed in [273, 274, 275].

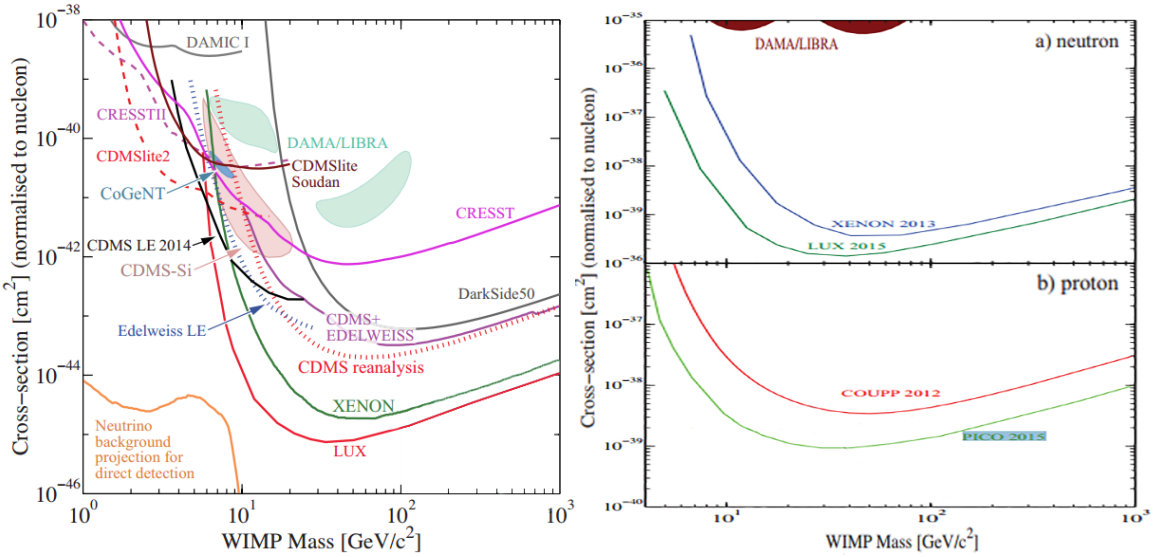

Figure 1.6: Direct detection bounds on DM-nucleon spin-independent cross-section (left panel) and spin-dependent cross-section (right panel), adapted from reference [32]. The shaded regions show the claimed DM signals by DAMA/LIBRA, CDMS-Si and CoGeNT collaborations. However, these regions of the parameter space are already ruled out by other experiments such as the LUX and XENON facilities.

by magnetic fields making it hard to identify the region where a possible signal originates.

There are many experimental facilities searching for indirect DM signal such as the Alpha Magnetic Spectrometer experiment (AMS-02) [295], Fermi Large Area Telescope (Fermi-LAT) [296], (IceCube) Southpole neutrino observatory [297], the Payload for Antimatter Matter Exploration and Light-nuclei Astrophysics (PAMELA) [298] and the High Energy Stereoscopic System (HESS) [299]. Several of these groups have claimed to observe an excess over the expected background [300, 301, 302, 303, 304, 305, 306, 307, 308] [1]. However, these observations do not constitute conclusive evidence for the existence of DM as they are consistent with astrophysical sources [312, 313, 314, 315, 316, 317, 318, 319, 320, 321,

[1] In particular, two groups have announced the observation of a signal of an x-ray line with energy around 3.5 keV which becomes stronger towards the centre of the galaxy [309, 310]. However, an independent analysis has shown no significant evidence for such an excess over the expected background [311].

322, 323, 324] and/or inconsistent with other observations [325, 326, 327, 328, 329, 330, 331, 332, 333]. The lack of a significant signal from the regions where DM is expected to be dominant can be translated into upper bounds on the DM decay or annihilation rates. In Section 2.5.5 we list the most stringent limits on the DM annihilation cross-section.

Production at colliders: If DM particles couple to the SM particles, they can be produced at particle colliders [such as the Large Hadron Collider (LHC) at CERN [334] and the proposed future International Linear Collider (ILC) [335]] provided that the colliding SM particles are energetic enough (for a recent review see [336]). Due to their very weak coupling to the SM particles, DM particles will not produce a detectable signal in colliders. However, their presence can be deduced from the consideration of momentum conservation. If produced at colliders, DM particles would result in an excess in the number of events with missing transverse momentum (energy). So far no signal for DM has been observed in collider experiments, which is translated into upper bounds on the DM interaction strength with the SM particles. The current bound on DM-SM spin-independent interaction strength from colliders is much weaker than those inferred from the DD experiments for DM mass $\gtrsim \mathcal{O}(\text{GeV})$. Nevertheless, for lower DM masses, the colliders' bounds are more stringent than the DD ones (see e.g. [283]). Moreover, the colliders' bounds on DM-SM spin-dependent interactions can be more stringent that the DM DD bounds (see e.g. [337]); see Figure 1.7.

The search for DM at colliders is complementary to the DD and ID DM searches in the sense that the existence of DM has to be confirmed by all these search techniques. Further, the DM search at colliders is more sensitive to the details of the DM-SM interactions and does not suffer from the astrophysical uncertainties that affect the DD and ID experiments. However, collider experiments have nothing to say about the mean lifetime of DM particles as the time needed for a DM particle to transverse the detector of a collider is much smaller than the DM mean lifetime. Thus, the existence of particle DM has to be established first by the DD and/or ID experiments.

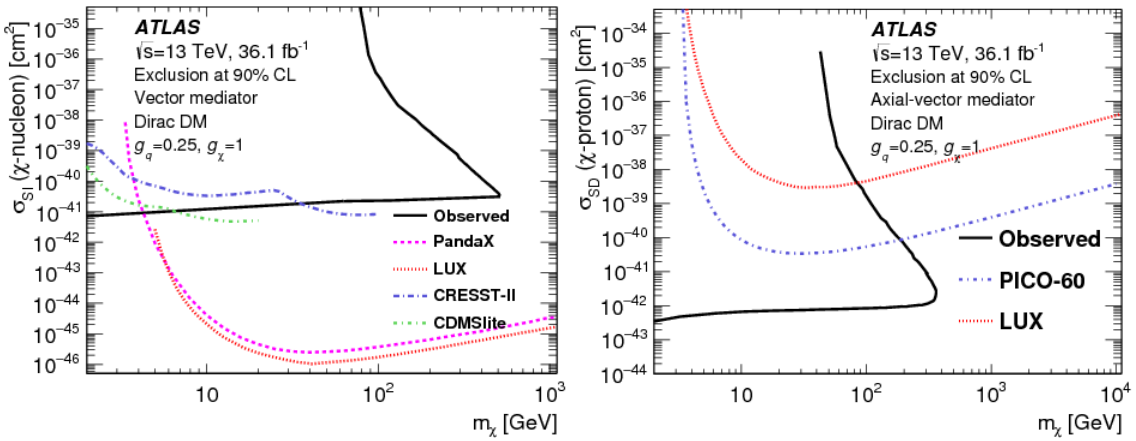

Figure 1.7: ATLAS (at LHC) bounds on DM-nucleon spin-indpendent (left panel) and spin-dependent (right panel) cross-sections assuming vector and axial vector mediator (the solid black curves), respectively (taken from reference [338]). However, these bounds are strongly model-dependent.

1.5.5.2 Axions and axion-like dark matter

Axions can be searched for using their coupling to photons [339, 340, 341],

$$\mathcal{L}_{\chi\gamma\gamma} = \frac{1}{4} g_{\chi\gamma\gamma}\, \chi F^{\mu\nu} \widetilde{F}_{\mu\nu} = -g_{\chi\gamma\gamma}\, \chi \mathbf{E}\cdot\mathbf{B}\,, \tag{1.75}$$

which is generic in axion models. Here χ denotes the axion field and $g_{\chi\gamma\gamma} = \alpha_{\rm EM}/(2\pi F_\chi)\,[E/N - 1.92(4)]$ with $\alpha_{\rm EM}$ being the fine structure constant, $F_\chi \equiv v_{\rm PQ}/N_{\rm DW}$ is the axion decay constant and E/N is the ratio of the electromagnetic to colour anomaly [342]. The mass of axions is related to the axion decay constant, $m_\chi = 5.70\mu{\rm eV}(10^{12}\,{\rm GeV}/F_\chi)$ (see e.g. [343]). As shown by Eq. (1.75), in the presence of a (strong and static) magnetic field axions/ALPs can convert into photons and vice versa. Using this concept, axions can be directly produced and/or detected. Similarly, many ALPs (in particular stringy axions) couple to photons via operators of the form of Eq. (1.75) (see e.g. [258]), and hence can be searched for the same way as axion. However in the case of ALPs, unlike the QCD axion, their masses are not related to their decay constants.

Galactic axions: If axions/ALPs constitute the entirety or part of DM, they should be present in our galaxy. Axion haloscopes such as Axion Dark Matter Experiment (ADMX) [344] are designed to detect galactic halo axions/ALPs passing through Earth via their possible conversion into photons in a cavity placed in a magnetic field. The possible conversion of axions/ALPs into photons is maximal if the axion/ALPs mass matches the resonant frequency of the cavity. By adjusting the cavity resonant frequency, haloscopes can perform a scan for axions/ALPs in a range of masses. It has been noted that the possible presence of the oscillating axion/ALPs background can induce a detectable oscillating electric dipole moment [345]. A new axions/ALPs detection experiment based on this concept: the Cosmic Axion Spin Precession Experiment (CASPEr) [346]) was recently proposed.

Solar axion experiments: Axions/ALPs can get produced at the core of the Sun via their coupling to photons. Being very light and very weakly-coupled, axions/ALPs can escape the Sun. Such axions/ALPs can be detected on Earth via their possible conversion into photons in a magnetic field. There are several helioscopes designed for this purpose such as the CERN Axion Solar Telescope (CAST) [347] and the proposed International Axion Observatory (IAXO) [348]. In these experiments, the magnetic field region is filled with a gas, which has the effect of giving mass to photons. The conversion of axions/ALPs into photons is maximum when the mass of axions/ALPs matches the effective photon mass in the gas. By adjusting the gas pressure, the effective mass of the photon in the gas gets modified allowing helioscopes to search for axions/ALPs in a range of masses.

Laser-induced Axions: A class of axion (or ALPs) detection experiments such as the Optical Search for QED Vacuum Birefringence, Axions and Photon Regeneration (OSQAR) [349] and Any Light Particle Search (ALPS) [350] use what is known as a "light shining through a wall" (LSW) technique. In these experiments, a laser beam traversing a magnetic field is pointed toward an absorber which does not allow the passage of any photons. Some photons of the laser beam may get converted into axions/ALPs in the presence of the magnetic

field. The produced axions/ALPs then get converted back to photons in a second magnetic field. Some other LSW experiments employ microwave resonators instead of lasers such as the CERN Resonant WISP Search (CROWS) [351] [1].

There are other laboratory-based direct and indirect axion/ALP searches (see e.g. [355, 356]). So far axions (and ALPs) have not been detected, which places bounds on the axions/ALPs coupling to photons, see Figure 1.8. Indirect searches for axions/ALPs can also be conducted by studying the possible effects of the axions'/ALPs' coupling to the SM particles on the evolution of stars. The lack of any detectable effect due to the possible presence of axions/ALPs inside stars places stringent constraints on axions'/ALPs' coupling to photons, electrons and nucleons. We summarise the most stringent bounds in Section 4.5.

[1] We note here that the axion/ALPs experiments mentioned above are also sensitive to another well-motivated DM candidate, the hidden (dark) photon which can convert into the SM photon and vice versa through kinetic mixing (see e.g. [352, 353] and references therein). There are already facilities dedicated to the search for dark photons such as the CAvity Search for Coupling of A Dark sEctor (CASCADE) [354].

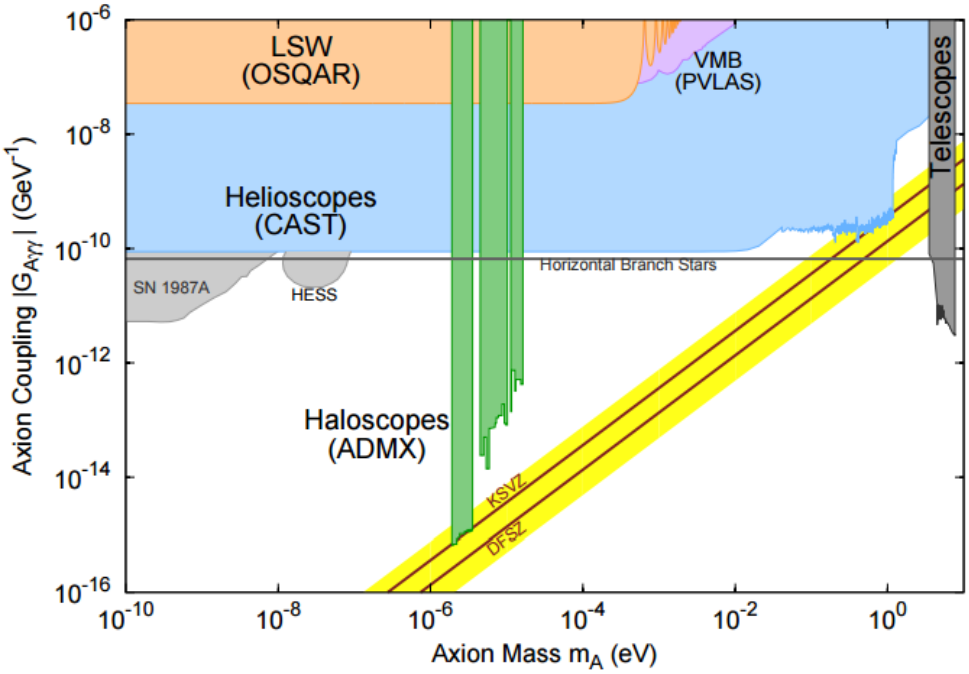

Figure 1.8: A representative sample of the current bounds on the axion and ALPs parameter space from experimental searches. The yellow band corresponds to the QCD axions. Taken from reference [32].

Chapter 2

Thermal and non-thermal production of dark matter

In this chapter, we aim to identify the gross features of the DM parameter space in a simple model-independent setup given the fact that the Universe could have been dominated by the energy density stored in a scalar condensate of inflaton/moduli field whose decay excites the SM d.o.f. and probably DM particles [1]. For the sake of simplicity, we assume that the decay of the scalar condensate is an instantaneous perturbative process [2]. We further assume that the SM d.o.f. produced in the decay of the scalar condensate quickly achieve full thermal equilibrium establishing a thermal bath with a well-defined temperature. With these

[1] During inflation, there could be many fields dynamically present [35, 357, 358] – some of which (those with masses well below the Hubble scale during inflation) may obtain quantum-induced vacuum fluctuations to be displaced at very large vacuum expectation values, $\mathcal{O}(M_{\rm P})$ [34, 37, 38] – commonly known as moduli. They typically couple very weakly via Planck-suppressed interactions. The moduli field behaves like a condensate [359], and begins its coherent oscillations when the Hubble expansion rate of the Universe drops to the mass of the moduli.

[2] In principle, the decay of the scalar condensate need not be perturbative nor instantaneous. For large enough inflaton/moduli coupling to the SM or DM fields, the decay process would be non-perturbative [360, 361]. However in this case, the inflaton/moduli condensate does not decay completely. One would still require the inflaton/moduli to decay perturbatively in order to fully drain the energy of the scalar condensate. We note here that in the particular case of the axion inflation model, most of the energy in the scalar condensate (of axions) can be transferred to a gauge field which couples to the condensate [362].

assumptions, we proceed to identify the regions of the parameter space corresponding to thermal (freeze-out and freeze-in) and non-thermal DM scenarios. We also show the different theoretical and observational bounds. Furthermore, for the non-thermal DM case, we identify the parameter regions corresponding to cold, warm and hot DM.

This chapter is organized as follows: in Section 2.1, we briefly review the evolution of DM as governed by the Boltzmann equation. We discuss the production of DM due to the decay of the inflaton/moduli condensate: thermal production (both freeze-out in Section 2.2 and freeze-in scenarios in Section 2.3), and non-thermal production in Section 2.4. In Section 2.5, we discuss various observational and theoretical constraints on DM. In Section 2.6, we present our numerical results for both thermal and non-thermal scenarios. Our conclusions are given in Section 2.7.

2.1 Evolution of dark matter: a brief review

The time evolution of the average DM (χ) number density, n_χ, and the departure from its thermal equilibrium value, $n_{\chi,eq}$, can be obtained by solving the Boltzmann equation [see Eq. (A.12)],

$$\dot{n}_\chi + 3Hn_\chi = a^{-3}\frac{\mathrm{d}}{\mathrm{d}t}(a^3 n_\chi) = \langle\sigma v\rangle(n_{\chi,eq}^2 - n_\chi^2)\,, \tag{2.1}$$

with $\langle\sigma v\rangle$ being the thermally-averaged total (unpolarised) annihilation cross-section (σ) summed over all possible scattering processes multiplied by the Møller velocity (see Appendix A). The $3Hn_\chi$ term in Eq. (2.1) accounts for the dilution of number density due to the expansion of the Universe, and the first (second) term on the right-hand side of Eq. (2.1) accounts for the increase (decrease) in the number density due to production from (annihilation into) the thermal bath particles. With the assumption of instantaneous inflaton/moduli decay at $t = \Gamma_\phi^{-1}$, where Γ_ϕ denotes the total decay rate of the inflaton/moduli field, the non-thermal contribution to the DM number density acts as an initial value which

is given by [1]

$$n_\chi^{(i)} \simeq B_\chi n_\phi(\Gamma_\phi^{-1}) \simeq B_\chi \frac{\pi^2 g_\rho}{30}\frac{T_{\rm rh}^4}{m_\phi}\,, \tag{2.2}$$

where $n_\phi \simeq \rho_\phi/m_\phi$ is the inflaton/moduli number density with m_ϕ being its mass and ρ_ϕ its energy density, and $B_\chi \equiv {\rm n}\,\Gamma(\phi\to {\rm n}\chi)/\Gamma_\phi$ denotes the branching ratio of inflaton/moduli decay to DM with n being the number of DM particles produced in each ϕ decay [2]. Here we made the assumption of instantaneous thermalisation of the ϕ decay products other than χ upon their excitation at $t=\Gamma_\phi^{-1}$ establishing a thermal bath with a well-defined temperature, i.e. $\rho_\phi|_{t\simeq\Gamma_\phi^{-1}} \simeq \rho_{\rm rad}(T_{\rm rh})$ with $T_{\rm rh}$ being the reheating temperature. The energy density of radiation at the time of reheating is given by

$$\rho_{\rm rad}(T_{\rm rh}) \simeq \frac{\pi^2}{30} g_\rho T_{\rm rh}^4\,, \tag{2.3}$$

where

$$g_\rho \equiv \sum_{i={\rm bosons}} g_i \left(\frac{T_i}{T}\right)^4 + \frac{7}{8}\sum_{i={\rm fermions}} g_i \left(\frac{T_i}{T}\right)^4 \tag{2.4}$$

is the effective number of relativistic d.o.f. associated with the radiation energy density with T being the temperature of the thermal bath and T_i is that of the species i whose number of internal d.o.f. is g_i (see e.g. [56]). Using Eq. (1.2), the Hubble expansion rate during RD is then given by

$$H(T) = \frac{\rho_{\rm rad}^{1/2}}{\sqrt{3}M_{\rm P}} = \left(\frac{\pi^2 g_\rho}{90}\right)^{1/2}\frac{T^2}{M_{\rm P}}\,. \tag{2.5}$$

Further, the average equilibrium number density of χ particles is given by

$$n_{\chi,eq} = g_\chi \int \frac{{\rm d}^3 p_\chi}{(2\pi)^3}\left\{\exp\left[\left(\sqrt{|\mathbf{p}_\chi|^2+m_\chi^2}-\mu_\chi\right)/T\right]\mp 1\right\}^{-1}, \tag{2.6}$$

[1] In a more general setup, we should have a term of the form ${\rm n}\,\Gamma(\phi\to {\rm n}\chi)\,n_\phi$ on the right hand side of Eq. (2.1). However, since we assume instantaneous decay of ϕ at $t=\Gamma_\phi^{-1}$, this contribution can be absorbed into the initial condition for n_χ.

[2] Since we are interested in model-independent constraints on the DM parameter space, we keep our discussion general in terms of the branching ratio, without specifying its exact formula in terms of the DM-inflaton/moduli coupling, their masses, and the n-body decay kinematics (for ${\rm n}\geq 2$, depending on the specific DM candidates). Hence, we absorb n in the definition of the branching fraction B_χ.

where g_χ is the number of internal d.o.f. of χ (e.g. spin or colour), T is the temperature, and μ_χ is the chemical potential of species χ (the energy associated with the change in particle number) which we assume to be zero (see Appendix A). Here $(-)$ is for bosonic χ species whereas $(+)$ is for fermionic χ species. In the absence of Bose-Einstein condensation or Fermi degeneracy, one can neglect the quantum statistical factors, and write the equilibrium number density as

$$n_{\chi,eq} \simeq g_\chi \int \frac{\mathrm{d}^3 p_\chi}{(2\pi)^3} \exp\left[-\left(\sqrt{|\mathbf{p}_\chi|^2 + m_\chi^2} - \mu_\chi\right)/T\right] . \tag{2.7}$$

It is useful to express Eq. (2.1) in terms of the dimensionless quantities (DM yields) $Y_\chi \equiv n_\chi/s$ and $Y_{\chi,eq} \equiv n_{\chi,eq}/s$ to scale out the redshift effect due to the expansion of the Universe. Here,

$$s = \frac{2\pi^2}{45} g_s T^3 \tag{2.8}$$

is the entropy density with

$$g_s \equiv \sum_{i=\text{bosons}} g_i \left(\frac{T_i}{T}\right)^3 + \frac{7}{8} \sum_{i=\text{fermions}} g_i \left(\frac{T_i}{T}\right)^3 \tag{2.9}$$

being the effective number of relativistic d.o.f. contributing to the total entropy density (see e.g. [56]). Recall that in the early Universe with RD, all particle species (apart from possibly χ and/or other hidden sector species) were in thermal equilibrium, i.e. g_s and g_ρ were the same [1]. Henceforth, we will not distinguish the two, and will take $g_\rho = g_s \equiv g$ which is valid for most of the thermal history of the Universe. Assuming an adiabatic and isentropic (constant entropy per comoving volume) expansion of the Universe, Eq. (2.1) can be re-written as [236, 363]

$$\frac{\mathrm{d}Y_\chi}{\mathrm{d}x} = \frac{s\langle\sigma v\rangle}{Hx} \left(1 + \frac{1}{3}\frac{\mathrm{d}\ln g}{\mathrm{d}\ln T}\right) \left(Y_{\chi,eq}^2 - Y_\chi^2\right) , \tag{2.10}$$

[1] g_s and g_ρ differ only when there are relativistic species not in equilibrium with photons which happens in the SM for temperatures below the electron mass when the neutrinos have already decoupled from the thermal bath, and $e^\pm$ pair-annihilation transfers entropy only to the photons, thus making g_s slightly higher than g_ρ today.

with the introduction of a new independent variable $x = m_\chi/T$. Here the initial DM yield is

$$Y_\chi^{(i)} \simeq \frac{3}{4} B_\chi \frac{T_{\rm rh}}{m_\phi} \,. \tag{2.11}$$

For a Maxwell-Boltzmann distribution, the equilibrium DM yield and thermally-averaged annihilation cross-section can respectively be expressed as

$$Y_{\chi,eq}(x) = \frac{45}{4\pi^4} \frac{g_\chi}{g} x^2 K_2(x) \,, \tag{2.12}$$

$$\langle \sigma v \rangle(x) = \frac{x}{8 m_\chi^5 K_2^2(x)} \int_{4m_\chi^2}^{\infty} {\rm d}s \, s^{1/2} (s - 4m_\chi^2) K_1 \left(\frac{x\sqrt{s}}{m_\chi} \right) \sigma(s) \,, \tag{2.13}$$

where we used Eqs. (2.8), (A.15) and (A.16). Here $K_n(x)$ is the n-th order modified Bessel functions of the second kind, and $\sqrt{s}$ is the total CM energy. At $x \ll 1$, $Y_{\chi,eq} = (45/2\pi^4)(g_\chi/g)$ whereas for $x \gtrsim 1$, $Y_{\chi,eq}$ exhibits an exponential suppression. The current abundance of the species χ – if non-relativistic today – is given by

$$\Omega_{\chi,0} h^2 \equiv \frac{\rho_{\chi,0}}{\rho_c/h^2} \simeq \frac{m_\chi s_0 Y_\chi(x_0)}{3(H_0/h)^2 M_{\rm P}^2} \simeq 2.744 \times 10^8 \, m_\chi Y_\chi(x_0) \,, \tag{2.14}$$

where we used the current values for the Hubble parameter, $H_0 \simeq 2.1332h \times 10^{-42} h$ GeV [56], and the entropy density $s_0 = 2891.2 \text{ cm}^{-3} (T_0/2.7255 \text{ K})^3$ [32]. The present yield of the DM species χ, $Y_\chi(x_0)$, is obtained by integrating Eq. (2.10) from $x = x_{\rm rh} \equiv m_\chi/T_{\rm rh}$ to $x = x_0 \equiv m_\chi/T_0$, where $T_0 = 2.7255(6)$ K is the present temperature of the CMB photons [32]. However, Eq. (2.10) is a form of the Riccati equation for which there is no general, closed-form analytic solution. Therefore, the current density $Y_\chi(x_0)$ in Eq. (2.14) has to be obtained either by numerically solving Eq. (2.10) or by approximating it with an analytic solution in some special cases.

As mentioned above, we seek a model-independent way to analyse the thermal and non-thermal properties of DM, produced directly or indirectly from the decay of inflaton/moduli condensate, in terms of their masses, the inflaton/moduli branching ratio into DM and the strength of DM coupling to the thermal bath.

For this purpose, we make the assumption that the inflaton/moduli condensate decays into the SM d.o.f. and DM is a perturbative and instantaneous process; hence on kinematic grounds, $m_\chi < m_\phi/2$ [1]. In this setup, the reheating temperature is the maximum attainable temperature due to the decay of the scalar condensate. Furthermore, the evolution of the DM particle number density can be described by its thermally-averaged interaction rate with the thermal bath,$\langle\sigma v\rangle$ [see Eq. (2.10)], i.e. depending on the size of $\langle\sigma v\rangle$, there are three possible scenarios [2]:

1. For large enough $\langle\sigma v\rangle$ (i.e. the DM interaction strength with the thermal bath particles is of order of the weak interactions), the χ particles quickly reach thermal equilibrium with the bath, thus losing their initial abundance, and follow the equilibrium distribution until their reaction rate eventually drops below the Hubble expansion rate, after which they freeze out as a 'thermal relic' with a constant comoving number density. This is the standard WIMP scenario [56] in which the final relic abundance is independent of the initial conditions or the details of the production mechanism. Depending on their mass and interaction rate, they could freeze out as a cold, warm, or hot relic [56]. It is well-known that $\langle\sigma v\rangle \sim 10^{-26}\,\mathrm{cm^3 s^{-1}}$ naturally gives the correct cold DM relic density inferred from the CMB measurement [13], almost independent of the DM mass. In the freeze-out scenario,

[1] We do not consider non-perturbative DM production processes during the coherent oscillations of the scalar condensate, e.g. super-heavy DM with $m_\chi \gg m_\phi$ for large enough amplitude of the inflaton/moduli field [364]. Even in the perturbative case, the decay of the inflaton/moduli can be an extended process which under the assumption of instantaneous thermalisation of the decay products may expose the Universe to temperatures much higher than $T_{\rm rh}$ [365] with the possibility of thermal excitation of super-heavy DM [366, 367]. We consider this possibility in Chapter 3.

[2] A concrete example is MSSM inflation in which case the LSP, e.g. gravitino or neutralino (which is a linear superposition of the neutral supersymmetric partners of the W, B and the CP-even Higgs bosons), could be excited directly from the inflaton/moduli decay or its decay products [368], besides the SM d.o.f. Since gravitinos mostly interact via Planck-suppressed interactions, their abundance will freeze out soon after their production and will be mainly determined by the reheating temperature, while neutralinos have weak interactions and can be quickly brought into kinetic equilibrium (though not necessarily chemical equilibrium) with the bath. Therefore, irrespective of how the neutralinos were initially created, their final abundance is always set by the thermal decoupling temperature, as long as $T_{\rm rh} \geq m_\chi$ [365]. On the other hand, for low reheating temperatures below the standard freeze-out temperature $T_F \sim m_\chi/20$, neutralinos could be a non-thermal DM candidate [235, 369].

the current abundance is inversely proportional to $\langle\sigma v\rangle$. As a consequence for a wide range of the χ masses and $\langle\sigma v\rangle \ll 10^{-26}\,\mathrm{cm^3 s^{-1}}$, the current abundance of χ particles is larger than the correct DM abundance.

2. The second possibility is that the interaction of χ particles with the thermal bath is too small to bring them into full thermal equilibrium with the cosmic bath but is sufficient to produce enough DM via the scattering of the bath particles into χ particles. However, as the Universe expands, the interaction rate decreases and the annihilation of the bath particles into χ's stops being significant and the DM species χ is said to be frozen-in. In this case, the χ abundance is directly proportional to $\langle\sigma v\rangle$ [367]. Again for large enough interaction rate, DM can be overproduced in a wide range of the χ masses. Further, the χ population could receive another contribution from the direct decay of the inflaton/moduli into χ particles. Therefore in this scenario, besides its mass, the abundance of the DM species χ is determined by $\langle\sigma v\rangle$ and the initial conditions (i.e. B_χ, m_ϕ and $T_{\rm rh}$). If the non-thermal contribution to the χ population is negligible, the DM abundance will be dominated by the thermally produced χ particles. Such a DM species is known as a "FIMP" [259, 260].

3. For even smaller interaction rates than those considered above, the thermal production of χ particles is insignificant, and they have to be produced non-thermally in order to make the observed DM abundance. This leads to a Super-WIMP (SWIMP)-like scenario [370], where the final abundance is primarily determined by the initial conditions which, in our case, are set by the inflaton/moduli mass, reheating temperature and branching ratio [371].

We discuss these possibilities in more detail below.

2.2 Freeze-out scenario

In this case, the χ particles were initially part of the cosmic thermal bath before they dropped out of thermal equilibrium at some freeze-out temperature T_F when

the annihilation rate $\Gamma_\chi = n_\chi \langle \sigma v \rangle$ fell below the Hubble expansion rate H [1]. Here the connection to the scalar condensate is lost, and the abundance of the species χ is set by its equilibrium distribution at freeze-out [2]. Now depending on the value of $x_F = m_\chi / T_F$, one can have the following three scenarios:

- Non-relativistic DM if $x_F \gg 3$. In which case the average momentum per DM particle $\ll m_\chi$ at the time of freeze-out. In this case, the thermal distribution, which the χ particles follow, exhibits a Boltzmann (exponential) suppression. As a result, the current abundance of the species χ is very dependent on the freeze-out temperature.

- If $x_F \ll 3$, the χ particles are relativistic at the time of their decoupling from the cosmic bath. Such a DM species is known as hot DM and its current yield, $Y_\chi(x_0)$, is approximated by its corresponding equilibrium value at freeze-out $Y_{\chi,eq}(x_F)$ [56, 372]. In this case and away from phase transitions at which the effective number of relativistic d.o.f. changes considerably (see e.g. [56]), the current abundance of the species χ is less sensitive to the freeze-out temperature.

- In the intermediate regime, $x_F \sim 3$, the χ particles are semi-relativistic when they decouple from the thermal bath. This case is similar to the non-relativistic freeze-out case; however, a more careful analysis is required since, strictly speaking, one needs to use the appropriate statistical distributions when calculating $\langle \sigma v \rangle$ which, in general, requires evaluating an expression with multiple integrals. Even if one uses the Boltzmann distribution to thermally average σv which can be a good approximation [373, 374], a Taylor expansion of $\langle \sigma v \rangle$ in terms of the average particle velocity is not very useful since the average velocity of χ particles is close to unity at the time of their decoupling from the thermal bath.

The three cases mentioned above are considered in more detail in Sections 2.2.1, 2.2.2 and 2.2.3, respectively.

[1] The freeze-out of DM can take place during the course of inflaton/moduli decay before radiation takes over [366, 367].

[2] The χ population can still receive a non-thermal contribution after they freeze out from the decay of other species [259].

2.2.1 Non-relativistic (cold) dark matter

For $x_F \gg 3$, the DM particles are mostly non-relativistic when they decouple from the thermal plasma. This leads to the usual cold DM scenario with free streaming lengths of sub-pc scale [375]. Further, approximate analytic formulas for their relic abundance can be obtained [236, 373, 376]. The key point is that the actual abundance Y_χ tracks with the equilibrium abundance $Y_{\chi,eq}$ during the early stages of evolution (for $x \lesssim x_*$), while at late stages ($x \gtrsim x_*$), $Y_{\chi,eq}$ is exponentially suppressed and has essentially no effect on the final abundance $Y_\chi(x_0)$. Here x_* is some intermediate matching point (not the freeze-out point x_F, as commonly assumed) where the deviation from equilibrium starts to grow exponentially. Hence, to calculate the freeze-out abundance more precisely, we track the evolution of the quantity $\Delta_\chi \equiv (Y_\chi - Y_{\chi,eq})/Y_{\chi,eq}$ which represents the departure from equilibrium. From Eq. (2.10), the evolution equation for Δ_χ is obtained with the form

$$\frac{\mathrm{d}\ln(1+\Delta_\chi)}{\mathrm{d}\ln x} = -\frac{\mathrm{d}\ln Y_{\chi,eq}}{\mathrm{d}\ln x} - \frac{\Gamma_{\chi,eq}}{H}\left(1+\frac{1}{3}\frac{\mathrm{d}\ln g}{\mathrm{d}\ln T}\right)\frac{\Delta_\chi(2+\Delta_\chi)}{1+\Delta_\chi}\,, \tag{2.15}$$

with $\Gamma_{\chi,eq} = n_{\chi,eq}\langle\sigma v\rangle = Y_{\chi,eq}s\langle\sigma v\rangle$ being the equilibrium annihilation rate where $\langle\sigma v\rangle$ is given by Eq. (2.13) [1]. Following the strategy developed in [376] to solve Eq. (2.15) for Δ_χ, we note that in the early stages of evolution, Y_χ tracks $Y_{\chi,eq}$ closely, and hence, $\Delta_\chi, \mathrm{d}\Delta_\chi/\mathrm{d}x \ll 1$. In this case, the left-hand side of Eq. (2.15) can be safely dropped, thus leading to

$$\begin{aligned}
\frac{\Delta_\chi(2+\Delta_\chi)}{1+\Delta_\chi} &\simeq -\frac{\mathrm{d}\ln Y_{\chi,eq}}{\mathrm{d}\ln x}\frac{H}{\Gamma_{\chi,eq}}\left(1+\frac{1}{3}\frac{\mathrm{d}\ln g}{\mathrm{d}\ln T}\right)^{-1} \\
&\simeq \frac{H}{sY_{\chi,eq}\langle\sigma v\rangle}\left(x-\frac{3}{2}-\frac{\mathrm{d}\ln g}{\mathrm{d}\ln T}\right)\left(1+\frac{1}{3}\frac{\mathrm{d}\ln g}{\mathrm{d}\ln T}\right)^{-1} \\
&\simeq \frac{2.51\times10^{-35}g^{1/2}}{g_\chi m_\chi\langle\sigma v\rangle}\left(\frac{(x-3/2)e^x}{x^{1/2}}\right)\,,
\end{aligned} \tag{2.16}$$

[1] Strictly speaking, Eq. (2.13) is only applicable for the non-relativistic case with $x_F \gg 1$. However, as noted in [373, 374], this is a good approximation (within 3% accuracy) even for the semi-relativistic case with $x_F \sim 1$. For the relativistic case $x_F \ll 1$, the final yield of χ particles is simply its equilibrium value.

where in the second line, we used $Y_{\chi,eq}(x \gg 1) = \frac{45}{2\pi^4}\left(\frac{\pi}{8}\right)^{1/2}\frac{g_\chi}{g}x^{3/2}e^{-x}$ [56] whereas in the third line we used Eqs. (2.5) and (2.8). Note that in the third line, $\langle\sigma v\rangle$ is measured in $\mathrm{cm}^3\,\mathrm{s}^{-1}$ units. As the χ particles start freezing out with increasing x while $Y_{\chi,eq}$ is exponentially decreasing, Δ_χ increases exponentially [see Eq. (2.16) above], eventually becoming much larger than 1. Thus, for some intermediate value of $x = x_*$, $\Delta_\chi \sim \mathcal{O}(1)$, and for $x > x_*$, it grows exponentially. We define x_* when $\Delta_\chi(x_*) \equiv \Delta_{\chi,*} = 1/2$ [1], and solve Eq. (2.16) iteratively for x_* as a function of m_χ, $\langle\sigma v\rangle$ and g_*. For the logarithmic derivative of of $g(T)$, we use the calculations of [377] for the SM relativistic d.o.f.. For the cases with no phase transition around $T_* = m_\chi/x_*$, $g(T)$ is almost constant, and hence, this term can be ignored in Eq. (2.16). Once the value of x_* is found, one can determine $T_* = m_\chi/x_*$ and $Y_\chi(x_*) = (3/2)Y_{\chi,eq}(x_*)$ (corresponding to $\Delta_{\chi,*} = 1/2$). The actual freeze-out temperature T_F is somewhere below T_*, since at $T = T_*$, $(\Gamma_\chi/H)_*$ is still larger than 1 [376].

For $x > x_*$, $Y_\chi \gg Y_{\chi,eq}$; hence, the $Y^2_{\chi,eq}$ term in Eq. (2.10) can be dropped. Therefore, the current yield of the species χ, $Y_\chi(x_0) \simeq Y_\chi(x_F)$, can be obtained by integrating Eq. (2.10) from $x = x_*$ to $x = x_F$,

$$Y_\chi(x_0) \simeq Y_\chi(x_*)\left[1 + \int_{x_*}^{x_F} \mathrm{d}x\, Y_\chi(x_*)\frac{s\langle\sigma v\rangle}{Hx}\left(1 + \frac{1}{3}\frac{\mathrm{d}\ln g}{\mathrm{d}\ln T}\right)\right]^{-1}, \tag{2.17}$$

which can be used in Eq. (2.14) to compute $\Omega_\chi h^2$. To perform the integration in Eq. (2.17), we need to know the x-dependence of $\langle\sigma v\rangle$ [as given by Eq. (2.13)] which is one of the key quantities that determine the current relic density. For $x_F \gg 3$, the χ particles are already non-relativistic at decoupling, and hence, one can expand $\langle\sigma v\rangle$ in a Taylor series in terms of the averaged relative velocity:

$$\langle\sigma v\rangle = a + b\left\langle v_r^2\right\rangle + \mathcal{O}\left(\left\langle v_r^4\right\rangle\right) = a + \frac{b'}{x} + \mathcal{O}\left(\frac{1}{x^2}\right). \tag{2.18}$$

For s-wave annihilation, only the first term is considered, and in this case, Eq. (2.17) can be evaluated to finally obtain an improved analytic solution for

[1] As verified in [376], other alternative choices of $\Delta_{\chi,*}$ change the final result only by about 0.1%.

the relic density (in the s-wave limit) [376]:

$$\Omega_{\chi,0}h^2 = \frac{9.93\times10^{-28}\ \mathrm{cm^3 s^{-1}}}{\langle\sigma v\rangle}\frac{x_*}{g_*^{1/2}}\frac{(\Gamma_\chi/H)_*}{1+\alpha_*(\Gamma_\chi/H)_*}\,, \tag{2.19}$$

where the subscript $*$ means the values evaluated at $x=x_*$, and

$$\alpha_* = \int_{T_F}^{T_*}\frac{\mathrm{d}T}{T_*}\left(\frac{g}{g_*}\right)^{1/2}\left(1+\frac{1}{3}\frac{\mathrm{d}\ln g}{\mathrm{d}\ln T}\right). \tag{2.20}$$

Here we substituted $Y_{\chi,*}=\langle\sigma v\rangle^{-1}(\Gamma_\chi/H)_*(H/s)_*$ where $(H/s)_*=(45/8\pi^2)^{1/2}m_\chi^{-1}$ $M_{\rm P}^{-1}(x/\sqrt{g})_*$. The analytic result in Eq. (2.19) agrees with the exact numerical result within $\sim 3\%$, almost independent of the DM mass. Note that for an arbitrary l-wave annihilation, the above formalism can be repeated by considering higher order term of the Taylor expansion of $\langle\sigma v\rangle$ in powers of $v_r^2\sim 1/x$. Here, we did not consider the model-dependent co-annihilation, resonant annihilation and the forbidden channel annihilation which can in principle result in a decrease in the final abundance of the species χ [378]. From Eq. (2.19), it is clear that the final abundance is inversely proportional to the thermal annihilation rate. Thus, the larger the cross-section, the longer the DM particles stay in equilibrium with the thermal bath, and hence, the lower the final abundance.

The dependence of the yield function on the annihilation rate for the thermal DM which has frozen out is illustrated in Figure 2.1. Here we have chosen $m_\chi=100$ GeV. The dashed black line shows the equilibrium distribution which is constant in the extreme relativistic regime ($x\ll 3$), and exponentially suppressed in the non-relativistic regime ($x\gg 3$), as can also be seen from Eq. (2.12) by taking the asymptotic limits of the Bessel function. The observed DM yield that corresponds to the relic density as measured by Planck, shown as the horizontal gray line, is obtained for the thermal annihilation rate of $\langle\sigma v\rangle=2.05\times10^{-26}\ \mathrm{cm^3 s^{-1}}$, as shown by the solid green line. As the annihilation rate decreases, the DM freezes out earlier (with smaller x_F), thus giving a larger relic density.

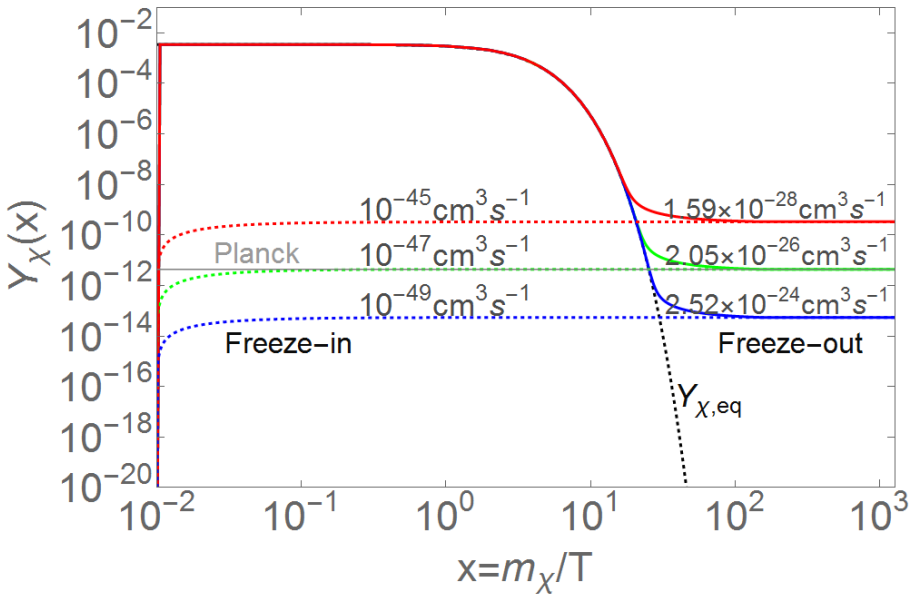

Figure 2.1: Illustration of the freeze-out and freeze-in scenarios in the evolution of thermal DM yield as a function of $x = m_\chi/T$ for different annihilation rates. Here the dashed black curve represents the equilibrium DM yield, the solid (red, green and blue) curves correspond to the freeze-out DM scenario and the dashed (red, green and blue) curves correspond to the freeze-in DM scenario. For the purpose of illustration, we have chosen $m_\chi = 100$ GeV and for the initial conditions, $m_\phi = 10^{13}$ GeV, $T_{\rm rh} = 10$ TeV, $B_\chi = 10^{-15}$. The horizontal gray line corresponds to the correct relic density [13].

2.2.2 Relativistic (hot) dark matter

In the other extreme limit, where the freeze-out occurs when the χ particles are still relativistic ($x_F \ll 3$) and the x-dependence of the equilibrium yield of χ particles is only through $g(x)$ which does not change much away from the phase transitions, the current yield of the species χ, $Y_\chi(x_0)$, is approximated by the corresponding equilibrium value at freeze-out, $Y_{\chi,eq}(x_F)$ [56, 372]. In this case, Eq. (2.6) gives $n_{\chi,eq} = (\zeta(3)/\pi^2) g_{\rm eff} T^3$, where $g_{\rm eff} = g_\chi$ $(3g_\chi/4)$ for bosonic (fermionic) χ, and $\zeta(x)$ is the Riemann zeta function. Using the entropy density as given by Eq. (2.8), we obtain $Y_{\chi,eq}(x_F) = 0.28\, g_{\rm eff}/g(x_F)$ which to a good approximation is insensitive to the details of freeze-out. From Eq. (2.14), the

present relic density is then given by

$$\Omega_{\chi,0}h^2 = 7.62\times10^{-2}\frac{g_{\rm eff}}{g(x_F)}\left(\frac{m_\chi}{1\,\mathrm{eV}}\right)\,. \tag{2.21}$$

Relativistic DM particles in our Universe will lead to large damping scales $\gtrsim 10$ Mpc (roughly the size of typical galaxy clusters), thereby suppressing the growth of small-scale structures. They would predict a top-down hierarchy in structure formation [379, 380], with small structures forming by fragmentation of larger ones, while observations have shown no convincing evidence of such effects, thereby imposing stringent upper limits on these 'hot' DM species. For instance, the SM neutrino contribution to the nonbaryonic DM relic density is currently constrained to be $\Omega_\nu h^2 \leq 0.0025$ at 95% CL [13]. Thus, hot DM cannot yield the total observed DM density in our Universe, and if it exists [1], must coexist with other cold/warm components (see e.g. [382, 383]).

2.2.3 Semi-relativistic dark matter

In the intermediate regime $x_F \sim 3$, the χ particles are semi-relativistic when they decouple from the thermal bath, in which case the thermally averaged cross-section $\langle\sigma v\rangle$ involves multiple integrals, and cannot be expanded in a Taylor series of the velocity-squared. One way is to approximate the cross-section by interpolating between its relativistic and non-relativistic expressions. For example, in the case of s-wave annihilation of two Dirac fermions the following ansatz was used [374] [2]:

$$\langle\sigma v\rangle = \frac{\alpha_\chi^2 m_\chi^2}{16\pi}\left(\frac{12}{x^2}+\frac{5+4x}{1+x}\right), \tag{2.23}$$

where α_χ denotes the coupling constant of the four-fermion interaction, which is taken to be a free parameter. Following this approach, it was shown [374] that

[1] Recently, the presence of a hot DM component at 3σ CL has been proposed to resolve the inconsistencies of the Planck measurements with other observations, such as the current Hubble rate, the galaxy shear power spectrum and galaxy cluster counts [381].

[2] For p-wave annihilation, a similar ansatz for the thermally averaged cross-section times Møller velocity holds [374]

$$\langle\sigma v\rangle = \frac{\alpha_\chi^2 m_\chi^2}{16\pi}\left(\frac{12}{x^2}+\frac{3+6x}{(1+x)^2}\right). \tag{2.22}$$

the Maxwell-Boltzmann distribution can still be used to compute $\langle\sigma v\rangle$, and the more appropriate Fermi-Dirac or Bose-Einstein distributions are only needed for the calculation of the freeze-out abundance $Y_{\chi,eq}(x_F)$. The current abundance of the DM species χ can then be calculated by using Eq. (2.23) to integrate Eq. (2.10) for $Y_\chi(x \gg x_F)$, where x_F is defined here as $\Gamma_{\chi,eq}(x_F) = H(x_F)$, and then substitute it into Eq. (2.14). This approach works well for DM species that freeze-out between $0.5 \lesssim x_F \lesssim 15$ to obtain $\Omega_{\chi,0}h^2$. We note here that for the case of s-wave annihilation using a constant value for $\langle\sigma v\rangle$ also works well in the semi-relativistic case, and induces an error of only about 6% at most, as compared to using the ansatz given by Eq. (2.23) above. We also note that similar to the case of cold DM, the abundance of a semi-relativistic DM species is inversely proportional to $\langle\sigma v\rangle$. This is not true for the hot DM case, where its abundance is insensitive to the interaction cross-section, as discussed in Section 2.2.2.

Note that a semi-relativistic DM species can act as warm DM if it is sufficiently light. The current observations do not rule out the possibility of the whole DM density being comprised of warm DM species (see e.g. [132, 384, 385]). In fact, warm DM can solve the Milky Way satellite galaxies problem and the larger amount of substructure [128, 129, 130, 131] predicted by cold DM simulations [114, 115, 116]. Nevertheless, there exist strong constraints from observations of early structure, in particular, from Lyman-α forest data [97, 386].

2.3 Freeze-in scenario

In this scenario, the χ particles are very weakly coupled to the bath, and hence, cannot reach thermal equilibrium with the cosmic bath before decoupling. However, the feeble interactions with the thermal bath could still produce χ particles [259, 260, 261]. In this case, the final abundance is directly proportional to the interaction strength; the larger the interaction rate is, the more χ particles are produced. In this sense, freeze-in can be viewed as the opposite process to freeze-out. The final relic density in the freeze-in scenario will, in general, be determined by both the interaction cross-section and the initial abundance which in turn depends on the reheating temperature and the branching ratio of the

inflaton/moduli to DM in our case. To see this, we note that the decoupling of χ particles, in this case, occurs for small values of x_F [1], where the equilibrium abundance $Y_{\chi,eq}$ is roughly independent of x, as can be seen from Eqs. (2.6) and (2.8),

$$Y_{\chi,eq}(x \ll 1) = \frac{45\zeta(3)}{2\pi^2}\frac{g_{\rm eff}}{g}\,. \tag{2.24}$$

Nevertheless, the DM thermally-averaged interaction rate can, in general, depend on x. However, this is a model-dependent issue, and since in this chapter we are interested in the identification of the gross features of the DM parameter space in a model-independent paradigm, we take $\langle\sigma v\rangle$ to be constant in x [2]. Hence, the general Boltzmann equation (2.10) can be approximated, in this case, to the following simple form:

$$\frac{{\rm d}Y_\chi}{{\rm d}x} \simeq \left(\frac{8\pi^2 g}{45}\right)^{1/2}\langle\sigma v\rangle\frac{m_\chi M_{\rm P}}{x^2}(Y^2_{\chi,eq} - Y^2_\chi) \simeq -\frac{A}{x^2}(Y^2_\chi - B)\,, \tag{2.25}$$

where A and B are roughly independent of x [3]. Eq. (2.25) has a simple analytic solution in terms of the initial values $x_i = m_\chi/T_{\rm rh}$ and $Y^{(i)}_\chi$, where the latter can be obtained from Eqs. (2.2) and (2.8):

$$Y^{(i)}_\chi = \frac{n^{(i)}_\chi}{s(T_{\rm rh})} \simeq \frac{3}{4}B_\chi\frac{T_{\rm rh}}{m_\phi}\,. \tag{2.26}$$

[1] The decoupling of FIMP DM from the cosmic bath can occur at larger x_F in some cases. For example, this is the case if the interaction of the DM particles with the thermal bath d.o.f. is mediated by a light particle [387].

[2] This is actually the case in some scenarios such as the case where DM interaction with the SM d.o.f. is dominated by a dimension-five coupling to the Higgs field [261]. In Chapter 3, we consider the case where the DM interaction with the SM d.o.f. being dominated by a dimension-six coupling to the SM fermions in which case the thermally average DM interaction rate has x-dependence.

[3] In general, $\langle\sigma v\rangle$ depends on x; however, its exact form is model dependent. For instance if χ particles are of fermionic nature and their interactions with the bath particles is mediated via a heavy mediator X, ($M_X \gg T_{\rm rh}, m_\chi$), $\sigma \sim m^2_\chi/(x^2 M^4_X)$ and hence $\langle\sigma v\rangle \propto x^{-2}$; we discuss this possibility in the next chapter. For now we treat $\langle\sigma v\rangle$ as a constant since here we are interested in identifying the gross feature of the (m_χ,$\langle\sigma v\rangle$) parameter space in a model-independent setup.

In the limit $x \to \infty$, the expression for $Y_\chi(x)$ simplifies further, and the final relic density can then be obtained using Eq. (2.14). This has two contributions:

$$\Omega_{\chi,0}h^2 \simeq 2.06 \times 10^8 \; B_\chi \frac{m_\chi}{m_\phi} \left(\frac{T_{\rm rh}}{1\ {\rm GeV}}\right) + \sqrt{g} \left(\frac{m_\chi}{1\,{\rm GeV}}\right)\left(\frac{T_{\rm rh}}{1\,{\rm GeV}}\right) \times \left(\frac{\langle\sigma v\rangle}{10^{-50}\,{\rm cm}^3\,{\rm s}^{-1}}\right)\left(5.84 \times 10^{-8}\,\frac{g_{\rm eff}^2}{g^2} - 4.26 \times 10^{-7} B_\chi^2 \frac{T_{\rm rh}^2}{m_\phi^2}\right), \quad (2.27)$$

where the first term represents the non-thermal contribution which only depends on the initial abundance, and the other two terms represent the thermal contribution which depend on the interaction rate. Note that the analytic expression (2.27) is valid as long as $m_\chi \ll T_{\rm rh}$, otherwise the thermal production will occur at higher values of x when the equilibrium distribution in Eq. (2.25) may no longer be flat, but exponentially decaying. For the FIMP scenario, it is usually assumed that the initial abundance is negligible, so that the final abundance is solely determined by the interaction strength in Eq. (2.27), as in the freeze-out scenario. This is illustrated in Figure 2.1 for a typical choice of parameters: $m_\chi = 100$ GeV, $m_\phi = 10^{13}$ GeV, $T_{\rm rh} = 10$ TeV, and $B_\chi = 10^{-15}$ so that the initial abundance given by Eq. (2.26) is negligible. The different dashed lines in Figure 2.1 correspond to the freeze-in scenario with various interaction rates, and hence, different final abundances. Note that the final abundance increases with increasing interaction rate, in contrast with the freeze-out scenario (the solid lines) where the final abundance decreases with increasing interaction rate. As shown here, the observed relic abundance shown by the gray horizontal line can be obtained in the freeze-in scenario for an interaction rate of 10^{-47} cm^{3}s^{-1}, which is much smaller than the typical value of 2×10^{-26} cm^{3}s^{-1}, as in the freeze-out scenario.

We should mention here that besides the freeze-out and freeze-in scenarios there could be other thermal production mechanisms for the DM in specific models, depending on its interaction with the SM particles and/or the model construction for the beyond SM sector. For instance, a keV-scale sterile neutrino DM can be produced by the Dodelson-Widrow mechanism [269], which is very similar to the freeze-in mechanism discussed above. Likewise, there could be other non-thermal DM production mechanisms such as the misalignment mech-

anism for axions and many ALP species (see e.g. [250]; for a recent review see e.g. [253, 254]).

2.4 Non-thermal dark matter production

As discussed in Section 2.1, we assume that the DM particles χ directly couple to the inflaton/moduli field, ϕ, so that they can be produced in the perturbative inflaton/moduli decay for $m_\chi < m_\phi/2$. For sufficiently low interaction rate, the DM particles are produced already decoupled from the thermal bath, in which case, the annihilation rate, and consequently, the right-hand side of Eq. (2.10) can be neglected, thus leading to $\mathrm{d}Y_\chi/\mathrm{d}x \simeq 0$. As a result, the final yield of the DM species χ is completely determined by the initial one given by Eq. (2.11). Using the general expression (2.14), this yields the non-thermal relic DM density

$$\Omega_{\chi,0}h^2 = 2.06 \times 10^8 \; B_\chi \frac{m_\chi}{m_\phi} \left(\frac{T_{\rm rh}}{1 \text{ GeV}}\right), \tag{2.28}$$

which can also be identified with the first term on the right-hand side of Eq. (2.27) where the other two terms are negligible. Thus, for super-weak interaction rates, the final abundance only depends on the reheating temperature and inflaton/moduli branching fraction for a given DM species and the inflaton/moduli masses [1]. Clearly, the non-thermal contribution to DM can be sizeable for large branching ratios. Some illustrative cases for the non-thermal DM are shown in Figure 2.2 for two typical values of the branching ratio $B_\chi = 10^{-5}$ and 10^{-15}. The choice of small values of B_χ will be justified below. The various contours show the reheating temperatures required to obtain the correct relic density $\Omega_\chi h^2 = 0.1198$ for given values of the inflaton/moduli and DM masses. These plots were obtained by numerically solving the Boltzmann equation (2.10) for a typical annihilation rate $\langle\sigma v\rangle = 10^{-60}\,\mathrm{cm^3 s^{-1}}$ (see Section 2.6 for details) following the procedure mentioned above, but the results agree quite well with the approximate analytic for-

[1] Similar results were obtained in [371, 388] for superheavy metastable DM candidates. Our result is valid for all non-thermal DM production mechanisms as long as it is a perturbative process.

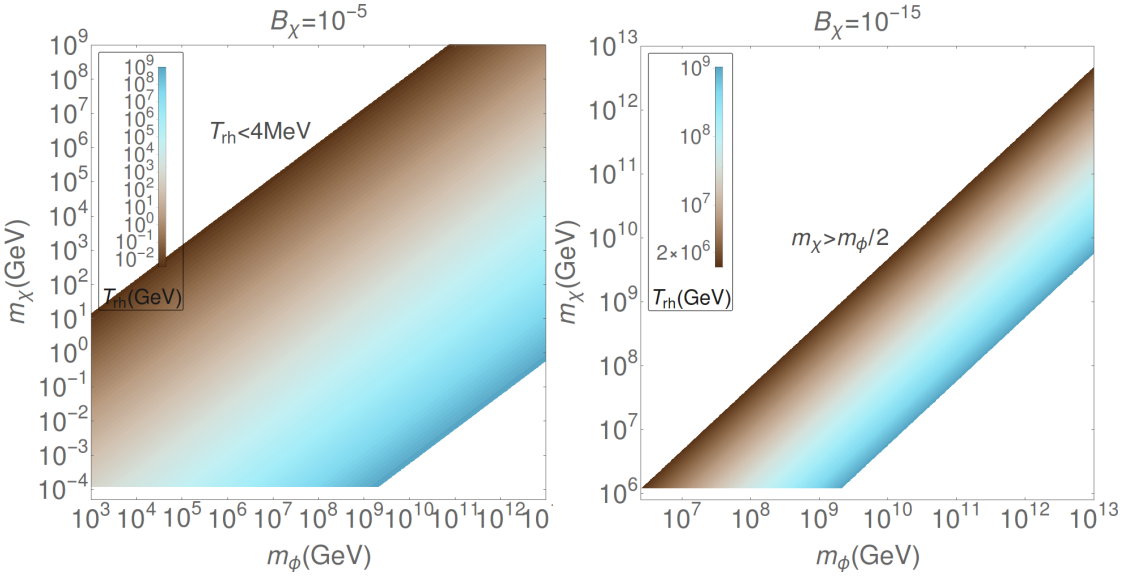

Figure 2.2: The coloured contours show the reheating temperature values required to give the correct relic density for non-thermal DM as a function of the inflaton/moduli and DM masses, for a given branching ratio.

mula given in Eq. (2.28). From Figure 2.2, it is clear that as the inflaton/moduli branching fraction increases, the allowed range of the DM masses shifts to lower values in order to satisfy the observed relic density, in accordance with Eq. (2.28). We have shown the results for the inflaton/moduli mass m_ϕ in the range 10^3 - 10^{13} GeV, the reheating temperature $T_{\rm rh}$ between 4 MeV–10^9 GeV and for the DM mass $m_\chi \leq m_\phi/2$. Note that a late-time entropy production would induce various cosmological effects, leading to a lower limit on the reheating temperature of about 1 MeV from BBN constraints [389], which, when combined with the CMB and large scale structure data, increases to about 4 MeV at 95% CL [390].

For $m_\chi \ll m_\phi$, the non-thermal DM directly produced from the inflaton/moduli decay will have a large velocity at the time of radiation-matter equality ($t_{\rm eq}$), unless the reheating temperature is sufficiently high to make the velocity small due to redshift. The comoving free-streaming length of non-thermal DM at radiation-matter equality is given by

$$\tilde{\lambda}_{\rm fs} = \int_{t_d}^{t_{\rm eq}} {\rm d}t \frac{v_\chi(t)}{a(t)}, \tag{2.29}$$

where $a(t)$ is the scale factor, $t_d = \Gamma_\phi^{-1}$ is the time at inflaton/moduli decay, and

$$v_\chi(t) = \frac{|\mathbf{p}_\chi|}{E_\chi} \simeq \frac{\epsilon m_\phi \frac{a(t_d)}{a(t)}}{\sqrt{m_\chi^2 + \left[\epsilon m_\phi \frac{a(t_d)}{a(t)}\right]^2}} \tag{2.30}$$

is the magnitude of the velocity of the DM particle with ϵ being the fraction of inflaton/moduli CM energy per χ particle in each decay. Integrating Eq. (2.29), and requiring that $\lambda_{\rm fs}(t_0) \lesssim 1$ Mpc, from Lyman-α constraints (for warm/cold DM), one obtains a lower limit on the reheating temperature [391]

$$T_{\rm rh} \gtrsim 10^6\,{\rm GeV}\left(\frac{\epsilon}{2}\right)\left(\frac{g}{200}\right)^{-1/4}\left(\frac{1\,{\rm GeV}}{m_\chi}\right)\left(\frac{m_\phi}{10^{13}\,{\rm GeV}}\right). \tag{2.31}$$

Combining this with Eq. (2.28), and requiring $\Omega_\chi h^2 \leq 0.1228$ to satisfy the observed relic density for cold/warm DM relics, we derive an upper limit on the branching ratio of the inflaton/moduli decay to DM: $B_\chi \lesssim (0.005/\epsilon)(g/200)^{1/4}$. This is complementary to what is already expected from the fact that for a standard cosmology, B_χ must be small in order to have a RD epoch immediately after reheating, followed by MD epoch only at a late stage.

2.5 Theoretical and experimental constraints

In this section, we summarise the various observational and theoretical constraints on the DM properties relevant for our analysis.

2.5.1 Overclosure

For any DM candidate, we must ensure that it does not lead to an overclosure of the Universe. Thus, we set the upper limit on the relic density of our χ particles coming from inflaton/moduli decay using the observed value $\Omega_{\rm DM,0}h^2 = 0.1198 \pm 0.0030$ (95% CL; Planck) [13]. We do not set a lower limit on $\Omega_{\chi,0}$ since for the cases in which the χ particles do not account for the total observed abundance, the

remaining fraction can be obtained by invoking a hidden-sector/multi-component DM scenario (see e.g. [382, 383, 392]).

2.5.2 Unitarity

The partial-wave unitarity of the scattering matrix, together with the conservation of total energy and momentum, impose a generic upper bound on the cross-section of thermal DM annihilation into the j-th partial wave [393]:

$$\sigma_j \leq \frac{4\pi(2j+1)}{m_\chi^2 v_r^2}\left(1-\frac{v_r^2}{4}\right), \tag{2.32}$$

where $v_r = 2\sqrt{1-4m_\chi^2/s}$ is the relative velocity between the two annihilating particles in the CM frame with total energy $\sqrt{s}$. Assuming that the s-wave piece with $j=0$ dominates in the partial-wave expansion, we obtain an upper bound on the thermally-averaged annihilation rate $\langle\sigma v\rangle$ as a function of the DM mass from Eq. (2.13), where σ is replaced with $(\sigma_0)_{\rm max}$ from Eq. (2.32). Since the current abundance of a non-relativistic frozen-out thermal relic scales as $\Omega_\chi \propto 1/\langle\sigma v\rangle$, the observed DM relic density constrains the mass of the thermal relic to be $m_\chi \lesssim 130$ TeV to satisfy the unitarity bound. Note, however, that this bound may not be applicable when the higher partial-waves are not suppressed, as is the case when the DM particles decouple from the thermal bath while still being relativistic.

2.5.3 Planck

Precision measurements of the CMB angular power spectrum by Planck put stringent constraints on the number of effective neutrino species ($N_{\rm eff}$), which parameterises the total radiation energy density of the Universe:

$$\rho_r = \rho_\gamma\left[1+\frac{7}{8}\left(\frac{T_\nu}{T_\gamma}\right)^4 N_{\rm eff}\right], \tag{2.33}$$

where $\rho_\gamma = (\pi^2/15)\,T^4$ is the energy density of photons, and the neutrino-to-photon temperature ratio is $T_\nu/T_\gamma = (4/11)^{1/3}$ assuming exactly three neutrino

flavors and their instantaneous decoupling. In the SCM, T_ν/T_γ is slightly higher than $(4/11)^{1/3}$ due to partial reheating of neutrinos when electron-positron pairs annihilate transferring their entropy to photons, thus giving $N_{\rm eff} = 3.046$ [394]. Now if the DM species remains in thermal equilibrium with the neutrinos or electrons and photons after neutrino decoupling, and transfers its entropy to them during its annihilation after it decouples at a later stage, it can increase or decrease the value of $N_{\rm eff}$ as we decrease the DM mass. Using the constraints on $N_{\rm eff}$ from Planck [13], together with the helium abundance Y_p, references [395, 396, 397] derived a robust lower bound of 2-10 MeV on the thermal DM mass, depending on whether it is a fermion (Dirac/Majorana) or scalar (real/complex) and whether it was in equilibrium with neutrinos or with electrons and photons.

Another generic lower bound on the cold DM mass can be obtained using the CMB and matter power spectrum observations which place an upper bound on the DM temperature-to-mass ratio: $T/m_\chi \leq 1.07\times10^{-14}(1+z)^2$ [398]. Evaluating this bound at radiation-matter equality with a redshift of $z_{\rm eq} = 3393$ [13] and $T_{\gamma,{\rm eq}} \simeq 0.77$ eV [56], we obtain a lower limit of $m_\chi \gtrsim 6.5$ keV, which is much weaker than the limit derived in [395, 396, 397] using $N_{\rm eff}$.

2.5.4 Dark radiation

The Planck constraints on $N_{\rm eff}$ can also be used to set an upper limit on the amount of dark radiation [1] at decoupling. From Eq. (2.33), the radiation energy density apart from the photon and SM neutrino contribution is given by

$$\Omega_{\rm dark}h^2 = \frac{7}{8}\left(\frac{4}{11}\right)^{4/3}\Delta N_{\rm eff}\ \Omega_\gamma h^2\,, \tag{2.34}$$

where $\Omega_\gamma h^2 = 2.473\times10^{-5}(T/2.7255)^4$ is the CMB radiation density [32], and $\Delta N_{\rm eff} = N_{\rm eff} - 3.046$. Using the 95% CL measured value of $N_{\rm eff} = 3.15^{+0.41}_{-0.40}$ from Planck (temperature anisotropy and lensing data)+Joint-Light-Curve Analysis (JLA) of type Ia supernovae catalogue+Baryon Acoustic Oscillation (BAO) measurements from large scale structure surveys [13], we obtain an upper limit on the

[1] Dark radiation refers to a hidden sector (dark) species which remains ultra-relativisitic until the era of photon decoupling.

amount of dark radiation from Eq. (2.34): $\Omega_{\rm dark}h^2 \leq 2.92\times10^{-6}$. This also sets the upper limit on the relic density of hot DM species. From the Ly-α constraints, we require $\lambda_{\rm fs}(t_0) \lesssim 1$ Mpc for cold/warm DM candidates.

2.5.5 BBN and CMB

The late annihilation of DM particles (after freeze out) can deposit hadronic and/or electromagnetic energy in the primordial plasma, thereby altering the history of BBN [399, 400, 401, 402] and recombination (CMB) [403, 404, 405, 406, 407, 408, 409, 410, 411]. These effects depend only on the type and rate of energy injection into the thermal bath allowing us to set rather model-independent bounds on the annihilation rate, especially for DM masses in the MeV-GeV range. During nucleosynthesis, the injection of hadronic and/or electromagnetic energy can affect the abundance of nuclei via (i) raising the neutron-to-proton ratio and therefore the primordial ^{4}He abundance, and (ii) high energy nucleons and photons disassociating nuclei. During recombination, the injected electromagnetic energy ionises hydrogen atoms, which results in an increased number of free electrons, causing the broadening of the surface of last scattering, and results in scale-dependent changes to the CMB temperature and polarisation power spectra, especially in the low multipole modes. The precision measurements of BBN and CMB from WMAP and Planck data have been used to set upper bounds on the DM annihilation cross-section $\langle\sigma v\rangle$, as a function of the DM mass [399, 400, 401, 406, 408, 409, 410, 411].

2.5.6 Indirect detection

The relic annihilations of WIMP DM may be indirectly observed by searching for their annihilation products such as charged particles, photons and neutrinos. In fact, a number of ID experiments have observed an excess of electrons and positrons in the charged cosmic ray flux [300, 303, 304], and this was recently confirmed with the precision measurements by AMS-02 [302]. Assuming a possible DM contribution to this positron excess and using the high quality of AMS-02

data, the authors of [412, 413] have performed a spectral analysis to put stringent constraints on the DM annihilation cross-section for various leptonic final states [1]. Similar constraints were obtained for the DM annihilation into hadronic final states [419, 420, 421] in order to explain the absence of a corresponding excess in the cosmic-ray antiproton flux in the PAMELA data [301, 422].

The DM annihilation to various SM final states can also lead to an observable photon flux which can be produced either by direct DM annihilation ('prompt' gamma-rays) or by inverse Compton scattering and synchrotron emission of the electrons and positrons created in the DM annihilation. These photon signals are preferentially searched for in regions with high DM densities and/or regions with reduced astrophysical background. The Fermi-LAT, with its unprecedented sensitivity to gamma rays in the MeV-TeV energy range, has performed deep searches for line spectrum (mono-energetic gamma-rays due to direct DM annihilation) [423] as well as continuum spectrum (through DM annihilation into intermediate states) [424] [2]. They have derived additional constraints on the DM annihilation cross-section from the isotropic diffuse gamma-ray emission in the galactic halo [426], nearby galaxy clusters [427], and nearby dwarf spheroidal galaxies [326]. Similar constraints were also derived from the galactic centre region for various DM density profiles [428] [3]. Complementing the Fermi-LAT range toward higher energies, the HESS collaboration has performed a number of DM searches up to multi-TeV DM masses [434, 435, 436].

[1] There are many DM interpretations for the AMS-02 signal (see e.g. [414, 415, 416, 417, 418]). On the other hand, this excess can be explained by pulsars [312, 313, 314] and other astrophysical sources [315]. Nevertheless, the absence of anisotropies in the electron-positron excess is compatible with an astrophysical origin [316]. Further, the Fermi/LAT measurement of the diffuse gamma-ray background [325], the Fermi/LAT observation of the Milky Way satellite dwarf galaxies [326], and the observational data from cool-core clusters [327] rule out the DM explanation of the electron-positron excess [328, 329, 330].

[2] There exists yet another class of spectral signature, namely, box-shaped gamma-ray spectrum, which arises if the DM annihilates/decays into intermediate particles which further decay into photons [425]. The cross-section limits derived using this feature are currently comparable to those obtained using the line-like spectral feature.

[3] A gamma-ray excess was observed by Fermi/LAT toward the galactic centre [305], to which many DM interpretations exist (see e.g. [429, 430, 431, 432, 433]) and many other astrophysical interpretations (see e.g. [317, 318, 319, 320, 321, 322, 323]). However, a recent study pointed out that the point-like nature of the sources required by substructure considerations rule out the DM interpretation of this galactic centre gamma-ray excess [324].

The DM annihilation can also produce neutrinos which, like gamma-rays, can travel essentially unabsorbed through the galaxy, and can be observed at large neutrino detectors on Earth. Constraints on the DM annihilation rate were derived by the IceCube (IC) experiment from the upper limits on the high-energy neutrino fluxes from the galactic halo [437, 438], galactic centre [439, 440], dwarf galaxies and clusters of galaxies [441] [1]. These limits are currently somewhat weaker than the gamma-ray limits for low DM masses, but become competitive at larger DM masses. Combining the Fermi/LAT data on the diffuse gamma-ray and the IceCube data on diffuse neutrino flux, robust constraints were derived on the DM annihilation rate for heavy DM masses (1 TeV - 10^{10} GeV) [447].

2.6 Results and discussion

Using the model-independent approach outlined in Section 2.1, we solve the Boltzmann equation (2.10) numerically for the evolution of DM produced from inflaton/moduli decay. Here we assume an s-wave annihilation, and take the annihilation rate $\langle\sigma v\rangle$ to be a free parameter [2]. Both thermal and non-thermal regions are identified in the $(m_\chi,\langle\sigma v\rangle)$ parameter space. Our results are shown in Figures 2.3 and 2.4 for a fixed inflaton/moduli mass $m_\phi = 10^{13}$ GeV. We consider two typical values of the reheating temperature $T_{\rm rh} = 10^9$ GeV and 10^4 GeV for our illustration purposes. We have considered DM masses only below the reheating temperature, and do not analyse scenarios in which DM could be produced during preheating or reheating (e.g. the WIMPzilla scenario [367]). For each

[1] The IceCube collaboration has reported the detection of a series of neutrino events in the energy range 30−2000 TeV with high statistical significance above the atmospheric background [306, 307, 308] for which many beyond SM explanations were proposed (see e.g. [442, 443, 444]). However, it was shown that these events are consistent with the SM expectation [445, 446]. Moreover, a recent analyses of the IceCube and ANTARES data in search of point-like origin of the astrophysical neutrinos shows no statistical significance above the background [331, 332, 333]. This rules out the DM interpretation of the IceCube neutrino events.

[2] For a p-wave annihilation, $\langle\sigma v\rangle$ depends on the temperature, and hence, cannot be taken as a free parameter in the Boltzmann equation. Our assumption also obliterates additional complications that could arise in special cases such as co-annihilation and resonant annihilation. However, these are highly model-dependent effects, and we cannot easily generalise our results to such scenarios. A more accurate, model-specific numerical analysis for the relic density can

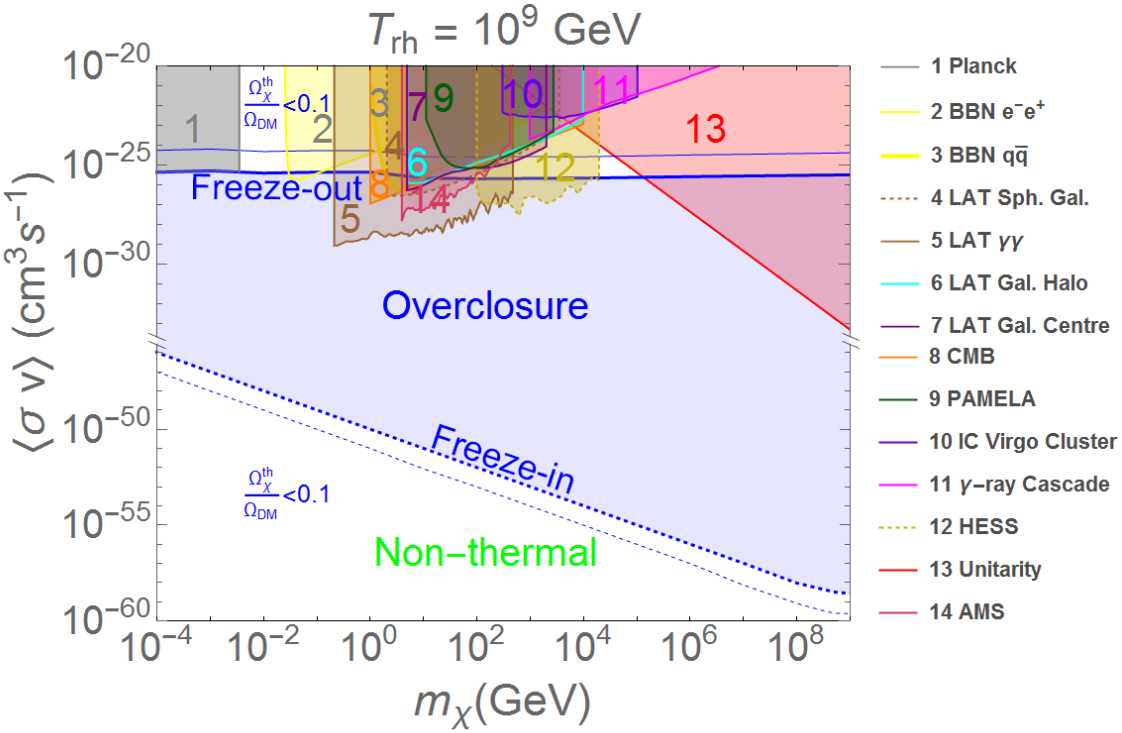

Figure 2.3: Model-independent constraints on the DM annihilation rate as a function of the DM mass for both thermal and non-thermal production mechanisms. Here we have chosen $m_\phi = 10^{13}$ GeV, $T_{\rm rh} = 10^9$ GeV and $B_\chi = 0$ as the initial parameters for the DM evolution. The blue-shaded region is excluded from relic density constraints, and the observed relic density is obtained at its boundary (shown by the thick solid and dashed blue curves). The thin solid and dashed blue curves show the parameters which result in a thermal abundance of χ particles corresponding to 10% of the observed DM relic density. The unshaded regions are allowed; however, non-thermal production mechanisms are required in order for χ particles to make the entirety of the observed DM abundance. In particular, in the unshaded region below the overclosure (blue) region of the parameter space, the χ particles are very weakly coupled to the cosmic bath such that the χ particles produced in the inflaton/moduli decay will not annihilate into bath particles and survive as a non-thermal contribution to DM. The various coloured-shaded regions in the thermal region are excluded (under certain assumptions) by the constraints given in Section 2.5; see text for details.

case shown in Figures 2.3 and 2.4, we calculate the current relic density of the thermal DM to show the overclosure region (blue-shaded) which rules out a wide

be done with publicly available codes [448, 449, 450].

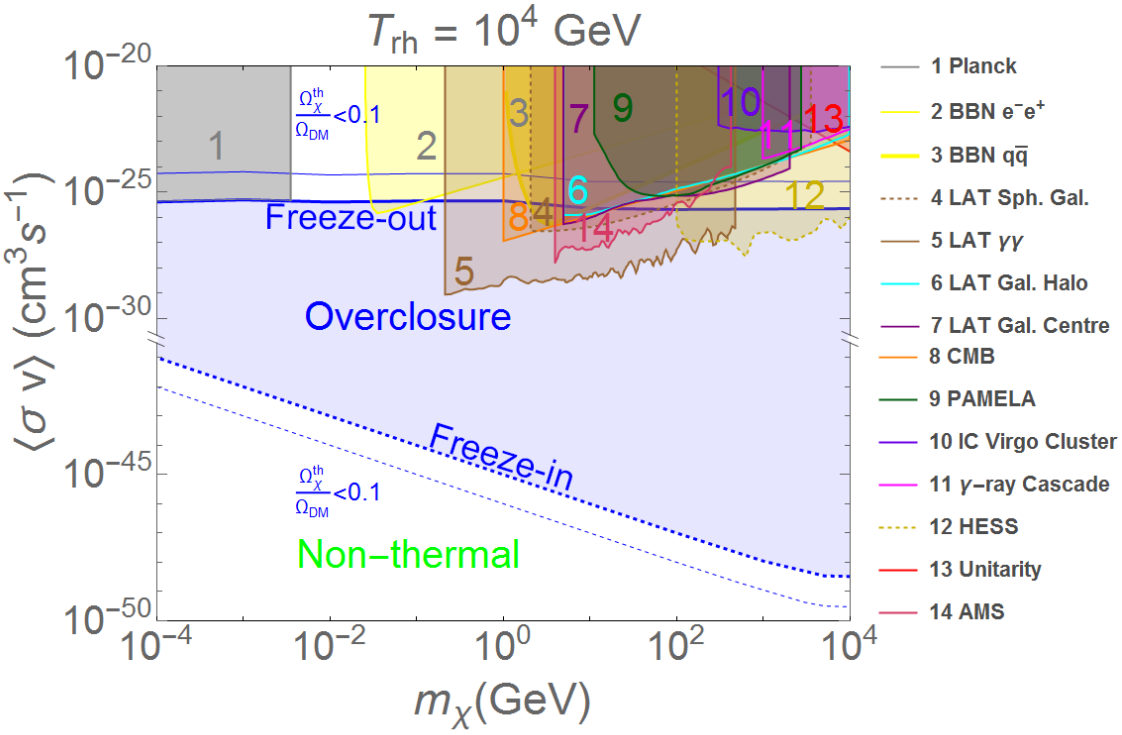

Figure 2.4: Same as Figure 2.3, except for $T_{\rm rh} = 10^4$ GeV.

range of the parameter space, irrespective of the initial choice of parameters.

In the remaining allowed parameter space, we identify the regions corresponding to both the freeze-out (above the overclosure region) and the freeze-in DM scenarios (below the overclosure region). In particular, the thin (thick) solid blue curve corresponds to the parameters that give 10% (100%) of the total DM abundance for the freeze-out scenario whereas the thin (thick) dashed blue curve represents the parameters that give 10% (100%) of the total DM abundance for the freeze-in scenario. Clearly, in the allowed regions and away from the thick curves another DM species and/or another production mechanism such as non-thermal production are needed. In particular, in the region of the parameter space corresponding to the freeze-in scenario, the χ coupling to the thermal bath particles is very weak and hence the χ population produced in the inflaton/moduli decay will not annihilate into bath particles and will survive as a non-thermal contribution to the DM abundance. Below the thin dashed blue curve the thermal contribution to the DM abundance is insignificant, and for χ particles to make the

entirety of DM, the population of χ particles has to be produced non-thermally from the decay of the inflaton/moduli (as discussed in Section 2.4.); otherwise, other DM species are required. Similarly, for the allowed freeze-out region of the parameter space, the contribution of other DM species is needed. Also, the late decay of another dark species into χ particles can increase the population of χ particles such that they may constitute the entirety of DM relic density. However, here we focus on the decay of inflaton/moduli in which the overclosure condition is determined solely by the initial conditions as discussed in Section 2.6.2 below.

2.6.1 Thermal case

In the thermal DM regime, the region above the overclosure region with large annihilation rate belongs to the freeze-out scenario, while in the unshaded region below the overclosure one with small annihilation rate belongs to either freeze-in or non-thermal DM scenario, depending on the interaction rate and initial conditions. The observed value of the relic density is obtained at the boundary between these regions with the overclosure region (shown by the thick solid and dashed blue lines). The thermal freeze-out region with large annihilation rate is severely constrained by many experimental searches, as discussed in Section 2.5, some of which are shown by the shaded regions 1-14 in Figures 2.3 and 2.4, and also summarised below:

- Region 1 (shaded in gray) is excluded by the recent Planck measurements of the effective number of neutrino species, as discussed in Section 2.5.3, assuming that the DM interacts with neutrinos or electrons and photons after the neutrino decoupling. This sets a robust lower bound of order of MeV on the thermal DM mass with large interaction rates. The precise value of the lower bound depends on whether the DM is a scalar or fermion and on whether it couples to neutrinos or to electrons and photons. The bound shown by region 1 assumes a Majorana fermion DM coupling to neutrinos. Note that [395, 396, 397] had originally derived this limit for a cold DM candidate, but this is generically applicable as long as the interaction rate is large enough to keep the DM in thermal equilibrium after the neutrino decoupling, thus transferring entropy at a late stage and affecting $N_{\rm eff}$.

- Regions 2 and 3 (shaded in light and dark yellow respectively) are excluded by the BBN data, as discussed in Section 2.5.5, and assuming DM annihilation into electron-positron and quark-antiquark pairs respectively [401]. Similarly, the region 8 (shaded in light orange) is excluded by constraints derived from a combination of the CMB power spectrum measurements from Planck, WMAP9, ACT and SPT, and low-redshift data sets from BAO, HST and supernovae [406].

- Region 4 (shaded in light brown and bounded by dashed brown curve) is excluded by the Fermi-LAT limit at 95% CL derived using the diffuse gamma-ray flux from a combined analysis of 15 dwarf spheroidal galaxies, for an NFW DM density profile and assuming DM annihilation into tau-antitau final states [326]. Region 6 (shaded in cyan) is excluded by the 3σ Fermi-LAT limit obtained using the diffuse gamma-ray emission in the Milky Way halo, assuming an NFW DM distribution and for annihilation into bottom-antibottom quark pairs [426]. Region 7 (shaded in light purple) is excluded by a similar analysis using the Fermi-LAT data from galactic centre [428]. The corresponding limits for other SM final states are weaker and are not shown here for clarity purposes.

- Region 5 (shaded in light brown and bounded by solid brown curve) is excluded by the Fermi-LAT 95% CL upper limit on the cross-section of DM annihilation to two photons from a dedicated search for the gamma-ray line spectrum [423, 451]. Region 12 (shaded in light gold) is excluded from a complementary search for the line spectrum by HESS [436, 452]. Note that these limits, although very stringent, can be evaded in most of the popular WIMP DM models, since the direct annihilation to photon final states is suppressed due to loop effects.

- Region 9 (shaded in dark green) is excluded by the measurements of the antiproton flux from PAMELA, and assuming the DM annihilation to $b\bar{b}$ final states [420]. These limits are applicable only to hadronic final states. Similarly, region 14 (shaded in purplish red) is excluded by the 95% CL

upper limits, derived from the AMS-02 data, on the DM annihilation cross-section for e^+e^- final state [412, 413]. The corresponding limits for other leptonic final states are somewhat weaker, and hence, are not shown here.

- Region 10 (shaded in violet) is excluded by the IceCube upper limit on the DM annihilation cross-section for neutrino final states for the Virgo galaxy cluster including sub-halos [441]. The corresponding limits for other final states as well as from searches in galactic halo [437, 438] and galactic centre [439, 440] are somewhat weaker.

- Region 11 (shaded in magenta) is excluded by the cascade gamma-ray constraints obtained using the Fermi-LAT diffuse gamma-ray background data up to very high energies [447]. The corresponding limits derived using the IceCube high-energy neutrino data are stronger at higher DM masses but weaker than the unitarity constraint (see Section 2.5.2).

- Region 13 (shaded in red) is excluded by the unitarity constraints [393], as discussed in Section 2.5.2, which sets an upper limit on the CDM mass of about 130 TeV for the allowed region, and rules out heavy thermal DM, even with annihilation rates many orders of magnitude below the thermal annihilation rate. This theoretical constraint is the most stringent one for very heavy DM and is applicable as long as the DM is produced thermally (via freeze-out).

Note that for the indirect detection constraints, we have shown only a few of them (typically the most stringent ones) for illustration purposes. Most of these limits have limited applicability, as they were derived assuming DM annihilation into a particular final state, and can be evaded in specific models where some of these annihilation channels might be suppressed due to various reasons. Also, note that additional constraints on the annihilation cross-section for a given DM mass might be derived using possible correlations with the DM direct detection cross-section limits [453, 454] and collider search limits from mono-jet [455, 456, 457], mono-photon [458, 459, 460], di-photon [461], mono-vector-boson [462, 463] and mono-Higgs [464, 465] final states with large missing energy. In the absence of a collider signal for DM, model-independent constraints can be derived on the

mass and interactions of a generic WIMP DM candidate from direct and indirect detection searches [466].

The other allowed thermal DM parameter space, namely, the region with very low interaction rates such as the FIMP scenario, is hard to constrain from the existing experimental limits. Various experimental tests of the freeze-in mechanism by measurements at colliders or by cosmological observations were outlined in [259]. However, these signals depend very much on the particular freeze-in scenario under consideration, and hence, it is difficult to derive model-independent constraints in the $(m_\chi, \langle\sigma v\rangle)$ parameter space, except for the generic dark radiation constraint as shown in Figures 2.3 and 2.4. Just to give an example of additional model-specific bounds, a keV-scale sterile neutrino DM, which has a small interaction rate due to its mixing with the active neutrinos, could radiatively decay to an active neutrino and a photon which will lead to a mono-energetic X-ray line [467], the absence of which puts severe constraints on such keV-scale DM models, including their production mechanisms [468].

2.6.2 Non-thermal case

Now we move on to discuss the non-thermal DM region (labelled in green) in Figures 2.3 and 2.4. As already discussed at length in Section 2.4, the final relic density of these DM particles is determined by the initial conditions, which in our case, are set by the inflaton/moduli and DM masses, the reheating temperature and the branching ratio of the inflaton/moduli decay to DM. For fixed reheating temperature and inflaton/moduli branching ratio, we show in Figures 2.5 and 2.6 the contours for relic density computed using Eq. (2.28) in the (m_ϕ, m_χ) plane. We also calculate the comoving free-streaming length using Eq. (2.29), and identify the regions with $\tilde{\lambda}_{\rm fs} \lesssim 100$ kpc as cold DM (CDM), with $\tilde{\lambda}_{\rm fs} \gtrsim 1$ Mpc as hot DM (HDM), and the rest as warm DM (WDM) [1]. Note that there is no well-defined boundary between these regions, and we have just chosen some typical values derived from various astrophysical data [97, 469] for our illustration

[1] A comoving free-streaming length of 100 kpc corresponds to a non-thermal DM species that becomes non-relativistic at temperature of several keV. We recall here that density perturbations of galaxy size today re-enter the Hubble patch at temperature $\sim$1 keV.

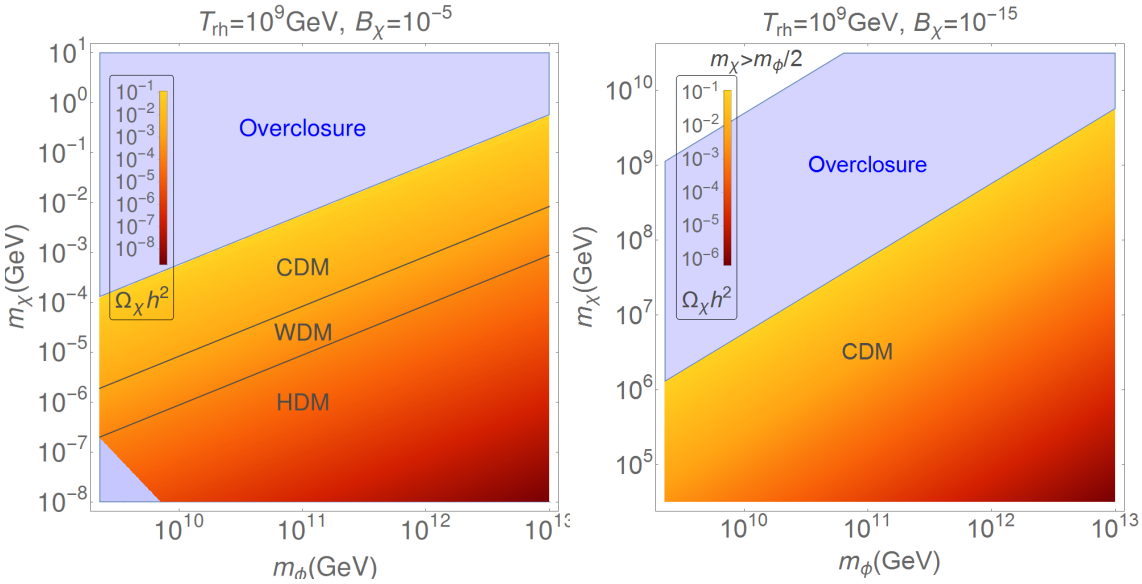

Figure 2.5: The colour-coded contours show the relic density of non-thermal DM produced from inflaton/moduli decay as a function of the inflaton/moduli and DM masses for a fixed reheated temperature $T_{\rm rh} = 10^9$ GeV and fixed inflaton/moduli branching ratios $B_\chi = 10^{-5}$ and 10^{-15}. We identify the cold, warm and hot DM regions in each case by assuming that the corresponding free-streaming length given by Eq. (2.29) should be < 0.1 Mpc, between 0.1–1 Mpc, and above 1 Mpc, respectively. The blue-shaded region for the CDM case is excluded by the overclosure constraint, as discussed in Section 2.5.1. The additional blue-shaded region in the HDM case is ruled out by the dark radiation limit, as discussed in Section 2.5.4.

purposes. We find that the observed DM relic density can be satisfied for a narrow parameter space in the CDM region (the boundary between the blue and orange regions), and the region above this is excluded due to overclosure constraints. For the HDM case with $T_{\rm rh} = 10^9$ GeV and $B_\chi = 10^{-5}$ (Figure 2.5, left panel), an additional portion of the parameter space (blue-shaded region at bottom-left corner) is ruled out due to the dark radiation constraint, as discussed in Section 2.5.4.

2.7 Conclusion

In this chapter, we have investigated the thermal and non-thermal properties of DM from inflaton/moduli decay in a model-independent manner, assuming

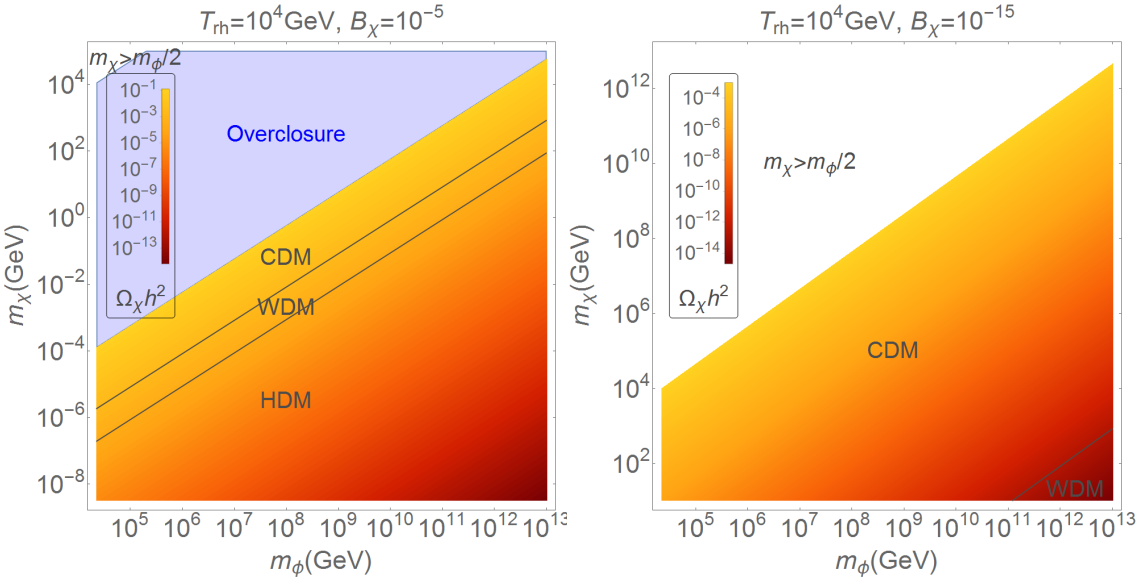

Figure 2.6: The labels are the same as in Figure 2.5. Here $T_{\rm rh} = 10^4$ GeV.

that the decay of inflaton/moduli and thermalisation of the resultant plasma have happened instantly at a given unique temperature. In the thermal DM scenario, the relic abundance of the DM species is determined by the freeze-out abundance, irrespective of the initial conditions or production mechanism, provided its interaction with the thermal bath is large enough to bring it into thermal equilibrium soon after its production. For smaller interaction rates when the DM does not attain thermal equilibrium, but can still be produced from the thermal bath; one can obtain the correct relic density through this freeze-in mechanism. On the other hand, if the interaction rate is negligibly small so that the DM is decoupled from the thermal bath from the beginning, the relic density is essentially determined by the initial conditions. Assuming that the DM has a non-zero coupling to the inflaton/moduli so that it can be directly produced from the inflaton/moduli decay, we have investigated all the above scenarios by tracking the evolution of the DM species from the very onset of its production. We have numerically solved the Boltzmann equation for DM number density, and have shown that the annihilation of the cosmic bath particles and inflaton decay into DM inevitably leads to an overclosure of the Universe for a large range of parameter space, especially for non-thermal DM scenarios. This

is an important constraint for hidden sector DM models with an arbitrary DM coupling to the inflaton. For the thermal DM scenario with large annihilation rates, we show the complementary constraints on the DM parameter space from various experimental searches. On the other hand, the other viable regions for both thermal and non-thermal DM candidates with very small interaction rate remain mostly unexplored.

Chapter 3

Ultra-violet freeze-in and inflationary observables

As shown in Chapter 2, the popular freeze-out DM scenario is subjected to a plethora of observational and theoretical constraints leaving only small viable regions of the parameter space. These allowed regions are already shrinking with the increasing sensitivity of DM detection experiments. Given the current rate of increase in the sensitivity of DM direct and indirect detection experiment, one would expect that either the DM will get discovered in the next few years or the freeze-out DM scenario will be ruled out. On the other hand, the region of the parameter space corresponding to the freeze-in scenario is subjected to almost no constraint and is beyond the reach of the current and near future DM experiments due to the very weak DM interactions with the visible sector in that region of the parameter space. This is also the case for many of the non-thermal DM candidates. Nevertheless, the CMB, which is measured with a great precision [2] and is expected to be measured with even greater precision in the near future, provides information from the early Universe. Motivated by this, we seek in this chapter to a establish a connection between the freeze-in scenario and inflationary observables which could provide us with a window of opportunity for unravelling the properties of DM beyond the standard freeze-out paradigm. We show that such a correlation indeed exists if the interaction of the DM with the visible sector

is mediated via a heavy particle which is a natural freeze-in scenario. Further, this connection surely exists for the non-thermal DM scenario.

3.1 Introduction

As discussed in Chapter 1, Primordial inflation can solve the initial condition problems of the SCM. In particular, it explains the formation of the large scale structures in our Universe and the observed features of the CMB spectrum [13]. Most likely both inflaton (the field deriving inflation) and DM require physics beyond the SM [1]. Although the masses and interactions of the inflaton and DM are still unknown, both must couple to the visible sector in some way, if not directly. It is also possible that the inflaton couples to DM. One can then imagine that the net DM abundance can be created via two processes:

(a) Decay: The inflaton, ϕ, could directly couple to the DM, χ, via re-normalisable interactions, as shown in Figure 3.1(a). For concreteness, we assume a fermionic DM, so that the interaction is of the Yukawa type, i.e. $y_{\phi\chi}\phi\bar{\chi}\chi$. We could also have a scalar DM with a trilinear coupling to the inflaton. Apart from the inflaton itself, any heavy hidden sector scalar field X could also directly decay to DM via re-normalisable interactions.

(b) Scattering: The inflaton must couple to the visible sector for the success of BBN. For instance, inflaton can couple to fermions via interactions of the form $y_{\phi b}\phi\bar{b}b$. Through such interactions, the cosmic thermal bath gradually gets established. Therefore, we can also create DM via inflaton mediation, as shown in Figure 3.1(b). One can generalise this scenario to envisage that any heavy mediator, such as a scalar particle X [2], could connect the thermal bath d.o.f. with the dark sector through the couplings $y_{Xb}X\bar{b}b$ and $y_{X\chi}X\bar{\chi}\chi$.

A rather natural outcome of this simple scenario is that the scale of inflation, determined by the inflaton potential $V(\phi)$, can be correlated with the DM properties in a rather intriguing way. If, for some reason, the DM does not thermalise

[1] The SM Higgs can play the role of inflaton if it couples non-minimally to gravity (see e.g. [470]).

[2] Considering for example a vector mediator instead does not change the results of our analysis.

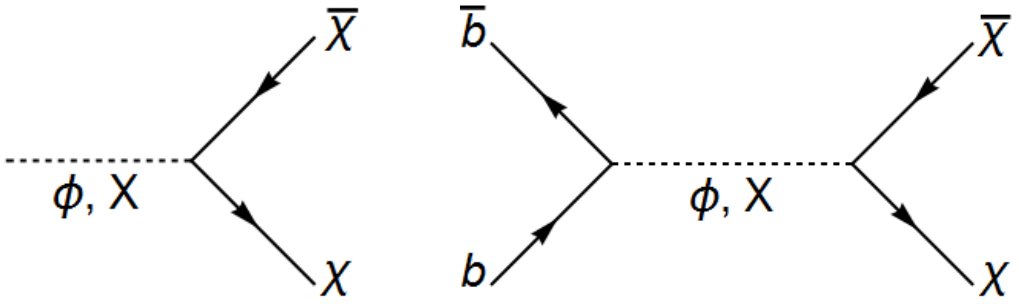

Figure 3.1: DM production from (a) non-thermal decay of inflaton/heavy scalar and (b) thermal scatterings of the cosmic bath d.o.f. mediated by inflaton/heavy scalar field.

with the primordial plasma during its evolution, it can, in principle, retain the memory of how it was excited at the first instance, either (a) directly via the inflaton decay or (b) indirectly via scatterings mediated by the inflaton or another heavy field. In case (a), the DM is essentially decoupled from the thermal bath since its creation. This leads to a non-thermal DM scenario, where the DM relic abundance is directly determined by the initial inflaton energy density (see Section 2.4). In case (b), if the effective coupling of the DM to the thermal bath is too small to thermalise the DM with the bath, but sufficient enough to produce the observed abundance of DM, it leads to the FIMP DM or freeze-in DM scenario in general (see section 2.3). In both cases, the final DM relic density is sensitive to the initial conditions set by inflation, unlike in the standard thermal freeze-out scenario (see section 2.2), thereby providing the possibility to directly link the DM properties with inflation, in particular to the tensor-to-scalar ratio, r.

The rest of this chapter is organised as follows: in Section 3.2, we discuss the equations governing the evolution of the inflaton, radiation, and DM density; we also evaluate the non-thermal and thermal DM production rates. We calculate the non-thermal and thermal contributions to DM abundance in Section 3.2. In Section 3.4, we discuss the class of inflationary models under consideration. We present our results in Section 3.5. We discuss the results and conclude this chapter in Section 3.6.

3.2 Inflaton decay and dark matter production

According to our set up, DM interacts with the visible sector through heavy mediators. Integrating out the heavy mediating states, the effective interaction between the bath particles and DM will be determined by a dimension-6, four-Fermion operator $\bar{\chi}\chi\bar{b}b/m_\phi^2$ or $\bar{\chi}\chi\bar{b}b/M_X^2$, which will be respectively suppressed by the mass square of inflaton or the heavy mediator field, with $\mathcal{O}(1)$ Yukawa couplings. This naturally leads to a FIMP or non-thermal DM scenario which we are interested in here (see sections 2.3 and 2.4). We will keep our discussion general, without referring to any particular DM model. Besides its couplings to fermions, the inflaton can interact with scalar d.o.f. such as the Higgs and the heavy mediator X via the couplings $y_{\phi\Phi}^2\phi^2|\Phi|^2$ and $y_{\phi X}^2\phi^2X^2$, respectively. For the sake of simplicity and illustration, we may assume the couplings $y_{\phi\Phi}, y_{\phi X} \approx 0$. Any reasonable value of $y_{\phi\Phi}(y_{\phi X}) \gtrsim m_\phi/\phi_{\rm end}$, where 'end' refers to the value at the end of inflation [$\phi_{\rm end} \equiv \phi(t_{\rm end})$], would in principle lead to a non-perturbative production of $X(\Phi)$ [360, 361], but in this case the inflaton does not decay completely. One would still require the inflaton to decay perturbatively, which will be guaranteed to happen in our case via $\phi\bar{b}b$ [364]. Further, in order to have a standard radiation-dominated era just after reheating, we require $y_{\phi\chi}, y_{\phi X} \ll y_{\phi b}$. We also require that $y_{\phi b} \ll 1$, in which case we can ignore issues like fermionic preheating [471, 472] [1] or fragmentation of the inflaton [473, 474]. This also ensures negligible radiative corrections to the inflationary potential [475].

The evolution of the inflaton field, ϕ, during the oscillation phase is governed by the following background equation of motion during the inflaton oscillations [see Eq. (1.26)] [2]:

$$\ddot{\phi} + (3H + \Gamma_\phi)\dot{\phi} + \partial_\phi V(\phi) = 0\,, \tag{3.1}$$

where we added a phenomenological decay term, $\Gamma_\phi\dot{\phi}$ [3] (see e.g. [56]), with Γ_ϕ

[1] The non-perturbative excitation of fermions can take place during the coherent oscillation of the inflaton field if $y_{\phi b} \gg m_\phi/\phi_{\rm end}$ [472].

[2] Here we assume that the inflaton self-coupling is sufficiently small such that the fluctuations in the inflaton field remains negligible.

[3] The perturbative decay of the coherently oscillating inflaton field can be treated as that of inflaton particles at rest [476].

being the total perturbative decay rate of the inflaton field which is obtained by summing all the partial decay rates. Multiplying Eq. (3.1) by $\dot{\phi}$ and averaging over the period of an oscillation, we obtain

$$\dot{\rho}_\phi + (3H + \Gamma_\phi)\langle\dot{\phi}^2\rangle \simeq 0\,, \tag{3.2}$$

where $\rho_\phi = \langle\frac{1}{2}\dot{\phi}^2 + V\rangle$ is the average inflaton energy density and $\dot{\rho}_\phi = \langle\dot{\phi}\ddot{\phi} + \dot{V}\rangle = \langle\dot{\phi}\ddot{\phi} + \dot{\phi}\partial_\phi V\rangle$. In many inflation models, the potential can be approximated by a quadratic one, $\frac{1}{2}m_\phi^2\phi^2$, around its minimum. This is quickly realised once the inflaton field starts oscillating. Here we take the minimum of the potential to be at $\phi = 0$. Using the virial theorem, we have $\frac{1}{2}\langle\dot{\phi}^2\rangle = \langle V\rangle$, and thus, Eq. (3.1) can be re-written as

$$\dot{\rho}_\phi + 3H\rho_\phi = -\Gamma_\phi\rho_\phi\,. \tag{3.3}$$

Further, once the inflaton field start oscillating around its minimum, its perturbative decay rate can be parametrised as $\Gamma_\phi \equiv \alpha_\phi m_\phi$ [1] where α_ϕ can be defined in terms of the reheating temperature, $T_{\rm rh}$, through the relation [56, 367]

$$H^2(\Gamma_\phi^{-1}) \simeq \frac{\Gamma_\phi^2}{4} = \frac{(\alpha_\phi m_\phi)^2}{4} \simeq \frac{1}{3M_{\rm P}^2}\frac{\pi^2}{30}gT_{\rm rh}^4\,, \tag{3.4}$$

which gives the following expression for α_ϕ:

$$\alpha_\phi = \left(\frac{2\pi^2}{45}\right)^{1/2} g^{1/2}\frac{T_{\rm rh}^2}{M_{\rm P}m_\phi}\,. \tag{3.5}$$

[1] For concreteness, we assume that inflatons decay dominantly to the SM fermions in which case the inflaton decay rate is given by

$$\Gamma_\phi \simeq \sum_b \Gamma(\phi\to\bar{b}b) \simeq \sum_b y_{\phi b}^2(m_\phi/8\pi)(1-4m_b^2/m_\phi^2)^{3/2} \simeq \sum_b (y_{\phi b}^2/8\pi)m_\phi \equiv \alpha_\phi m_\phi\,,$$

where $\alpha_\phi = \sum_b y_{\phi b}^2/(8\pi)$.

Eq. (3.3) can now be easily solved to obtain

$$\rho_\phi(t) = \rho_\phi(t_{\rm end}) \left(\frac{a(t_{\rm end})}{a(t)}\right)^3 e^{\Gamma_\phi (t_{\rm end}-t)} \,. \tag{3.6}$$

At $t \lesssim \Gamma_\phi^{-1}$, the inflaton dominates the energy density of the Universe (id) and hence $\rho^{\rm id}(t) \simeq \rho_\phi^{\rm id}(t) \simeq \rho_\phi(t_{\rm end})[a(t_{\rm end})/a(t)]^3$. On the other hand at $t \gtrsim \Gamma_\phi^{-1}$ the Universe is dominated by the energy density of the visible sector relativistic d.o.f. which for simplicity we assume to thermalise upon production establishing a thermal bath with a well-defined temperature [1]. In which case the thermal bath can be treated as one fluid whose evolution is governed by the following Boltzmann equation (see e.g.[56]):

$$\dot\rho_{\rm rad} + 4H\rho_{\rm rad} = (1-B_\chi)\Gamma_\phi \rho_\phi \simeq \Gamma_\phi \rho_\phi \,, \tag{3.7}$$

where $\rho_{\rm rad}$ denotes the energy density of relativistic d.o.f. and $B_\chi = \Gamma(\phi \to \chi\bar\chi)/\Gamma_\phi \ll 1$ (see Section 2.4). Changing the independent variable to the scale factor instead of cosmic time ($\mathrm{d}/\mathrm{d}t = \dot a\, \mathrm{d}/\mathrm{d}a$), Eq. (3.7) can be re-written as

$$\frac{\mathrm{d}[\rho_{\rm rad} a(t)^4]}{\mathrm{d}a(t)} \simeq \frac{\Gamma_\phi}{H}[\rho_\phi(t_{\rm end}) a(t_{\rm end})^3] \,, \tag{3.8}$$

where the Hubble parameter, $H \simeq \sqrt{(\rho_\phi + \rho_{\rm rad})/(3M_{\rm P}^2)}$, depends on the inflaton energy density during inflaton domination [$H^{\rm id} \simeq (\rho_\phi/3)^{1/2} M_{\rm P}^{-1} = \{\rho_\phi(t_{\rm end})/3\}^{1/2}$ $\{a(t_{\rm end})/a(t)\}^{3/2} M_{\rm P}^{-1}$], in which case Eq. (3.8) can be easily integrated to obtain

$$\rho_{\rm rad}^{\rm id} \simeq \frac{2\sqrt{3}}{5}\Gamma_\phi M_{\rm P} \rho_\phi(t_{\rm end})^{1/2} \left[\left(\frac{a(t_{\rm end})}{a(t)}\right)^{3/2} - \left(\frac{a(t_{\rm end})}{a(t)}\right)^4\right] . \tag{3.9}$$

This allows us to estimate the temperature of the ambient relativistic d.o.f. during

[1] In general, the thermalisation of the inflaton decay productions is an extended process (see e.g. [477]). Nevertheless, the thermalisation process can be efficient enough in a fairly wide range of the parameter space [478].

the inflaton domination epoch [367]:

$$T^{\rm id} = \left(\frac{30}{\pi^2 g}\rho_{\rm rad}^{\rm id}\right)^{1/4} \simeq \left(\frac{432}{\pi^4 g^2}\right)^{1/8} \Gamma_\phi^{1/4} M_{\rm P}^{1/4} \rho_\phi(t_{\rm end})^{1/8} \left[\left(\frac{a(t_{\rm end})}{a(t)}\right)^{3/2} - \left(\frac{a(t_{\rm end})}{a(t)}\right)^4\right]^{1/4}. \quad (3.10)$$

It is clear from Eq. (3.10) that during inflaton domination the temperature of the building up thermal bath increases to a maximum value [365],

$$T_{\rm max} \simeq \frac{1.64}{\sqrt{\pi}} g^{-1/4} \Gamma_\phi^{1/4} M_{\rm P}^{1/4} \rho_\phi(t_{\rm end})^{1/8}, \quad (3.11)$$

which occurs at $a(t_{\rm max})/a(t_{\rm end}) = (64/9)^{1/5} \simeq 1.48$ and then decreases as $a^{-3/8} \propto t^{-1/4}$ till the end of the inflaton domination era. On the other hand, during RD ($t \gtrsim \Gamma_\phi^{-1}$), $\rho_{\rm rad} = (\pi^2/30) g\, T^4 \propto a^{-4} \propto t^{-2}$ and consequently the temperature of the plasma decreases as $a^{-1} \propto t^{-1/2}$.

Given that the DM species, χ, couples weakly to both the inflaton and the thermal bath d.o.f. (indirectly through a scalar mediator), its production and evolution can be traced by the following Boltzmann equation [see Eqs. (A.8) and (A.19)]:

$$\dot{n}_\chi + 3Hn_\chi \simeq 2\,\Gamma(\phi \to \bar{\chi}\chi)\, n_\chi + \sum_{\bar{b}b \to \chi\bar{\chi}} \langle \sigma(\bar{b}b \to \chi\bar{\chi}) v_{\rm Mol} \rangle\, n_{b,eq}^2 = 2B_\chi \Gamma_\phi n_\chi + \gamma_\chi\,, \quad (3.12)$$

where n_χ is the average number density of the χ particles, $n_\phi \simeq \rho_\phi/m_\phi$ is the average number density of inflatons and $\Gamma(\phi \to \bar{\chi}\chi)$ is the inflaton decay rate into χ's which is given by

$$\Gamma(\phi \to \bar{\chi}\chi) \simeq y_{\phi\chi}^2 \frac{m_\phi}{8\pi} \left(1 - \frac{4m_\chi^2}{m_\phi^2}\right)^{3/2}. \quad (3.13)$$

This leads to the following branching fraction:

$$B_\chi \equiv \frac{\Gamma(\phi \to \bar{\chi}\chi)}{\Gamma_\phi} \sim \frac{y_{\phi\chi}^2}{8\pi\alpha_\phi} \sim \frac{y_{\phi\chi}^2}{\sum_b y_{\phi b}^2 c_b} \ll 1\,. \quad (3.14)$$

Note that the finite temperature effects on the inflaton decay rate are negligible as long as the maximum attainable temperature, $T_{\rm max} \ll m_\phi$ [367, 479]. In Eq. (3.12) γ_χ denotes the thermal production rate of DM from the annihilation of the bath particles and is given by [see Eq. (A.21)]

$$\gamma_\chi = \sum_{b\bar{b}\to\chi\bar{\chi}} \frac{g_b^2 T}{32\pi^4} \int_{s_{\rm min}}^{\infty} {\rm d}s\, s^{1/2}(s-4m_b^2) K_1(s^{1/2}/T)\, \sigma(b\bar{b}\to\chi\bar{\chi})\,, \tag{3.15}$$

where $g_b = 2$ is the spin d.o.f. of a given fermionic bath species, m_b is its mass (we take into account the plasma induced thermal masses for the bath particles [480]) and $s_{\rm min} = \max(4m_\chi^2, 4m_b^2)$. With the following change of variables: $t \equiv (s - s_{\rm min})^{1/2}/(2T)$, Eq. (3.15) can be re-written as

$$\gamma_\chi = \sum_{b\bar{b}\to\chi\bar{\chi}} \frac{2 g_b^2 T^6}{\pi^4} \int_0^{\infty} {\rm d}t\, t(t^2+t_{\rm m}^2)^{1/2}(t^2+t_{\rm m}^2-z_b^2) K_1\Big(2\sqrt{t^2+t_{\rm m}^2}\Big)\, \sigma(b\bar{b}\to\chi\bar{\chi})\,, \tag{3.16}$$

where $z_b \equiv m_b/T$ and $t_{\rm m} \equiv \sqrt{s_{\rm min}}/(2T)$. The cross-section of the scattering of two bath particles into DM via a scalar mediator, X, is given by [1]

$$\begin{aligned}
\sigma(b\bar{b}\to\chi\bar{\chi}) &= \frac{y_{X\chi}^2 y_{Xb}^2}{16\pi} c_b \sqrt{\frac{s-4m_\chi^2}{s-4m_b^2}} \frac{(s-4m_b^2)(s-4m_\chi^2)}{s[(s-M_X^2)^2+\Gamma_X^2 M_X^2]} \\
&= \frac{y_{X\chi}^2 y_{Xb}^2 c_b (t^2+t_{\rm m}^2-z_b^2)^{1/2}(t^2+t_{\rm m}^2-x^2)^{3/2}}{4\pi(t^2+t_{\rm m}^2)[\{1-(2T/M_X)^2(t^2+t_{\rm m}^2)\}^2+(\Gamma_X/M_X)^2]} \Big(\frac{T^2}{M_X^4}\Big),
\end{aligned} \tag{3.17}$$

with c_b being the colour factors. For simplicity, we focus on the case of a heavy mediator, i.e. $M_X \gg T_{\rm max}$ in which case $\sigma(b\bar{b}\to\chi\bar{\chi}) \propto T^2/M_X^4$. Consequently, the thermal production rate of χ particles, given by Eq. (3.16), can be expressed as

$$\gamma_\chi = \mathcal{I}(T)\, \frac{T^8}{M_X^4}\,. \tag{3.18}$$

For $m_\chi, m_b \ll T \ll M_X$, an analytical expression for $\mathcal{I}(T)$ can be obtained by

[1] Here, we have assumed that $\Gamma_X \ll M_X$.

integrating Eq. (3.16) which gives

$$\mathcal{I}(T) = \frac{3y_{X\chi}^2 \sum_b y_{Xb}^2 g_b^2 c_b}{2\pi^5[1+(\Gamma_X/M_X)^2]}\,, \tag{3.19}$$

which clearly is independent of temperature [see also Figure 3.2(a)].

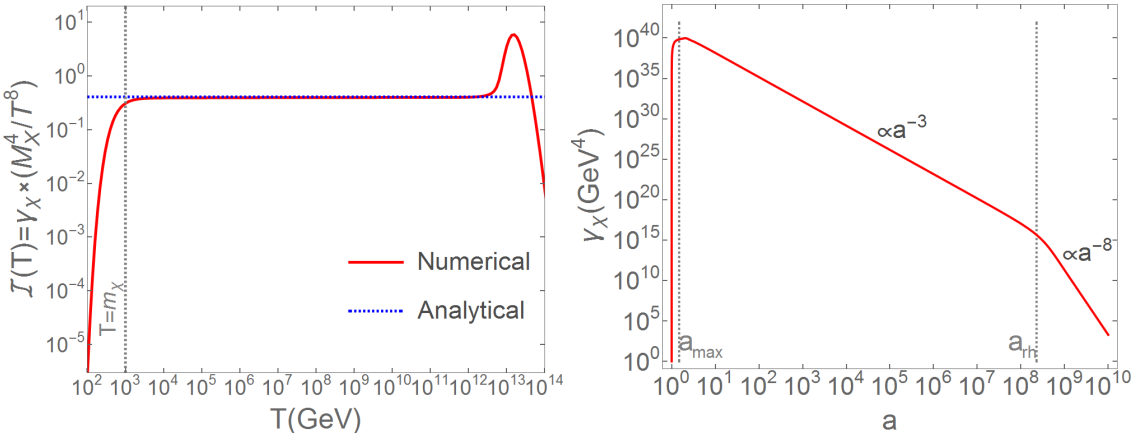

(a) (b)

Figure 3.2: (a) A plot of $\mathcal{I}(T) = \gamma_\chi/(T^8/M_X^4)$ [see Eq. (3.18)] as a function of temperature. Here the solid red curve shows the numerical calculation while the dashed blue curve shows the analytical approximation [see Eq. (3.19)] which clearly works very well for $m_\chi \ll T \ll M_X$. However for $T \lesssim m_\chi/3$, $\mathcal{I}(T)$ decreases as the temperature decreases due to the smaller phase space, for $T \sim \sqrt{s}/6 \sim M_X/6$, $\mathcal{I}(T)$ is larger due to the resonant annihilation, and for $T \sim \sqrt{s}/6 \gg M_X/6$, $\mathcal{I}(T)$ deceases rapidly as the temperature increases because the cross-section decreases as $\propto s^{-1} \propto T^{-2}$. (b) The evolution of the DM thermal interaction rate as a function of the scale factor, a, (normalised to $a_{\rm end}$) during inflaton domination, $a \lesssim a_{\rm rh}$, ($\gamma_\chi \propto a^{-3}$) and during radiation domination, $a \gtrsim a_{\rm rh}$, ($\gamma_\chi \propto a^{-8}$). Here for the sake of illustration we set $M_X = 10^{14}$ GeV, $m_\chi = 1$ TeV and $T_{\rm rh} = 10^9$ GeV.

3.3 Thermal and non-thermal dark matter abundance

The total present DM relic abundance is roughly given by the sum of thermal (th) and non-thermal (nth) components [235]:

$$\Omega_{\chi,0}h^2 \simeq \Omega^{\rm nth}_{\chi,0}h^2 + \Omega^{\rm th}_{\chi,0}h^2 \simeq 2.74\times 10^8\,(n^{\rm nth}_{\chi,0}+n^{\rm th}_{\chi,0})\frac{m_\chi}{s_0}\,, \tag{3.20}$$

where $n^{\rm nth}_\chi$ and $n^{\rm th}_\chi$ respectively denote the non-thermal and thermal contributions to the population of the DM species χ, and s is the entropy density [see Eq. (2.8)]. With the assumptions mentioned in Section 3.2, namely, (i) $y_{\phi\chi} \ll y_{\phi b} \ll m_\phi/\phi_{\rm end}$ which insures that the decay of ϕ is purely a perturbative process and (ii) $m_\chi \ll m_\phi$, we proceed to derive analytical expressions for the DM abundance produced either thermally or non-thermally.

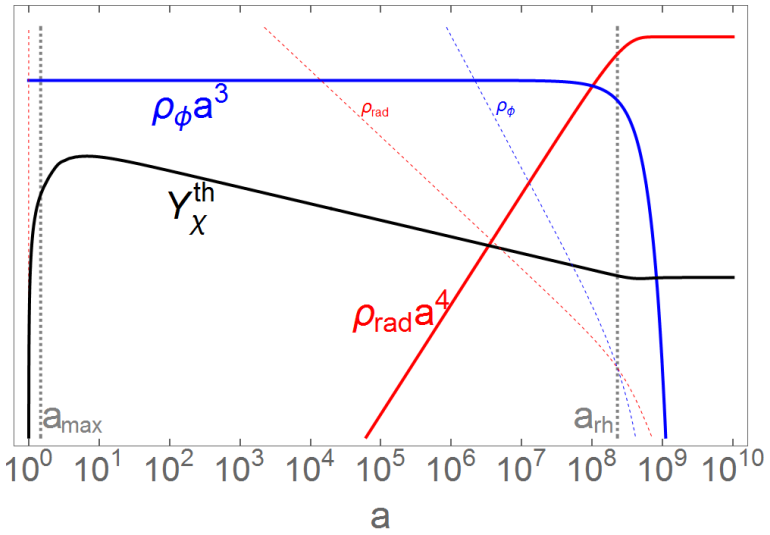

Figure 3.3: Evolution of the DM yield, $Y_\chi = n_\chi/s$, (shown by the thick black curve), the energy densities of the inflaton ($\rho_\phi a^3$ shown by thick solid blue curve and ρ_ϕ shown by the dashed thin blue curve) and radiation energy density ($\rho_{\rm rad}a^4$ shown by thick solid curve and $\rho_{\rm rad}$ shown by the dashed thin red curve) as a function of the scale factor, a, normalised to its initial value, $a_{\rm end}$, where the different quantities are scaled to fit in the same plot. Here we set $m_\chi = 1$ TeV, $M_X = 10^{14}$ GeV and $T_{\rm rh} = 10^9$ GeV.

3.3.1 Non-thermal contribution

Let us first compute the abundance of the χ particles produced non-thermally [see Figure 3.1(a)] which is sourced by the first term on the right hand side of Eq. (3.12) where the inflaton branching ratio to χ's is given by Eq. (3.14). Eq. (3.12) can be easily integrated for the non-thermal contribution to obtain [1]

$$n_{\chi}^{\rm nth}(t) = 2B_{\chi}\Gamma_{\phi}\frac{\rho_{\phi}(t_{\rm end})}{m_{\phi}}\left(\frac{a(t_{\rm end})}{a(t)}\right)^{3}\left[1-e^{\Gamma_{\phi}(t_{\rm end}-t)}\right]. \tag{3.21}$$

Evaluating the resultant expression for $n_{\chi}^{\rm nth}$ at $T_{\rm rh}$ [2], and accounting for the inflaton population decaying at $T<T_{\rm rh}$ and the accompanying entropy release [365] [3], we reproduce the non-thermal contribution to the current DM relic density (see Section 2.4)

$$\begin{aligned}\frac{\Omega_{\chi,0}^{\rm nth}h^{2}}{0.12} &\simeq 3.93\times10^{5}B_{\chi}\left(\frac{g}{100}\right)^{-1/4}\left(\frac{\alpha_{\phi}}{10^{-13}}\right)^{1/2}\left(\frac{m_{\chi}}{1\,{\rm GeV}}\right)\left(\frac{m_{\phi}}{10^{13}\,{\rm GeV}}\right)^{-3/4}\left(\frac{\rho_{\phi}(t_{\rm end})}{(10^{16}\,{\rm GeV})^{4}}\right)^{1/8}\\ &\simeq 4.44\times10^{5}B_{\chi}\left(\frac{m_{\chi}}{1\,{\rm GeV}}\right)\left(\frac{m_{\phi}}{10^{13}\,{\rm GeV}}\right)^{-1}\left(\frac{T_{\rm rh}}{10^{9}\,{\rm GeV}}\right).\end{aligned} \tag{3.22}$$

Here we have used Eq. (3.5) for α_{ϕ} and Eq (3.10) to change the dependence from $a_{\rm rh}$ to $T_{\rm rh}$ in the second line. Clearly, $\Omega_{\chi,0}^{\rm nth}h^{2}$ depends on the inflaton energy at the end of inflation, $\rho_{\phi}(t_{\rm end})$. It is also sensitive to the steepness of the inflationary potential around the minimum characterised by m_{ϕ}.

3.3.2 Thermal contribution

As for the thermal contribution, one can easily show that the relevant contribution comes from the X-mediated DM production in Figure 3.1(b). In particular,

[1] For simplicity, we integrate the non-thermal and thermal contributions separately. In principle, there should be cross terms [see e.g. (2.27)]. However, these terms are relatively small and can be neglected.

[2] At $t_{\rm rh}\sim\Gamma_{\phi}^{-1}$ over 60% of the inflaton population has already decayed and the density of the remaining inflatons drops faster as a function of the scale factor at $t\gtrsim t_{\rm rh}$, i.e. during RD (see Figure 3.3).

[3] Note that the conservation of the comoving entropy density ensures that $\frac{n_{\chi}}{s}\big|_{T\ll T_{\rm rh}} = \frac{n_{\chi}}{s}\big|_{T=T0}$.

$\bar{b}b \to \phi \to \bar{\chi}\chi$ would yield a sub-dominant DM contribution compared to $\bar{b}b \to X \to \bar{\chi}\chi$. This is due to the fact that both thermal and non-thermal contribution to DM abundance in the inflaton-mediation case are proportional to $y_{\phi\chi}$ [see Eqs. (3.19), (3.14) and (3.12)], which has to be small in order not to non-thermally overproduce DM (see Section 2.4). The thermal contribution due to inflaton mediation dominates only when $T_{\rm max} \gg m_\phi$, in which case the thermal corrections to the inflaton decay rate also become important [479]. On the other hand, such complications do not arise in case of the X-mediation as long as $M_X \gg T_{\rm max}$ [1].

To compute the contribution of the thermally produced χ particles to the DM abundance we re-write Eq. (3.12) in terms of the scale factor while ignoring the non-thermal contribution,

$$\frac{\mathrm{d}}{\mathrm{d}a(t)}[n_\chi^{\rm th} a(t)^3] \simeq \frac{a(t)^2}{H}\,\gamma_\chi\,, \tag{3.23}$$

where $\gamma_\chi \propto T(a)^8/M_X^4$ for $m_\chi \ll T \ll M_X$[see Eq. (3.18)]. During inflaton domination, $H^{\rm id} \simeq \{\rho_\phi(t_{\rm end})/3\}^{1/2}\{a(t_{\rm end})/a(t)\}^{3/2} M_{\rm P}^{-1}$ and the temperature of the ambient plasma is given by Eq. (3.10), in which case Eq. (3.23) can be integrated to obtain

$$\begin{aligned} n_\chi^{\rm th,id} \simeq & \frac{432\sqrt{3}}{7\pi^9}\,\frac{(\sum_b y_{Xb}^2 g_b^2 c_b)\, y_{X\chi}^2 \Gamma_\phi^2 M_{\rm P}^3\, \rho_{\phi,\rm end}^{1/2}}{g^2 M_X^4 (1+\Gamma_X^2/M_X^2)} \\ & \times \left[7\left(\frac{a_{\rm end}}{a}\right)^{3/2} - 25\left(\frac{a_{\rm end}}{a}\right)^3 + 21\left(\frac{a_{\rm end}}{a}\right)^4 - 3\left(\frac{a_{\rm end}}{a}\right)^{13/2}\right], \end{aligned} \tag{3.24}$$

provided that $m_\chi \lesssim T_{\rm rh}$. Further during RD ($t \gtrsim t_{\rm rh}$), $\gamma_\chi \propto T^8 \propto a^{-8}$ [see Figure 3.2(b)], and hence Eq. (3.23) will in turn go as $\mathrm{d}[n_\chi^{\rm th} a(t)^3]/\mathrm{d}a(t) \propto a(t)^{-4}$. This means that except for a dilution factor due to the entropy released directly after the transition to the radiation domination phase, the DM thermal yield becomes constant directly after the end of reheating $Y_\chi^{\rm th}(T \ll T_{\rm rh}) \simeq \zeta\, Y_\chi^{\rm th}(T = T_{\rm rh})$, where ζ is the dilution factor.

[1] Typically the mediator, X, is heavier than the inflaton and hence it is sitting at the minimum of its potential during and after inflation. Thus large couplings of a heavy mediator to a SM fermion or DM do not lead to non-perturbative excitations of either the SM fermion or DM.

From Eqs. (2.8), (3.10) and (3.24) [see also Figure 3.3], one can see that the thermal yield of the DM species χ, increases initially very fast to reach a maximum at $a(t)/a(t_{\rm end}) \simeq 6.73$ and then decreases as $a(t)^{-3/2}$ till the end of reheating beyond which $Y_\chi^{\rm th}$ becomes constant up to a small correction factor due to the entropy release at $T \lesssim T_{\rm rh}$. Thus, evaluating $Y_\chi^{\rm th}$ at $T = T_{\rm rh}$ and accounting for the entropy dilution factor, we obtain

$$\begin{aligned}\frac{\Omega_{\chi,0}^{\rm th}h^2}{0.12} &\simeq 7.39\times10^{-3}\, y_{X\chi}^2 \sum_b y_{Xb}^2 g_b^2 c_b \left(\frac{g}{100}\right)^{-9/4}\left(\frac{\alpha_\phi}{10^{-13}}\right)^{3/2}\left(\frac{m_\chi}{1\,\text{GeV}}\right)\left(\frac{M_X}{10^{13}\,\text{GeV}}\right)^{-4} \\ &\quad\times \left(\frac{m_\phi}{10^{13}\,\text{GeV}}\right)^{3/4}\left(\frac{\rho_\phi(t_{\rm end})}{(10^{16}\,\text{GeV})^4}\right)^{3/8} \\ &\simeq 1.26\times10^{-2}\, y_{X\chi}^2 \sum_b y_{Xb}^2 g_b^2 c_b \left(\frac{g}{100}\right)^{-3/2}\left(\frac{m_\chi}{1\ \text{GeV}}\right)\left(\frac{M_X}{10^{13}\ \text{GeV}}\right)^{-4}\left(\frac{T_{\rm rh}}{10^{9}\ \text{GeV}}\right)^{3}.\end{aligned} \tag{3.25}$$

Here again we have used Eq. (3.5) for α_ϕ and Eq (3.10) to change the dependence from $a_{\rm rh}$ to $T_{\rm rh}$ in the second line. It is clear that $\Omega_{\chi,0}^{\rm th}h^2$ is also sensitive to the inflaton energy at the end of inflation and the inflaton mass around the minimum of the potential.

3.4 Inflationary set up

To illustrate the connection between the non-thermal and thermal (frozen in via heavy mediator) DM and the inflationary observables (in particular the tensor to scalar ratio), we consider a simple class of inflationary models with an α-attractor potential [481, 482] [1]:

$$V(\phi) = \frac{3}{4}M_{\rm P}^2M^2\left[1 - e^{-\sqrt{\frac{2}{3\alpha}}\frac{\phi}{M_{\rm P}}}\right]^2 \equiv \frac{3}{4}M_{\rm P}^2M^2\left[1 - x(\phi)\right]^2, \tag{3.26}$$

where α is a free parameter and M is some mass scale governing inflation. For $\alpha = 1$, this is just the Starobinsky model [483], whereas in the limit $\alpha \to \infty$,

[1] Our results could be easily extended to other inflationary potentials.

Eq. (3.26) reduces to the simple quadratic chaotic inflation potential [42] with constant mass, $M/\sqrt{\alpha} \simeq \sqrt{6\pi^2 A_s}\, M_{\rm P}/N$, where N denotes the number of e-folds. In this class of models, inflation occurs above the scale of $M_{\rm P}$ and terminates at $\phi_{\rm end} \simeq \sqrt{3\alpha/2}\, \ln(1+2/\sqrt{3\alpha}) M_{\rm P}$ which approaches $\sqrt{2} M_{\rm P}$ in the limit $\alpha \to \infty$. The potential at the end of inflation is then given by

$$V_{\rm end} \equiv V(\phi_{\rm end}) \simeq \frac{9 M^2 M_{\rm P}^2}{(2\sqrt{3}+3\sqrt{\alpha})^2}\,. \tag{3.27}$$

Moreover, the mass scale M can be expressed in terms of the amplitude of scalar perturbations, A_s [482, 484]

$$\frac{M}{M_{\rm P}} = \sqrt{\frac{128\pi^2 A_s}{3\alpha}}\frac{x_{\rm obs}}{(1-x_{\rm obs})^2}\,, \tag{3.28}$$

where $x_{\rm obs} \equiv x(\phi_{\rm obs})$ which can be evaluated once N is known [482, 484]:

$$\begin{aligned} N &= \int_{\phi_{\rm end}}^{\phi_{\rm obs}} \frac{V {\rm d}\phi}{M_{\rm P}^2 \partial_\phi V} + \frac{1}{\sqrt{6\alpha}} \frac{\phi_{\rm obs} - \phi_{\rm end}}{M_{\rm P}} \\ &= \frac{3}{4}\alpha \left(\frac{1}{x_{\rm obs}} - \frac{1}{x_{\rm end}} \right) + \left(\frac{3}{4}\alpha - \frac{1}{2} \right) \ln \left(\frac{x_{\rm obs}}{x_{\rm end}} \right), \end{aligned} \tag{3.29}$$

where $x_{\rm end} \equiv x(\phi_{\rm end}) = (1+2/\sqrt{3\alpha})^{-1}$. Here the number of e-folds can be estimated by [41]

$$N \simeq 56 - \frac{2}{3}\ln\left(\frac{10^{16}{\rm GeV}}{\rho_\phi(t_{\rm end})^{1/4}}\right) - \frac{1}{3}\ln\left(\frac{10^9{\rm GeV}}{T_{\rm rh}}\right), \tag{3.30}$$

provided that the reheating phase is matter-dominated. Eq. (3.30) gets modified if the cosmic fluid does not effectively behave as a non-relativistic one. Using Eq. (3.29), the tensor-to-scalar ratio for the potential in Eq. (3.26) is given by

$$r(\alpha) = \frac{64 x_{\rm obs}^2(\alpha)}{3\alpha[1-x_{\rm obs}(\alpha)]^2}\,. \tag{3.31}$$

For $\alpha = \mathcal{O}(1)$, $M \simeq \sqrt{24\pi^2\alpha A_s}\, M_{\rm P}/N$ and $r \simeq 12\alpha/N^2$, whereas for $\alpha \gg 1$, $M \simeq \sqrt{6\pi^2\alpha A_s}\, M_{\rm P}/N$ and $r \simeq 8/N$. In Figure 3.4, we show a plot of the potential,

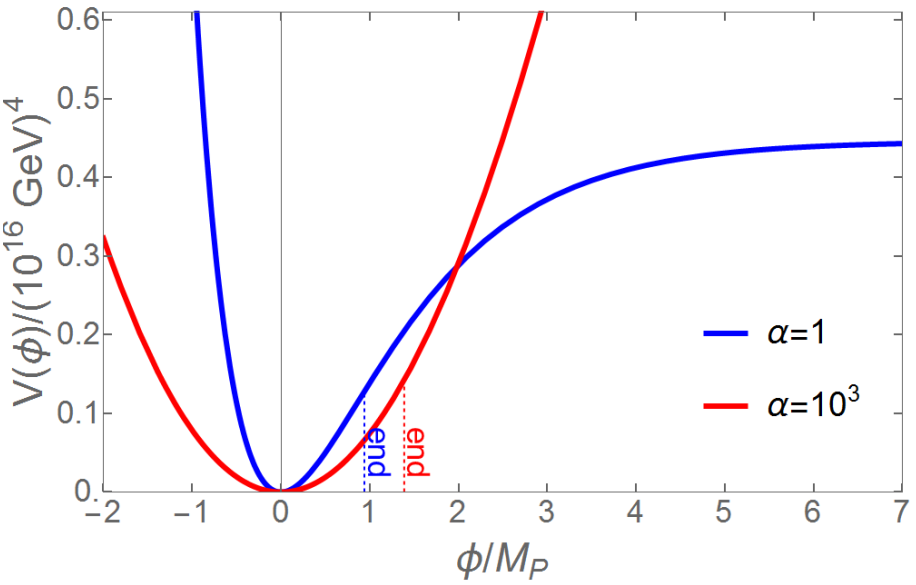

Figure 3.4: Shape of the potential given by Eq. (3.26) for $\alpha = 1$ and 10^3. Here 'end' refers to the end of inflation.

Eq. (3.26), for $\alpha = 1$ which leads to $r \simeq \mathcal{O}(0.004)$, and $\alpha = 10^3$ which leads to $r \simeq \mathcal{O}(0.1)$. We also show the value of ϕ at which inflation terminates in each case. In Figure 3.5(a), we show the inflaton potential energy at the end of inflation as a function of $r(\alpha)$ for 50 and 60 e-folds, since the precise value of N depends on the details of reheating process [41]; see Eq. (3.29). Once inflation ends, the field ϕ starts oscillating around the minimum of the potential with an effective mass

$$m_{\phi,\text{eff}} \simeq [\partial_\phi^2 V(\phi)]^{1/2} \simeq \frac{M}{\sqrt{\alpha}} \left[2e^{-2z} - e^{-z}\right]^{1/2}, \tag{3.32}$$

where $z = \sqrt{2/3\alpha}\,\phi/M_{\rm P}$. The evolution of the zero-mode of ϕ during the oscillation phase follows the equation of motion given by Eq. (3.1). For the potential given by Eq. (3.26), the amplitude of ϕ oscillations quickly drops with the expansion of the Universe right after the end of inflation; it becomes roughly 0.1–0.2 of its initial value after only one oscillation. Thus, after a few oscillations, ϕ becomes confined to a small region around the minimum of the potential for which the potential can be approximated by a quadratic one with a constant mass,

$m_\phi \equiv m_{\phi,\rm eff}(\phi \ll M_{\rm P}) \simeq M/\sqrt{\alpha}$. In Figure 3.5(b), we show m_ϕ as a function of $r(\alpha)$ for $N=50$ and 60.

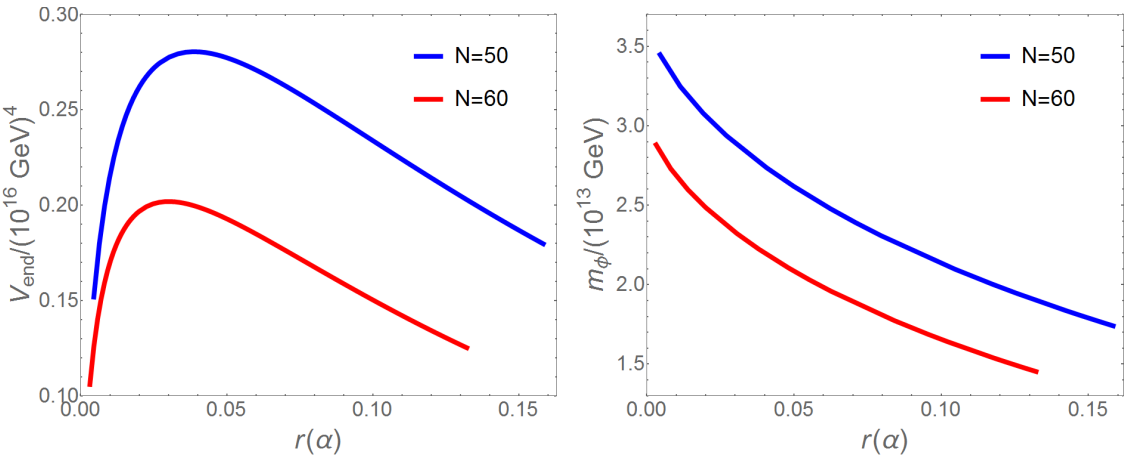

(a) (b)

Figure 3.5: (a) The inflaton energy density at the end of inflation and (b) the effective inflaton mass for $\phi \ll M_{\rm P}$ as a function of $r(\alpha)$ for $N=50\,(60)$ shown by the blue (red) curve.

3.5 Results

In Section 3.3, we have obtained approximate analytical expressions for the DM non-thermal and thermal abundances, and argued that in both cases, the details of the inflationary potential are carried over to DM abundance via both m_ϕ and $\rho_\phi(t_{\rm end}) \simeq V_{\rm end}$ (see Figure 3.5 for the class of potentials under consideration), thereby establishing a connection between $\Omega_{\chi,0}^{\rm th(nth)}h^2$ and $r(\alpha)$. In order to precisely capture this connection between $\Omega_{\chi,0}h^2$ and r, we integrate Eqs. (3.3), (3.7) and (3.12) numerically for different $r(\alpha)$ values. The resulting DM thermal and non-thermal abundances are shown in Figs. 3.6 (a) and (b), respectively, for a typical choice of parameters: $m_\chi = 0.3$ GeV and $\alpha_\phi \simeq 1.1\times10^{-13}$. We find that for the thermal case, $\Omega_{\chi,0}^{\rm th} \propto r^{-3/8}$, while for the non-thermal case, $\Omega_{\chi,0}^{\rm nth} \propto r^{4/5}$. This is an interesting connection, especially the former one, since it relates thermal production of DM at the time of reheating and thermalisation of the Universe

with the value of r which provides a promising probe for the FIMP-like scenario in near future. In other words, if the tensor-to-scalar ratio is measured in future, one can test the properties of FIMP DM through this connection in the context of a given inflationary model.

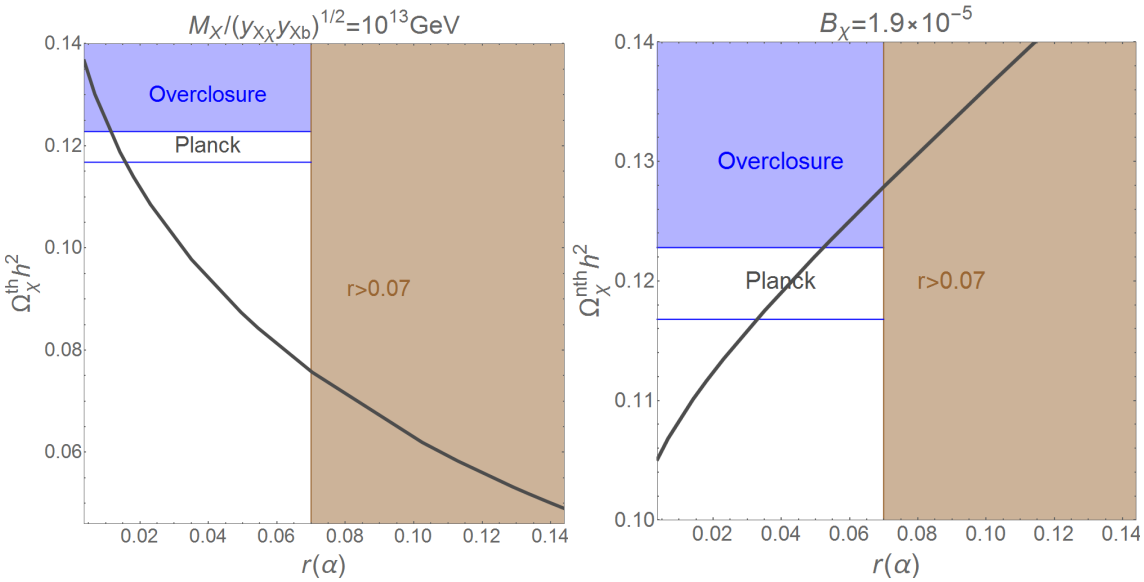

(a) (b)

Figure 3.6: Dark matter (a) thermal and (b) non-thermal abundance as a function of the tensor-to-scalar ratio. Here we fix $m_\chi = 0.3$ GeV and $\alpha_\phi \simeq 1.1\times10^{-13}$. The brown regions are ruled out by the CMB bound on tensor-to-scalar ratio [55] and in the blue regions DM are overproduced. The regions labelled by Planck correspond to the Planck (2σ) favoured DM abundance [13].

To examine the dependence on the mediator mass, we scan the (m_χ, M_X) parameter space for the correct DM abundance while fixing the mediator couplings to DM and the thermal bath d.o.f. In Figure 3.7, we show the DM thermal abundance heat map as a function of m_χ and M_X for $r \simeq 0.004$. We have fixed $\alpha_\phi \simeq 1.1\times10^{-13}$, so that $T_{\rm rh} \sim \mathcal{O}(10^9)$ GeV. For larger r, the allowed range of (m_χ, M_X) shifts to larger values of m_χ and smaller M_X values. Similarly, for smaller α_ϕ, i.e. smaller reheating temperature, the allowed region of the parameter space shifts to larger DM masses and smaller mediator masses, and vice versa. For very small values of the branching fraction $B_\chi \ll 1$, the thermal contribution given by Eq. (3.25) can be dominant over the non-thermal contribution given by

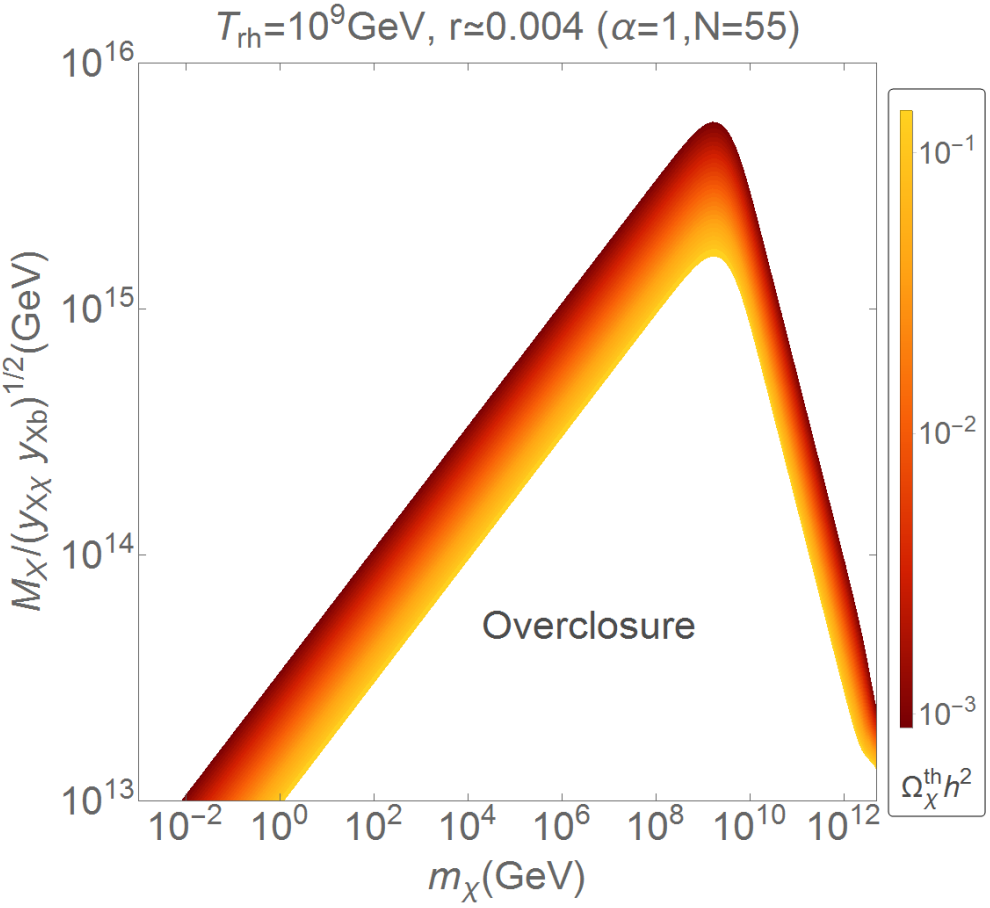

Figure 3.7: Map of the DM thermal abundance as a function of m_χ and M_X for $r \simeq 0.004$ and $T_{\rm rh} \simeq 10^9$ GeV.

Eq. (3.22), and can account for the observed DM abundance for m_χ as low as roughly 300 MeV/$(y_{X_\chi} y_{X_b})^2$. The unshaded region labelled by overclosure (below the coloured region) gives $\Omega_{\chi,0}h^2 > 0.1228$, which is ruled out at 2σ by the latest Planck data [13]. The rest of the unshaded region (above the coloured region) is still allowed, though for practical purposes, the corresponding DM thermal abundance becomes negligible, and one has to allow for a non-thermal contribution to the DM abundance or to invoke a multi-component DM to explain the observed abundance, see e.g. [382, 383]. Note that for $m_\chi \gtrsim T_{\rm rh}$, the thermal production rate is suppressed due to a smaller phase space. This can be seen from the right hand parts of the allowed (m_χ, M_X) parameter space in Figure 3.7.

3.6 Discussion and conclusion

So far the CMB experiments have seen no evidence for the existence of primordial tensor perturbations. The current CMB upper limit on the tensor-to-scalar ratio is $r < 0.07$ at 95% CL from the joint analysis of Keck Array and BICEP-2 Collaborations [55]. Nevertheless, if the tensor-to-scalar ratio is measured in future, it will provide an important indirect handle on the dark sector physics. In this chapter, we have shown that a connection between the tensor-to-scalar ratio and the DM abundance, indeed, exists for both non-thermally and thermally produced DM. This connection is clear in the non-thermal case [Figure 3.1(a)] as the DM relic abundance is directly determined from the inflaton energy density, which in turn depends on $r(\alpha)$ [see Eq. (3.27) and (3.31); see also Figure 3.5(a)], besides the sensitivity of the inflaton decay rate to the shape of the inflationary potential around the minimum which also depends on $r(\alpha)$ [see Eq. (3.13), (3.31) and (3.32); see also Figure 3.5(b)]. Thus, the connection between the DM properties and the primordial fluctuations is straightforward. We also showed that such an interesting connection also exists in case (b) [see Figure 3.1(b)] if the mediator mass is between $T_{\rm max}$ and $M_{\rm P}$. This can be understood from Eqs. (3.10), (3.12) and (3.18), where the term sourcing the DM thermal abundance is proportional to $T^8 \sim \rho_{\rm rad}^2$ and since the thermal bath itself arises from the decay of inflaton [see Eq. (2.3)], a connection between $\Omega^{\rm th}_{\chi,0}h^2$ and $r(\alpha)$ can be established.

Before we conclude, let us briefly mention that we could have also imagined a similar mechanism for producing baryon/lepton (B/L) asymmetry, either from the direct decay of the inflaton, if the inflaton were carrying any B/L number [485], or from the intermediate condensate X carrying B/L number [359], as e.g. in GUT-baryogenesis [56]. As a concrete example, in non-supersymmetric models, we can realise high-scale thermal leptogenesis via the production and decay of right-handed heavy Majorana neutrinos [486]. In either case, we would be able to relate the scale of inflation, and therefore the tensor-to-scalar ratio, with the magnitude of the L-asymmetry. In the latter case, one would require a weak washout regime in order to retain the sensitivity towards the initial conditions.

To conclude, if the future observations could pin down the exact value of the tensor-to-scalar ratio, it would serve as an interesting way to constrain the

hidden sector, including the properties of the DM feebly interacting with the thermal bath and the DM produced in inflaton decay, which are otherwise very hard to probe. Although for the sake of illustration we have used a particular class of inflationary potential to derive our results, the idea of connecting the DM abundance to the primordial tensor perturbations should hold true for a generic model of inflation.

Chapter 4

Axionic dark radiation and constraints

In this chapter, we turn our attention to a well-motivated WISP DM candidate, the axion, which arise as a by-product in an elegant solution to the strong CP problem, the PQ mechanism. We briefly review the origin of axions and the different theoretical and observational constraints. Moreover, we discuss the dynamics of PQ symmetry breaking and the possibility of thermal and non-thermal production of ultra-relativistic axions which can significantly increase the effective number of relativistic d.o.f., $N_{\rm eff}$. This allows us to place constraints on the axion parameter space, especially on the axion dark matter window with large decay constant which is expected to be probed by future experiments. In addition, an upper bound on the reheating temperature can be placed, which further constrains the thermal history of our Universe.

4.1 Introduction

The strong CP problem is one of the outstanding puzzle of particle physics today. It is a well-known fact that QCD allows a CP-violating term of the form

$(g_s^2\bar{\Theta}/32\pi^2)\, G^{a\mu\nu}\widetilde{G}^a_{\mu\nu}$ [1] where $G^a_{\mu\nu}$ denotes the gluon field strength tensor, $\widetilde{G}^{a\mu\nu} \equiv \frac{1}{2}\epsilon^{\mu\nu\rho\sigma}G^a_{\rho\sigma}$ is its dual with $\epsilon_{\mu\nu\alpha\beta}$ being the totally-antisymmetric tensor (in four-dimensional Minkowski space, $\epsilon_{0123} = -\epsilon^{0123} = 1$), and $\bar{\Theta} = \Theta + \arg\det M_{\text{quarks}}$ is a constant physical parameter arising from the non-trivial nature of the QCD vacuum and the instanton effects [251, 252], and the quark mixing matrix [487, 488]. The $\bar{\Theta}$-term gives rise to an electric dipole moment (EDM) for the neutron (see e.g. [489, 490, 491, 492]):

$$d_n \simeq (1.08\text{-}11) \times 10^{-16}\bar{\Theta}\, e\,\text{cm}\,. \tag{4.1}$$

The current stringent experimental bound on the EDM of neutron, $|d_n| < 9.3 \times 10^{-29}\, e\,\text{cm}$ (at 90% CL) [493, 494, 495], implies that $|\bar{\Theta}| < 9 \times 10^{-13}$. Such a small value for $\bar{\Theta}$ is quite unnatural posing a fine-tuning problem in the SM. A way out of this dilemma is possible if at least one quark is massless in which case the $\bar{\Theta}$-term can be eliminated via a chiral rotation of the massless quark, $q \to e^{i\alpha\gamma_5}q$, making use of the chiral anomaly [496, 497]. Nevertheless, different experimental measurements and lattice QCD simulations rule out this possibility (see e.g. [32, 498, 499]). Another solution is that we happen to live in a Hubble patch where the $\bar{\Theta}$ parameter is very tiny [500].

Nevertheless, the strong CP problem can be elegantly solved by the PQ mechanism in which a global $\text{U}(1)_{\text{PQ}}$ symmetry with a colour anomaly is introduced, and the CP violating $\bar{\Theta}$-term can then be dynamically relaxed to zero [243, 244]. The $\text{U}(1)_{\text{PQ}}$ symmetry takes the form of a chiral rotation of the SM quarks: $u, d \to e^{i\alpha\gamma_5 X_{u,d}}\, u, d$ where $X_u + X_d \neq 0$ to ensure the colour anomaly. However, the quark Yukawa terms are not invariant under this transformation. Therefore, to realise the $\text{U}(1)_{\text{PQ}}$ symmetry, physics beyond the SM is necessary. In the original PQ mechanism, an extra Higgs doublet was introduced such that one of the doublets couples to the right-handed up-type quarks and the other couples to right-handed down-type quarks. Both the Higgs doublet, $\Phi_{1,2}$, were assigned PQ charges in such a way that the quark Yukawa terms remain invariant under the $\text{U}(1)_{\text{PQ}}$ phase rotations. Around the EW scale, both doublets acquire

[1] This term violates both parity (P) and time reversal (T) but conserves charge conjugation (C). Thus, it violates CP.

vacuum expectation values (VEVs), $v_{1,2}$, breaking the $SU(2)_L \otimes U(1)_Y \otimes U(1)_{\rm PQ}$ symmetry and giving masses to up- and down-type quarks, respectively. The two Higgs doublets contain eight d.o.f. in total, three of which get absorbed in giving masses to the SM gauge bosons. Among the remaining d.o.f., a pseudoscalar state coined the axion, corresponds to the Goldstone boson of the broken $\mathrm{U}(1)_{\rm PQ}$ symmetry [245, 246]. In the PQ model, the axion is identified as the common phase of the two Higgs doublets orthogonal to the weak hypercharge. The axion, which is massless at the classical level due to its shift symmetry, acquires a periodic potential and consequently a mass inversely proportional to the PQ symmetry breaking scale, $v_{\rm PQ} = v_{\rm EM} \equiv \sqrt{v_1^2 + v_2^2} \simeq 246$ GeV, due to non-perturbative QCD effects [251, 252]. Further owing to the shift symmetry, the axion couples only derivatively to other fields apart from its coupling to gluons and photons which arise due to the chiral anomaly and its mixing with neutral pions, respectively. Hence, axion interactions with all other fields are suppressed by the axion decay constant, $F_\chi = v_{\rm PQ} \simeq 246\,\mathrm{GeV}$. Due to the smallness of the axion decay constant, the original PQ proposal was soon ruled out by several experiments and astrophysical observations [501, 502, 503]. Nevertheless, other variants of the PQ mechanism, known as "invisible" axion models, circumvent the problem by creating a hierarchy between the PQ breaking and EW scales via the introduction of a new SM complex singlet field whose VEV breaks the PQ symmetry (for a review see e.g. [504]) [1].

The scale of PQ symmetry breaking is subjected to several observational constraints. For instance, the observation of the supernova SN1987A, white dwarfs and globular clusters set a lower bound of $(2\text{–}4) \times 10^8$ GeV on the scale of PQ symmetry breaking [2] (see e.g. [247, 248, 249] and references therein). With such a high PQ symmetry breaking scale, the axion can be a good dark matter (DM) candidate [250, 509, 510] as its couplings to other fields are suppressed by powers of $v_{\rm PQ}$. In fact, the energy stored in the coherent oscillations of axions today can make the entirety of the observed DM abundance via the misalignment mecha-

[1] In Appendix B, we briefly review the most widely discussed viable PQ models, KSVZ-model [505, 506] and DFSZ-model [507, 508].

[2] More precisely, on the axion decay constant, $F_\chi = v_{\rm PQ}/N_{\rm DW}$, where $N_{\rm DW}$ is the number of domain walls; $N_{\rm DW} \geq 1$ for KSVZ models [505, 506], and $N_{\rm DW} = 6$ for DFSZ models [507, 508].

nism [250] for $v_{\rm PQ} \sim 7{\times}10^{11}\,{\rm GeV}\, N_{\rm DW} \langle \Theta_1^2 \rangle^{-0.84}$ [253, 511, 512] where $\langle \Theta_1^2 \rangle^{1/2}$ is the rms axion misalignment angle at the beginning of the axion oscillation phase.

On the other hand (as discussed in Section 1.3), many puzzles of early Universe cosmology can be solved by an early epoch of accelerated expansion, inflation. During inflation, if there exists any light field, such as moduli, whose mass is well below $\mathcal{O}(H_{\rm inf})$, they obtain vacuum induced quantum fluctuations of $\mathcal{O}(H_{\rm inf}/2\pi)$ [37, 38], where $H_{\rm inf}$ denotes the Hubble parameter during inflation. In this case, such a light moduli can obtain large VEV, i.e. $\mathcal{O}(M_{\rm P})$. Typically, the moduli field behaves like a condensate within our Hubble patch [359], and begins its coherent oscillations when the Hubble expansion rate of the Universe drops to the mass of the moduli.

Similarly, if the PQ field is light compared to the Hubble expansion rate during inflation, then the PQ field can also be displaced from its minimum, which is determined by $v_{\rm PQ}$, and consequently after the end of inflation the PQ field will start coherent oscillations when its mass exceeds the time dependent Hubble scale. The PQ field can also be displaced away from $v_{\rm PQ}$ during inflation if it is coupled to the inflaton field [500], and later starts oscillating once the inflaton begins its own coherent oscillations around the minimum of its potential. If the initial VEV of the PQ field during inflation is displaced by $\gg v_{\rm PQ}$, the initial phase of its oscillations takes place around the origin. This can lead to the restoration of the PQ symmetry and the formation of dangerous topological defects [513, 514, 515] [1]. This non-thermal restoration of the PQ symmetry can be avoided if the amplitude of the PQ field at the beginning of the oscillation phase is less than $\lesssim 10^4 v_{\rm PQ}$ [520] or, if there is a coupling between the PQ field and the total energy density of the inflaton, and the oscillation of the PQ field is driven by a higher order term

[1] For $N_{\rm DW} = 1$ (i.e. for KSVZ-like models with only one extra heavy quark species), these defects are unstable and decay to cold axions leading to an upper bound on the PQ breaking scale, $v_{\rm PQ} \lesssim (4.6\text{–}7.2) \times 10^{10}\,{\rm GeV}\,(\Omega_\chi/\Omega_{\rm DM})^{0.84}$, where Ω_χ denotes the cold axions abundance and $\Omega_{\rm DM}$ is the observed abundance of DM [516, 517]. On the other hand, when $N_{\rm DW} > 1$ (i.e. for DFSZ-like models or KSVZ-like models with several extra heavy quark species), the topological defects are stable and dominate the energy density of the Universe ruling out such scenarios unless one fine-tunes a bias term that explicitly breaks the shift symmetry, and in this case $v_{\rm PQ}$ is constrained to be less than $\mathcal{O}(10^{10})\,{\rm GeV}$ in order to avoid the overproduction of cold axions [517, 518, 519].

in the potential [521, 522]. Note that similar constraints would follow had we considered a moduli field instead of inflaton.

Once the amplitude of the PQ field drops below $v_{\rm PQ}$, the oscillation of the field continues around its minimum at $v_{\rm PQ}$. In such a case, there will be no non-perturbative production of QCD axion during the second phase of the oscillation (see Chapter 5), but it can still lead to dangerous consequences from a perturbative decay of the PQ field.

In a wide range of parameter space, the coherent oscillation of the PQ field can decay dominantly into ultra-relativistic axions. If this decay occurs at sufficiently late times, the resultant axions will not thermalise with the plasma keeping their initial abundance and momenta. Such hot axions will act as dark radiation, increasing the effective number of relativistic d.o.f., i.e. $N_{\rm eff}$. The value of $N_{\rm eff}$ is constrained by the observation of CMB [13], allowing us to put constraints on the PQ parameter space. In particular, we place an interesting constraint on the axion dark matter window with large decay constant which is expected to be probed by future experiments such as CASPEr [346]. Moreover, an upper bound on the reheating temperature can be placed, which further constrains the thermal history of our Universe.

Note that the constraints on the extra relativistic species induced by heavy decaying particles are extensively discussed in the literature. These include the discussion in the context of the supersymmetric axion models [523], and in the context of the heavy moduli decay in string cosmology [524, 525], where reheating SM d.o.f. remains a challenge.

Instead of considering these scenarios, where the mass of decaying particles is generically controlled by the supersymmetry breaking effects, here we focus on the standard non-supersymmetric PQ mechanism, in which the decaying particle is identified as the radial component of the PQ field. The mass of the radial field is determined by the self-coupling constant and the PQ symmetry breaking scale. We show that an upper bound on the reheating temperature can be placed, which is relevant to axion DM with a large decay constant.

The rest of this chapter is structured as follows: in Section 4.2, we review the dynamics of the PQ symmetry breaking followed by a brief review of axion thermalisation and thermal production in Section 4.3. In Section 4.4, we discuss the

non-thermal production of ultra-relativistic axions from the coherent oscillation of the radial component of the PQ field. We then discuss the different constraints on the axion parameter space in Section 4.5. Finally, we conclude our discussion in Section 4.6.

4.2 Dynamics of the PQ symmetry breaking and the coherent oscillation of the PQ field

Let us now consider the dynamics of the PQ symmetry breaking during the evolution of a real scalar field ϕ in the background. The field ϕ could be an inflaton or moduli. Our main focus in this chapter is to understand the dynamics of the PQ field and ϕ field after inflation. The PQ symmetry breaking can be realised via the following Mexican hat potential for the PQ field denoted below by S.

$$V(\phi, S) = \lambda \left(|S|^2 - \frac{v_{\rm PQ}^2}{2} \right)^2 - g\,\phi^2 |S|^2 + U(\phi)\,, \tag{4.2}$$

where $g, \lambda > 0$ [1] and $v_{\rm PQ} = N_{\rm DW} F_\chi$ is the PQ breaking scale with F_χ and $N_{\rm DW}$ being the axion decay constant and the domain walls number, respectively, and $U(\phi)$ is the potential of the scalar field ϕ which can be approximated by a quadratic one,

$$U(\phi) = \frac{1}{2} m_\phi^2 \phi^2\,. \tag{4.3}$$

A minor departure from a quadratic potential will not affect our discussion once ϕ starts oscillating around its minimum. Note that the coupling in Eq. (4.2), $g\,\phi^2|S|^2$, shifts the minimum of the PQ field to: $|S|_{\rm m} = [v_{\rm PQ}^2/2 + (g/2\lambda)\phi^2]^{1/2}$. For

[1] Here we consider a negative coupling to ϕ, i.e. $g > 0$, in which case the effective PQ breaking scale, $v_{\rm PQ,eff} \equiv \sqrt{2}\langle |S| \rangle$, can be much larger than $v_{\rm PQ}$ causing the PQ field to oscillate once the slow-roll conditions break down, if ϕ is treated as an inflaton. This can also ameliorate the isocurvature bound on $v_{\rm PQ}$, since large $v_{\rm PQ,eff}$ reduces the power spectrum of isocurvature perturbation along the angular direction given by $\Delta_{\rm iso}^2 = (4/\langle \Theta_1^2 \rangle)(N_{\rm DW} H_{\rm inf}/2\pi v_{\rm PQ,eff})^2 (\Omega_\chi/\Omega_{\rm DM})^2$ [521], which is bounded to be $< 7.8 \times 10^{-11}$ from CMB data [13]. On the other hand, if $g < 0$ and $\sqrt{g}\,\phi_i/(\sqrt{\lambda}\,v_{\rm PQ}) \gtrsim \mathcal{O}(1)$, the PQ symmetry gets broken after inflation leading to the formation of topological defects. However, the dynamics of the oscillations should not be different in either case.

convenience, let us write the PQ field in terms of polar coordinates,

$$S = \frac{\varrho}{\sqrt{2}} e^{i\Theta}. \tag{4.4}$$

The equations of motion for ϕ and the PQ radial field ϱ are then given by

$$\Box\phi + 3H\dot{\phi} + \partial_\phi U - g\varrho^2\phi = 0\,, \tag{4.5}$$
$$\Box\varrho + 3H\dot{\varrho} + \left[\lambda(\varrho^2 - v_{\rm PQ}^2) - g\phi^2\right]\varrho = 0\,, \tag{4.6}$$

where $\Box = \partial_t^2 - \nabla^2/a^2(t)$. In Eq. (4.6), we have ignored an irrelevant coupling to the angular field Θ, $\varrho^2\partial_\mu\Theta\partial^\mu\Theta$. Furthermore, we focus on the evolution of the zero-modes; separating the background part from Eqs. (4.5) and (4.6) by writing ϕ as $\bar{\phi}(t)+\delta\phi(t,\mathbf{x})$ and similarly for ϱ, we obtain

$$\ddot{\bar{\phi}} + 3H\dot{\bar{\phi}} + [m_\phi^2 - g\bar{\varrho}^2]\bar{\phi} = 0\,, \tag{4.7}$$
$$\ddot{\bar{\varrho}} + 3H\dot{\bar{\varrho}} + \left[\lambda(\bar{\varrho}^2 - v_{\rm PQ}^2) - g\bar{\phi}^2\right]\bar{\varrho} = 0\,, \tag{4.8}$$

where over-barred quantities are the background values. Now depending on the value of the parameters g and λ, there will be two cases.

4.2.1 Case I: $\sqrt{g}\,\phi_i/(\sqrt{\lambda}v_{\rm PQ}) \ll 1$

In the limit when $\sqrt{g}\phi_i/(\sqrt{\lambda}\,v_{\rm PQ}) \ll 1$, where ϕ_i denotes the amplitude of ϕ at the beginning of the oscillation phase after the end of inflation, the coupling between the PQ field and ϕ can be ignored. In this case, the minimum of the potential along the ϱ direction occurs at $v_{\rm PQ}$. Assuming it starts from a large value [34, 56], the ϱ field follows an attractor solution [526]:

$$\varrho = \left(2\lambda\int_\phi^{\phi_*} U_\phi^{-1} d\phi\right)^{-1/2}. \tag{4.9}$$

Clearly, the effective PQ breaking scale, $v_{\rm PQ,eff} = \langle\varrho\rangle$ can be much larger than $v_{\rm PQ}$ during the slow-roll phase. If ϕ is the inflaton, large $v_{\rm PQ,eff}$ ($\gg H_{\rm inf}$) is actually

desirable in order to suppress the isocurvature fluctuations along the angular direction.

We demand that the PQ field does not come to dominate the energy density of the Universe during the slow-roll phase, which gives the constraint

$$\lambda \lesssim \frac{H_{\rm inf}^2 M_{\rm P}^2}{\varrho_i^4} \,. \tag{4.10}$$

Here, ϱ_i is the typical value of ϱ during inflation. Once the Hubble parameter drops below its mass, the PQ radial field starts oscillating. Due to the large amplitude, $\varrho_i \gg v_{\rm PQ}$, the initial oscillations will take place around $\varrho = 0$. This can result in large amplification of the quantum fluctuations in the PQ field especially along the massless angular direction (see Chapter 5), which may lead to the restoration of the PQ symmetry and consequently the formation of potentially dangerous topological defects unless $\varrho_i \lesssim 10^4 v_{\rm PQ}$ [520]. Note that we shall adhere to this bound on ϱ_i here.

4.2.2 Case II: $\sqrt{g}\,\phi_i/(\sqrt{\lambda}\,v_{\rm PQ}) \gg 1$

In this case, the minimum of the PQ field gets shifted away from $v_{\rm PQ}$ via the coupling $g\,\varrho^2\phi^2$,

$$\varrho_{\rm m} \simeq (g/\lambda)^{1/2}\,\phi \,. \tag{4.11}$$

If the PQ radial field is sufficiently heavy, $m_{\varrho,\rm eff} \simeq |\lambda(3\varrho^2 - \varrho_{\rm m}^2)|^{1/2} \gtrsim H_{\rm inf}$, it will be sitting at its minimum, $\varrho = \varrho_{\rm m} \gg v_{\rm PQ}$, during the slow-roll phase. On the other hand, if ϱ is light, $m_{\varrho,\rm eff} \ll H_{\rm inf}$, it can get displaced from $\varrho_{\rm m}$, i.e. ϱ will get shifted even further away from $v_{\rm PQ}$ due to inflaton vacuum induced quantum fluctuations. This results in an even larger initial amplitude of ϱ once it start oscillating. We follow Ref. [521], and take the amplitude of the PQ radial field at the beginning of the oscillation phase to be $\varrho_{\rm m}$. Once the PQ field starts oscillating around its minimum, the PQ field sooner or later stops tracking its minimum to oscillate around the origin with its own frequency. To see this, let us define $\Xi = \bar{\varrho}/\varrho_{\rm m}$;

substituting it in Eq. (4.8), we obtain

$$\frac{\mathrm{d}^2\Xi}{\mathrm{d}(\ln t)^2} + F\frac{\mathrm{d}\Xi}{\mathrm{d}(\ln t)} + (Ht)^2\left[\lambda\frac{\varrho_{\rm m}^2}{H^2}(\Xi^2-1)+G\right]\Xi = 0\,, \tag{4.12}$$

with

$$F = Ht\left(\frac{2}{H\sigma_{\rm m}}\frac{\mathrm{d}\varrho_{\rm m}}{\mathrm{d}t}+3\right)-1 \simeq -1\,,$$

and

$$G = \frac{1}{\varrho_{\rm m}H^2}\frac{\mathrm{d}^2\varrho_{\rm m}}{\mathrm{d}t^2}+\frac{3}{\varrho_{\rm m}H}\frac{\mathrm{d}\varrho_{\rm m}}{\mathrm{d}t}\,,$$

where we substituted $\varrho_{\rm m}=[(g/\lambda)\langle\phi^2\rangle]^{1/2}\propto t^{-1}$ with $\langle\phi^2\rangle$ being the time average of ϕ^2 over its oscillation period. Initially, the PQ radial field is following its minimum $\varrho_{\rm m}$, i.e. Ξ is roughly constant in time. Upon the breakdown of the slow-roll conditions, ϕ starts oscillating with frequency m_ϕ and amplitude decaying as $a(t)^{3/2}$. Due to its coupling to ϕ $[g\,\phi^2\varrho^2\propto a(t)^{-5}]$, the PQ radial field may continue tracking $\varrho_{\rm m}$ for a while. As the damping coefficient F becomes negative once ϕ starts oscillating, the ϱ tracking of its minimum is rendered unstable and the amplitude of Ξ will increase with time. Once the term $\lambda\varrho^4\propto a(t)^{-4}$ takes over, the amplitude of Ξ will continue increasing as $a(t)^{1/2}$ and the oscillation of ϱ will follow the solution [527]:

$$\varrho \sim \frac{\varrho_i}{a(\tau)}\cos[c\sqrt{\lambda}\,\varrho_i(\tau-\tau_i)]\,, \tag{4.13}$$

where $c\simeq 0.8472$ is a constant and $\tau=\tau_i+\int \mathrm{d}t/a(t)$ denotes the conformal time. Since $\varrho_i/v_{\rm PQ}\simeq(g/\lambda)^{1/2}(\phi_i/v_{\rm PQ})\gg 1$, the oscillation of ϱ will initially take place around $\varrho=0$.

In both the cases, i.e. case-I and case-II, described above, the first phase of the oscillation around the origin terminates when the amplitude of $\varrho\propto a(t)^{-1}$ drops below $v_{\rm PQ}$, i.e. at

$$t_c = \begin{cases} t_i\left(\frac{a(t_c)}{a(t_i)}\right)^{3/2}\simeq H_{\rm inf}^{-1}\left(\frac{\varrho_i}{v_{\rm PQ}}\right)^{3/2}, & (t_c\le t_{\rm rh}) \\ t_{\rm rh}\left(\frac{a(t_i)}{a(t_{\rm rh})}\right)^2\left(\frac{a(t_c)}{a(t_i)}\right)^2\simeq H_{\rm inf}^{-4/3}t_{\rm rh}^{-1/3}\left(\frac{\varrho_i}{v_{\rm PQ}}\right)^2, & (t_c>t_{\rm rh})\,, \end{cases} \tag{4.14}$$

with $t_{\rm rh}$ being the time of the reheating and t_i being the time at the end of the slow roll inflation. Here, we assumed that the Universe is dominated by matter during the reheating epoch, i.e. $a(t) \propto t^{2/3}$ for $t_i < t < t_{\rm rh}$. At $t > t_c$, the amplitude of ϱ is less than $v_{\rm PQ}$, and hence its oscillation takes place around $v_{\rm PQ}$. If the PQ symmetry does not get restored during the oscillation phase either thermally (if $v_{\rm PQ} < T_{\rm rh}$) or non-thermally (if $v_{\rm PQ} \lesssim 10^{-4} \varrho_i$), the energy density of the radial field will be dominated by the zero-mode, $\rho_\varrho(t \geq t_c) \simeq (\lambda v_{\rm PQ}^4/4)\,[a(t_c)/a(t)]^3$. Consequently at $t > t_c$, the oscillation of ϱ can be treated as ϱ particles with mass $m_\varrho = \sqrt{2\lambda}\, v_{\rm PQ}$ setting at rest [476], which as we show below decay dominantly into ultra-relativistic axions.

4.3 Thermalisation and thermal production of relativistic axions

If the decay process of the ϕ field is sufficiently efficient to reheat the Universe to a high temperature (such a scenario can be envisaged in SM gauge invariant models of inflation [368, 528]), axions may thermalise with the cosmic plasma. Later on, they decouple from the plasma with thermal distributions.

Note that the axion field, $\chi \equiv \Theta F_\chi$, couples to the SM particles via $v_{\rm PQ}$-suppressed operators. Nevertheless, such an interaction can lead to the thermalisation of axions. Before EW symmetry breaking, the axion interaction rate with SM particles is dominated by its couplings to quarks q and gluons g via the axion coupling to gluons, $\chi\, G^{a\mu\nu}\widetilde{G}^a_{\mu\nu}/F_\chi$ [529] [1]. This is true for all axion models. The relevant processes are then [529, 531]:

1. $g + \chi \leftrightarrows q + \bar{q}$,
2. $q + \chi \leftrightarrows q + \chi$ and $\bar{q} + \chi \leftrightarrows \bar{q} + \chi$,
3. $g + \chi \leftrightarrows g + g$.

[1] In DFSZ models the axion interaction rate with the SM fields is dominated by the axion tree level coupling to quarks after EW symmetry breaking [530]. However, the possible thermalisation of axions occurs at temperature much higher than the EW scale, and in such a case, the dominant contribution to the interaction rate arises from the axion-gluon coupling.

These interactions lead to CM cross-sections of the form [531] [1]

$$\tilde{\sigma}_{\rm CM} = A \ln\left(\frac{s}{m_D^2}\right) + B\,, \tag{4.15}$$

where $m_D = \sqrt{8\pi\alpha_s}\,T$ is the Debye mass [532], and A and B are constants whose values are respectively given by

1. $A = 0,\ \ B = \frac{N_f}{6\pi^2}\frac{\alpha_s^3}{F_\chi^2}$,
2. $A = \frac{N_f}{\pi^2}\frac{\alpha_s^3}{F_\chi^2}$, $B = -\frac{3N_f}{4\pi^2}\frac{\alpha_s^3}{F_\chi^2}$,
3. $A = \frac{15}{2\pi^2}\frac{\alpha_s^3}{F_\chi^2}$, $B = -\frac{55}{8\pi^2}\frac{\alpha_s^3}{F_\chi^2}$,

with $N_f = 6$. Now using Eq. (A.18) one obtains the following interaction rate [531] [2]:

$$\begin{aligned}\Gamma_{\chi,eq} &= \left\{12\left[-\ln(2\pi\alpha_s) + 2\frac{\zeta'(3)}{\zeta(3)} - 2\gamma\right] + \frac{3}{2}\ln(2) + \frac{83}{4}\right\}\frac{\zeta(3)}{\pi^4}\frac{\alpha_s^3 T^3}{F_\chi^2} \\ &\simeq 7.1\times 10^{-6}\left(\frac{\alpha_s}{1/35}\right)^3\frac{T^3}{F_\chi^2}\,.\end{aligned} \tag{4.16}$$

Assuming that the SM quarks and gluons are part of the thermal bath, the Boltzmann equation governing the number density of axions is given by [see Eq. (A.17)]

$$\dot{n}_\chi + 3Hn_\chi = \Gamma_{\chi,eq}(n_{\chi,eq} - n_\chi)\,, \tag{4.17}$$

where $n_{\chi,eq} = (\zeta(3)/\pi^2)\,T^3$ denotes the equilibrium average number density of axions, and the Hubble parameter during RD is given by Eq.(2.5) [3]. Introducing

[1] Here for convenience, the cross-sections are not averaged over the initial d.o.f.

[2] The tree level thermally-averaged interaction rate quoted above, $\Gamma_{\chi,eq}n_{\chi,eq}$ where $n_{\chi,eq}$ denotes the equilibrium number density of axions, is roughly the same as the one obtained using the thermal field formalism [530] for sufficiently small gauge coupling, $g_s = \sqrt{4\pi\alpha_s}$, which corresponds to sufficiently high temperature. They differ significantly only when $g_s \gtrsim 1$ which corresponds to $T \lesssim 5\times 10^3$ GeV. Since we are interested in axions with large F_χ which decouple from the plasma at $T \gg 5\times 10^3$ GeV, the simple tree level calculation which gives the axion interaction rate, Eq. (4.16), and also used throughout this section, is sufficient.

[3] Here, we consider the evolution of n_χ during radiation domination, i.e for $T \leq T_{\rm rh}$. However, the Universe may have been exposed to temperatures higher than $T_{\rm rh}$ [367]. Nevertheless, from the axion production point of view, $T_{\rm rh}$ is effectively the maximum temperature as axions produced at $T > T_{\rm rh}$ get diluted away by the entropy produced in ϕ decay [530].

the function $\eta_\chi \equiv n_\chi/n_{\chi,eq}$ and changing the dependence from time to $x \equiv T_{\rm rh}/T$, where $T_{\rm rh}$ is the reheating temperature, Eq. (4.17) can be re-written as

$$x^2 \frac{{\rm d}\eta_\chi}{{\rm d}x} = K(1-\eta_\chi)\,, \tag{4.18}$$

where

$$K \equiv x\frac{\Gamma_{\chi,eq}}{H} \simeq 5\times 10^2 \left(\frac{g}{100}\right)^{-1/2}\left(\frac{\alpha_s}{1/35}\right)^3\left(\frac{T_{\rm rh}}{10^{10}\,{\rm GeV}}\right)\left(\frac{F_\chi}{10^{10}\,{\rm GeV}}\right)^{-2}. \tag{4.19}$$

Clearly, axions reach full thermal equilibrium with the SM particles if $K \gg 1$, i.e. when $T_{\rm rh}$ is sufficiently high. Assuming that g remains constant during the course of integration, Eq. (4.18) can be easily solved to obtain [531]

$$\eta_\chi = 1 - \ e^{K(x^{-1}-1)}\,, \tag{4.20}$$

where we assumed that $\eta_\chi(x=1)=0$. Axions decouple from the plasma when $K \sim x$ (equivalently $\Gamma_{\chi,eq} \sim H$). In other words, axions decouple at

$$T_{\chi,{\rm dec}} \simeq 10^7\,{\rm GeV}\left(\frac{g}{100}\right)^{1/2}\left(\frac{\alpha_s}{1/35}\right)^{-3}\left(\frac{v_{\rm PQ}/N_{\rm DW}}{10^{10}\ {\rm GeV}}\right)^2. \tag{4.21}$$

Since axions with $v_{\rm PQ} \gtrsim 4\times 10^8$ GeV decouple from the plasma at $T \gg m_Z$, where m_Z denotes the Z-boson mass, they are colder than photons at the time of last scattering as photons get reheated by the annihilation of other SM particles when the latter become non-relativistic. Therefore the contribution of thermally-produced axions to $N_{\rm eff}$ is quite small [530, 533]. Nevertheless, as a consequence of the above discussion, the axions produced non-thermally in the decay of the PQ radial field at temperature $\ll T_{\chi,{\rm dec}}$ will never be in thermal contact with the plasma, and hence keep their comoving number density and comoving momenta. To see this let us consider the loss in the number density of the non-thermally produced axions due to their possible scatterings into SM particles. Ignoring Fermi blocking and stimulated emission, the Boltzmann equation governing the

time evolution of the axion number density can be written as [see Eq. (A.5)]

$$\dot{n}_\chi + 3Hn_\chi = -\sum\int \mathrm{d}\tilde{p}_\chi \mathrm{d}\tilde{p}_a \mathrm{d}\tilde{p}_i \mathrm{d}\tilde{p}_j (2\pi)^4 \delta^{(4)}(P_\chi + P_a - P_i - P_j)\, f_\chi f_{a,eq} |\mathcal{M}|^2, \quad (4.22)$$

where the sum is over all the possible processes and $\mathrm{d}\tilde{p}_j = \mathrm{d}^3 p_j/[(2\pi)^3 2E_j]$. Here we ignore the axion production from the plasma. Again we assume that the SM particles (a, i and j) are in thermal equilibrium. Using the definition of the unpolarised cross-section, $\tilde{\sigma}$ (see Eq. [A.11)], we obtain

$$\int \mathrm{d}\tilde{p}_i \mathrm{d}\tilde{p}_j (2\pi)^4 \delta^{(4)}(P_\chi + P_a - P_i - P_j)\, |\mathcal{M}|^2 = \tilde{\sigma} v_{\rm Mol}\, 2E_\chi 2E_a \,. \quad (4.23)$$

Therefore, Eq. (4.23) can be re-written as (see Appendix A.2)

$$\dot{n}_\chi + 3Hn_\chi \simeq -\Gamma(\chi\, a \to i\, j)\, n_\chi \,, \quad (4.24)$$

with

$$\Gamma(\chi\, a \to i\, j) = \frac{1}{n_\chi} \sum\int \mathrm{d}\tilde{p}_\chi \mathrm{d}\tilde{p}_a\, f_\chi f_{a,eq}\, \tilde{\sigma} v_{\rm Mol}\, 2E_\chi 2E_a \,, \quad (4.25)$$

being the averaged interaction rates where $v_{\rm Mol} = [(P_\chi^\mu P_{a\mu})^2 - m_\chi^2 m_a^2]^{1/2}/(E_\chi E_a)$ is the Møller velocity. In the relativistic limit, $v_{\rm Mol}\, 2E_\chi 2E_a \simeq 2s$ where $s = m_\chi^2 + m_a^2 + 2E_\chi E_a - 2\mathbf{p}_\chi \cdot \mathbf{p}_a \simeq 2E_\chi E_a(1 - \cos\theta)$ is the squared total CM energy. We are free to evaluate Eq. (4.25) in the CM frame. Expressing $\mathbf{p}_\chi$ and $\mathbf{p}_a$ in polar coordinates, Eq. (4.25) can be re-written as

$$\Gamma(\chi\, a \to i\, j) = \frac{1}{4\pi^4 n_\chi} \sum\int_{-1}^{1} \frac{1}{2} \mathrm{d}\cos\theta \int_0^\infty \mathrm{d}p_\chi\, p_\chi^2 \int_0^\infty \mathrm{d}p_i\, p_i^2\, f_\chi f_{i,eq}\, \tilde{\sigma}_{\rm CM} \,. \quad (4.26)$$

For non-thermal axions produced from the decay of ϱ particles, one can approximate the phase space distribution of axions as

$$f_\chi(p_\chi, t) = 2\pi^2 n_\chi(t_{\rm d}) \left(\frac{a(t_{\rm d})}{a(t)}\right)^3 \frac{\delta(p_\chi - \bar{p}_\chi)}{g_\chi p_\chi^2} \,, \quad (4.27)$$

with $\bar{p}_\chi = p_\chi(t_{\rm d})\, [a(t_{\rm d})/a(t)] = (m_\varrho/2)[a(t_{\rm d})/a(t)]$ where for simplicity we assumed

a sudden decay of ϱ at $t=t_{\rm d}$ [1]. Again we focus on the axion interactions with the SM quarks and gluons via the axion anomalous coupling listed above. Substituting for $\tilde{\sigma}_{\rm CM}$ from Eq. (4.15) with the corresponding values of A and B for each of the above listed interactions into Eq. (4.26) and summing up all the contributions, we obtain

$$\Gamma(\chi\, a\to i\, j) = \left\{12\left[\ln\left(\frac{\bar{p}_\chi}{T}\right) - \ln(2\pi\alpha_s) + \frac{\zeta'(3)}{\zeta(3)} - \gamma_{_E}\right] + \frac{3}{2}\ln(2) + \frac{11}{4}\right\}\frac{\zeta(3)}{\pi^4}\frac{\alpha_s^3 T^3}{F_\chi^2}$$
$$\simeq \{4.5 + 3.5\ln(\bar{p}_\chi/T)\}\times 10^{-6}\left(\frac{\alpha_s}{1/35}\right)^3\frac{T^3}{F_\chi^2}\,, \tag{4.28}$$

where $\gamma_{_E}\simeq 0.5772$ is the Euler's constant and $\zeta'(3)\simeq -0.1981$. Clearly, the factor $\ln(\bar{p}_\chi/T)$ is constant since during RD, $T\propto a(t)^{-1}$ away from the phase transitions. As one would expect, $\Gamma(\chi\, a\to i\, j)$ is larger than its thermal counterpart, $\Gamma_{\chi,eq}$ which is given by Eq. (4.16) due to the monochromatic momentum distribution of axions produced in ϱ decay provided that $p_\chi(t_{\rm d})\gg T$. However, this enhancement is not significant, $\Gamma(\chi\, a\to i\, j)/\Gamma_{\chi,eq}\simeq 1+\{\ln(\bar{p}_\chi/T)-0.8\}/\{2.0-\ln[\alpha_s/(1/35)]\}$, i.e. $\Gamma(\chi\, a\to i\, j)$ is only enhanced by a logarithmic factor. Again introducing the function $\eta_\chi = n_\chi/n_{\chi,eq}$ and the independent variable $x\equiv T_{\rm d}/T$, where $T_{\rm d}$ is the temperature corresponding to the time $t_{\rm d}$, the Boltzmann Eq. (4.24) can be re-written as

$$x^2\frac{d\eta_\chi}{dx}\simeq -K\eta_\chi\,, \tag{4.29}$$

where $K\equiv x\Gamma(\chi\, a\to i\, j)/H$. Eq. (4.29) admits the following solution:

$$\eta_\chi(x)\simeq \eta(x_{\rm d})\; e^{K(x^{-1}-1)}\,. \tag{4.30}$$

Since $x^{-1}=T/T_{\rm d}\leq 1$, axions keep their initial abundance if $K\ll 1$. In other words, axions produced non-thermally at $T_{\rm d}\ll T_{\chi,{\rm dec}}$ will keep their comoving number density and comoving momenta.

[1] In general, the decay of the ϱ particles takes place over an extended period of time leading to a smeared momentum distribution for axions due to the expansion effect [534].

4.4 Non-thermal production of axions dark radiation

Let us now consider the decay of the coherent oscillation of the radial component of the PQ field, ϱ. If the PQ symmetry does not get restored during the initial phase of oscillation, which takes place around $\varrho=0$, ρ_ϱ will be dominated by the zero mode of ϱ. For $t \geq t_c$, the oscillation of σ continues around $\varrho = v_{\rm PQ}$ with initial amplitude $\sim v_{\rm PQ}$. As the coherent oscillation of ϱ behaves as ϱ particles at rest [476], the latter cannot scatter into other species. However, they can decay into the particle species to which they couple. For instance, the ϱ particles couple to axions via the vertex $\tilde{\varrho}\,\partial_\mu\chi\partial^\mu\chi/v_{\rm PQ}$, where $\tilde{\varrho}=\varrho-v_{\rm PQ}$, allowing them to decay into axions with the following rate:

$$\Gamma(\varrho\to 2\chi) = \frac{1}{32\pi}\frac{m_\varrho^3}{v_{\rm PQ}^2} = \frac{\lambda^{3/2}}{8\sqrt{2}\pi}v_{\rm PQ}\,. \tag{4.31}$$

Moreover, the ϱ particles can decay into species other than axions. For example, in the KSVZ-like models [505, 506] (see Appendix B.1 for a brief review), ϱ couples to the extra heavy coloured fermions Q via the vertex $(m_Q/v_{\rm PQ})\,\varrho\,\bar{Q}Q$ leading to the following ϱ decay rate:

$$\Gamma(\varrho\to\bar{Q}Q) = \frac{3m_Q^2 m_\varrho}{8\pi v_{\rm PQ}^2}\left(1-\frac{4m_Q^2}{m_\varrho^2}\right)^{3/2}, \tag{4.32}$$

where for concreteness we assumed that the heavy quarks are colour triplets. The perturbative decay of ϱ into extra heavy quarks is only allowed if $m_Q < m_\varrho/2$ [1]. Similarly, in the DFSZ-like models [507] (see Appendix B.2 for a brief review), ϱ

[1] The decay of ϱ to extra heavy quarks with $m_Q > m_\varrho/2$ can take place via non-perturbative effects during the first phase of ϱ oscillation as the extra heavy quarks become effectively massless during parts of each oscillation of ϱ [535]. However, once the amplitude of ϱ drops below $v_{\rm PQ}$, the extra heavy quarks cannot be made massless and hence this non-perturbative decay channel is no longer open.

couples to the two Higgs doublets leading to the following decay rates:

$$\Gamma(\sigma \to 2\Phi_{1,2}) \simeq \frac{\lambda_{S1,2}^2}{8\pi m_\varrho} v_{\rm PQ}^2 \simeq \frac{\lambda_{S1,2}^2}{8\pi\sqrt{2\lambda}} v_{\rm PQ}\,, \tag{4.33}$$

where $\lambda_{S1,2}$ have to be $< (v_{\rm EW}/v_{\rm PQ})^2$ in order not to affect EW symmetry breaking [536]. Comparing Eqs. (4.32) and (4.33) to Eq. (4.31), we can see that ϱ will decay mostly into axions in KSVZ-like models provided that $m_Q > m_\varrho/2$ or $m_Q < m_\varrho/(2\sqrt{3})$, and similarly in DFSZ-like models as long as $\lambda > (v_{\rm EW}/v_{\rm PQ})^2$. As a result, all or at least a large portion of the energy stored in the ϱ field will ultimately be transferred to the axion field.

We now proceed to estimate the axion energy density produced from the decay of the radial component of the PQ field. For simplicity, we will assume that the Universe is dominated by matter during the reheating epoch [1]. We further assume that all the ϱ particles instantaneously decay at $t = t_{\rm d}$ which can take place during inflaton domination (i.e. $t_{\rm d} < t_{\rm rh}$) if $\lambda \geq (256\pi^4 g/45)^{1/3}(T_{\rm rh}^2/v_{\rm PQ} M_{\rm P})^{2/3}$. Otherwise, the ϱ decay process occurs during the RD epoch (i.e. $t_{\rm d} > t_{\rm rh}$).

The energy density of ϱ at $t = t_{\rm c}$ is roughly $(\lambda/4)\, v_{\rm PQ}^4$. Later at $t = t_{\rm d}$, ρ_ϱ becomes $(\lambda/4)\, v_{\rm PQ}^4 [a(t_{\rm c})/a(t_{\rm d})]^3$. Assuming a sudden transition from inflaton domination to RD at $t = t_{\rm rh}$, the energy density stored in the ϱ coherent oscillation can be expressed as

$$\rho_\varrho(t_{\rm d}) \simeq \frac{\lambda}{4} v_{\rm PQ}^4 \begin{cases} \left(\frac{t_{\rm c}}{t_{\rm d}}\right)^2, & (t_{\rm d} \leq t_{\rm rh}) \\ \left(\frac{t_{\rm c}}{t_{\rm rh}}\right)^2 \left(\frac{t_{\rm rh}}{t_{\rm d}}\right)^{3/2}, & (t_{\rm d} > t_{\rm rh} > t_c) \\ \left(\frac{t_{\rm c}}{t_{\rm d}}\right)^{3/2}, & (t_{\rm d} > t_c > t_{\rm rh})\,, \end{cases} \tag{4.34}$$

where $t_c \simeq H_{\rm inf}^{-1}(\varrho_i/v_{\rm PQ})^{3/2} \leq t_{\rm rh}$ if $\varrho_i/v_{\rm PQ} \leq (90/\pi^2 g)^{1/3}(H_{\rm inf} M_{\rm P}/T_{\rm rh}^2)^{2/3}$; otherwise, $t_c \simeq t_{\rm rh}(H_{\rm inf} t_{\rm rh})^{-4/3}(\varrho_i/v_{\rm PQ})^2$. The energy density of ϱ comes to dominate

[1] In principle, the effective equation of state during the reheating phase can be different from that of a matter dominated Universe, i.e. the equation of state parameter, $\omega_{\rm eff} > 0$ [537], in which case the energy density of the ϱ field will be less diluted due to the slower expansion rate during the reheating phase, $a(t) \propto t^{2/[3(1+\omega_{\rm eff})]}$. As a result, the abundance of the extra-relativistic axions due to ϱ decay will be larger leading to a more stringent bound on the axion parameter space.

the energy density of the Universe before it decays if the following condition is violated:

$$\lambda < 0.15 \times \frac{H_{\rm inf}^8 M_{\rm P}^{10}}{g(T_{\rm rh}) \varrho_i^{12} T_{\rm rh}^4 v_{\rm PQ}^2} \,. \tag{4.35}$$

The number density of ϱ particles at $t_{\rm d}$ is $n_\varrho(t_{\rm d}) = \rho_\varrho(t_{\rm d})/m_\varrho$. These ϱ particles decay dominantly into axions, and hence the number and energy density of axions at $t_{\rm d}$ are $n_\chi(t_{\rm d}) \simeq 2 n_\varrho(t_{\rm d})$ and

$$\rho_\chi(t_{\rm d}) \simeq 2[m_\chi^2 + (m_\varrho/2)^2]^{1/2} n_\varrho(t_{\rm d}) \simeq [1 + (2m_\chi/m_\varrho)^2]^{1/2} \rho_\varrho(t_{\rm d}) \,,$$

respectively [1]. In the range of interest, $v_{\rm PQ} \gtrsim 10^8$ GeV, axions are relativistic at the era of photon decoupling ($z_{\rm dec} \simeq 1090$ [13]) and hence the factor $2m_\chi/m_\varrho$ can be safely ignored. Thus, with the help of Eq. (4.34), the axion energy density during the time interval $\max(t_{\rm d}, t_{\rm rh}) < t < t_{\rm eq}$, where $t_{\rm eq}$ is the time at radiation-matter equality, is given by

$$\rho_\chi(t) \simeq \frac{\lambda}{4} v_{\rm PQ}^4 \begin{cases} \left(\frac{t_{\rm c}}{t_{\rm d}}\right)^2 \left(\frac{t_{\rm d}}{t_{\rm rh}}\right)^{8/3} \left(\frac{t_{\rm rh}}{t}\right)^2 , & (t_{\rm d} \leq t_{\rm rh}) \\ \left(\frac{t_{\rm c}}{t_{\rm rh}}\right)^2 \left(\frac{t_{\rm rh}}{t_{\rm d}}\right)^{3/2} \left(\frac{t_{\rm d}}{t}\right)^2 , & (t_{\rm d} > t_{\rm rh} > t_c) \\ \left(\frac{t_{\rm c}}{t_{\rm d}}\right)^{3/2} \left(\frac{t_{\rm d}}{t}\right)^2 , & (t_{\rm d} > t_c > t_{\rm rh}) \,. \end{cases} \tag{4.36}$$

If the PQ radial field does not come to dominate the energy density of the Universe before it decay [2], Eq. (4.36) can be re-written as

$$\frac{\rho_\chi}{\rho_\gamma} \simeq 0.37 \left(\frac{g(T_{\rm rh})}{100}\right)^{1/3} \left(\frac{10^{13}\,{\rm GeV}}{H_{\rm inf}}\right)^2 \left(\frac{\varrho_i}{M_{\rm P}}\right)^3 \left(\frac{v_{\rm PQ}}{10^{15}\,{\rm GeV}}\right)^{1/3} \left(\frac{T_{\rm rh}}{10^{10}\,{\rm GeV}}\right)^{4/3} \tag{4.37}$$

[1] Here again we assume a monochromatic momentum distribution for axions due to the instantaneous decay of ϱ particles at $t = t_{\rm d}$.

[2] If the PQ radial field had dominated the energy density of the Universe before it decayed, we would have had a Universe different from the one we live in since the PQ radial field decays dominantly into axions.

for $t_{\rm d} \leq t_{\rm rh}$, and

$$\frac{\rho_\chi}{\rho_\gamma} \simeq 0.04 \left(\frac{g(T_{\rm rh})}{100}\right)^{1/4} \left(\frac{\lambda}{10^{-11}}\right)^{1/4} \left(\frac{10^{13}\,{\rm GeV}}{H_{\rm inf}}\right)^2 \left(\frac{\varrho_i}{M_{\rm P}}\right)^3 \left(\frac{v_{\rm PQ}}{10^{15}\,{\rm GeV}}\right)^{1/2} \left(\frac{T_{\rm rh}}{10^{10}\,{\rm GeV}}\right) \quad (4.38)$$

for $t_{\rm d} > t_{\rm rh}$, where $\rho_\gamma = (\pi^2/15)\, T^4$ denotes the energy density of photons.

4.5 Constraints on the axion parameter space

The axion parameter space is subjected to a plethora of experimental, astrophysical and cosmological bounds. We first review the most stringent ones and then discuss the bound arising from the decay of the coherent oscillation of ϱ into axions.

- **Supernovae**: Considering an extra energy loss channel in stars due to the emission of axions and comparing this to observations enables one to set upper bounds on the axion couplings and hence lower bounds on the axion decay constant, $F_\chi = v_{\rm PQ}/N_{\rm DW}$. The most stringent and model-independent bound on F_χ arises for the observation of the supernova SN1987A signal, where the axion emission due to the nucleon bremsstrahlung ${\rm N\,N} \to {\rm N\,N}\,\chi$, if present, would have shortened the neutrino burst duration (for a review, see e.g. [247] and references therein). This places the following bound on F_χ [249]:

$$F_\chi / \tilde{C}_{\rm N} \gtrsim 2 \times 10^9\ {\rm GeV}\,, \quad (4.39)$$

  where $\tilde{C}_{\rm N} = ({\rm Y}_p C_p^2 + {\rm Y}_n C_n^2)^{1/2}$, C_p and C_n are axion-nucleon couplings ($\mathcal{L}_{\chi{\rm NN}} = C_{\rm N} \partial_\mu \chi \bar{\rm N} \gamma^\mu \gamma_5 {\rm N}/2F_\chi$ for $N = p, n$), and ${\rm Y}_p \simeq 0.3$ and ${\rm Y}_n \simeq 0.7$ are the proton and neutron fractions, respectively. In the KSVZ models $C_p = -0.47(3)$ and $C_n = -0.02(3)$, whereas in the DFSZ models $C_p = -0.617 + 0.435 \sin^2\beta \pm 0.025$ and $C_n = 0.254 - 0.414 \sin^2\beta \pm 0.025$ with $\tan\beta$ being the ratio of VEVs of two Higgs doublets [343]. Substituting for these values in Eq. (4.39), we have

$$F_\chi \gtrsim (2\text{–}4) \times 10^8\,{\rm GeV}\,. \quad (4.40)$$

Note that the neutrino burst duration of supernova SN1987A is less sensitive to the axion-nucleon coupling for $F_\chi \lesssim 6\times10^5\,\text{GeV}$ [247, 538], since axions with smaller F_χ would have been trapped at earlier stages. Nevertheless, their interaction with oxygen nuclei could have induced excitations in the oxygen nuclei resulting in the release of gamma ray that would have been seen at the Kamiokande detector [539]. As a result, axions with $F_\chi \lesssim 2\times10^5\,\text{GeV}$ are ruled out.

- **Globular clusters**: Another bound on F_χ arises from the observation of globular clusters [540]. The possible axion energy loss via the Primakoff process would accelerate the helium consumption reducing the helium-burning lifetimes of horizontal-branch stars. This places an upper bound on the axion-photon coupling, Eq. (1.75), $g_{\chi\gamma\gamma} < 6.6\times10^{-11}\,\text{GeV}^{-1}$ [541]. This translates to a lower bound of roughly $3\times10^7\,\text{GeV}$ and $1\times10^7\,\text{GeV}$ on F_χ for KSVZ and DFSZ models, respectively. The same argument of axion energy loss in the core of globular clusters stars can be used to constrain the axion-electron coupling relevant for the DFSZ models. The axion-electron coupling would lead to the emission of axions from the core of red giants in globular clusters via the bremsstrahlung process $e+Ze\to e+Ze+\chi$. Observations of red giants place an upper bound on the axion-electron coupling [$\mathcal{L}_{\chi ee} = -g_{\chi ee}\,\chi\bar{e}\gamma_5 e$ with $g_{\chi ee} = m_e\cos^2\beta/(3F_\chi)$], $g_{\chi ee}\lesssim 4.3\times10^{-13}$ [542]. This translates to a lower bound on the axion decay constant, $F_\chi \gtrsim 4.0\times10^8\,\cos^2\beta\,\text{GeV}$.

- **White dwarfs**: Moreover, the axion-electron coupling $g_{\chi ee}$ can also be constrained from the observation of white dwarfs. If $g_{\chi ee}$ were large, it would increase the cooling rate of white dwarfs due to axion emission, which places an upper bound of 3×10^{-13} on $g_{\chi ee}$ [543]. This translates to a lower bound of $6\times10^8\,\text{GeV}\,\cos^2\beta$ on the axion decay constant for the DFSZ-like models.

- **Laboratory and hot DM bounds**: In addition to the astrophysical bounds discussed above, laboratory experiments rule out axions with $F_\chi \lesssim \mathcal{O}(10\text{–}10^2)\,\text{GeV}$ [502, 503]. Thus in short, astrophysical observations and

laboratory experiments rule out axions with decay constant $F_\chi \lesssim (2\text{–}4) \times 10^8\,\text{GeV}$, except for a possible small window, $2{\times}10^5\,\text{GeV} \lesssim F_\chi \lesssim 6{\times}10^5\,\text{GeV}$, particular to KSVZ-like models. We note that axions with F_χ in this window are ruled out from cosmological considerations. Axions can be produced thermally if $T_\text{rh} > T_{\chi,\text{dec}}$, where $T_{\chi,\text{dec}}$ is given by Eq. (4.21). In particular, axions with decay constant $F_\chi \lesssim \mathcal{O}(10^7)\,\text{GeV}$ can be produced thermally and decouple from the plasma after the QCD phase transition. Hence, they contribute to the radiation density (not necessarily as an effectively massless d.o.f.) and later on act as hot DM, which sets an upper bound of around 1 eV on the mass of axion or equivalently a lower bound of around $6{\times}10^6$ GeV on F_χ [544]. This rules out KSVZ-axions with F_χ in the small window not ruled out by astrophysical observations.

- **DM abundance**: On the other hand, the axion decay constant can be bounded from above. The first upper bound on F_χ arises from the requirement that the abundance of cold axions today does not exceed the observed DM abundance, which implies that [511]

$$F_\chi \lesssim 7 \times 10^{11} \langle \Theta_1^2 \rangle^{-0.84}\,\text{GeV}\,. \tag{4.41}$$

  Typically, $\langle \Theta_1^2 \rangle^{1/2}$ is $\mathcal{O}(1)$, and in such a case, $F_\chi \lesssim 7{\times}10^{11}\,\text{GeV}$. However, in principle $\langle \Theta_1^2 \rangle^{1/2}$ can be smaller than $\mathcal{O}(1)$, relaxing the upper bound on F_χ.

- **Isocurvature bound**: if the PQ symmetry is broken before or during the early stages of inflation, large quantum fluctuations along the massless angular direction, $\delta\Theta = N_\text{DW} H_\text{inf}/(2\pi \upsilon_{\text{PQ,eff}})$, develop [1]. For sufficiently large PQ scale, axions do not thermalise with the cosmic plasma [see Eq. (4.21)], and hence the fluctuations along the angular direction show up on the CMB sky as isocurvature perturbations with the following power spectrum

[1] Similarly, the radial field can acquire quantum fluctuations of $\mathcal{O}(H_\text{inf})$ if it is sufficiently light during inflation, $m_\varrho \ll H_\text{inf}$. This may contribute to the isocurvature perturbations as the radial field dominantly decays into axions.

(see [521] are references therein):

$$\Delta^2_{\rm iso} = \frac{4}{\langle\Theta_1^2\rangle}\left(\frac{N_{\rm DW}H_{\rm inf}}{2\pi v_{\rm PQ,eff}}\right)^2\left(\frac{\Omega_\chi}{\Omega_{\rm DM}}\right)^2, \tag{4.42}$$

where $\Omega_\chi h^2 \simeq 0.2\langle\Theta_1^2\rangle(F_\chi/10^{12}\,{\rm GeV})^{1.19}$ is the abundance of DM axions [511]. The recent measurement of the CMB [13] constrains the DM abundance, $\Omega_{\rm DM}h^2 = 0.1198 \pm 0.0030$ (at 95% CL), and the CDM uncorrelated isocurvature perturbations, $\alpha_c \equiv \Delta^2_{\rm iso}(k_*)/[\Delta^2_{\rm iso}(k_*)+\Delta^2_{\mathscr{R}}(k_*)] < 0.033$ where $A_s \equiv \Delta^2_{\mathscr{R}}(k_*) = 2.142 \pm 0.098 \times 10^{-9}$ (at 95% CL) is the amplitude of adiabatic perturbations. This places the following upper bound on the axion decay constant:

$$F_\chi < 9.6 \times 10^7\,{\rm GeV}\left(\frac{v_{\rm PQ,eff}}{\langle\Theta_1^2\rangle^{1/2}N_{\rm DW}H_{\rm inf}}\right)^{0.84}. \tag{4.43}$$

The above bound need not be applied if ϕ is a moduli field.

- **Superradiance**: Another interesting upper bound on F_χ arises from the consideration of the supperradiance effect of astrophysical rotating black holes [545]. Axions with a large decay constant have a Compton wavelength comparable to the size of astrophysical black holes thus forming a bound system with different energy levels [546, 547, 548]. Such axions can then superradiate extracting rotational energy and angular momentum from the black hole through consecutive scatterings off the ergosphere and hence populating several energy levels. Axions can then emit gravitational waves via different processes [1] resulting in a continuous extraction of angular momentum from the host black hole [547, 548]. This would result in the absence of highly spinning black holes in a mass range corresponding to the range of F_χ for axions involved in superradiance. The measurement of the spin of stellar mass black holes disfavours axions with decay constant in the range $3\times10^{17}\,{\rm GeV} \lesssim F_\chi \lesssim 10^{19}\,{\rm GeV}$ [548].

[1] Axions can annihilate into gravitons in the presence of the gravitational potential of the hosting black hole. Axions can also transit between levels which have the same angular quantum number but different energies emitting gravitational waves.

- **Dark radiation**: Axions are massless at the tree level, as they are protected by a shift symmetry, but they acquire a small mass, $m_\chi = 5.70(6)(4)\,\text{eV}\,(F_\chi/10^6\text{GeV})^{-1}$ [343], due to the QCD instanton effect [251, 252]. As a result, the axion is a natural candidate for dark radiation provided that F_χ is sufficiently large. Hence, they contribute to the effective number of relativistic d.o.f. other than photons N_{eff}, which is defined via the relation, Eq. (2.33), that parameterises the total radiation density of the Universe. Using Eq. (2.33), the contribution from relativistic axions to N_{eff} can be estimated as

$$\Delta N_{\text{eff}} = N_{\text{eff}} - N_{\text{eff}}^{\nu} = \frac{8}{7}\left(\frac{11}{4}\right)^{4/3}\frac{\rho_\chi}{\rho_\gamma}\,, \tag{4.44}$$

  where $N_{\text{eff}}^{\nu} = 3.046$ is the contribution from three active neutrinos. Note that Eq. (4.44) applies only for axion species that remains relativistic till the era of photon decoupling. Observation of the CMB sets an upper bound $N_{\text{eff}} < 3.15^{+0.41}_{-0.40}$ at the time of photon decoupling [13]. Thus, $\Delta N_{\text{eff}} \lesssim 0.52$ which puts an upper bound on the abundance of relativistic axions. This can be used to constrain the parameter space of axion models.

Now we turn to the case where axions are produced non-thermally from the decay of the coherent oscillation of the radial component of the PQ field, ϱ. Such axions have very large initial momenta and, furthermore, they can be very light provided that F_χ is sufficiently large. It is important here to note that for sufficiently large F_χ, axions are never in thermal contact with the plasma and hence keep their initial abundance and momenta, see Eq. (4.21). Therefore, such axions are most likely to act as dark radiation contributing to N_{eff}. From Eqs. (4.37), (4.38) and (4.44), one can see that for large F_χ, ΔN_{eff} can be much larger than 0.52. In other words, too much axionic dark radiation is produced. This further constrains the axion parameter space.

We plot various observational constraints in Figs. 4.1 and 4.2 where we fix the number of domain walls, $N_{\text{DW}} = 1$ and consequently $F_\chi = v_{\text{PQ}}$. We have seen that different astrophysical observations rule out axions with

$$F_\chi \lesssim (2\text{–}4)\times 10^8\,\text{GeV} \quad \text{and} \quad F_\chi \gtrsim 3\times 10^{17}\,\text{GeV}.$$

These bounds are shown in Figs. 4.1 and 4.2 by the blue and brown regions, respectively. The current observational result on the DM abundance [13] puts an upper bound on the axion decay constant, $F_\chi \lesssim 7\times10^{11}\langle\Theta_1^2\rangle^{-0.84}\,\text{GeV}$. In Figs. 4.1 and 4.2, we show the DM bound on F_χ for different values of $\Theta_1 \cong \langle\Theta_1^2\rangle^{1/2}$ by the dotted black lines. The regions to the right of these lines are ruled out.

On the other hand, if the initial amplitude of the oscillation satisfies $\varrho_i \gtrsim 10^4\, v_{\rm PQ}$, the PQ symmetry can get restored non-thermally, which leads to the formation of topological defects [520]. In order to avoid this, we require that

$$\varrho_i \lesssim \min(M_{\rm P}, 10^4 v_{\rm PQ})\,. \tag{4.45}$$

It is worth noting here that the PQ symmetry is not restored during inflation as long as $v_{\rm PQ,eff} \simeq \varrho_i \gg H_{\rm inf}/2\pi$. However, the PQ symmetry can get restored thermally if $T_{\rm rh} \gtrsim v_{\rm PQ} = N_{\rm DW} F_\chi$. Such a parameter space is shown in Figs. 4.1 and 4.2 by the yellow regions. In principle, the Universe may have been exposed to temperatures much higher than $T_{\rm rh}$ during the reheating epoch [367]. This makes the bound even more stringent. We stress here that the restoration of the PQ symmetry and the subsequent formation of topological defects are only dangerous if $N_{\rm DW} > 1$. For models with $N_{\rm DW} = 1$, however, these topological defects are unstable and decay into cold axions rendering the DM bound even stronger, $F_\chi \lesssim (4.6\text{–}7.2)\times 10^{10}\,\text{GeV}$ [516, 517].

For the case of ϕ being the inflaton, we show the isocurvature bound on F_χ for $\Theta_1 = 1,\, 0.1,\, 0.01$ and 0.001 in Figs. 4.1 and 4.2 by the solid red lines. For $m_\phi = 10^{13}$ GeV (Figure 4.1), the isocurvature bound is much stronger than the DM one. In this case, the entire parameter space is ruled out when $\Theta_1 = 1$. For larger values of $N_{\rm DW}$, the isocurvature bound is even stronger.

The coherent oscillations of the PQ radial field lead to the excitation of ultra-relativistic axions, which act as dark radiation and hence affect the expansion rate of the Universe. In a region of the parameter space, the radial field can come to dominate the energy density of the Universe, leading to an axionic dark radiation dominated Universe. This scenario does not produce the Universe we live in and hence can be ruled out. We show the region of the parameter space where this scenario occurs in dark orange shade in Figs. 4.1 and 4.2. Even if the radial

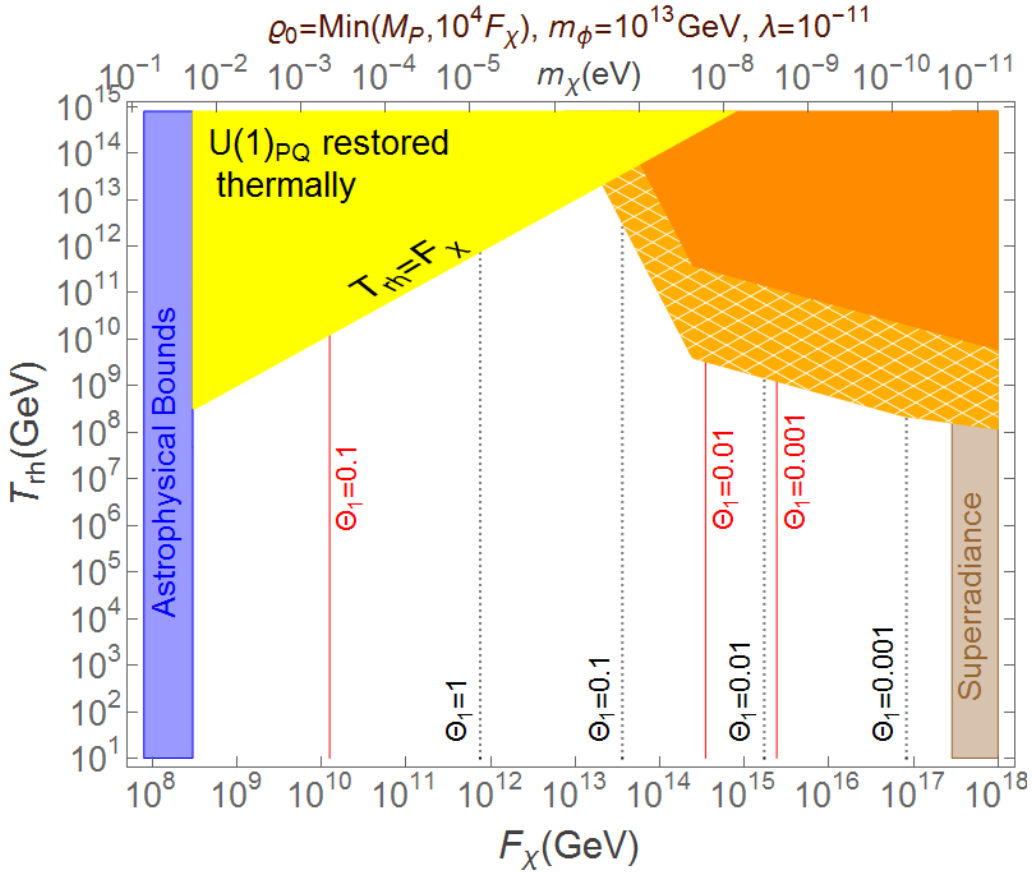

Figure 4.1: Observational constraints on the reheating temperature $T_{\rm rh}$ and the axion decay constant F_χ. In the region shaded in dark orange, ϱ comes to dominate the energy density of the Universe before it decays and hence is ruled out. The adjacent hatched region shaded in lighter orange is ruled out by the CMB bound on $N_{\rm eff}$. The blue region is ruled out by laboratory experiments and the observation of supernova SN1987A and globular cluster stars. In the yellow region, the PQ symmetry gets thermally restored. The vertical dotted black lines indicate the DM upper bound on F_χ whereas the vertical solid red lines refer to the isocurvature upper bound on F_χ for different values of misalignment angle. For $\Theta_1 = 1$, the entire parameter space is ruled out by the CMB bound on the isocurvature perturbations. Note that the isocurvature bound need not apply if ϕ were a moduli field, the issue is rather model dependent.

field does not come to dominate the energy density before it decays, the resultant axionic contribution to $N_{\rm eff}$ can exceed the CMB bound [13]. This additionally rules out the hatched orange region shown in Figure 4.1 and 4.2. This constraint consequently puts an upper bound on $T_{\rm rh}$, since if $T_{\rm rh}$ is large the ϕ field decays

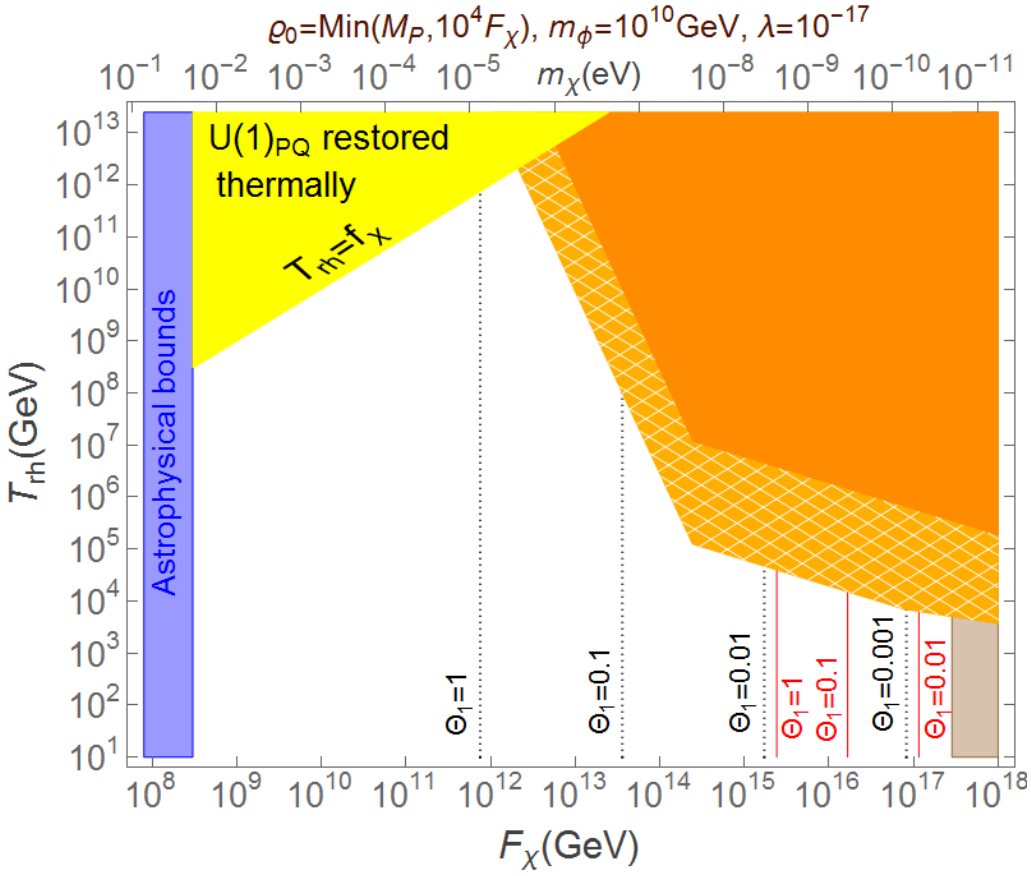

Figure 4.2: Same as Figure (4.1) but for $m_\phi = 10^{10}$ GeV and $\lambda = 10^{-17}$.

faster and the energy density of oscillating ϱ field becomes relatively large. With the help of Eqs. (4.38) and (4.44), the bound on the reheating temperature can be expressed as

$$T_{\rm rh} \lesssim 2.6\times10^{10}\,{\rm GeV}\left(\frac{g(T_{\rm rh})}{100}\right)^{-1/4}\left(\frac{\lambda}{10^{-11}}\right)^{-1/4}\left(\frac{\varrho_i}{M_{\rm P}}\right)^{-3}\left(\frac{H_{\rm inf}}{10^{13}\,{\rm GeV}}\right)^{2}\left(\frac{v_{\rm PQ}}{10^{15}\,{\rm GeV}}\right)^{-1/2}. \quad (4.46)$$

We also note that the duration of the oscillation of the ϱ field becomes long if the initial amplitude is large $\varrho_i \lesssim 10^4\, v_{\rm PQ}$, which enhances the constraint in the large F_χ region. Furthermore, if $H_{\rm inf}$ (or the energy density of ϕ) becomes small, the energy density of the SM plasma is reduced, which makes the abundance of ultra-relativistic axions relatively large. As a result, a stronger constraint is obtained for a smaller value of $m_\phi \approx H_{\rm inf}$, as shown in Figure 4.2. In Figs. 4.1 and 4.2,

we fix λ to the maximum allowed value $\lambda \lesssim H_{\rm inf}^2 M_{\rm P}^2/|S|_i^4$ given by Eq. (4.10). Note that, since the axion energy density is given by $\rho_\chi \propto v_{\rm PQ}^4 = (N_{\rm DW} F_\chi)^4$ [see Eq. (4.36)], for $N_{\rm DW} > 1$ our bound becomes even stronger. Furthermore, to obtain conservative bounds, we assumed that the Universe is dominated by matter during the reheating phase, i.e. the effective equation of state parameter, $\omega_{\rm eff} = 0$. If the Universe has an effective equation of state parameter $\omega_{\rm eff} > 0$ during the reheating phase, the axionic dark radiation bound would be even stronger.

4.6 Conclusion

The PQ mechanism presents a neat solution to the strong CP problem, and the angular field, the axion, can be a good DM candidate due to its largely suppressed couplings to all SM particles. However, axions being very light can also act as dark radiation if they are produced with large momenta at sufficiently late times. We showed that this could happen if the PQ radial field, ϱ, were displaced from $v_{\rm PQ}$ due to an initial condition or a direct coupling to the inflaton/moduli field. The perturbative decay of ϱ which we have discussed here happens when the PQ field oscillates coherently, during which most of the co-moving energy density stored in these coherent oscillations gets transferred into light axions. The energy density of axions which contribute to the radiation energy density is constrained by a number of observations listed above. The bound is mostly relevant to larger values of the axion decay constant.

Axion DM with a large decay constant are expected to be probed by future experimental studies such as CASPEr [346]. Since it is impossible to realise such a large PQ scale in the post-inflationary PQ symmetry breaking scenario [549], one should seriously consider the pre-inflationary PQ symmetry breaking scenario if axion DM were to be found in such experiments. We have seen that the cosmological evolution of the PQ field is quite non-trivial in such a scenario, and the overproduction of ultra-relativistic axions leads to an upper bound on the reheating temperature, which further constrains the thermal history of the Universe. Furthermore, one can also expect many ϕ fields to oscillate simultaneously, either

arising from inflation [550], or due to multi-moduli fields, whose effects can be discussed by following similar arguments developed in this chapter.

Chapter 5

Non-perturbative production of axion-like particles

Axion-like particles or ALPs (χ) are quite generic in many scenarios for physics beyond the SM. ALPs usually arise as the pseudoscalar Goldstone bosons associated with spontaneously broken global $U(1)$ symmetries [1]. Similar to the case of QCD axions [243, 245, 246], whose mass arises due to the non-perturbative QCD instantons [251, 252], ALPs gain their masses from various non-perturbative quantum effects such as world-sheet instantons [551] and brane instantons [552] in the context of string theory. The masses of ALPs could be large or small depending on the action of the instanton [258]. Due to the remnant shift symmetries, which themselves may get broken down to n-fold discrete symmetries by the quantum instanton effects, and apart form their anomalous coupling to gauge fields, ALPs couple only derivatively to other fields via operators of dimension-five or higher suppressed by the corresponding symmetry breaking scale (for a review, see [241]). Among the fields to which ALPs can couple are inflaton and moduli (see e.g. [524, 525, 553, 554, 555, 556, 557]) which act as scalar condensates (see e.g. [359]), and begin their coherent oscillations once their slow-roll conditions break down.

[1] A Nambu-Goldstone boson arises as massless excitation of the angular part of the complex scalar field whose VEV spontaneously breaks the $U(1)$ symmetry.

Due to their weak interaction with baryonic matter fields, ALPs can act as perfect DM candidates (for a review see e.g. [558]). Nevertheless, the decay of scalar condensate into ALPs can give rise to a non-thermal distribution of DM or dark radiation, depending on the mass of ALPs. One has to make sure that ALPs produced perturbatively/non-perturbatively match the current observation from the BBN [95], and the current CMB bound on DM and dark radiation abundances [13].

Although weakly interacting, ALPs can be produced non-perturbatively from the coherent oscillations of the homogeneous condensate of inflaton/moduli [1]. In this chapter, we study such production mechanism of ALPs via their derivative coupling to the scalar condensate. Let us denote χ as an ALP species with a mass m_χ, which couples to the scalar condensate, ϕ, via non-renormalisable operators suppressed by powers of the mass scale Λ. For the purpose of illustration, we fix the initial amplitude of the oscillations of the scalar condensate, Φ_i, to be $M_{\rm P}$, without loss of generality. As we show below what matters here is the ratio: Φ_i/Λ. The rate at which particle production takes place is sensitive to this value.

This chapter is structured as follows: in Section 5.1, we discuss the ALPs' interactions with a homogeneous scalar condensate, i.e. inflaton/moduli, their equation of motion and their energy density. In Section 5.2, we study the non-perturbative production of ALPs without and with expansion effects in the $\Phi_i \lesssim \Lambda$ regime. In Section 5.3, we study the excitation of light, $m_\chi < m_\phi$, and heavy, $m_\chi \gtrsim m_\phi$, ALPs in the regime $\Phi_i \gtrsim \Lambda$ while ignoring the effect of cosmic expansion in Section 5.3.1. We then repeat the analysis taking into account of the expansion effect in Section 5.3.2. Finally, we conclude this chapter in Section 5.4.

[1] Without loss of generality, we will not distinguish between inflaton and moduli since we are interested in particle production taking place once the inflaton/moduli field starts oscillating around its minimum. Nevertheless in the context of preheating after inflation, the strength of inflaton coupling to ALPs may be bounded due to the constraints on different observational signatures that may arise during inflation such as isocurvature perturbations [559, 560, 561], and non-Gaussianity [562, 563], and PBHs [564].

5.1 Interactions and equations of motion

Let us consider the following Lagrangian with derivative couplings of the form [1]:

$$\mathcal{L} = \frac{1}{2}\partial^{\mu}\phi\partial_{\mu}\phi - V(\phi) + \frac{1}{2}\partial^{\mu}\chi\partial_{\mu}\chi - \frac{1}{2}m_{\chi}^{2}\chi^{2} + \frac{1}{2\Lambda^{2}}\phi^{2}\partial^{\mu}\chi\partial_{\mu}\chi\,, \tag{5.1}$$

where ϕ is a scalar condensate of the inflaton/moduli, which sets its coherent oscillations around the minimum of the potential once the Hubble expansion rate drops below the mass of the scalar field or more generally when the slow-roll conditions of the scalar field breaks down. The stress-energy tensor for the Lagrangian under consideration is given by

$$\begin{aligned} T_{\mu\nu} =& \partial_{\mu}\phi\partial_{\nu}\phi - \frac{1}{2}g_{\mu\nu}[g^{\alpha\beta}\partial_{\alpha}\phi\partial_{\beta}\phi - V(\phi)] + \left(1+\frac{\phi^{2}}{\Lambda^{2}}\right)\left(\partial_{\mu}\chi\partial_{\nu}\chi - \frac{1}{2}g_{\mu\nu}g^{\alpha\beta}\partial_{\alpha}\chi\partial_{\beta}\chi\right) \\ &+ \frac{1}{2}g_{\mu\nu}m_{\chi}^{2}\chi^{2}\,. \end{aligned} \tag{5.2}$$

Assuming FLRW background, the energy density of the χ field can be written as

$$\rho_{\chi} = \frac{1}{2}\left(1+\frac{\phi^{2}}{\Lambda^{2}}\right)\left[\dot{\chi}^{2} + \frac{1}{a^{2}}(\nabla\chi)^{2}\right] + \frac{1}{2}m_{\chi}^{2}\chi^{2}\,, \tag{5.3}$$

where the pre-factor $(1+\phi^{2}/\Lambda^{2})$ exhibits an oscillatory behaviour with an amplitude which decays with the expansion of the Universe. When the amplitude of ϕ drops well below Λ, the oscillating part of this pre-factor, i.e. ϕ^{2}/Λ^{2}, can be ignored. Further, the equations of motion for ϕ and χ can respectively be expressed as

$$\Box\phi + 3H\dot{\phi} + \partial_{\phi}V(\phi) - \frac{\phi}{\Lambda^{2}}\partial^{\mu}\chi\partial_{\mu}\chi = 0 \tag{5.4}$$

$$\left(1+\frac{\phi^{2}}{\Lambda^{2}}\right)(\Box\chi + 3H\dot{\chi}) + \frac{2\phi}{\Lambda^{2}}\partial^{\mu}\phi\partial_{\mu}\chi + m_{\chi}^{2}\chi = 0\,. \tag{5.5}$$

[1] For the purpose of illustration, we consider only the dimension-six operator, $\phi^{2}\partial^{\mu}\chi\partial_{\mu}\chi/2\Lambda^{2}$, which is enough to capture the non-perturbative behaviour. Note that operators of odd order such as the dimension-five operator, $\phi\,\partial^{\mu}\chi\partial_{\mu}\chi/\Lambda$, may lead to ghost-like behaviour of χ as its kinetic term can oscillate to negative values if the initial amplitude of the scalar condensate oscillations is large, $\Phi_{i} > \Lambda$ [565].

For simplicity, we will assume that $V(\phi)$ is quadratic around its minimum [1]. In general, an effective quadratic minimum is quickly realised once the inflaton/moduli condensate starts oscillating. Thus, during the oscillation phase

$$V(\phi) \simeq \frac{1}{2} m_\phi^2 \phi^2 \,, \tag{5.6}$$

with $m_\phi = \partial^2 V/\partial\phi^2|_{\phi=o}$ being the inflaton/moduli mass where the minimum is taking to be at $\phi = 0$. Assuming that ϕ is a homogeneous condensate and ignoring the back-reactions, the equation of motion for ϕ, given by Eq. (5.4), during the oscillation phase can be re-written as

$$\ddot{\phi} + 3H\dot{\phi} + m_\phi^2 \phi \simeq 0 \,. \tag{5.7}$$

which admits the following solution:

$$\phi(t) \simeq \Phi(t) \sin(m_\phi t) \sim \frac{\Phi_i}{m_\phi t} \sin(m_\phi t) \,, \tag{5.8}$$

where $\Phi_i \sim M_{\rm P}$ is the initial amplitude of ϕ during the oscillation phase. Note that during the coherent oscillations, the average equation of state is that of the MD epoch and hence the Hubble expansion rate is given by: $H(t) \sim (2/3t)$. The equation of motion for the χ field, Eq. (5.5), can be re-written as

$$\Box\chi + \left(3H + \frac{2\phi\dot{\phi}/\Lambda^2}{1+\phi^2/\Lambda^2}\right)\dot{\chi} + \left(\frac{m_\chi^2}{1+\phi^2/\Lambda^2}\right)\chi = 0 \,. \tag{5.9}$$

Expanding χ in terms of Fourier modes, the energy density of a given mode would then be given by [see Eq. (5.3)]

$$\rho_k = \left(1 + \frac{\phi^2}{\Lambda^2}\right)\left[\frac{1}{2}|\dot{\chi}_k|^2 + \frac{1}{2}\omega_{k,\rm eff}^2 |\chi_k|^2\right] , \tag{5.10}$$

[1] One can relax this condition and have oscillations around any kind of potential, but for many examples, such as moduli oscillations, it is a fairly good approximation to consider coherent oscillations around a quadratic potential. A small deviation from a quadratic potential would not affect the physical outcome drastically, see [368].

where $\omega_{k,\rm eff}$, denoting the effective frequency of a χ_k oscillation, is given by

$$\omega_{k,\rm eff} = \left(\frac{k^2}{a^2} + \frac{m_\chi^2}{1+\phi^2/\Lambda^2}\right)^{1/2}. \tag{5.11}$$

For simplicity of the notation, we will use ω_k instead of $\omega_{k,\rm eff}$ to denote the effective frequency of the mode χ_k. In terms of ρ_k, the energy density of χ is given by

$$\rho_\chi = \frac{1}{2\pi^2}\int \mathrm{d}k\, k^2 \rho_k\,. \tag{5.12}$$

Further, the equation of motion for the χ field, Eq. (5.9), can be re-expressed as

$$\ddot{\chi}_k + [3H(t) + \alpha(t)]\dot{\chi}_k + \omega_k^2(t)\chi_k = 0\,, \tag{5.13}$$

Introducing the dimensionless measure of time $z = m_\phi t$, Eq. (5.13) can be re-written as

$$\chi_k'' + [3\tilde{H} + \tilde{\alpha}(z)]\chi_k' + \tilde{\omega}_k^2(z)\chi_k = 0\,, \tag{5.14}$$

where 'prime' denotes derivative w.r.t. z, and

$$\tilde{\alpha}(z) \equiv \frac{\alpha(t)}{m_\phi} = \frac{2\phi\phi'/\Lambda^2}{1+\phi^2/\Lambda^2} \simeq \frac{(\Phi^2/\Lambda^2)\sin(2z)}{1+(\Phi^2/\Lambda^2)\sin^2(z)}\,, \tag{5.15}$$

and

$$\tilde{\omega}_k^2(z) \equiv \frac{\omega_k^2(t)}{m_\phi^2} = \frac{k^2}{m_\phi^2 a^2} + \frac{m_\chi^2/m_\phi^2}{1+\phi^2/\Lambda^2} \simeq \frac{k^2}{m_\phi^2 a^2} + \frac{m_\chi^2/m_\phi^2}{1+(\Phi(z)^2/\Lambda^2)\sin^2(z)}\,. \tag{5.16}$$

are the oscillating part of the scaled damping coefficient and effective frequency squared, respectively. As we show below, the oscillating damping term leads to tachyonic instabilities which is important for particle production. Here $\tilde{H} \sim 2/(3z)$ and $\Phi \sim \Phi_i/z$. We now proceed to discuss the evolution of the dynamical system for two cases: $\Lambda \gtrsim \Phi_i$ and $\Lambda \lesssim \Phi_i$.

5.2 Excitation of ALPs when $\Lambda \gtrsim \Phi_i$

Let us first consider the case where $\Phi_i/\Lambda \lesssim 1$. Expanding $\tilde{\alpha}$ and $\tilde{\omega}_k^2$ (given by Eqs. (5.15) and (5.16), respectively) to first order in Φ^2/Λ^2, one obtains

$$\tilde{\alpha}(z) \simeq \frac{\Phi^2}{\Lambda^2}\sin(2z)\,, \tag{5.17}$$

and

$$\tilde{\omega}_k^2(z) \simeq \frac{k^2}{m_\phi^2 a^2} + \frac{m_\chi^2}{m_\phi^2}\left(1 - \frac{\Phi^2}{2\Lambda^2}\right) + \frac{m_\chi^2}{m_\phi^2}\frac{\Phi^2}{2\Lambda^2}\cos(2z)\,. \tag{5.18}$$

Let us for now ignore the effect of cosmic expansion, i.e. by setting $a(z) = 1$, and consequently $\tilde{H}(z) = 0$ and $\Phi(z) = \Phi_i$. Further, introduce the following transformation:

$$\chi_k \equiv \mathcal{X}_k(z)U(z) = \mathcal{X}_k(z)\exp\left[-\int_{z_i}^{z}\frac{\tilde{\alpha}(\tilde{z})}{2}\mathrm{d}\tilde{z}\right]^{1}, \tag{5.19}$$

Eq. (5.14) can be recast into the form

$$\mathcal{X}_k'' + \left[A_k - \frac{p^2}{2} - 2(p+q)\cos(2z) + \frac{p^2}{2}\cos(4z)\right]\mathcal{X}_k = 0\,, \tag{5.20}$$

where

$$A_k = \frac{k^2}{m_\phi^2} + \frac{m_\chi^2}{m_\phi^2}\left(1 - \frac{\Phi^2}{2\Lambda^2}\right), \tag{5.21}$$

and

$$p = \frac{\Phi^2}{2\Lambda} \lesssim \frac{1}{2}, \qquad q = \frac{\Phi^2}{4\Lambda^2}\frac{m_\chi^2}{m_\phi^2} \lesssim \frac{1}{4}\frac{m_\chi^2}{m_\phi^2}. \tag{5.22}$$

[1]The function $U(z) = \exp\left[-\int_{z_i}^{z}\{\tilde{\alpha}(\tilde{z})/2\}\mathrm{d}\tilde{z}\right]$ can be easily integrated to hold $U(z) = \exp[(\Phi^2/4\Lambda^2)\{\cos(2z) - \cos(2z_i)\}]$. This is a purely periodic function with a period π and hence it has no contribution to the possible growth of χ_k. Further, upon the inclusion of the expansion effect, Φ decays as z^{-1} and hence such oscillatory behaviour goes away within a few oscillations of ϕ. We also note that $U(z)$ is independent of both k and m_χ.

Eq. (5.20) is a specific case of Hill's equation [566] with two harmonics known as the Whittaker-Hill equation [567] [1]. In principle one should include higher orders in Φ^2/Λ^2 from the Taylor expansions of $\tilde{\alpha}$ and $\tilde{\omega}_k^2$ which would result in the presence of higher harmonics. Note that in the absence of the $\cos(4z)$ term, Eq. (5.20) reduces to a simpler form of Hill's equation known as the Mathieu equation [569, 570]. Using the Floquet theorem, Hill's equation (including Whittaker-Hill and Mathieu forms) admits a solution of the form

$$\mathcal{X}_k = C_1 f(z) e^{\mu z} + C_2 f(-z) e^{-\mu z} \tag{5.23}$$

where C_1 and C_2 are real constants, $f(z)$ is a periodic function with a period π, and μ is known as the Floquet exponent which, in general, is complex. The real part of the Floquet exponent, $\Re e(\mu)$, characterises the instabilities of Hill's equation. Focusing on the special cases of Mathieu and Whittaker-Hill equations, the instability bands of the latter is broader and consequently $\Re e(\mu)$ is larger provided that $p = \Phi^2/2\Lambda^2 \gtrsim 1$. For the case under consideration $p \lesssim \frac{1}{2}$. Moreover, including the expansion effect, the amplitude of ϕ oscillations, Φ, drops to 0.1–0.2 of its initial value within only one oscillation (see Chapter 3 and [364]) rendering the coefficients of the $\cos(4z)$ term and higher harmonics negligibly small compared to that of the leading harmonic. Therefore, for simplicity, we will consider only the leading harmonic, in which case Eq. (5.20) simplifies to the following Mathieu equation:

$$\mathcal{X}_k'' + \Omega_k^2 \mathcal{X}_k = \mathcal{X}_k'' + [\tilde{A}_k - 2\tilde{q}\cos(2z)]\mathcal{X}_k = 0\,, \tag{5.24}$$

where

$$\tilde{A}_k = \frac{k^2}{m_\phi^2} + \frac{m_\chi^2}{m_\phi^2}\left(1 - \frac{\Phi^2}{2\Lambda^2}\right) - \frac{\Phi^4}{8\Lambda^4}, \tag{5.25}$$

and

[1] For analysis of the instabilities of Whittaker-Hill equation see [568].

$$\tilde{q} = \frac{\Phi^2}{2\Lambda^2}\left(1+\frac{m_\chi^2}{2m_\phi^2}\right) \lesssim \frac{1}{2}\left(1+\frac{m_\chi^2}{2m_\phi^2}\right). \tag{5.26}$$

The parameters $\tilde{A}_k$ and $\tilde{q}$ are related by

$$\tilde{A}_k = k^2 + 2\tilde{q}\left(\frac{2\Lambda^2}{\Phi^2}-1\right) - 2\left(1-\frac{\Phi^2}{4\Lambda^2}\right)^2. \tag{5.27}$$

In Figure 5.1, we show the instability bands of the Mathieu equation in gray. Here, the brown line is for $\tilde{A}_k = 2\tilde{q}$ below which the $\mathcal{X}_k$-modes (consequently those of χ_k) become tachyonic. We show the allowed values of the parameters, given by Eq. (5.27), for $\Phi_i/\Lambda = 0.2, 0.5$ and 1 by the red, blue, and black lines, respectively; the solid lines are for $k \ll m_\phi$, the dashed lines are for $k = m_\phi$ and the dotted lines are for $k = 3m_\phi$ [1]. We note that there are *tachyonic* instabilities induced by the oscillating damping term when

$$\frac{k}{m_\phi} < \frac{\Phi}{\Lambda}\left(1+\frac{\Phi^2}{8\Lambda^2}\right)^{1/2} \lesssim 1 \qquad \text{if} \quad k \gg m_\chi \tag{5.28}$$

or

$$\frac{m_\chi}{m_\phi} < \frac{\Phi}{\Lambda}\left[\frac{1+(\Phi^2/8\Lambda^2)}{1-(\Phi^2/\Lambda^2)}\right]^{1/2} \qquad \text{if} \quad k \ll m_\chi \text{ [2]}. \tag{5.29}$$

These tachyonic events take place at

$$N_\phi\pi - \tilde{z}_k < z < N_\phi\pi + \tilde{z}_k\,,$$

where $\tilde{z}_k = \frac{1}{2}\cos^{-1}(\tilde{A}_k/2\tilde{q})$ and $N_\phi = 0, 1, 2, \ldots$ is the number of ϕ oscillations since the beginning of the oscillation phase. Using the WKB approximation, one can estimate the growth rate of χ_k after N_ϕ oscillations by

$$\chi_k \propto \mathcal{X}_k \propto e^{2N_\phi\beta_k}\,, \tag{5.30}$$

[1] Note that the instability bands for the case $\Phi_i/\Lambda = 1$ (i.e. $p = \frac{1}{2}$) should be a bit broader due to the effect of higher harmonics (see e.g. [571]).

[2] There would be no tachyonic instabilities had the oscillating damping term been absent in which case the squared frequency of oscillation would be given by Eq. (5.16) which is always positive.

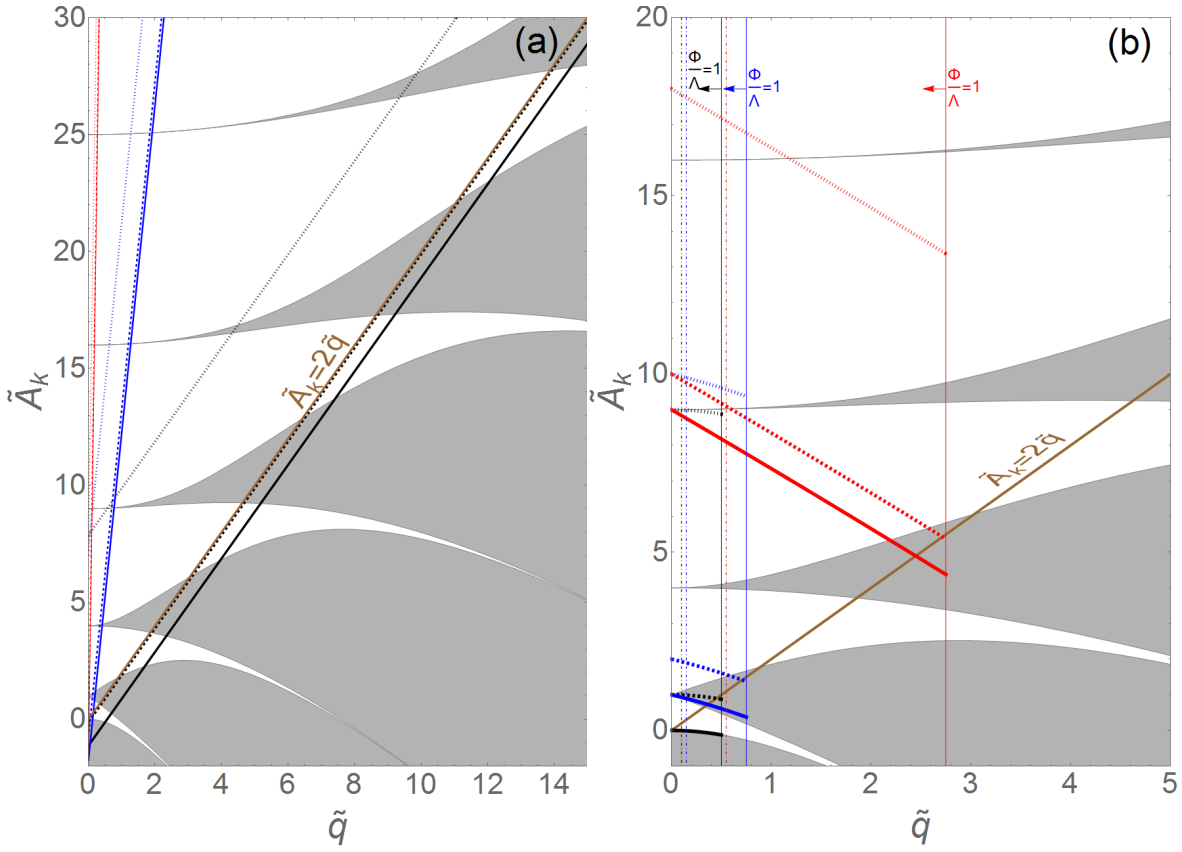

(a) (b)

Figure 5.1: The instability bands of the Mathieu equation, Eq. (5.24), are shown in gray. **(a)** The brown line $\tilde{A}_k = 2\tilde{q}$ indicates the lower limit below which tachyonic instabilities may exist. The red, blue and black line show the allowed values of the parameters for $\Phi/\Lambda = 0.2, 0.5$ and 1, respectively. Here the solid, dashed and dotted lines corresponds to $k/m_\phi \ll 1$, $k/m_\phi = 1$ and $k/m_\phi = 3$, respectively. **(b)** The black, blue and red solid curves show the allowed values of the parameters for $m_\chi \ll m_\phi$, $m_\chi = m_\phi$ and $m_\chi = 3m_\phi$, respectively. Again, the thick solid, dashed and dotted curves corresponds to $k/m_\phi \ll 1$, $k/m_\phi = 1$ and $k/m_\phi = 3$, respectively. The thin, solid, vertical lines correspond to $\Phi_i/\Lambda = 1$ whereas the dot-dashed ones correspond to $\Phi_i/\Lambda = 0.2$. Clearly, for $k \lesssim m_\phi$, the $\mathcal{X}_k$-modes (and consequently χ_k-modes) can become tachyonic provided that Φ_i/Λ is very close to unity.

where the factor 2 in the exponent is due to $\mathcal{X}_k$ (or χ_k) becoming tachyonic twice during each ϕ oscillation. Here

$$\beta_k = \int_{\pi-\tilde{z}_k}^{\pi+\tilde{z}_k} \sqrt{-\Omega_k^2}\, \mathrm{d}z = 2\,(2\tilde{q} - \tilde{A}_k)^{1/2} E\left(\tilde{z}_k; \frac{4\tilde{q}}{2\tilde{q} - \tilde{A}_k}\right), \tag{5.31}$$

with $E(\theta;l) = \int_0^\theta (1-l^2\sin^2\tilde{\theta})^{1/2}\,\mathrm{d}\tilde{\theta}$ being the incomplete elliptic integral of the second kind where $\theta < \pi/2$ and $0 < l^2 < 1$ [572]. The exponent β_k can be approximated by [573]

$$\beta_k = -\frac{x}{\sqrt{q}}\tilde{A}_k + 2x\sqrt{\tilde{q}} < \frac{1.35 - 1.20(k^2/m_\phi^2)}{[1+(m_\chi^2/2m_\phi^2)]^{1/2}}\,, \tag{5.32}$$

where $x = \frac{\sqrt{\pi}}{2\sqrt{2}}\frac{\Gamma(3/4)}{\Gamma(5/4)} \simeq 0.85$ with $\Gamma(z)$ being the gamma function. It is clear from Eq. (5.32) that there are no tachyonic instabilities for $k \gtrsim m_\phi$ [see also Eq. (5.28) and Figure 5.1]. It is also clear that the tachyonic growth is most efficient for modes with $m_\chi \ll m_\phi$. In Figure (5.2), we show the growth of $\mathcal{X}_k$ for $k, m_\chi \ll m_\phi$, normalised to the initial value, due to the tachyonic instabilities. The characteristic exponent β_k for $\Phi_i/\Lambda = 0.2$ is given by

$$\beta_k = \frac{0.24 - 6.00(k^2/m_\phi^2) - 5.75(m_\chi^2/m_\phi^2)}{[1+(m_\chi^2/2m_\phi^2)]^{1/2}}\,. \tag{5.33}$$

which is significantly smaller than when Φ_i/Λ is close to unity. Thus, the growth rate, in this case, is much slower than the case when Φ_i/Λ is close to unity (see also Figure 5.2) [1]. It is also clear from Eq. (5.33) that only modes with $k, m_\chi \ll m_\phi$ can become tachyonic in this case [see also Eq. (5.29) and Figure 5.1].

Let us now consider the *parametric* resonance which may occur for $k \gtrsim m_\phi$ [see Eq. (5.28)], or $m_\chi \gtrsim m_\phi$ when Φ_i/Λ is smaller than unity [see Eq. (5.29)]. For simplicity, we split the the parameter space into two regions: (1) $\tilde{q} < 1$ and (2) $\tilde{q} \geq 1$.

(1) When $\tilde{q} < 1$: This is known as the *narrow* resonance regime and takes place when $m_\chi/m_\phi < \{2[(2\Lambda^2/\Phi^2) - 1]\}^{1/2}$. In this regime, the first instability band is the most important one. For simplicity, let us consider two cases (a) $k > m_\chi$ and (b) $k < m_\chi$.

- Case (a): when $k > m_\chi$. A $\mathcal{X}_k$-mode enters the first instability band if

[1] We note that for small values of Φ/Λ, the analytical expressions Eqs. (5.31) and (5.33) overestimate the growth rate of $\mathcal{X}_k$. This is because the WKB approximation is only accurate for $A_k < 2q - 2\sqrt{q}$ (see e.g. [573]).

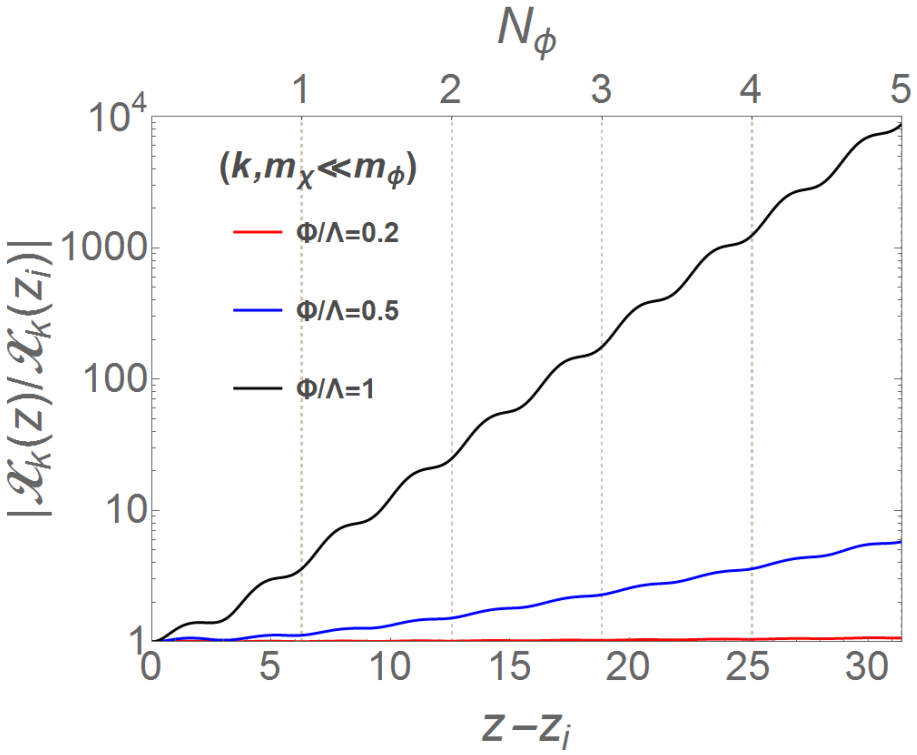

Figure 5.2: The tachyonic growth of $\mathcal{X}_k$ for $k, m_\chi \ll m_\phi$ during the first five ϕ oscillations while ignoring the effect of expansion. Here N_ϕ denotes the number of ϕ oscillations since the commencement of the oscillation phase. Here the red, blue and black curves are for $\Phi_i/\Lambda = 0.2, 0.5$ and 1, respectively.

$1-\tilde{q} \lesssim \tilde{A}_k \lesssim 1+\tilde{q}$ [569], i.e.

$$\left[1 - \frac{\Phi^2}{2\Lambda^2}\right]^{1/2} \lesssim \frac{k}{m_\phi} \lesssim \left[1 + \frac{\Phi^2}{2\Lambda^2}\right]^{1/2}, \tag{5.34}$$

which results in the parametric amplification of $\mathcal{X}_k$ (or χ_k) for $m_\chi < m_\phi$. The real part of the Floquet exponent for the first instability band is given by $\Re e(\mu_k) = \frac{1}{2}\sqrt{\tilde{A}_k^2 - (\tilde{q}-1)^2}$ [569]. For the case at hand, $\mu_k \lesssim 0.4$. Further, the parametric resonance occurs twice per each ϕ oscillation; hence the growth of $\mathcal{X}_k$ (or χ_k) after N_ϕ oscillations can be estimated by

$$\chi_k \propto \mathcal{X}_k \propto e^{2N_\phi \Re e(\mu_k)\Delta z} \lesssim (2.23)^{N_\phi}, \tag{5.35}$$

where $\Delta z \lesssim 1$ is the time a $\mathcal{X}_k$-mode spends in the resonance band. In Figure 5.3, we show the parametric amplification of $\mathcal{X}_k$, normalised to the initial value, for $k = m_\phi \gg m_\chi$, and $\Phi_i/\Lambda = 0.2$ and 1 by the red and black curves, respectively.

- Case (b): when $k < m_\chi$. In this case, $\mathcal{X}_k$-modes with

$$\left[\frac{1-(\Phi^2/2\Lambda^2)}{1-(\Phi^2/4\Lambda^2)}\right]^{1/2} \lesssim \frac{m_\chi}{m_\phi} \lesssim \left[\frac{1+(\Phi^2/2\Lambda^2)}{1-(3\Phi^2/4\Lambda^2)}\right]^{1/2}, \tag{5.36}$$

and $k < m_\phi$ enters the first resonance band. The real part of the Floquet exponent characterising the growth rate can be estimated to be $\Re e(\mu) \lesssim 0.5$. Thus, after N_ϕ oscillations, the growth rate of $\mathcal{X}_k$ (or χ_k) is given by

$$\chi_k \propto \mathcal{X}_k \propto e^{2N_\phi \Re e(\mu_k)\Delta z} \lesssim (2.80)^{N_\phi}\,. \tag{5.37}$$

(1) When $\tilde{q} \geq 1$: This takes place when $m_\chi/m_\phi \geq \{2[(2\Lambda^2/\Phi^2)-1]\}^{1/2}$ in which case $\tilde{q} \simeq (\Phi^2/2\Lambda^2)(m_\chi^2/2m_\phi^2)$. As can be seen from Figure 5.1(a), in this regime the resonant amplification of $\mathcal{X}_k$ can occur in instability bands beyond the first one depending on the values of $\tilde{A}_k$, $\tilde{q}$ and Φ/Λ (or k, m_χ and Φ/Λ). Nevertheless, the resonance still takes place in narrow bands. This is clear from Eqs. (5.26) and (5.27), and Figure 5.1. Changing m_χ, both $\tilde{A}_k$ and $\tilde{q}$ change (since $\tilde{A}_k$ and $\tilde{q}$ are proportional to m_χ^2); as a result, the dynamical system gets pushed out of the resonance band if it was initially in a one. More explicitly, for a given m_χ, the parametric amplification of $\mathcal{X}_k$ takes place in a narrow momentum range. For instance, when $m_\chi \simeq 14.07\, m_\phi$ and $\Phi_i/\Lambda = 1$ (i.e. $\tilde{q} = 50$), the parametric resonance takes place in a part of the eighth band, $\tilde{A}_k \simeq 100.1$–102.5, or equivalently $k \simeq (1.1\text{–}1.9)\, m_\phi$. In Figure 5.5, we show the parametric growth of the $\mathcal{X}_k$-mode with $m_\chi = 14.07\, m_\phi$ and $k = 1.1\, m_\phi$ for $\Phi = 0.2$ and 1 by the red and black curves, respectively. Nevertheless, the resonance can occur for a wide range of momenta provided that Φ_i/Λ is a bit smaller than unity. For example, when $m_\chi \simeq 13.78\, m_\phi$ and $\Phi_i/\Lambda = 0.99$ (i.e. $\tilde{q} = 47$), the parametric resonance occurs for modes with $0 \leq k/m_\phi \lesssim 1.7$; see Figure 5.6.

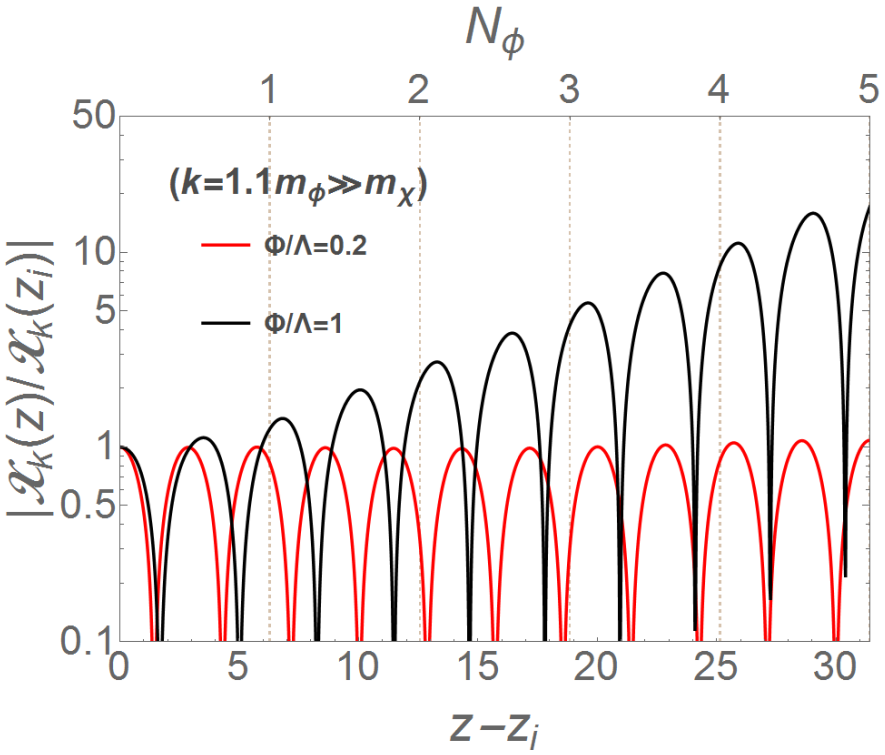

Figure 5.3: The parametric growth of $\mathcal{X}_k$-mode with $k = 1.1\, m_\phi \gg m_\chi$ during the first five ϕ oscillations while ignoring the effect of expansion. Here the red and black curves are for $\Phi_i/\Lambda = 0.2$ and 1, respectively.

Taking into account cosmic expansion: Let us now include the effect of expansion of the Universe. In this case, the amplitude of ϕ oscillations, Φ, dies out with time. In fact, Φ drops to roughly 0.1–0.2 of its initial value after the first oscillation. One can see from Figure 5.1, that all resonant modes are pushed to the narrow tips of the resonance bands rendering the parametric amplification of $\mathcal{X}_k$ totally inefficient after only one ϕ oscillation. This can be easily seen from Figures 5.1, 5.3, 5.4, 5.5 and 5.6. Similarly, all tachyonic modes, except modes with $k, m_\chi \ll m_\phi$, are pushed out of the tachyonic region within only one ϕ oscillation. Further, the characteristic exponent for the tachyonic mode with $k, m_\chi \ll m_\phi$ becomes significantly smaller after the first ϕ oscillation [see Eq. (5.33)]. It becomes even smaller in the subsequent ϕ oscillations rendering the tachyonic growth of these modes inefficient. One can see from Figure 5.2, that the tachyonic growth of modes with $k, m_\chi \ll m_\phi$ becomes completely inefficient

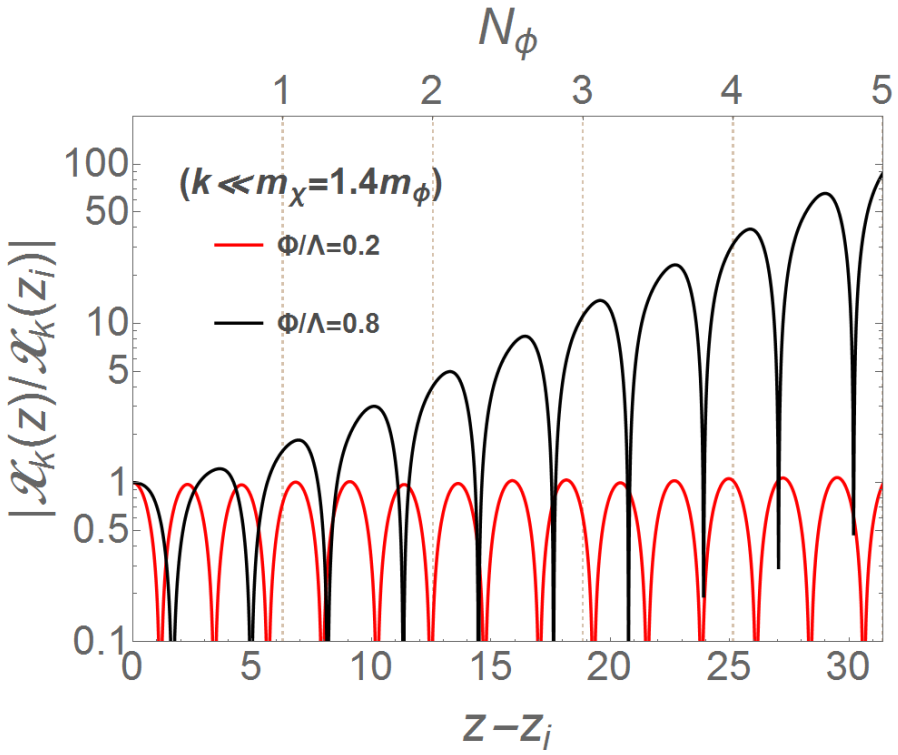

Figure 5.4: The parametric growth of $\mathcal{X}_k$ for $k \ll m_\chi = 1.4\, m_\phi$ during the first five ϕ oscillations while ignoring the effect of expansion. Here the red and black curves are for $\Phi_i/\Lambda = 0.2$ and 0.8, respectively.

after the first ϕ oscillation. This is also the case for all other tachyonic modes. Taking into account the redshift of $\mathcal{X}_k$ (or χ_k), one can see that any amplification of $\mathcal{X}_k$ (or equivalently χ_k), that may take place during the first ϕ oscillation, will go away with time.

To conclude this section, one can safely state that for $\Lambda \gtrsim \Phi_i$ there is no significant amplification of χ_k. In other words, there is no significant non-perturbative particle production of χ quanta in this case. The decay from the ϕ condensate to χ quanta will be primarily perturbative (see e.g. [524]).

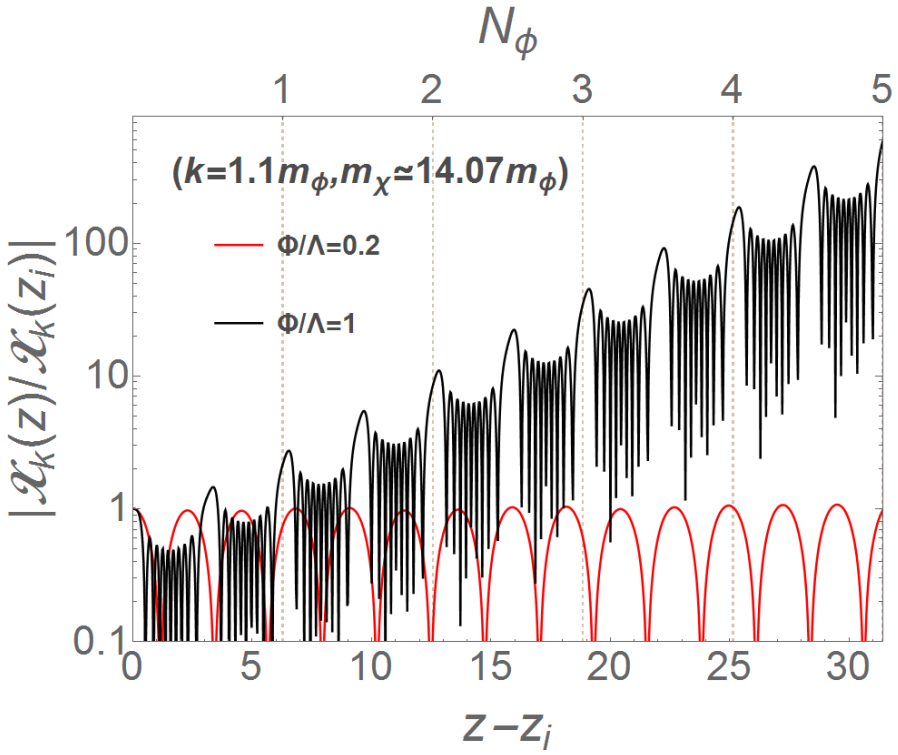

Figure 5.5: The parametric growth of $\mathcal{X}_k$ for $m_\chi \simeq 14.07\ m_\phi$ and $k = 1.1\, m_\phi$ during the first five ϕ oscillations. Here the red and black curves are for $\Phi_i/\Lambda = 0.2$ and 1, respectively.

5.3 Excitation of ALPs when $\Lambda \lesssim \Phi_i$

Now, let us consider the case when $\Phi_i/\Lambda \gtrsim 1$. For convenience, let us make a transformation of the form of Eq. (5.19) [1]. As a result, Eq. (5.14) becomes

$$\mathcal{X}_k'' + 3\tilde{H}\mathcal{X}_k' + \Omega_k^2\ \mathcal{X}_k = 0\,, \tag{5.38}$$

[1] Again, we show below that $U(z) = \exp\left[-\int_{z_i}^{z} \frac{\tilde{\alpha}(\tilde{z})}{2} \mathrm{d}\tilde{z}\right]$ is merely an oscillating function and has no contribution to the possible growth of χ_k.

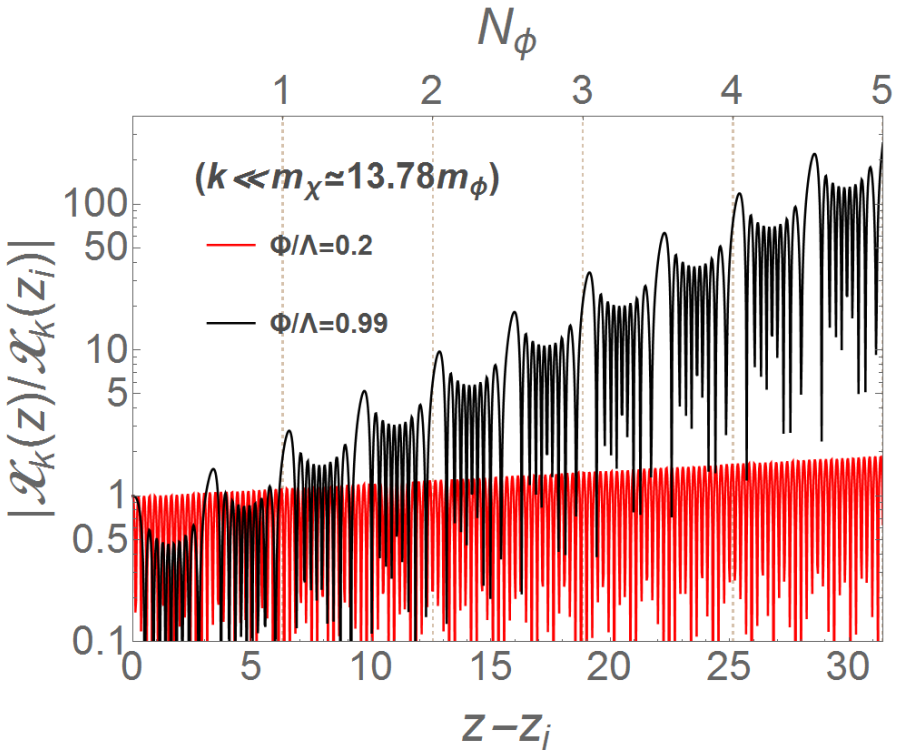

Figure 5.6: The parametric growth of $\mathcal{X}_k$ for $k \ll m_\chi \simeq 13.78\, m_\phi$ during the first five ϕ oscillations. Here the red and black curves are for $\Phi_i/\Lambda = 0.2$ and 0.99, respectively.

with

$$\begin{aligned}\Omega_k^2 =& \frac{k^2}{m_\phi^2 a^2} + \frac{(m_\chi^2/m_\phi^2) - (\phi\phi'' + \phi'^2 + 3\tilde{H}\phi\phi')/\Lambda^2}{(1+\phi^2/\Lambda^2)} + \frac{(\phi\phi'/\Lambda^2)^2}{(1+\phi^2/\Lambda^2)^2} \\ \simeq& \frac{k^2}{m_\phi^2 a^2} + \frac{(m_\chi^2/m_\phi^2) - (\Phi^2/\Lambda^2)\cos(2z) - (3\Phi^2/2\Lambda^2)\tilde{H}\sin(2z)}{[1+(\Phi^2/\Lambda^2)\sin^2(z)]} \\ &+ \frac{(\Phi^4/4\Lambda^4)\sin^2(2z)}{[1+(\Phi^2/\Lambda^2)\sin^2(z)]^2}\,,\end{aligned} \tag{5.39}$$

being the square of the scaled frequency of the $\mathcal{X}_k$ oscillation.

5.3.1 Non-perturbative excitations of ALPs, ignoring cosmic expansion

Let us first discuss the non-perturbative amplification of $\mathcal{X}_k$ (equivalently, χ_k) for the case $\Phi_i/\Lambda \gtrsim 1$ while ignoring the effect of expansion. In this case, Eq. (5.38) simplifies to

$$\mathcal{X}_k'' + \Omega_k^2 \, \mathcal{X}_k = 0 \,, \tag{5.40}$$

and the frequency of the $\mathcal{X}_k$ oscillation, Eq. (5.39), now reads

$$\Omega_k^2 \simeq \frac{k^2}{m_\phi^2} + \frac{(m_\chi^2/m_\phi^2) - (\Phi^2/\Lambda^2)\cos(2z)}{[1 + (\Phi^2/\Lambda^2)\sin^2(z)]} + \frac{(\Phi^4/4\Lambda^4)\sin^2(2z)}{[1 + (\Phi^2/\Lambda^2)\sin^2(z)]^2} \,. \tag{5.41}$$

Figure 5.7 shows the time behaviour of the scaled squared frequency, Ω_k^2 for modes with $k = 3m_\phi \gg m_\chi$ (left panel) and $m_\chi = 3m_\phi \gg k$ (right panel) for $\Phi_i/\Lambda = 20$. Moreover, the exponential part of Eq. (5.19), $U(z)$, can now be easily evaluated to obtain

$$\begin{aligned} U(z) =& \exp\left[-\int_{z_i}^{z} \frac{\tilde{\alpha}(\tilde{z})}{2} \mathrm{d}\tilde{z}\right] = \exp\left[-\frac{1}{2}\int_{z_I}^{z} \frac{(\Phi^2/\Lambda^2)\sin(2z)}{1 + (\Phi^2/\Lambda^2)\sin^2(z)} d\tilde{z}\right] \\ =& \frac{[1 + (\Phi^2/2\Lambda^2)\cos(2z_i)]^{1/2}}{[1 + (\Phi^2/2\Lambda^2)\cos(2z)]^{1/2}} \,, \end{aligned} \tag{5.42}$$

which is clearly a pure periodic function with a period π. Hence, it does not lead to any enhancement of χ_k. Moreover upon the inclusion of the expansion effect, Φ dies out with time and consequently such oscillatory behaviour goes away within a few ϕ oscillations. Note that $U(z)$ is independent of both k and m_χ. Let us now proceed to discuss the non-perturbative production mechanism for two mass regimes: (1) light ALPs with mass $m_\chi \ll m_\phi$ and (2) heavy ALPs with $m_\chi \gtrsim m_\phi$.

5.3.1.1 Non-perturbative production of light ALPs, $m_\chi \ll m_\phi$

One can see from Eq. (5.41), see also Figure 5.7(a), that modes with $k/m_\phi \lesssim \Phi/\Lambda$ becomes tachyonic during short time intervals, around $z = N_\phi \pi, \; N_\phi = 0, 1, 2, \cdots$.

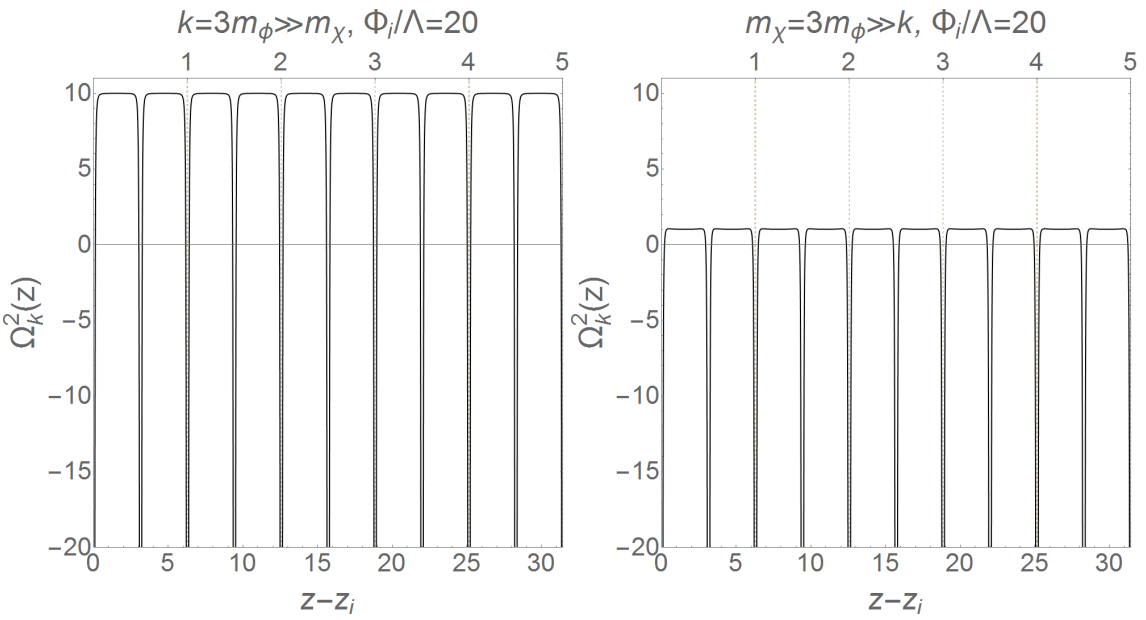

(a) (b)

Figure 5.7: The time evolution of Ω_k^2 for $k = 3m_\phi \gg m_\chi$ (left panel) and $m_\chi = 3m_\phi \gg k$ (right panel), where the effect of expansion is ignored. Here $\Phi_i/\Lambda = 20$. The Ω_k^2 becomes negative for two short periods of time during each oscillation of ϕ. The corresponding number of ϕ oscillations is shown on the upper horizontal axis.

More precisely, Ω_k^2 becomes negative during the time intervals, $\Delta z = z_+ - z_-$, where

$$z_\pm \simeq N_\phi \pi \pm \left\{ \left[\frac{\Phi^2}{\Lambda^2} \left(1 + \frac{k^2}{m_\phi^2} \right) \right]^{-1/4} - \left(\frac{1}{3} + \frac{k^2}{2m_\phi^2} \right) \left[\frac{\Phi^2}{\Lambda^2} \left(1 + \frac{k^2}{m_\phi^2} \right) \right]^{-3/4} \right\} . \quad (5.43)$$

This leads to *tachyonic* excitation of χ modes with momenta in the range $0 \leq k/m_\phi \lesssim \Phi/\Lambda$. We again note that these tachyonic instabilities are caused by the oscillating damping coefficient, Eq. (5.15). On the other hand, from Figure 5.7(a), one can see that Ω_k^2 sharply changes around $z = N_\phi \pi$, before it becomes negative. Hence, one would expect violation of the adiabaticity condition (i.e. $|\Omega_k'/\Omega_k^2|$ becomes $\gtrsim 1$) around the time intervals where $\Omega_k^2 < 0$. Indeed, this is the case provided that $k/m_\phi \lesssim \Phi/\Lambda$ [see Figure 5.8(a)]. More precisely, the adiabaticity

gets violated during the time intervals, $\Delta\tilde{z}_- = z_- - \tilde{z}_-$ and $\Delta\tilde{z}_+ = \tilde{z}_+ - z_+$, where

$$\tilde{z}_\pm \simeq N_\phi \pi \pm \left[\frac{m_\phi^3}{k^3}\frac{2\Lambda^2}{\Phi^2}\right]^{1/5} \tag{5.44}$$

and $z_\pm$ are given by Eq. (5.43). This leads to the *parametric* amplification of $\mathcal{X}_k$(or χ_k)-modes with momenta, $m_\phi \lesssim k \lesssim m_\phi\, \Phi/\Lambda$. It is important to note that the parametric enhancement of $\mathcal{X}_k$ (or χ_k) takes place only for very short time periods around the tachyonic dimples in Ω_k^2 [see Figures 5.7(a) and 5.8(a)]. In other words, both production mechanisms, tachyonic and parametric excitations, go side by side. In Figure (5.9), we show the time evolution of $\mathcal{X}_k$, normalised to the initial value, for $\Phi_i/\Lambda = 20$ and $k = 3m_\phi \gg m_\chi$, while ignoring the effect of expansion. One can see that $\mathcal{X}_k$ exhibits an oscillatory behaviour, except for short time intervals, where the aforementioned instabilities reside. During these time intervals, $\mathcal{X}_k$ increases rapidly to stabilize at a larger value after each period of instability. We also show $\rho_k(z)$, defined by Eq. (5.10), in Figure 5.10. Clearly, the growth rate is much larger than the case where $\Phi_i/\Lambda \lesssim 1$ (see Figures 5.2 and 5.3).

5.3.1.2 Non-perturbative production of heavy ALPs, $m_\chi \gtrsim m_\phi$

The perturbative production of ALPs with $m_\chi > m_\phi/2$ is kinematically forbidden. However, the excitation of such heavy particles can still take place during the coherent oscillations of ϕ condensate via non-perturbative effects. Similar to the case of light ALPs, Ω_k^2 becomes tachyonic for short time periods, around $z = N_\phi\pi,\ N_\phi = 0, 1, 2, \cdots$, provided that $k, m_\chi \lesssim m_\phi(\Phi/\Lambda)$ [see Eq. (5.41)]. This occurs twice per each oscillation of ϕ, see Eq. (5.41) and Figure 5.7(b). More precisely, $\Omega_k^2 < 0$ during the time intervals, $\Delta z = z_+ - z_-$ around $z = N_\phi\pi$, where

$$z_\pm = N_\phi\pi \pm \left(\frac{\Lambda}{\Phi}\right)^{1/2} - \left(\frac{1}{3} + \frac{m_\chi^2}{4m_\phi^2}\right)\left(\frac{\Lambda}{\Phi}\right)^{3/2} - \left(\frac{m_\chi^4}{32m_\phi^4} - \frac{m_\chi^2}{4m_\phi^2} - \frac{1}{20}\right)\left(\frac{\Lambda}{\Phi}\right)^{5/2} \tag{5.45}$$

for $k < m_\chi$ whereas for $k > m_\chi$, $z_\pm$ are given by Eq. (5.43). During these time periods, *tachyonic* amplification of $\mathcal{X}_k$-modes with momenta in the range $0 \leq$

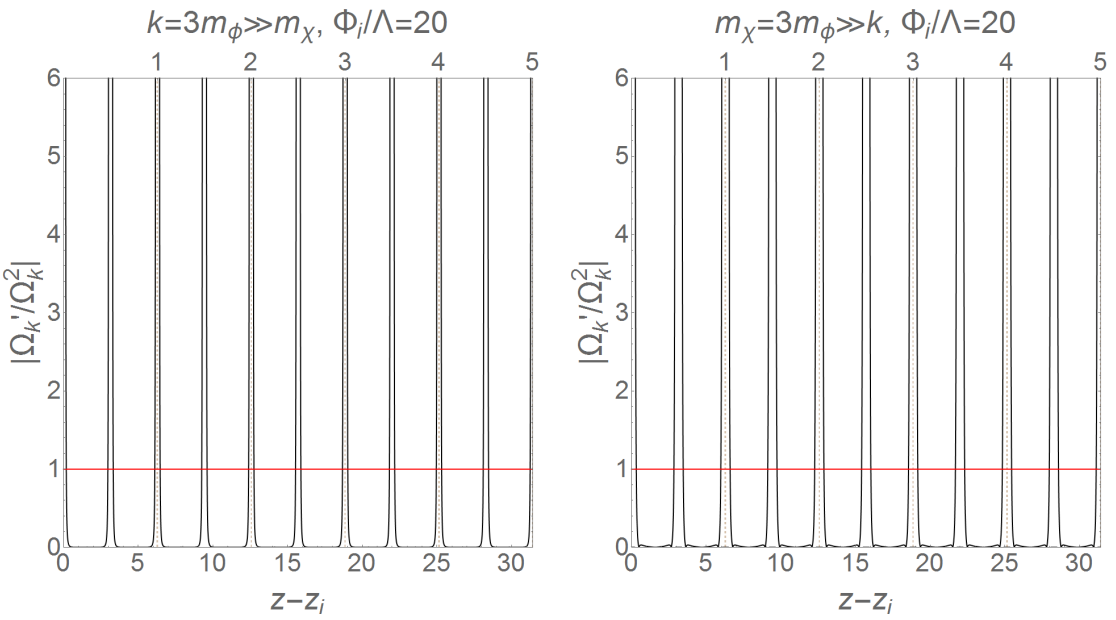

Figure 5.8: The time evolution of $|\Omega_k'/\Omega_k^2|$ for $k = 3\,m_\phi \gg m_\chi$ (left panel) and $m_\chi = 3\,m_\phi \gg k$ (right panel), where the effect of expansion is ignored. One can see easily that the adiabaticity gets violated around the time intervals where Ω_k^2 becomes tachyonic which takes place twice per each oscillation of ϕ. Here $\Phi_i/\Lambda = 20$.

$k \lesssim \Phi/\Lambda$ can take place. In Figure 5.7(b), we show the time evolution of Ω_k^2 for $\Phi_i/\Lambda = 20$, $m_\chi = 3\,m_\phi \gg k$ while ignoring the effect of expansion.

Moreover, around the time intervals of tachyonic instabilities mentioned above, Ω_k^2 for $\mathcal{X}_k$-modes with $m_\chi > k$ changes sharply. As a result, the evolution of Ω_k becomes non-adiabatic during short time intervals around the tachyonic dimples residing at $z = N_\phi \pi$ [see Figure 5.8(b)]. This leads to the parametric amplification of $\mathcal{X}_k$-modes with momenta in the range $0 \leq k \lesssim m_\chi$. Moreover, analogous to the case of light ALPs, tachyonic and parametric production of particles with $m_\chi \lesssim k \lesssim m_\phi\, \Phi/\Lambda$ is also possible. Therefore, during the short time intervals of parametric and tachyonic instabilities, heavy ALPs with momenta in the range $0 \leq k \lesssim m_\phi\, \Phi/\Lambda$ can be excited. In Figure 5.11, we show the time evolution of $\mathcal{X}_k$ for $m_\chi = 4\,m_\phi \gg k$ and $\Phi_i/\Lambda = 20$ while ignoring the effect of expansion. We also show ρ_k as a function of the dimensionless measure of time, z, in Figure 5.12. One can easily see that $\mathcal{X}_k$ (and ρ_k) gets largely enhanced at every interval of

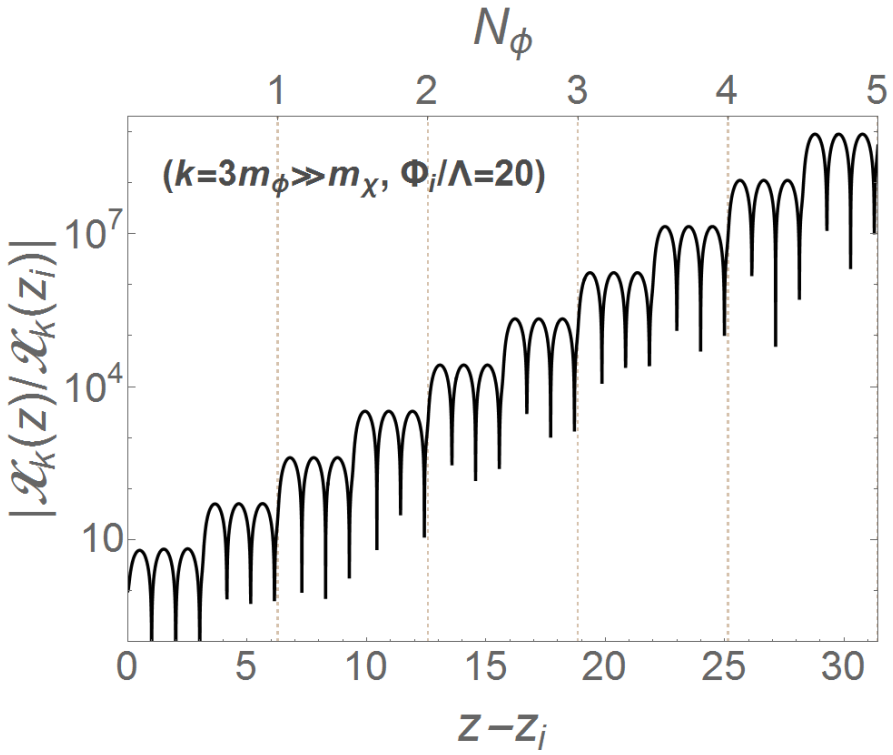

Figure 5.9: The time evolution of $\mathcal{X}_k$ for $\Phi_i/\Lambda = 20$ and $k = 3m_\phi \gg m_\chi$, where the effect of expansion is neglected.

instability taking place twice per each oscillation of ϕ. However, comparing this to Figures 5.9 and 5.10, one can see that the non-perturbative amplification of $\mathcal{X}_k$ modes (and ρ_k) with momenta, $k > m_\chi, m_\phi$ is more efficient than those with momenta, $k < m_\chi$ [1].

5.3.2 Non-perturbative excitations of ALPs, with expansion

Let us now include the effect of expansion. This results in lowering the ALPs production rate in two ways. First, the energy density of ALPs with a given momentum, ρ_k, dilutes with the expansion. This becomes obvious at late times

[1] The maximum amplification of $\mathcal{X}_k$ with $k > m_\chi$ happens for $k \sim m_\phi$ whereas for the case where $k < m_\chi$ the maximum amplification happens for $m_\chi \sim 8m_\phi$. We verify that the parametric excitation of ALPs is more efficient in the former case.

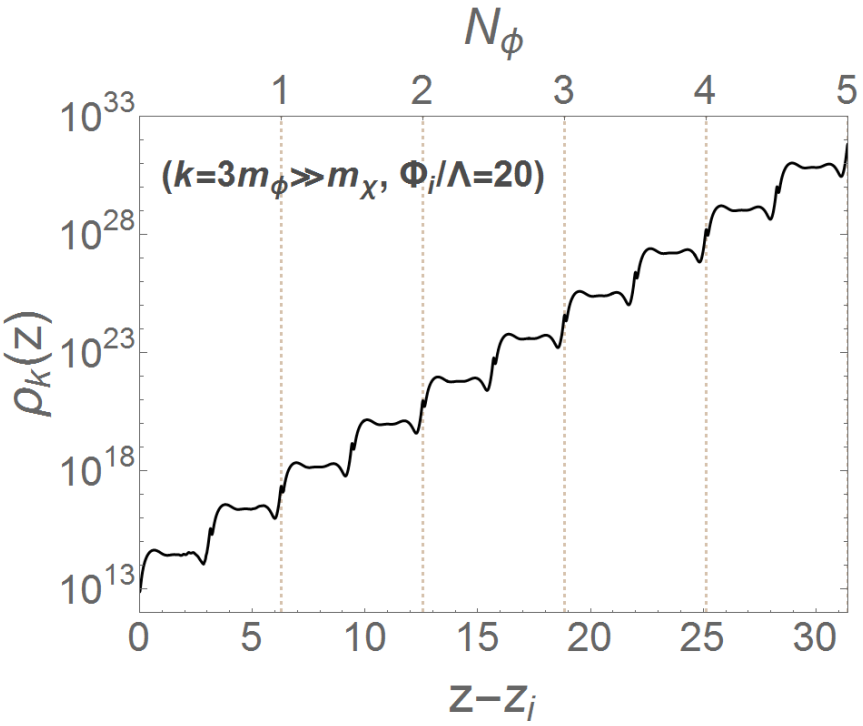

Figure 5.10: The time evolution of ρ_k for $\Phi_i/\Lambda = 20$ and $k = 3m_\phi \gg m_\chi$, where the effect of expansion is neglected.

where the excitation of χ_k quanta is less significant. Second, the amplitude of the ϕ oscillations dies out with expansion, $\Phi \propto a^{-3/2} \propto t^{-1}$, causing the tachyonic dimples in Ω_k^2 to become less and less deeper with time, see Figure 5.13. In the case of heavy ALPs ($m_\chi \gtrsim m_\phi$), these tachyonic dimples completely disappear within a very few ϕ oscillations. Therefore, one would expect that the non-perturbative excitation of χ quanta will cease being significant after a few oscillations of ϕ.

5.3.2.1 Non-perturbative production of light ALPs, $m_\chi \ll m_\phi$

We saw earlier that the non-perturbative production of light ALPs with $m_\chi \ll m_\phi$ is dominated by modes with momenta in the range $m_\phi \lesssim k \lesssim m_\phi \Phi/\Lambda$. For these modes and away from the tachyonic dimples, Ω_k^2 behaves as k^2/a^2, in which case it redshifts to lower values with the dimples keep being present, albeit becoming shallower, see Figure 5.13(a). As a result, the violation of adiabaticity due to the sharp change in Ω_k^2 on the sides of these dimples becomes more and more moderate

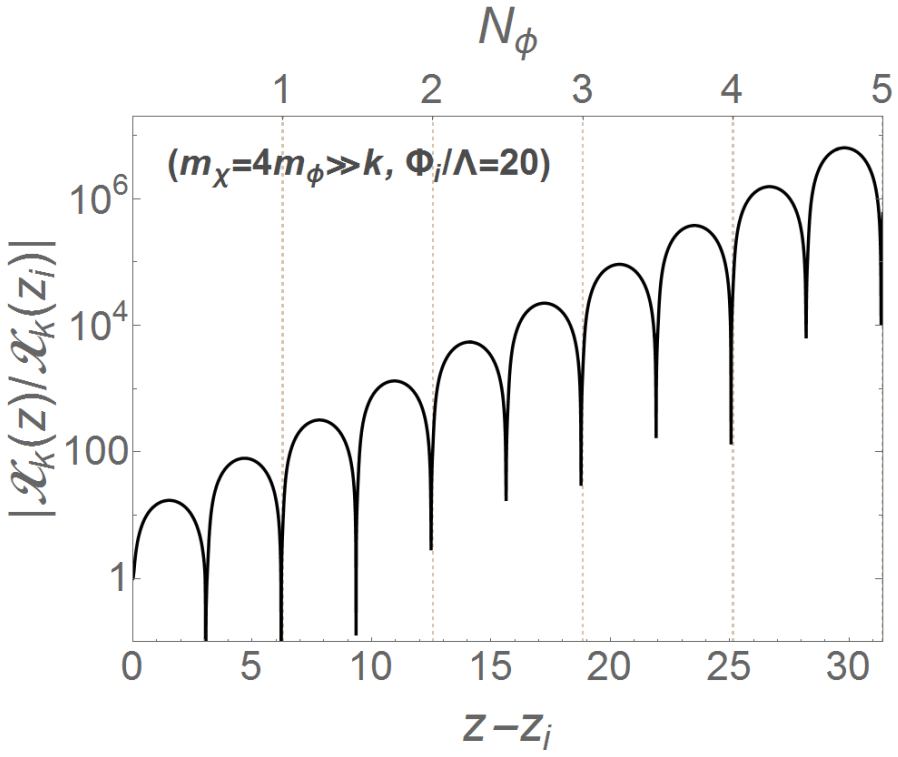

Figure 5.11: Same as Figure 5.9, but for $m_\chi = 4\, m_\phi \gg k$.

with time. Hence, the non-perturbative excitations of χ quanta becomes less and less efficient with time, until it is completely taken over by the expansion of the Universe. Nevertheless, as we shall see, one would still end up exciting a large abundance of ALPs even, in this case, provided that $\Phi_i/\Lambda \gg 1$. In Figure (5.14), we show the evolution of ρ_k for $\Phi_i/\Lambda = 20$ and $k = 2m_\phi \gg m_\chi$ taking into account the effect of expansion. One can see that the non-perturbative production of ALPs becomes insignificant within a few ϕ oscillations (roughly at the end of the third oscillation of ϕ in this case). Next, we calculate the energy density of the χ particles, defined by Eq. (5.12). For $\Phi_i/\Lambda = 20$, $m_\phi = 10^{13}$ GeV and $m_\chi \ll k$, we show the time evolution of $\rho_\chi/(\rho_{\phi,i} a^{-3})$ in Figure (5.15). In this case, a small portion of the condensate's energy (roughly 0.2%) gets transferred to the excitations of the χ field. However, when $\Phi_i/\Lambda \simeq 26$, most of the energy stored in the ϕ field can be drained in which case the problem becomes non-linear and full numerical simulation is needed. For smaller inflaton/moduli mass, the fraction of the condensate energy transferred as excitation of ALPs is less efficient

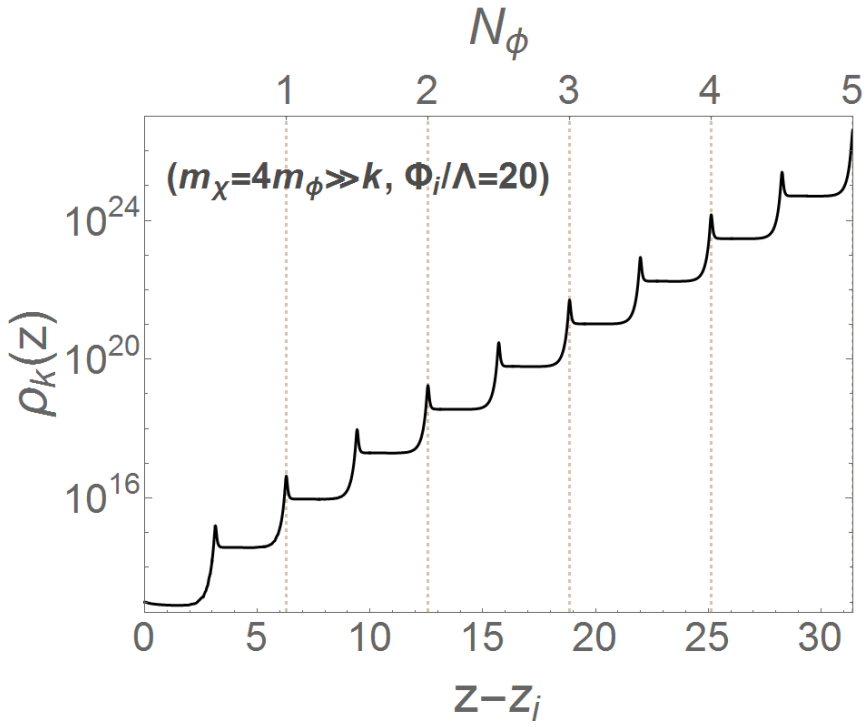

Figure 5.12: Same as Figure 5.10, but for $m_\chi = 4\, m_\phi \gg k$.

[roughly $\rho_\chi/(\rho_{\phi,i} a^{-3}) \propto m_\phi$]; see Figure 5.18 below. Hence, a larger value of Φ_i/Λ is required to drain a significant portion of the condensate's energy in the form of excitations of the χ field.

5.3.2.2 Non-perturbative production of heavy ALPs, $m_\chi \gtrsim m_\phi$

Let us now consider the effect of expansion on the non-perturbative production of heavy ALPs. We saw that the non-perturbative excitation of modes with $k, m_\phi < m_\chi$ is far less efficient than for modes with $m_\phi < m_\chi < k$, see Figures 5.10 and 5.12. Including the expansion effect, the difference in efficiency between the two cases becomes even more pronounced for the following reason: as the amplitude of ϕ oscillations decays with time, Ω_k^2 behaves differently for $k > m_\chi$ and $k < m_\chi$. For the former case Ω_k^2 tends toward smaller values with the tachyonic dimples in Ω_k^2 keep being present, albeit becoming shallower and the violation of the adiabaticity condition on the sides of these dimples becomes milder with time, see Figure 5.13(a). On the other hand, for $k < m_\chi$, Ω_k^2 tends toward

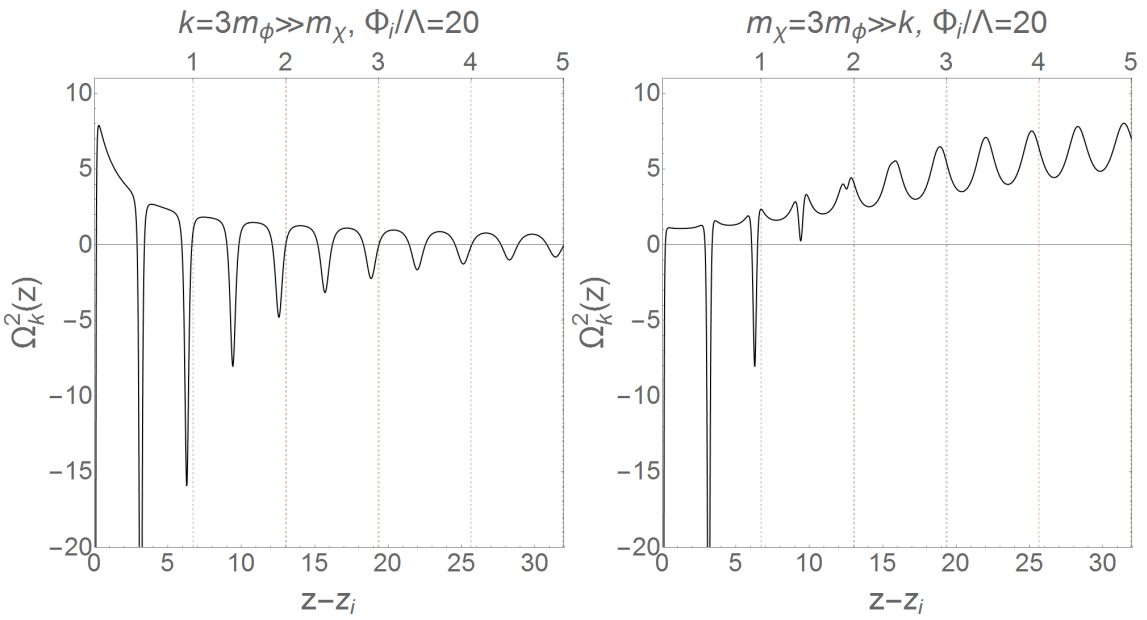

Figure 5.13: Same as Figure 5.7, but now the cosmic expansion is included. Clearly, the tachyonic dimples become shallower with time. They even go away completely within a very few ϕ oscillations for the case of heavy ALPs.

larger positive values, i.e. toward its maximum value which is m_χ^2. Thus, the tachyonic dimples, which are becoming shallower with time, disappear in a very few ϕ oscillations; see Figure 5.13(b). Consequently, after a few ϕ oscillations, the adiabaticity condition is no longer violated. Therefore, one would expect that the non-perturbative excitation of modes with $k > m_\chi$ last longer than that for modes with $k < m_\chi$. This renders the non-perturbative particle production in the latter case less efficient, which can be also seen from Figs. (5.14) and (5.16) that show the time evolution of ρ_k for $k > m_\chi$ and $k < m_\chi$, respectively, where $\Phi_i/\Lambda = 20$ and $m_\phi = 10^{13}$ GeV. For the latter case, the particle production ceases being efficient roughly after the first ϕ oscillation whereas it keeps being significant roughly till the end of the third ϕ oscillation for the former case. Now we proceed to calculate the ρ_χ for heavy ALPs ($m_\chi > m_\phi$) taking into account the effect of expansion. In Figure 5.17, we show the ratio of the energy density of ALPs with $m_\chi = 2m_\phi$ to that of ϕ particles. It is evident that particle creation is less efficient for heavy ALPs as compared to light ones. This is because of the smallness of

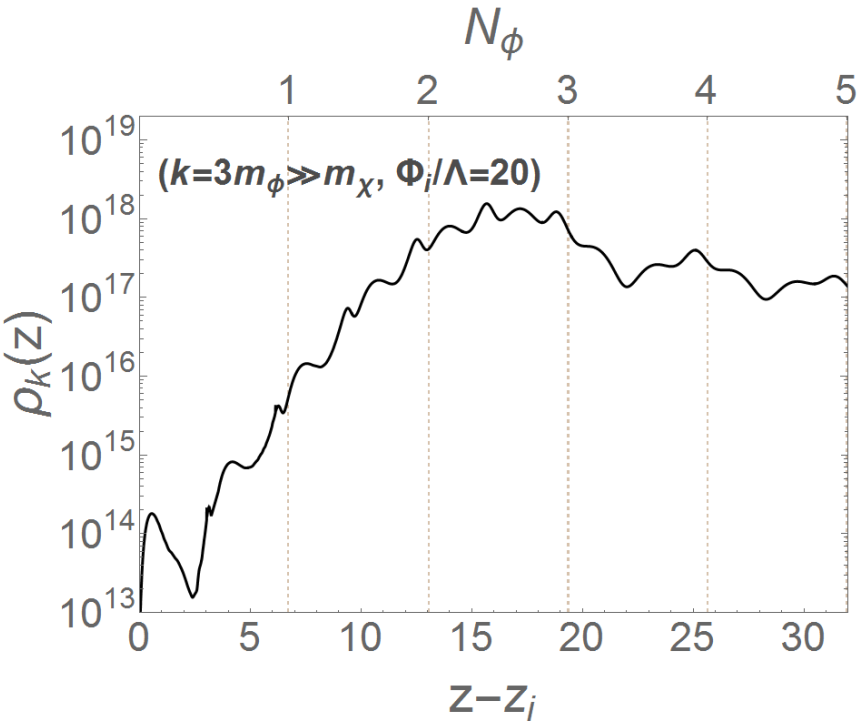

Figure 5.14: Same as Figure 5.10 but now the cosmic expansion is taken into account.

the window for the more efficient non-perturbative production of modes with momenta $k > m_\chi, m_\phi$ (i.e. $m_\chi < k \lesssim m_\phi \Phi_i/\Lambda$ with $m_\chi \gtrsim m_\phi$) in contrast to the case $m_\chi < m_\phi$. Therefore, in order for the non-perturbative production of heavy ALPs to be efficient, a larger Φ_i/Λ is required; see Figure 5.18 below. For instance, when $m_\chi = 3m_\phi$ and $m_\phi = 10^{13}$ GeV, most of the condensate's energy can be transferred to the χ field within few oscillations of the scalar condensate ϕ provided that $\Phi_i/\Lambda \gtrsim 45$. Heavier ALPs require even larger values of Φ_i/Λ. In Figure 5.18, we show a plot of the maximum energy density of χ field to the redshifted initial energy density of the scalar condensate as a function of the ratio Φ_i/Λ. The dashed and solid curves correspond to $m_\phi = 10^{10}$ GeV and $m_\phi = 10^{13}$ GeV, respectively. Here the black curves are for light ALPs whereas the red and blue curves are for heavy ALPs (for $m_\chi = 2m_\phi$ and $m_\chi = 3m_\phi$, respectively). One can easily see the difference in efficiency between the two cases. It is also clear that the ratio Φ_i/Λ being $\gg 1$ is crucial for efficient particle creation.

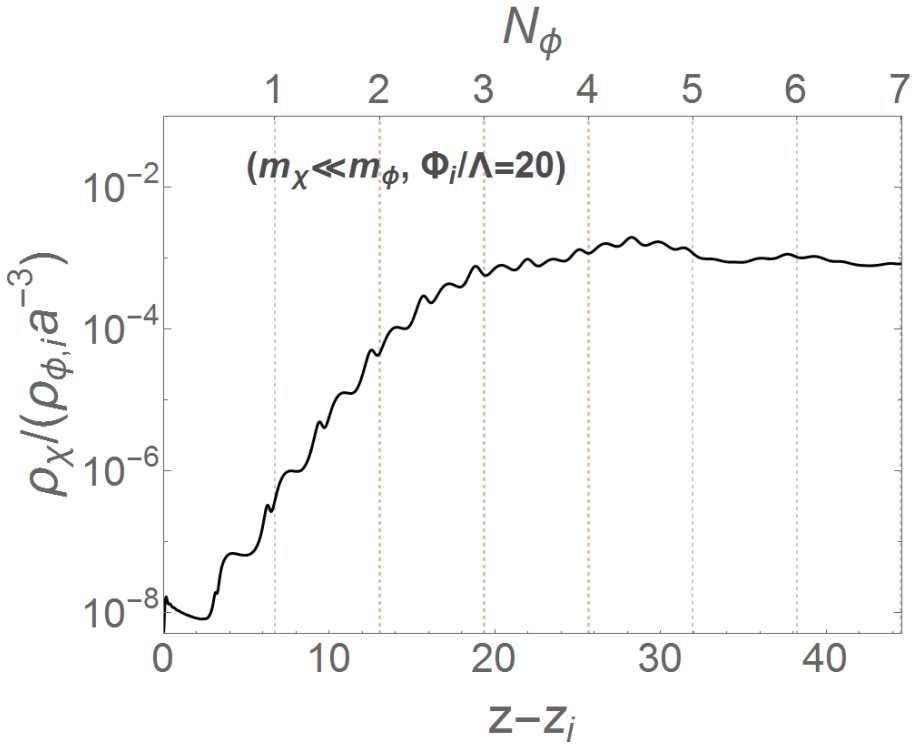

Figure 5.15: The time evolution of $\rho_\chi/(\rho_{\phi,i}a^{-3})$ for light ALPs ($m_\chi \ll m_\phi$) where m_ϕ is fixed to 10^{13} GeV, $\Phi_i/\Lambda = 20$ and the effect of cosmic expansion is taken into account.

5.4 Conclusion

In this chapter, we have considered the non-perturbative production of ALPs during the coherent oscillations of a scalar condensate with mass m_ϕ. ALPs couple only derivatively to other fields including the inflaton or any moduli field. To illustrate our point, we focused on the dimension-six operator: $\phi^2(\partial\chi)^2/2\Lambda^2$. We have shown that there is no significant non-perturbative production of ALPs when $\Phi_i/\Lambda \lesssim 1$. Nevertheless, when $\Phi_i/\Lambda \gg 1$, the non-perturbative excitation of ALPs can be significant. In this case, ALPs with masses in the range 0–$m_\phi\Phi_i/\Lambda$ can be copiously produced via non-perturbative effect. If Φ_i/Λ is sufficiently large ($\Phi_i/\Lambda \gtrsim 26$ for $m_\chi \ll m_\phi$, $\Phi_i/\Lambda \gtrsim 33$ for $m_\chi = 2m_\phi$ and $\Phi_i/\Lambda \gtrsim 45$ for $m_\chi = 3m_\phi$ when $m_\phi = 10^{13}$ GeV, or $\Phi_i/\Lambda \gtrsim 40$ for $m_\chi \ll m_\phi$, $\Phi_i/\Lambda \gtrsim 48$ for $m_\chi = 2m_\phi$ and $\Phi_i/\Lambda \gtrsim 66$ for $m_\chi = 3m_\phi$ when $m_\phi = 10^{10}$ GeV) most of the energy density of the

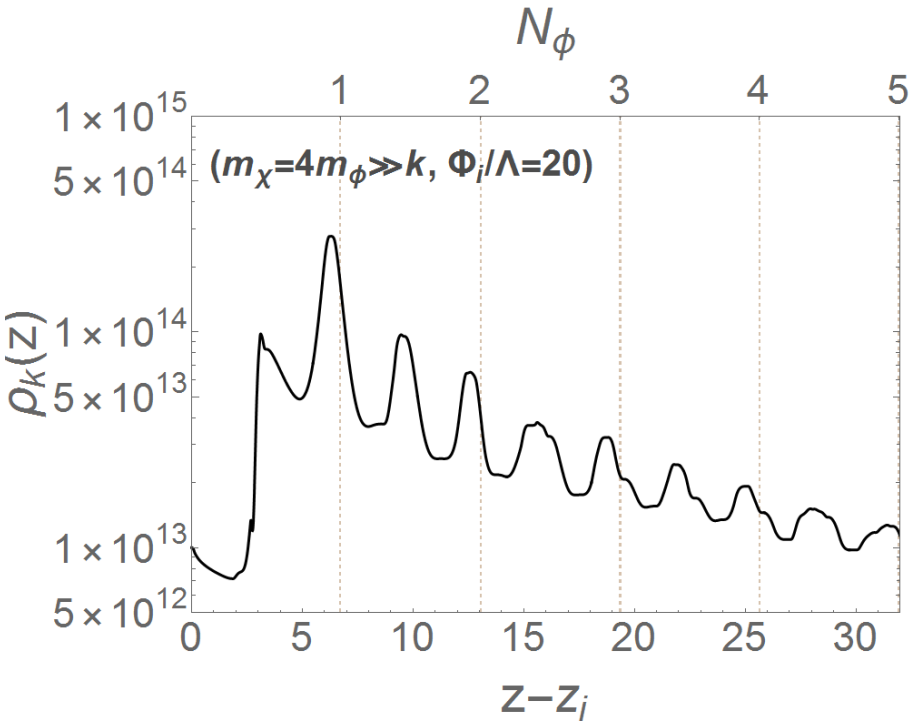

Figure 5.16: The time evolution of ρ_k for $m_\chi = 4m_\phi \gg k$ where the effect of cosmic expansion is included.

scalar condensate can be drained as excitations of the χ field [1].

Thus, irrespective of the scalar condensate being of inflatons or moduli, these non-perturbative effects could cause an alarming problem for ALPs-dominated Universe, as it would lead to a significant departure from the Standard Model cosmology and could spoil the success of BBN, unless the ALPs are unstable and decay sufficiently early before the era of BBN [2]. Moreover, if χ is stable enough to be DM, one can show that ALPs with a wide mass range can overclose the universe. Only in a very fine-tuned region of the parameter space can one match the observed DM abundance and the CMB constraint on the effective number of

[1] In such a case, the problem becomes non-linear due to the mode-mode interactions and full numerical simulations are needed. One also has to consider the couplings of the scalar condensate to other fields.

[2] In principle, ALPs can also couple to other fields allowing their decay to lighter species. For instance, ALPs can couple to gauge bosons or fermions via the operators: $\xi_1 \chi F_{\mu\nu}\tilde{F}^{\mu\nu}/\Lambda$ and $\xi_2 \partial^\mu \chi \bar{\psi}\gamma_\mu\gamma_5\psi/\Lambda$ which respectively lead to the following decay rates: $\Gamma_\chi \sim \xi_1^2 m_\chi^3/\Lambda^2$ and $\Gamma_\chi \sim \xi_2^2 m_\psi^2 m_\chi/\Lambda^2$ in the χ rest frame. These already slow decay rates are even slower in the cosmic frame for light ALPs due to the time dilation effect.

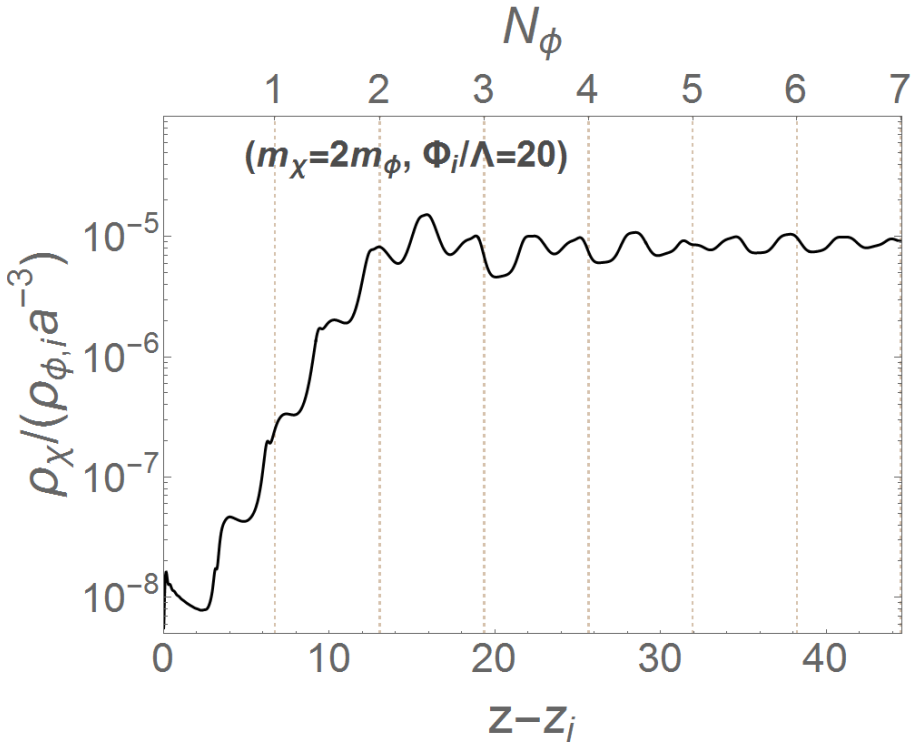

Figure 5.17: The time evolution of $(\rho_\chi/\rho_{\phi,i}a^{-3})$ for $\Phi_i/\Lambda = 20$ and $m_\chi = 2m_\phi$, where $m_\phi = 10^{13}$ GeV. Here the cosmic expansion is included.

relativistic species, $N_{\rm eff} = 3.15^{+0.41}_{-0.40}$ [13]. These pieces of information can be used to constrain the ALP's parameter space.

To conclude, the most important aspect of our analysis suggests that ALPs can efficiently be produced in the early Universe during the coherent oscillations of the inflaton or a moduli condensate provided that $\Phi_i/\Lambda \gg 1$. The summary plot is Figure 5.18, which shows the fraction of the condensate's energy density that gets transferred into ALPs as a fuction of Φ_i/Λ and the mass of the condensate. We note, however, that in many scenarios $\Phi_i/\Lambda < 1$, in which case the non-perturbative production of ALPs is utterly inefficient.

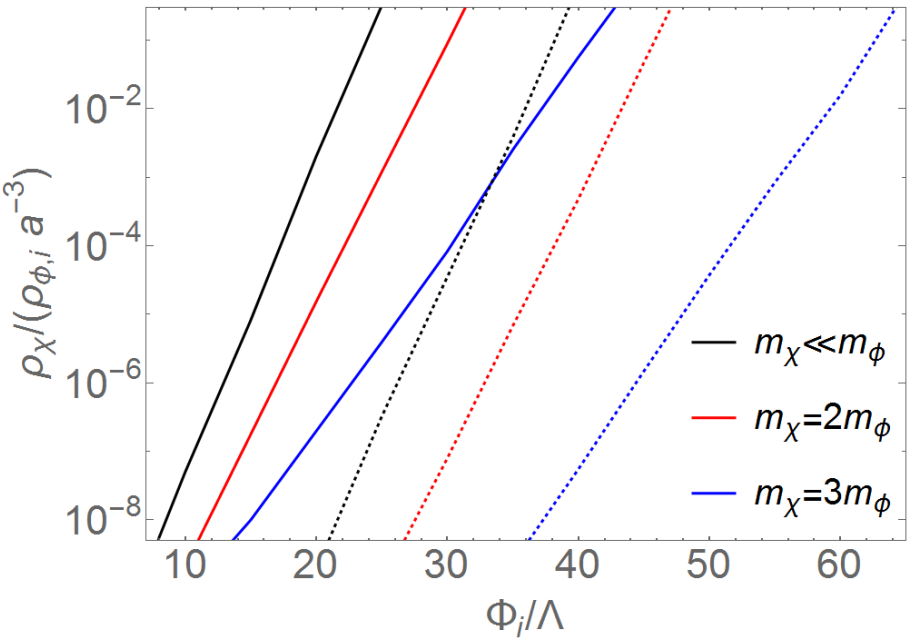

Figure 5.18: The above figure shows $\rho_\chi/(\rho_{\phi,i}a^{-3})$ as a function of ratio Φ_i/Λ for $m_\phi = 10^{10}$ GeV (dashed curves) and $m_\phi = 10^{13}$ GeV (solid curves). The black curves correspond to light ALPs whereas the red and blue curves are for heavy ALPs. Here the effect of cosmic expansion is taken into account.

Chapter 6

Conclusions

There is overwhelming evidence in support of the existence of DM in our Universe. It is most likely that DM is of particle nature. However, the origin and nature of the DM particles remain a mystery. There are already tremendous experimental efforts in search of DM. On the theory side, there are plenty of DM candidates, most of which belong to extensions of the SM (or new theories) which were proposed to address other problems, such as axions which arise in the PQ solution to the strong CP problem. Some of these candidates could be on the verge of discovery like WIMPs which may get discovered in the next few years.

In this thesis, we have investigated some of the DM production mechanisms in the context of inflationary cosmology. We have also utilised the current experimental and theoretical bounds to constrain the DM parameter space.

In Chapter 2, we presented a simple model-independent investigation of the parameter space for DM production after inflation. We showed that a big chunk of the parameter space is ruled out by the observational upper bound on the DM abundance. We identified the region of the parameter space corresponding to WIMP DM and the freeze-out scenario in general. We showed that the abundance of DM in this region arises from the annihilations of the cosmic bath particles and that it is insensitive to the initial conditions. Including the current experimental and theoretical bounds we show that only small parts of this region are still viable. Thus, with the current and near future experimental sensitivity, WIMP DM will soon be either discovered or ruled out.

We also identified the region of the parameter space corresponding to FIMP DM and the freeze-in scenario in general, which happens for much lower DM interaction rates with the thermal bath as compared to the freeze-out scenario. As a result, frozen-in DM particles were never part of the cosmic bath in contrast to frozen-out DM particles. We showed that this region of the parameter space is mostly unexplored territory. We showed that the abundance of DM in this region is sensitive to the initial conditions set by inflaton decay, despite receiving a contribution from the annihilations of the cosmic bath particles which can dominate the DM abundance.

For even smaller DM interaction rate with the bath particles, DM has to be produced mostly non-thermally from inflaton decay in order to make the observed DM abundance. We explored the parameter space for the non-thermal DM production. We showed that for even a small DM branching fraction, the decay of inflatons could overproduce DM particles. We also identified the regions of the non-thermal DM parameter space corresponding to cold, warm and hot DM.

In Chapter 3, we focused on the unexplored freeze-in region of the parameter space. We showed that a DM species whose interactions with the cosmic bath is mediated via a heavy (scalar or vector) particle makes a natural FIMP candidate. The role of the mediator can be played by the inflaton itself; however in this case, the non-thermal contribution from inflaton decay dominates the DM abundance. Therefore, another massive species is needed. We have presented a scan of the parameter space for the production of such FIMP DM species. We also showed that for such FIMP DM species and non-thermally produced DM as well, a connection to the inflationary observables (in particular to the tensor-to-scalar ratio) can be established. Such a connection could provide a handle on the ultraviolet freeze-in DM scenario.

We then focused on one of the very popular DM candidates, the axion, in Chapter 4. The dominant contribution to axion abundance comes from what is known as the misalignment mechanism. We showed that if the PQ symmetry, whose excitations along the massless angular direction represent the axion, gets spontaneously broken before or during the early stages of inflation, ultra-relativistic axions can be produced abundantly. This is because the massive

radial PQ field can get displaced from the minimum of the potential due to having a mass smaller than the Hubble parameter during inflation or having a direct coupling to the inflaton. The radial PQ field later decays dominantly to ultra-relativistic axions which contribute to the effective number of relativistic degrees of freedom. The latter is constrained by cosmological observations allowing us to place bounds on the axion parameter space and the reheating temperature as well. We also showed the current observational and theoretical bounds.

We finally considered the possible non-perturbative production of ALPs in Chapter 5. ALPs couple to other fields including the inflaton or moduli only via non-renormalisable operators suppressed by some mass scale. We showed that if ALPs do couple to the inflaton or moduli, they can be abundantly produced during the coherent oscillations of inflaton/moduli via non-perturbative effects provided that the initial amplitude of the inflaton/moduli oscillations is much larger than the associated mass scale. On the other hand, if the amplitude of the oscillations is below the associated mass scale, the non-perturbative production of ALPs is completely inefficient.

To sum up, we have presented some model- independent and dependent bounds on certain DM scenarios. We also investigated some possible methods to constrain other DM candidates which we intend to utilise to constrain the parameter spaces of these candidates in future work.

Appendix A

Boltzmann equation for dark matter

The evolution of the phase space distribution of a certain particles species, χ, in a fluid of multiple constituents $\chi, A_1, A_2, \ldots, B_1, B_2, \ldots$ is described by the Boltzmann equation which in a general curved space-time takes the form (see e.g. [574, 575])

$$\begin{aligned}\hat{\mathbf{L}}[f_\chi] \equiv \frac{df_\chi}{d\lambda} &= \frac{dx^\alpha}{d\lambda}\frac{\partial f_\chi}{\partial x^\alpha} + \frac{dP^\alpha_\chi}{d\lambda}\frac{\partial f_\chi}{\partial P^\alpha_\chi} = P^\alpha_\chi \frac{\partial f_\chi}{\partial x^\alpha} - \Gamma^\alpha_{\mu\nu} P^\mu_\chi P^\nu_\chi \frac{\partial f_\chi}{\partial P^\alpha_\chi} \\ &= \frac{1}{2}\hat{\mathbf{C}}[f_\chi, f_{A_1}, f_{A_2}, \ldots, f_{B_1}, f_{B_2}, \ldots]\,, \end{aligned} \tag{A.1}$$

where $\hat{\mathbf{L}}$ and $\hat{\mathbf{C}}$ respectively denote the Liouville and Collision operators acting on the phase space distribution of that species, $f_\chi \equiv f_\chi(x^\alpha(\lambda), P^\alpha_\chi(\lambda))$, and λ is an affine parameter characterising the world-line along which we consider the variation of f_χ. Here we made the assumption that between collisions the χ particles are only acted upon gravitationally and hence we substituted the geodesic equation: $\mathrm{d}P^\alpha_\chi/\mathrm{d}\lambda + \Gamma^\alpha_{\mu\nu} P^\mu_\chi P^\nu_\chi = 0$, where $P^\alpha_\chi = \mathrm{d}x^\alpha/\mathrm{d}\lambda$, into Eq. (A.1) above.

For the homogeneous and isotropic FRLW background, the phase space density is also spatially homogeneous and isotropic, i.e. $f_\chi \equiv f_\chi(p_\chi, t)$ where $p_\chi \equiv |\mathbf{p}_\chi|$,

in which case the Boltzmann equation [Eq. (A.1)] simplifies to (see e.g. [574])

$$\frac{\partial f_\chi}{\partial t} - Hp_\chi \frac{\partial f_\chi}{\partial p_\chi} = \frac{1}{2E_\chi(p_\chi)} \hat{C}[f_\chi, f_{A_1}, f_{A_2}, \ldots, f_{B_1}, f_{B_2}, \ldots] \,. \tag{A.2}$$

Integrating over the momentum space of the χ particle species $[g_\chi \int \mathrm{d}p_\chi^3/(2\pi)^3]$, we obtain the following Boltzmann equation governing the time evolution of the average number density of χ particles:

$$\begin{aligned} \dot{n}_\chi + 3Hn_\chi =& \int \mathrm{d}\tilde{p}_\chi \, \hat{\mathbf{C}}[f_\chi, f_a, \ldots, f_i, f_j, \ldots] \\ =& \sum_{\chi A \leftrightarrow B} \int \mathrm{d}\tilde{p}_\chi \mathrm{d}\tilde{p}_A \mathrm{d}\tilde{p}_B (2\pi)^4 \delta^{(4)}(P_\chi + P_A - P_B) \left\{ |\mathcal{M}|^2_{B \to \chi A} f_{B_1} f_{B_2} \ldots \right. \\ & \left. \times (1 \pm f_\chi)(1 \pm f_{A_1}) \ldots - |\mathcal{M}|^2_{\chi A \to B} f_\chi f_{A_1} \ldots (1 \pm f_{B_1})(1 \pm f_{B_2}) \ldots \right\} , \end{aligned} \tag{A.3}$$

where $\mathrm{d}\tilde{p}_i \equiv g_i \mathrm{d}^3p/[(2\pi)^3 2E_i(p_i)]$ with g_i being the number of internal d.o.f. of the i^{th} particle species, $\mathrm{d}\tilde{p}_A \equiv \prod_i \mathrm{d}\tilde{p}_{A_i}$, $\mathrm{d}\tilde{p}_B \equiv \prod_j \mathrm{d}\tilde{p}_{B_j}$, $P_A \equiv \sum_i P_{A_i}$, $P_B \equiv \sum_j P_{B_j}$, $A \equiv \{A_1, A_2, \ldots\}$ and $B \equiv \{B_1, B_2, \ldots\}$. Here the sum, $\sum_{\chi A \leftrightarrow B}$, runs over all the allowed processes and the factors $(1 \pm f_i)$ account for the quantum statistical effects, namely Pauli blocking [$(-)$ for fermions] and stimulated emission [$(+)$ for bosons], and $|\mathcal{M}|^2$ is the transition amplitude averaged over the internal d.o.f. of both the initial and final states with the appropriate symmetry factors included. In Eq. (A.3), we used the definition of the average number density given by

$$n_i(t) = \int \frac{g_i \mathrm{d}^3 p_i}{(2\pi)^3} f_i(p, t) \,, \tag{A.4}$$

with f_i being the phase space distribution of the species i where $f_{i,eq} = [\exp[(E_i - \mu_i)/T] \mp 1]^{-1}$ is the corresponding equilibrium distribution $[(+)$ for fermions and $(-)$ for bosons].

In full generality, the Boltzmann equations are a set of coupled partial integro-differential equations which can be impossible to solve. However, the Boltzmann equations can be greatly simplified via some physical assumptions. First ne-

glecting CP-violation, we have $|\mathcal{M}|^2_{B\to\chi A} = |\mathcal{M}|^2_{\chi A\to B} = |\mathcal{M}|^2$ [1]. Further in the dilute limit – which is a good approximation for many cosmological problems – the quantum statistical effects can be neglected and one can use Boltzmann distribution, $f_i = \exp[(-E_i - \mu_i)/T]$, instead of the Fermi-Dirac and Bose-Einstein counterparts. Consequently, Eq. (A.3) simplifies to

$$\dot{n}_\chi + 3Hn_\chi = \sum_{\chi A\leftrightarrow B} \int \mathrm{d}\tilde{p}_\chi \mathrm{d}\tilde{p}_A \mathrm{d}\tilde{p}_B (2\pi)^4 \delta^{(4)}(P_\chi + P_A - P_B)\, |\mathcal{M}|^2 \times \{f_{B_1} f_{B_2} \ldots - f_\chi f_{A_1} \ldots\}\,. \tag{A.5}$$

From Eq. (A.5), it is clear that the average χ number density depends on the expansion rate of the Universe and the collisional integral on the right hand side. The latter may include scattering and decay processes. In what follows, we will assume that the χ species is DM; as a result, we will not consider the decay of χ as DM should be stable on time scale larger than the age of the Universe. Let us now consider the production of DM via the decay and scattering of other particle species.

A.1 Non-thermal dark matter

Dark matter can be produced non-thermally in the decay of a heavier unstable species, a [2]. From Eq. (A.5), the Boltzmann equation governing the time evolution of the daughter DM particles, χ, produced in the decay process, $a \to \chi\psi$, can be written as

$$\begin{aligned}\dot{n}_\chi + 3Hn_\chi &= \int \mathrm{d}\tilde{p}_a \mathrm{d}\tilde{p}_\chi \mathrm{d}\tilde{p}_\psi (2\pi)^4 \delta^{(4)}(P_a - P_\chi - P_\psi)\, |\mathcal{M}|^2 \{f_a - f_\chi f_\psi\} \\ &= \Gamma(a\to\chi\psi)\, n_a - \int \mathrm{d}\tilde{p}_a \mathrm{d}\tilde{p}_\chi \mathrm{d}\tilde{p}_\psi (2\pi)^4 \delta^{(4)}(P_a - P_\chi - P_\psi)\, |\mathcal{M}|^2 f_\chi f_\psi\,,\end{aligned} \tag{A.6}$$

[1] CP violating interactions – if present – play a crucial role in baryogenesis (see e.g. [56]) and leptogenesis (see e.g. [486]). They are also important for the asymmetric DM scenario (see e.g. [576]).

[2] Other non-thermal DM production mechanism exist. For example axions or axion-like particles can be produced via the misalignment mechanism [250, 509, 510, 577].

where in the second line of Eq. (A.6), we used the standard expression for the two-body decay rate (see e.g. [45]),

$$\begin{aligned}\Gamma(a\to\chi\psi) &= \frac{1}{2E_a}\int \mathrm{d}\tilde{p}_\chi \mathrm{d}\tilde{p}_\psi (2\pi)^4\delta^{(4)}(P_a-P_\chi-P_\psi)\,|\mathcal{M}|^2 \\ &= \frac{1}{2m_a}\int \frac{\mathrm{d}^3p_\chi}{(2\pi)^3 2E_\chi}\frac{\mathrm{d}^3p_\psi}{(2\pi)^3 2E_\psi}(2\pi)^4\delta(\sqrt{s}-E_\chi-E_\psi)\delta^{(3)}(\mathbf{p}_\chi+\mathbf{p}_\psi)\,|\mathcal{M}|^2 \\ &= \frac{1}{8m_a}\int \frac{p^2\mathrm{d}p\,\mathrm{d}\cos\theta\,\mathrm{d}\phi}{(2\pi)^3 E_\chi E_\psi}\,\frac{(2\pi)\delta(p-p_f)|\mathcal{M}|^2}{(p/E_\chi)+(p/E_\psi)}\bigg|_{E_i=(m_i^2+p^2)^{1/2}} \\ &= \frac{p_f}{8\pi m_a}\,\frac{|\mathcal{M}|^2}{E_\chi+E_\psi}\bigg|_{E_i=(m_i^2+p_f^2)^{1/2}} = \frac{p_f}{8\pi m_a^2}|\mathcal{M}|^2\,, \end{aligned} \tag{A.7}$$

where we evaluated the expression in the CM frame. Here $p=p_\chi=p_\psi$, $p_f=\{[s-(m_\chi+m_\psi)^2][s-(m_\chi-m_\psi)^2]\}^{1/2}/(2s^{1/2})$, $E_\chi=(s^{1/2}/2)(1+m_\chi^2/s-m_\psi^2/s)$ and $E_\psi=(s^{1/2}/2)(1+m_\psi^2/s-m_\chi^2/s)$. In cases of interest to us, the inverse decay process is either exponentially suppressed (if ψ and/or χ is a part of a thermal bath with temperature much below the mass of a) or even kinematically blocked (if neither of the daughter particles is a part of a thermal bath). As a result, Eq. (A.6) reduces to

$$\dot{n}_\chi + 3Hn_\chi = \Gamma(a\to\chi\psi)\,n_a = \mathrm{B}(a\to\chi\psi)\,\Gamma_a\,n_a\,, \tag{A.8}$$

where Γ_a denotes the total decay rate of particle species a and $\mathrm{B}(a\to\chi\psi)\equiv\Gamma(a\to\chi\psi)/\Gamma_a$ is its branching fraction to the decay channel $a\to\chi\psi$. For a decay process that results in the production of n χ particles, a factor n should be added to the right hand side of Eq. (A.8).

A.2 Thermally produced dark matter

Dark matter can also be produced via inelastic scatterings of the thermal bath particles, $ab\to\chi\psi$ in which case [with the help of Eq. (A.5)], the Boltzmann

equation governing the abundance of DM particles, χ, can be written as

$$\dot{n}_\chi + 3Hn_\chi = \sum_{ab\leftrightarrow\chi\psi}\int \mathrm{d}\tilde{p}_a \mathrm{d}\tilde{p}_b \mathrm{d}\tilde{p}_\chi \mathrm{d}\tilde{p}_\psi (2\pi)^4 \delta^{(4)}(P_a + P_b - P_\chi - P_\psi)\,|\mathcal{M}|^2 \times \{f_a f_b - f_\chi f_\psi\}\,. \tag{A.9}$$

Let us consider the following cases.

A.2.1 Case 1: Freeze-out of dark matter

The DM particles are initially in thermal equilibrium with the cosmic thermal bath. As the Universe expands, the number densities of different species dilute and hence the interaction rates decrease with time. Once the interaction rate of a particle species with the thermal bath becomes smaller than the expansion rate, the species decouples from the thermal bath. Such a species is said to be frozen-out. For concreteness, let us consider the case of fermionic DM, χ ($\bar{\chi}$), that interact with the cosmic bath fermions, a ($\bar{a}$), $a\bar{a}\leftrightarrow\chi\bar{\chi}$ in which case Eq. (A.9) can be re-written as

$$\begin{aligned}\dot{n}_\chi + 3Hn_\chi &= \sum_{a\bar{a}\leftrightarrow\chi\bar{\chi}}\int \mathrm{d}\tilde{p}_\chi \mathrm{d}\tilde{p}_{\bar{\chi}} \mathrm{d}\tilde{p}_a \mathrm{d}\tilde{p}_{\bar{a}} (2\pi)^4 \delta^{(4)}(P_a + P_b - P_\chi - P_\psi)\,|\mathcal{M}|^2 \{f_{a,eq} f_{\bar{a},eq} - f_\chi f_{\bar{\chi}}\} \\ &= \sum_{a\bar{a}\leftrightarrow\chi\bar{\chi}}\int \mathrm{d}\tilde{p}_\chi \mathrm{d}\tilde{p}_{\bar{\chi}} \left(e^{-(\mu_a+\mu_{\bar{a}})/T} - \frac{n_\chi n_{\bar{\chi}}}{n_{\chi,eq} n_{\bar{\chi},eq}}\right) e^{-(E_\chi + E_{\bar{\chi}})/T} \\ &\quad \times \int \mathrm{d}\tilde{p}_a \mathrm{d}\tilde{p}_{\bar{a}} (2\pi)^4 \delta^{(4)}(P_a + P_{\bar{a}} - P_\chi - P_{\bar{\chi}})\,|\mathcal{M}|^2\,,\end{aligned} \tag{A.10}$$

where the δ-function imposes energy conservation, $E_a + E_{\bar{a}} = E_\chi + E_{\bar{\chi}}$. Here we assumed that the χ particles are in kinetic equilibrium with the thermal bath and hence substituted $f_{\chi(\bar{\chi})} = \frac{n_{\chi(\bar{\chi})}}{n_{\chi(\bar{\chi}),eq}} e^{-E_\chi(\bar{\chi})/T}$ in the second line of Eq. (A.10) (see e.g. [236, 578]). Note that $\mu_a + \mu_{\bar{a}} = \mu_\chi + \mu_{\bar{\chi}} = 0$ (provided that the reaction $a\bar{a}\to\gamma\gamma$ takes place at sufficiently fast rate), $n_a = n_{\bar{a}}$ and $n_\chi = n_{\bar{\chi}}$ for the case of negligible CP asymmetry under consideration. Further using the standard expression for the total unpolarised cross-section (see e.g. [45, 236]), one can write:

$$\int \mathrm{d}\tilde{p}_a \mathrm{d}\tilde{p}_{\bar{a}} (2\pi)^4 \delta^{(4)}(P_a + P_{\bar{a}} - P_\chi - P_{\bar{\chi}}) \, |\mathcal{M}|^2 = 2E_\chi 2E_{\bar{\chi}} \sigma(\chi\bar{\chi} \to a\bar{a}) v_{\mathrm{Mol}} \,, \quad \text{(A.11)}$$

where $v_{\mathrm{Mol}} = [(P_\chi^\mu P_{\bar{\chi}\mu})^2 - m_\chi^4]^{1/2}/(E_\chi E_{\bar{\chi}}) = \sqrt{(\mathbf{v}_\chi - \mathbf{v}_{\bar{\chi}})^2 - (\mathbf{v}_\chi \times \mathbf{v}_{\bar{\chi}})^2}$ is the Møller velocity. Substituting into Eq. (A.10), we have

$$\begin{aligned} \dot{n}_\chi + 3Hn_\chi &= (n_{\chi,eq}^2 - n_\chi^2) \frac{1}{n_{\chi,eq}^2} \sum_{\chi\bar{\chi}\to a\bar{a}} \int \frac{g_\chi \mathrm{d}^3 p_{\bar{\chi}}}{(2\pi)^3} \frac{g_{\bar{\chi}} \mathrm{d}^3 p_{\bar{\chi}}}{(2\pi)^3} f_{\chi,eq} f_{\bar{\chi},eq} \, \sigma(\chi\bar{\chi} \to a\bar{a}) v_{\mathrm{Mol}} \\ &= \sum_{\chi\bar{\chi}\to a\bar{a}} \langle \sigma(\chi\bar{\chi} \to a\bar{a}) v_{\mathrm{Mol}} \rangle (n_{\chi,eq} n_{\bar{\chi},eq} - n_\chi n_{\bar{\chi}}) \\ &= \langle \sigma_{\mathrm{tot}} v_{\mathrm{Mol}} \rangle (n_{\chi,eq}^2 - n_\chi^2) \,, \end{aligned} \quad \text{(A.12)}$$

with

$$\begin{aligned} \langle \sigma_{\mathrm{tot}} v_{\mathrm{Mol}} \rangle &= \frac{1}{n_{\chi,eq}^2} \sum_{\chi\bar{\chi}\to a\bar{a}} \int \frac{g_\chi \mathrm{d}^3 p_{\bar{\chi}}}{(2\pi)^3} \frac{g_{\bar{\chi}} \mathrm{d}^3 p_{\bar{\chi}}}{(2\pi)^3} e^{-(E_\chi + E_{\bar{\chi}})/T} \, \sigma(\chi\bar{\chi} \to a\bar{a}) v_{\mathrm{Mol}} \\ &= \frac{1}{n_{\chi,eq}^2} \sum_{\chi\bar{\chi}\to a\bar{a}} \frac{g_\chi^2}{8\pi^4} \int_{-1}^{1} \mathrm{d}\cos\theta \int_{m_\chi}^{\infty} p_\chi E_\chi \mathrm{d}E_\chi \int_{m_\chi}^{\infty} p_{\bar{\chi}} E_{\bar{\chi}} \mathrm{d}E_{\bar{\chi}} \, e^{-(E_\chi + E_{\bar{\chi}})/T} \, \sigma(\chi\bar{\chi} \to a\bar{a}) v_{\mathrm{Mol}} \,, \end{aligned} \quad \text{(A.13)}$$

being the thermal average of the total (unpolarised) cross-section times the Møller velocity, $v_{\mathrm{Mol}} = [(P_\chi^\mu P_{\bar{\chi}\mu})^2 - m_\chi^4]^{1/2}/(E_\chi E_{\bar{\chi}}) = [s(s-4m_\chi^2)]^{1/2}/(2E_\chi E_{\bar{\chi}})$. Following [236], we change the integration variables E_1, E_2 and θ to $E_+ \equiv E_\chi + E_{\bar{\chi}}$, $E_- \equiv E_\chi - E_{\bar{\chi}}$ and the CM squared energy, $s = 2m_a^2 + 2E_a E_{\bar{a}} - 2p_a p_{\bar{a}} \cos\theta$. Eq. (A.13) can be re-written as

$$\begin{aligned} \langle \sigma_{\mathrm{tot}} v_{\mathrm{Mol}} \rangle &= \frac{1}{n_{\chi,eq}^2} \sum_{\chi\bar{\chi}\to a\bar{a}} \frac{g_\chi^2}{64\pi^4} \int_{s_{\min}}^{\infty} \mathrm{d}s [s(s-4m_\chi^2)]^{1/2} \sigma(\chi\bar{\chi} \to a\bar{a}) \int_{\sqrt{s}}^{\infty} \mathrm{d}E_+ e^{-E_+/T} \int_{E_-^{(-)}}^{E_-^{(+)}} \mathrm{d}E_- \\ &= \frac{1}{n_{\chi,eq}^2} \sum_{\chi\bar{\chi}\to a\bar{a}} \frac{g_\chi^2 T}{32\pi^4} \int_{s_{\min}}^{\infty} \mathrm{d}s \, s^{1/2} (s-4m_\chi^2) K_1(s^{1/2}/T) \, \sigma(\chi\bar{\chi} \to a\bar{a}) \,, \end{aligned} \quad \text{(A.14)}$$

where $s_{\min} = \max(4m_a^2, 4m_\chi^2)$, $E_-^{(\pm)} \equiv \pm[s^{-1}(s-4m_\chi^2)(E_+^2 - s)]^{1/2}$ and $K_n(x)$ is the n^{th}-order modified Bessel function of the second kind. Further, one can express $n_{\chi,eq}$ as

$$n_{\chi,eq} = g_\chi \int \frac{\mathrm{d}^3 p_{\bar{\chi}}}{(2\pi)^3} e^{-E_\chi/T} = \frac{g_\chi}{2\pi^2} \int_{m_\chi}^{\infty} \mathrm{d}E_\chi E_\chi \sqrt{E_\chi^2 - m_\chi^2}\, e^{-E_\chi/T} = \frac{g_\chi}{2\pi^2} m_\chi^2 T K_2(m_\chi/T)\,. \tag{A.15}$$

Using the above expression for the equilibrium number denstity, Eq. (A.14) now reads [236]

$$\langle \sigma_{\rm tot} v_{\rm Mol} \rangle = \frac{1}{8 m_\chi^4 T K_2^2(m_\chi/T)} \sum_{\chi\bar{\chi}\to a\bar{a}} \int_{s_{\rm min}}^{\infty} \mathrm{d}s\, s^{1/2} (s - 4m_\chi^2) K_1(s^{1/2}/T)\, \sigma(\chi\bar{\chi} \to a\bar{a})\,, \tag{A.16}$$

Another case of interest to us is when a bosonic DM species, χ, initially in thermal equilibrium with the cosmic bath through the interactions $\chi a \leftrightarrow ij$, freezes-out. From Eqs. (A.10)-(A.12), the Boltzmann equation governing the number density of χ particles can be written as

$$\dot{n}_\chi + 3Hn_\chi = \Gamma_\chi (n_{\chi,eq} - n_\chi)\,, \tag{A.17}$$

where

$$\Gamma_\chi = \frac{1}{n_{\chi,eq}} \sum_{\chi a \to ij} \int \mathrm{d}\tilde{p}_\chi \mathrm{d}\tilde{p}_a f_{\chi,eq} f_{a,eq}\, 2E_\chi 2E_a \sigma(\chi a \to ij) v_{\rm Mol}\,, \tag{A.18}$$

is the average interaction rate with $v_{\rm Mol} = [(P_\chi^\mu P_{a\mu})^2 - m_\chi^2 m_a^2]^{1/2}/(E_\chi E_a)$.

A.2.2 Case 2: Freeze-in of dark matter

Let us now consider the case where DM is feebly interacting with the thermal bath such that it does not reach kinetic nor chemical equilibrium with the bath, i.e. the DM interaction rate with the thermal bath is always smaller than the expansion rate. Nevertheless, the DM interaction rate can still be large enough to produce DM with the observed abundance. For concreteness, we will again focus on the case of fermionic DM, $\chi(\bar{\chi})$, produced from the annihilation of the bath fermions, $a\bar{a} \to \chi\bar{\chi}$, in which case the DM number density evolves according

to the Boltzmann equation [see Eq. (A.9)],

$$\dot{n}_\chi + 3Hn_\chi = \sum_{a\bar{a}\to\chi\bar{\chi}} \langle \sigma(a\bar{a}\to\chi\bar{\chi}) v_{\rm Mol} \rangle \, n_{a,eq} n_{\bar{a},eq} = \gamma_\chi \,, \tag{A.19}$$

with [see Eqs. (A.13) and (A.14)]

$$\begin{aligned}
\gamma_\chi =& \sum_{a\bar{a}\to\chi\bar{\chi}} \int \mathrm{d}\tilde{p}_a \mathrm{d}\tilde{p}_{\bar{a}} \mathrm{d}\tilde{p}_\chi \mathrm{d}\tilde{p}_{\bar{\chi}} (2\pi)^4 \delta^{(4)}(P_a + P_{\bar{a}} - P_\chi - P_{\bar{\chi}}) \, |\mathcal{M}|^2 f_{a,eq} f_{\bar{a},eq} \\
=& \sum_{a\bar{a}\to\chi\bar{\chi}} \int \frac{g_a \mathrm{d}^3 p_a}{(2\pi)^3} \frac{g_{\bar{a}} \mathrm{d}^3 p_{\bar{a}}}{(2\pi)^3} e^{-(E_a + E_{\bar{a}})/T} \, \sigma(a\bar{a}\to\chi\bar{\chi}) v_{\rm Mol} \\
=& \sum_{a\bar{a}\to\chi\bar{\chi}} \frac{g_a^2}{64\pi^4} \int_{s_{\rm min}}^\infty \mathrm{d}s [s(s-4m_a^2)]^{1/2} \sigma(a\bar{a}\to\chi\bar{\chi}) \int_{\sqrt{s}}^\infty \mathrm{d}E_+ e^{-E_+/T} \int_{E_-^{(-)}}^{E_-^{(+)}} \mathrm{d}E_- \;\;,
\end{aligned} \tag{A.20}$$

where $v_{\rm Mol} = [(P_a^\mu P_{\bar{a}\mu})^2 - m_a^4]^{1/2}/(E_a E_{\bar{a}}) = [s(s-4m_a^2)]^{1/2}/(2E_a E_{\bar{a}})$, $s_{\rm min} = \max(4m_a^2, 4m_\chi^2)$, and $E_-^{(\pm)} \equiv \pm[s^{-1}(s-4m_a^2)(E_+^2 - s)]^{1/2}$. Again for the CP-invariant case under consideration, $\mu_a + \mu_{\bar{a}} = 0$ (provided that the reaction $a\bar{a}\to\gamma\gamma$ takes place at sufficiently fast rate). Here we assume that the DM abundance is initially negligible and hence $f_\chi f_{\bar{\chi}} \ll f_{\chi,eq} f_{\bar{\chi},eq}$ (i.e. $f_\chi f_{\bar{\chi}} \ll f_{a,eq} f_{\bar{a},eq}$) as the DM interaction with the cosmic bath is sufficiently small such that it does not reach thermal equilibrium with the bath. In the second line of Eq. (A.20), we used the standard expression for the unpolarised cross-section [see Eq. (A.11)]. Carrying out the integration over E_- and E_+, one obtains

$$\gamma_\chi = \sum_{a\bar{a}\to\chi\bar{\chi}} \langle \sigma(a\bar{a}\to\chi\bar{\chi}) v_{\rm Mol} \rangle \, n_{a,eq}^2 = \sum_{a\bar{a}\to\chi\bar{\chi}} \frac{g_a^2 T}{32\pi^4} \int_{s_{\rm min}}^\infty \mathrm{d}s \, s^{1/2} (s-4m_a^2) K_1(s^{1/2}/T) \, \sigma(a\bar{a}\to\chi\bar{\chi}) \,. \tag{A.21}$$

Appendix B

Axion Model

In this appendix, we briefly review the most widely discussed viable PQ mechanisms, namely the Kim-Shifman-Vainshtein-Zakharov (KVSZ) model [505, 506] and the Dine-Fischler-Srednicki-Zhitnisky (DFSZ) model [507, 508].

B.1 KSVZ-like models

In the KSVZ-like models, a new complex scalar singlet S (PQ field) and heavy quarks Q_j (at least one) are added to the SM. The PQ field S couples to the extra heavy quarks Q_j via the vertices

$$\mathcal{L} \supset -h_j(\bar{Q}_L^j S Q_R^j + \text{h.c.})\,, \tag{B.1}$$

where for simplicity we assumed real diagonal Yukawa coupling matrix. Under $\mathrm{U}(1)_{\mathrm{PQ}}$, S and Q_j transform as $Q_j \to \exp(i\gamma_5\alpha)Q_j$ and $S \to \exp(-2i\alpha)S$, respectively, and all the other fields are invariant. The PQ symmetry gets spontaneously broken when S develops a VEV, $\langle|S|\rangle = v_{\mathrm{PQ}}/\sqrt{2}$, due to a Mexican-hat potential which gives mass to the extra heavy quarks, $m_{Q_j} = h_j v_{\mathrm{PQ}}/\sqrt{2}$. Moreover, the following couplings of the PQ radial field σ and the angular field χ (axion) to the

heavy quarks arise,

$$\mathcal{L} \supset -m_{Q_j}\frac{\tilde{\sigma}}{v_{\rm PQ}}\bar{Q}^j Q^j + \frac{1}{2}\frac{\partial_\mu \chi}{v_{\rm PQ}}\bar{Q}^j\gamma^\mu\gamma_5 Q_j\,, \tag{B.2}$$

where $\tilde{\sigma} = \sigma - v_{\rm PQ}$. Note that there are no couplings between the axion and the SM quarks and leptons at tree-level since the SM fields do not carry PQ charges. Assuming that there is at least one heavy quark Q with $m_Q < m_\sigma/2$, the decay rate of the σ into the heavy quark sector is given by

$$\Gamma(\sigma \to \bar{Q}Q) \simeq \frac{3m_Q^2 m_\sigma}{8\pi v_{\rm PQ}^2}\left(1 - \frac{4m_Q^2}{m_\sigma^2}\right)^{3/2}, \tag{B.3}$$

where Q is the heaviest of the extra quarks with $m_Q < m_\sigma/2$. Equation (B.3) has to be multiplied by a factor n if we have instead n nearly degenerate quarks. Here for concreteness, we assumed that Q is a colour triplet.

B.2 DFSZ-like models

In the DFSZ-like models, the original PQ model which contains two Higgs doublets, $\Phi_{1,2}$, is augmented with a complex scalar singlet, S (PQ field) which carries PQ charge and transforms as $S \to e^{i\alpha X_S} S$ under the $\mathrm{U}(1)_{\rm PQ}$ phase rotation. Similarly, the two Higgs doublets, the SM quarks, and the SM charged leptons all carry PQ charges and transform non-trivially under the $\mathrm{U}(1)_{\rm PQ}$ group: $\Phi_{1,2} \to e^{i\alpha X_{1,2}}\Phi_{1,2}$, $u, d \to e^{i\alpha\gamma_5 X_{u,d}}\, u, d$ and $l \to e^{i\alpha\gamma_5 X_l}\, l$. The PQ field couples to the two Higgs doublets via the following vertices:

$$\mathcal{L} \supset -|S|^2(\lambda_{1S}|\Phi_1|^2 + \lambda_{2S}|\Phi_2|^2) - \lambda_{S12}[S^2\Phi_1\epsilon\Phi_2 + S^{*2}(\Phi_1\epsilon\Phi_2)^*]\,, \tag{B.4}$$

where ϵ is the totally anti-symmetric tensor. Note that although the SM fermions carry $\mathrm{U}(1)_{\rm PQ}$ charges, they do not couple to the S field via re-normalisable operators. Once the PQ symmetry gets broken by the VEV of the PQ field, $\langle|S|\rangle = v_{\rm PQ}/\sqrt{2} \gg v_{\rm EW}$, the two Higgs doublets acquire extra mass terms $(\lambda_{1S}v_{\rm PQ}^2/2)|\Phi_1|^2$

and $(\lambda_{2S} v_{\rm PQ}^2/2)|\Phi_2|^2$, respectively. Here for simplicity, we assume that the mixing term is sufficiently small, $\lambda_{S12} \ll \lambda_{1S}, \lambda_{2S}$. Later on the two Higgs doublets acquire VEVs, $v_{1,2}$, breaking the $SU(2)_L \otimes U(1)_Y$ gauge symmetry. The EW VEV is then $v_{\rm EW} = \{v_1^2 + v_2^2 - [\lambda_{1S}/(2\lambda_1) + \lambda_{2S}/(2\lambda_2)]\, v_{\rm PQ}^2\}^{1/2}$ where $\lambda_{1,2}$ are respectively the quartic couplings of $\Phi_{1,2}$. Since $v_{\rm PQ} \gg v_{\rm EW}$, the PQ field couplings to both the Higgs doublets have to be very small, $\lambda_{1S}, \lambda_{2S}, \lambda_{S12} < (v_{\rm EW}/v_{\rm PQ})^2$ [536]. Above the EW scale, the PQ radial field, σ, couples to the Higgs doublets via the vertices:

$$\begin{aligned} \mathcal{L} \supset & - \lambda_{1S} v_{\rm PQ} \tilde{\sigma} |\Phi_1|^2 - \lambda_{2S} v_{\rm PQ} \tilde{\sigma} |\Phi_2|^2 - \lambda_{S12} v_{\rm PQ} \tilde{\sigma} \Phi_1 \epsilon \Phi_2 \\ & - \frac{\lambda_{1S}}{2} \tilde{\sigma}^2 |\Phi_1|^2 - \frac{\lambda_{2S}}{2} \tilde{\sigma}^2 |\Phi_2|^2 - \frac{\lambda_{S12}}{2} \tilde{\sigma}^2 \Phi_1 \epsilon \Phi_2 \,, \end{aligned} \tag{B.5}$$

where $\tilde{\sigma} = \sigma - v_{\rm PQ}$. The decay rates of σ into these fields are respectively given by

$$\Gamma(\sigma \to 2\Phi_{1,2}) \simeq \frac{\lambda_{S1,2}^2}{8\pi m_\sigma} v_{\rm PQ}^2 \simeq \frac{\lambda_{S1,2}^2}{8\pi\sqrt{2\lambda}} v_{\rm PQ} \,, \tag{B.6}$$

where for simplicity we assumed that each Higgs doublet contains two complex fields. Note that there is also a cross coupling, which leads to a similar decay rate of σ.

References

[1] A. Einstein. The Foundation of the General Theory of Relativity. *Annalen Phys.*, 49:769–822, 1916. 2

[2] R. Adam et al. Planck 2015 results. I. Overview of products and scientific results. *Astron. Astrophys.*, 594:A1, 2016. 2, 85

[3] P. A. R. Ade et al. Planck 2015 results. XVI. Isotropy and statistics of the CMB. *Astron. Astrophys.*, 594:A16, 2016. 2, 15

[4] C. L. Bennett et al. Nine-Year Wilkinson Microwave Anisotropy Probe (WMAP) Observations: Final Maps and Results. *Astrophys. J. Suppl.*, 208:20, 2013. 2, 10

[5] S. Alam et al. The Eleventh and Twelfth Data Releases of the Sloan Digital Sky Survey: Final Data from SDSS-III. *Astrophys. J. Suppl.*, 219(1):12, 2015. 2, 10, 34

[6] SDSS Collaboration, F. D. Albareti, et al. The Thirteenth Data Release of the Sloan Digital Sky Survey: First Spectroscopic Data from the SDSS-IV Survey MApping Nearby Galaxies at Apache Point Observatory. *ArXiv e-prints*, August 2016. 2, 10, 34

[7] D. Saadeh, S. M. Feeney, A. Pontzen, H. V. Peiris, and J. D. McEwen. How isotropic is the Universe? *Phys. Rev. Lett.*, 117(13):131302, 2016. 2

[8] W. de Sitter. Einstein's theory of gravitation and its astronomical consequences, Third Paper. *Mon. Not. Roy. Astron. Soc.*, 78:3–28, 1917. 2

[9] A. Friedmann. Über die Krümmung des Raumes. *Z. Phys.*, 10(377):377–386, 1922. English translation: On the Curvature of Space. *Gen. Rel. and Grav.*, 31(12):1991–2000, 1999. 2, 4

[10] G. Lemaitre. A homogeneous universe of constant mass and increasing radius accounting for the radial velocity of extra-galactic nebulae. *Mon. Not. Roy. Astron. Soc.*, 91:483–490, 1931. 2, 4

[11] H. P. Robertson. Relativistic cosmology. *Rev. Mod. Phys.*, 5:62–90, January 1933. 2, 4

[12] A. G. Walker. Complete Symmetry in Flat Space. *J. London Math. Soc.*, 19:219, 1944. 2, 4

[13] P. A. R. Ade et al. Planck 2015 results. XIII. Cosmological parameters. *Astron. Astrophys.*, 594:A13, 2016. 2, 3, 6, 8, 9, 10, 21, 26, 27, 29, 34, 35, 57, 63, 64, 70, 72, 86, 101, 102, 109, 110, 121, 125, 126, 127, 128, 133, 160

[14] A. G. Riess et al. Observational evidence from supernovae for an accelerating universe and a cosmological constant. *Astron. J.*, 116:1009–1038, 1998. 3

[15] S. Perlmutter et al. Measurements of Omega and Lambda from 42 high redshift supernovae. *Astrophys. J.*, 517:565–586, 1999. 3

[16] J. C. Kapteyn. First Attempt at a Theory of the Arrangement and Motion of the Sidereal System. *Astrophys. J.*, vol. 55:302, 1922. 3, 31

[17] J. H. Oort. The force exerted by the stellar system in the direction perpendicular to the galactic plane and some related problems. *Bull. Astron. Inst. Netherlands*, 6:249–287, 1932. 3, 31

[18] F. Zwicky. Die Rotverschiebung von extragalaktischen Nebeln. *Helv. Phys. Acta*, 6:110–127, 1933. 3, 32

[19] F. Zwicky. On the Masses of Nebulae and of Clusters of Nebulae. *Astrophys. J.*, 86:217–246, 1937. 3, 32

[20] H. W. Babcock. The rotation of the Andromeda Nebula. *Lick Observatory Bulletin*, 19:41–51, 1939. 3

[21] V. C. Rubin and W. K. J. Ford. Rotation of the Andromeda Nebula from a Spectroscopic Survey of Emission Regions. *Astrophys. J.*, 159:379–403, 1970. 3, 31

[22] K. C. Freeman. On the disks of spiral and SO Galaxies. *Astrophys. J.*, 160:811, 1970. [Erratum: Astrophys. J. 161, 802 (1970)]. 3, 31

[23] J. P. Ostriker, P. J. E. Peebles, and A. Yahil. The size and mass of galaxies, and the mass of the universe. *Astrophys. J.*, 193:L1–L4, 1974. 3, 31

[24] V. C. Rubin, N. Thonnard, and W. K. J. Ford. Extended rotation curves of high-luminosity spiral galaxies. I - The angle between the rotation axis of the nucleus and the outer disk of NGC 3672. *Astrophys. J.*, 217:L1–L4, October 1977. 3

[25] A. H. Guth. Inflationary universe: A possible solution to the horizon and flatness problems. *Phys. Rev. D*, 23:347–356, January 1981. 3

[26] A. D. Linde. A New Inflationary Universe Scenario: A Possible Solution of the Horizon, Flatness, Homogeneity, Isotropy and Primordial Monopole Problems. *Phys. Lett.*, B108:389–393, 1982. 3

[27] A. Albrecht and P. J. Steinhardt. Cosmology for Grand Unified Theories with Radiatively Induced Symmetry Breaking. *Phys. Rev. Lett.*, 48:1220–1223, 1982. 3

[28] V. F. Mukhanov, H. A. Feldman, and Brandenberger R. H. Theory of cosmological perturbations. Part 1. Classical perturbations. Part 2. Quantum theory of perturbations. Part 3. Extensions. *Phys. Rept.*, 215:203–333, 1992. 3, 15, 21, 23

[29] V. Mukhanov. *Physical Foundations of Cosmology*. Cambridge University Press, Oxford, 2005. 3, 15, 21, 23, 25

[30] D. S. Gorbunov and V. A. Rubakov. *Introduction to the theory of the early universe: Cosmological perturbations and inflationary theory.* Hackensack, USA: World Scientific (2011) 489 p, 2011. 3, 15, 21, 23, 25, 26, 27

[31] E. Gawiser and J. Silk. The Cosmic microwave background radiation. *Phys. Rept.*, 333:245–267, 2000. 8

[32] C. Patrignani et al. Review of Particle Physics. *Chin. Phys.*, C40(10):100001, 2016. 8, 46, 51, 56, 72, 106

[33] G. F. Smoot et al. Structure in the COBE differential microwave radiometer first year maps. *Astrophys. J.*, 396:L1–L5, 1992. 8, 34

[34] A. D. Linde. Particle physics and inflationary cosmology. *Contemp. Concepts Phys.*, 5:1–362, 1990. 9, 10, 52, 111

[35] H. P. Nilles. Supersymmetry, Supergravity and Particle Physics. *Phys. Rept.*, 110:1–162, 1984. 10, 52

[36] S. B. Giddings, S. Kachru, and J. Polchinski. Hierarchies from fluxes in string compactifications. *Phys. Rev.*, D66:106006, 2002. 10

[37] A. A. Starobinsky. Stochastic de Sitter (inflationary) stage in the early Universe. *Lect. Notes Phys.*, 246:107–126, 1986. 10, 52, 108

[38] A. D. Linde. Hard art of the universe creation (stochastic approach to tunneling and baby universe formation). *Nucl. Phys.*, B372:421–442, 1992. 10, 52, 108

[39] A. D. Linde, D. A. Linde, and A. Mezhlumian. From the Big Bang theory to the theory of a stationary universe. *Phys. Rev.*, D49:1783–1826, 1994. 10

[40] A. Riotto. Inflation and the theory of cosmological perturbations. In *Astroparticle physics and cosmology. Proceedings: Summer School, Trieste, Italy, Jun 17-Jul 5 2002*, pages 317–413, 2002. 10, 19

[41] D. H. Lyth and A. R. Liddle. *The primordial density perturbation: Cosmology, inflation and the origin of structure*. Cambridge University Press, Cambridge, UK, 2009. 10, 19, 98, 99

[42] A. D. Linde. Chaotic inflation. *Physics Letters B*, 129(3):177–181, 1983. 13, 98

[43] H. Kodama and M. Sasaki. Cosmological Perturbation Theory. *Prog. Theor. Phys. Suppl.*, 78:1–166, 1984. 15, 21, 23

[44] D. Baumann. Inflation. In *Physics of the large and the small, TASI 09, proceedings of the Theoretical Advanced Study Institute in Elementary Particle Physics, Boulder, Colorado, USA, 1-26 June 2009*, pages 523–686, 2011. 15, 19, 21, 23

[45] M. E. Peskin and D. V. Schroeder. *An Introduction to quantum field theory*. Reading, USA: Addison-Wesley (1995) 842 p, 1995. 18, 19, 168, 169

[46] S. Dodelson. *Modern Cosmology*. Academic Press, Amsterdam, 2003. 19, 29, 41

[47] T. S. Bunch and P. C. W. Davies. Quantum Field Theory in de Sitter Space: Renormalization by Point Splitting. *Proc. Roy. Soc. Lond.*, A360:117–134, 1978. 19

[48] M. D. Schwartz. *Quantum Field Theory and the Standard Model*. Cambridge University Press, 2014. 19

[49] P. A. R. Ade et al. Planck 2015 results. XVII. Constraints on primordial non-Gaussianity. *Astron. Astrophys.*, 594:A17, 2016. 19, 23

[50] A. R. Liddle and D. H. Lyth. COBE, gravitational waves, inflation and extended inflation. *Phys. Lett.*, B291:391–398, 1992. 20

[51] E. R. Harrison. Fluctuations at the threshold of classical cosmology. *Phys. Rev.*, D1:2726–2730, 1970. 21

[52] Y. B. Zeldovich. A Hypothesis, unifying the structure and the entropy of the universe. *Mon. Not. Roy. Astron. Soc.*, 160:1P–3P, 1972. 21

[53] J. M. Maldacena. Non-Gaussian features of primordial fluctuations in single field inflationary models. *JHEP*, 05:013, 2003. 21

[54] D. H. Lyth. What would we learn by detecting a gravitational wave signal in the cosmic microwave background anisotropy? *Phys. Rev. Lett.*, 78:1861–1863, 1997. 22, 23

[55] P. A. R. Ade et al. Improved Constraints on Cosmology and Foregrounds from BICEP2 and Keck Array Cosmic Microwave Background Data with Inclusion of 95 GHz Band. *Phys. Rev. Lett.*, 116:031302, 2016. 23, 101, 103

[56] E. W. Kolb and M. S. Turner. The Early Universe. *Front. Phys.*, 69:1–547, 1990. 23, 29, 41, 54, 55, 56, 57, 59, 61, 63, 72, 88, 89, 90, 103, 111, 167

[57] V. A. Rubakov. Cosmology. In *Proceedings, 2011 European School of High-Energy Physics (ESHEP 2011)*, pages 151–195, 2014. 28

[58] G. Bertone and D. Hooper. A History of Dark Matter. *Submitted to: Rev. Mod. Phys.*, 2016. 30

[59] H. W. Babcock. The rotation of the Andromeda Nebula. *Lick Observatory Bulletin*, 19:41–51, 1939. 31

[60] L. M. J. S. Volders. Neutral hydrogen in M 33 and M 101. *Bulletin of the Astronomical Institutes of the Netherlands*, 14:323, September 1959. 31

[61] C. J. Peterson, V. C. Rubin, W. K. Ford, Jr., and M. S. Roberts. Extended rotation curves of high-luminosity spiral galaxies. III - The spiral galaxy NGC 7217. *Astrophys. J.*, 226:770–776, December 1978. 31

[62] G. R. Blumenthal, S. M. Faber, J. R. Primack, and M. J. Rees. Formation of galaxies and large-scale structure with cold dark matter. *Nature*, 311:517–525, 1984. 31, 34, 36

[63] V. Springel et al. Simulations of the formation, evolution and clustering of galaxies and quasars. *Nature*, 435:629–636, June 2005. 31, 34

[64] S. McAlpine et al. The EAGLE simulations of galaxy formation: public release of halo and galaxy catalogues. *Astron. Comput.*, 15:72–89, 2016. 31, 34

[65] J. F. Navarro, C. S. Frenk, and S. D. M. White. The Structure of cold dark matter halos. *Astrophys. J.*, 462:563–575, 1996. 31

[66] J. Einasto. Kinematics and dynamics of stellar systems. *Trudy Inst. Astrofiz. Alma-Ata*, 51(87), 1965. 31

[67] A. Burkert. The Structure of dark matter halos in dwarf galaxies. *IAU Symp.*, 171:175, 1996. [Astrophys. J.447,L25(1995)]. 31

[68] Y. Sofue and V. Rubin. Rotation curves of spiral galaxies. *Ann. Rev. Astron. Astrophys.*, 39:137–174, 2001. 32

[69] R. R. Munoz et al. Exploring Halo Substructure with Giant Stars: The Dynamics and Metallicity of the Dwarf Spheroidal in Bootes. *Astrophys. J.*, 650:L51–L54, 2006. 32

[70] N. Kaiser and G. Squires. Mapping the dark matter with weak gravitational lensing. *Astrophys. J.*, 404:441–450, February 1993. 32

[71] P. Schneider. Detection of (dark) matter concentrations via weak gravitational lensing. *Mon. Not. Roy. Astron. Soc.*, 283:837–853, 1996. 32

[72] D. M. Wittman et al. Detection of weak gravitational lensing distortions of distant galaxies by cosmic dark matter at large scales. *Nature*, 405:143–149, 2000. 32

[73] D. Clowe et al. A direct empirical proof of the existence of dark matter. *Astrophys. J.*, 648:L109–L113, 2006. 32, 38

[74] R. Massey, T. Kitching, and J. Richard. The dark matter of gravitational lensing. *Rept. Prog. Phys.*, 73:086901, 2010. 32

[75] A. G. Bergmann, V. Petrosian, and R. Lynds. Gravitational lens models of arcs in clusters. *Astrophys. J.*, 350:23–35, February 1990. 32

[76] D. Clowe, A. Gonzalez, and M. Markevitch. Weak lensing mass reconstruction of the interacting cluster 1E0657-558: Direct evidence for the existence of dark matter. *Astrophys. J.*, 604:596–603, 2004. 33

[77] M. Markevitch et al. A Textbook example of a bow shock in the merging galaxy cluster 1E0657-56. *Astrophys. J.*, 567:L27, 2002. 33

[78] https://apod.nasa.gov/apod/ap170115.html, 2016. 33

[79] W. H. Tucker, H. Tananbaum, and R. A. Remillard. A search for 'failed clusters' of galaxies. *Astrophys. J.*, 444:532–547, May 1995. 33

[80] M. Markevitch et al. Direct constraints on the dark matter self-interaction cross-section from the merging galaxy cluster 1E0657-56. *Astrophys. J.*, 606:819–824, 2004. 33, 36

[81] http://chandra.harvard.edu/photo/2008/macs/, 2016. 33

[82] http://spacetelescope.org/images/heic0709a/, 2016. 33

[83] M. Bradac et al. Revealing the properties of dark matter in the merging cluster MACSJ0025.4-1222. *Astrophys. J.*, 687:959, 2008. 33

[84] M. J. Jee et al. Discovery of a Ringlike Dark Matter Structure in the Core of the Galaxy Cluster Cl 0024+17. *Astrophys. J.*, 661:728–749, 2007. 33

[85] P. J. E. Peebles. Large scale background temperature and mass fluctuations due to scale invariant primeval perturbations. *Astrophys. J.*, 263:L1–L5, 1982. 34, 36

[86] A. D. Chernin. The Rest Mass of Primordial Neutrinos and Gravitational Instability in the Hot Universe. *Sov. Astr.*, 25:14–16, February 1981. 34, 36

[87] W. Hu and S. Dodelson. Cosmic microwave background anisotropies. *Ann. Rev. Astron. Astrophys.*, 40:171–216, 2002. 35

[88] M. Tegmark et al. Cosmological Constraints from the SDSS Luminous Red Galaxies. *Phys. Rev.*, D74:123507, 2006. 34, 39

[89] W. J. Percival et al. The shape of the SDSS DR5 galaxy power spectrum. *Astrophys. J.*, 657:645–663, 2007. 34, 39

[90] S. Cole et al. The 2dF Galaxy Redshift Survey: Power-spectrum analysis of the final dataset and cosmological implications. *Mon. Not. Roy. Astron. Soc.*, 362:505–534, 2005. 34, 39

[91] S. Burles, K. M. Nollett, and M. S. Turner. Big bang nucleosynthesis predictions for precision cosmology. *Astrophys. J.*, 552:L1–L6, 2001. 34, 39

[92] R. H. Cyburt. Primordial nucleosynthesis for the new cosmology: Determining uncertainties and examining concordance. *Phys. Rev.*, D70:023505, 2004. 34, 39

[93] G. Steigman. Primordial Nucleosynthesis in the Precision Cosmology Era. *Ann. Rev. Nucl. Part. Sci.*, 57:463–491, 2007. 34, 39

[94] B. D. Fields, K. Freese, and D. S. Graff. Chemical abundance constraints on white dwarfs as halo dark matter. *Astrophys. J.*, 534:265–276, 2000. 34

[95] B. D. Fields, P. Molaro, and S. Sarkar. Big-Bang Nucleosynthesis. *Chin. Phys.*, C38, 2014. 34, 39, 133

[96] D. Kirkman et al. The cosmological baryon density from the deuterium-to-hydrogen ratio in qso absorption systems: D/h toward q1243+3047. *The Astrophysical Journal Supplement Series*, 149(1):1, 2003. 34, 39

[97] M. Viel, G. D. Becker, J. S. Bolton, and M. G. Haehnelt. Warm dark matter as a solution to the small scale crisis: New constraints from high redshift Lyman-α forest data. *Phys. Rev.*, D88:043502, 2013. 35, 65, 81

[98] J. S. Bolton, M. G. Haehnelt, M. Viel, and V. Springel. The Lyman-alpha forest opacity and the metagalactic hydrogen ionization rate at z 2-4. *Mon. Not. Roy. Astron. Soc.*, 357:1178, 2005. 35

[99] L. Randall, J. Scholtz, and J. Unwin. Cores in Dwarf Galaxies from Fermi Repulsion. *Mon. Not. Roy. Astron. Soc.*, 467:1515, 2017. 35

[100] W. Hu, R. Barkana, and A. Gruzinov. Cold and fuzzy dark matter. *Phys. Rev. Lett.*, 85:1158–1161, 2000. 35

[101] L. Hui, J. P. Ostriker, S. Tremaine, and E. Witten. Ultralight scalars as cosmological dark matter. *Phys. Rev.*, D95(4):043541, 2017. 35

[102] P. S. Corasaniti, S. Agarwal, D. J. E. Marsh, and S. Das. Constraints on dark matter scenarios from measurements of the galaxy luminosity function at high redshifts. *Phys. Rev.*, D95(8):083512, 2017. 35

[103] B. J. Carr and S. W. Hawking. Black holes in the early Universe. *Mon. Not. Roy. Astron. Soc.*, 168:399–415, 1974. 35, 40

[104] R. Massey et al. The behaviour of dark matter associated with four bright cluster galaxies in the 10 kpc core of Abell 3827. *Mon. Not. Roy. Astron. Soc.*, 449(4):3393–3406, 2015. 36

[105] F. Kahlhoefer, K. Schmidt-Hoberg, J. Kummer, and S. Sarkar. On the interpretation of dark matter self-interactions in Abell 3827. *Mon. Not. Roy. Astron. Soc.*, 452(1):L54–L58, 2015. 36

[106] D. N. Spergel and P. J. Steinhardt. Observational evidence for selfinteracting cold dark matter. *Phys. Rev. Lett.*, 84:3760–3763, 2000. 36

[107] J. Zavala, M. Vogelsberger, and M. G. Walker. Constraining Self-Interacting Dark Matter with the Milky Way's dwarf spheroidals. *Monthly Notices of the Royal Astronomical Society: Letters*, 431:L20–L24, 2013. 36

[108] M. Rocha et al. Cosmological Simulations with Self-Interacting Dark Matter I: Constant Density Cores and Substructure. *Mon. Not. Roy. Astron. Soc.*, 430:81–104, 2013. 36

[109] R. J. Wilkinson, J. Lesgourgues, and C. Boehm. Using the CMB angular power spectrum to study Dark Matter-photon interactions. *JCAP*, 1404:026, 2014. 36

[110] C. Boehm et al. Using the Milky Way satellites to study interactions between cold dark matter and radiation. *Mon. Not. Roy. Astron. Soc.*, 445:L31–L35, 2014. 36

[111] S. W. Randall et al. Constraints on the Self-Interaction Cross-Section of Dark Matter from Numerical Simulations of the Merging Galaxy Cluster 1E 0657-56. *Astrophys. J.*, 679:1173–1180, 2008. 36

[112] D. Harvey et al. The non-gravitational interactions of dark matter in colliding galaxy clusters. *Science*, 347:1462–1465, 2015. 36

[113] J. F. Navarro, C. S. Frenk, and S. D. M. White. The Structure of cold dark matter halos. *Astrophys. J.*, 462:563–575, 1996. 36

[114] M. Boylan-Kolchin, J. S. Bullock, and M. Kaplinghat. Too big to fail? The puzzling darkness of massive Milky Way subhaloes. *Mon. Not. Roy. Astron. Soc.*, 415:L40, 2011. 36, 65

[115] A. A. Klypin, A. V. Kravtsov, O. Valenzuela, and F. Prada. Where are the missing Galactic satellites? *Astrophys. J.*, 522:82–92, 1999. 36, 65

[116] B. Moore et al. Dark matter substructure within galactic halos. *Astrophys. J.*, 524:L19–L22, 1999. 36, 65

[117] D. Feldman, Z. Liu, and P. Nath. The Stueckelberg Z-prime Extension with Kinetic Mixing and Milli-Charged Dark Matter From the Hidden Sector. *Phys. Rev.*, D75:115001, 2007. 36

[118] S. Davidson, S. Hannestad, and G. Raffelt. Updated bounds on millicharged particles. *JHEP*, 05:003, 2000. 36

[119] S. D. McDermott, H. Yu, and K. M. Zurek. Turning off the Lights: How Dark is Dark Matter? *Phys. Rev.*, D83:063509, 2011. 36

[120] K. Kadota, T. Sekiguchi, and H. Tashiro. A new constraint on millicharged dark matter from galaxy clusters. 2016. 36

[121] A. Kamada, K. Kohri, T. Takahashi, and N. Yoshida. Effects of electrically charged dark matter on cosmic microwave background anisotropies. *Phys. Rev.*, D95(2):023502, 2017. 36

[122] M. Pospelov and T. ter Veldhuis. Direct and indirect limits on the electromagnetic form-factors of WIMPs. *Phys. Lett.*, B480:181–186, 2000. 36

[123] K. Sigurdson et al. Dark-matter electric and magnetic dipole moments. *Phys. Rev.*, D70:083501, 2004. [Erratum: Phys. Rev.D73,089903(2006)]. 36

[124] V. Barger, W. Keung, and D. Marfatia. Electromagnetic properties of dark matter: Dipole moments and charge form factor. *Phys. Lett.*, B696:74–78, 2011. 36

[125] P. Gondolo and K. Kadota. Late Kinetic Decoupling of Light Magnetic Dipole Dark Matter. *JCAP*, 1606:012, 2016. 36

[126] Y. Gao, C. M. Ho, and R. J. Scherrer. Anapole Dark Matter at the LHC. *Phys. Rev.*, D89(4):045006, 2014. 36

[127] A. Jenkins, C. S. Frenk, F. R. Pearce, P. A. Thomas, J. M. Colberg, Simon D. M. White, H. M. P. Couchman, J. A. Peacock, G. Efstathiou, and A. H. Nelson. Evolution of structure in cold dark matter universes. *Astrophys. J.*, 499:20, 1998. 36

[128] P. Bode, J. P. Ostriker, and N. Turok. Halo formation in warm dark matter models. *Astrophys. J.*, 556:93–107, 2001. 36, 65

[129] M. R. Lovell et al. The Haloes of Bright Satellite Galaxies in a Warm Dark Matter Universe. *Mon. Not. Roy. Astron. Soc.*, 420:2318–2324, 2012. 36, 65

[130] S. Paduroiu, Y. Revaz, and D. Pfenniger. Structure formation in warm dark matter cosmologies: Top-Bottom Upside-Down. 2015. 36, 65

[131] R. Kennedy, C. Frenk, S. Cole, and A. Benson. Constraining the warm dark matter particle mass with Milky Way satellites. *Mon. Not. Roy. Astron. Soc.*, 442(3):2487–2495, 2014. 36, 65

[132] W. B. Lin, D. H. Huang, X. Zhang, and R. H. Brandenberger. Nonthermal production of WIMPs and the subgalactic structure of the universe. *Phys. Rev. Lett.*, 86:954, 2001. 36, 65

[133] R. Foot and S. Vagnozzi. Dissipative hidden sector dark matter. *Phys. Rev.*, D91:023512, 2015. 37

[134] R. Foot. Dissipative dark matter explains rotation curves. *Phys. Rev.*, D91(12):123543, 2015. 37

[135] O. Chashchina, R. Foot, and Z. Silagadze. Radial acceleration relation and dissipative dark matter. *Phys. Rev.*, D95(2):023009, 2017. 37

[136] R. Foot and S. Vagnozzi. Solving the small-scale structure puzzles with dissipative dark matter. *JCAP*, 1607(07):013, 2016. 37

[137] J. Fan, A. Katz, L. Randall, and M. Reece. Dark-Disk Universe. *Phys. Rev. Lett.*, 110(21):211302, 2013. 37

[138] J. Fan, A. Katz, L. Randall, and M. Reece. Double-Disk Dark Matter. *Phys. Dark Univ.*, 2:139–156, 2013. 37

[139] J. I. Read et al. A dark matter disc in three cosmological simulations of Milky Way mass galaxies. *Mon. Not. Roy. Astron. Soc.*, 397:44, 2009. 37

[140] M. Milgrom. A modification of the Newtonian dynamics as a possible alternative to the hidden mass hypothesis. *Astrophys. J.*, 270:365–370, July 1983. 37

[141] M. Milgrom. A Modification of the Newtonian dynamics: Implications for galaxies. *Astrophys. J.*, 270:371–383, 1983. 37

[142] M. Milgrom. A modification of the Newtonian dynamics: implications for galaxy systems. *Astrophys. J.*, 270:384–389, 1983. 37

[143] K. G. Begeman, A. H. Broeils, and R. H. Sanders. Extended rotation curves of spiral galaxies: Dark haloes and modified dynamics. *Mon. Not. Roy. Astron. Soc.*, 249:523, 1991. 38

[144] R. H. Sanders and S. S. McGaugh. Modified Newtonian dynamics as an alternative to dark matter. *Ann. Rev. Astron. Astrophys.*, 40:263–317, 2002. 38

[145] M. Milgrom and R. H. Sanders. MOND rotation curves of very low mass spiral galaxies. *Astrophys. J.*, 658:L17, 2007. 38

[146] R. H. Sanders and E. Noordermeer. Confrontation of MOND with the rotation curves of early-type disc galaxies. *Mon. Not. Roy. Astron. Soc.*, 379:702–710, 2007. 38

[147] S. McGaugh and M. Milgrom. Andromeda Dwarfs in Light of MOND. II. Testing Prior Predictions. *Astrophys. J.*, 775:139, 2013. 38

[148] R. B. Tully and J. R. Fisher. A New method of determining distances to galaxies. *Astron. Astrophys.*, 54:661–673, 1977. 38

[149] S. S. McGaugh, J. M. Schombert, G. D. Bothun, and W. J. G. de Blok. The Baryonic Tully-Fisher relation. *Astrophys. J.*, 533:L99–L102, 2000. 38

[150] S. S. McGaugh. A Novel Test of the Modified Newtonian Dynamics with Gas Rich Galaxies. *Phys. Rev. Lett.*, 106:121303, 2011. [Erratum: Phys. Rev. Lett.107,229901(2011)]. 38

[151] J. D. Bekenstein. Relativistic gravitation theory for the MOND paradigm. *Phys. Rev.*, D70:083509, 2004. [Erratum: Phys. Rev.D71,069901(2005)]. 38

[152] J. W. Moffat. Scalar-tensor-vector gravity theory. *JCAP*, 0603:004, 2006. 38

[153] J. Bruneton and G. Esposito-Farese. Field-theoretical formulations of MOND-like gravity. *Phys. Rev.*, D76:124012, 2007. [Erratum: Phys. Rev.D76,129902(2007)]. 38

[154] A. Aguirre, J. Schaye, and E. Quataert. Problems for MOND in clusters and the Ly-alpha forest. *Astrophys. J.*, 561:550, 2001. 38

[155] R. H. Sanders. Clusters of galaxies with modified Newtonian dynamics (MOND). *Mon. Not. Roy. Astron. Soc.*, 342:901, 2003. 38

[156] R. H. Sanders. Neutrinos as cluster dark matter. *Mon. Not. Roy. Astron. Soc.*, 380:331–338, 2007. 38

[157] G. W. Angus and A. Diaferio. The abundance of galaxy clusters in MOND: Cosmological simulations with massive neutrinos. *Mon. Not. Roy. Astron. Soc.*, 417:941, 2011. 38

[158] M. Milgrom. Marriage à-la-MOND: Baryonic dark matter in galaxy clusters and the cooling flow puzzle. *New Astron. Rev.*, 51:906–915, 2008. 38

[159] G. W. Angus, A. Diaferio, B. Famaey, and K. J. van der Heyden. Cosmological simulations in MOND: the cluster scale halo mass function with light sterile neutrinos. *Mon. Not. Roy. Astron. Soc.*, 436:202, 2013. 38

[160] G. W. Angus et al. Modified Baryonic Dynamics: two-component cosmological simulations with light sterile neutrinos. *JCAP*, 1410(10):079, 2014. 38

[161] G. W. Angus, H. Shan, H. Zhao, and B. Famaey. On the Law of Gravity, the Mass of Neutrinos and the Proof of Dark Matter. *Astrophys. J.*, 654:L13–L16, 2007. 38

[162] G. W. Angus, B. Famaey, and A. Diaferio. Equilibrium configurations of 11eV sterile neutrinos in MONDian galaxy clusters. *Mon. Not. Roy. Astron. Soc.*, 402:395, 2010. 38

[163] C. Skordis, D. F. Mota, P. G. Ferreira, and C. Boehm. Large Scale Structure in Bekenstein's theory of relativistic Modified Newtonian Dynamics. *Phys. Rev. Lett.*, 96:011301, 2006. 38

[164] X. Xu, B. Wang, and P. Zhang. Testing the tensor-vector-scalar Theory with the latest cosmological observations. *Phys. Rev.*, D92(8):083505, 2015. 38

[165] A. Abramovici and Z. Vager. Test of Newton's Second Law at Small Accelerations. *Phys. Rev.*, D34:3240–3241, 1986. 38

[166] J. H. Gundlach et al. Laboratory Test of Newton's Second Law for Small Accelerations. *Phys. Rev. Lett.*, 98:150801, 2007. 38

[167] S. Little and M. Little. Laboratory test of Newton's law of gravity for small accelerations. *Class. Quant. Grav.*, 31(19):195008, 2014. 38

[168] P. D. Mannheim. Making the Case for Conformal Gravity. *Found. Phys.*, 42:388–420, 2012. 38

[169] A. H. Chamseddine and V. Mukhanov. Mimetic Dark Matter. *JHEP*, 11:135, 2013. 38

[170] A. H. Chamseddine, V. Mukhanov, and A. Vikman. Cosmology with Mimetic Matter. *JCAP*, 1406:017, 2014. 38

[171] A. Golovnev. On the recently proposed Mimetic Dark Matter. *Phys. Lett.*, B728:39–40, 2014. 38

[172] S. Mukohyama. Dark matter as integration constant in Horava-Lifshitz gravity. *Phys. Rev.*, D80:064005, 2009. 38

[173] X. Calmet and I. Kuntz. What is modified gravity and how to differentiate it from particle dark matter? *Eur. Phys. J.*, C77(2):132, 2017. 38

[174] E. P. Verlinde. On the Origin of Gravity and the Laws of Newton. *JHEP*, 04:029, 2011. 38

[175] E. P. Verlinde. Emergent Gravity and the Dark Universe. *SciPost Phys.*, 2:016, 2017. 38

[176] M. Milgrom and R. H. Sanders. Perspective on MOND emergence from Verlinde's "emergent gravity" and its recent test by weak lensing. 2016. 38

[177] F. Lelli, S. S. McGaugh, and J. M. Schombert. Testing Verlinde's Emergent Gravity with the Radial Acceleration Relation. *Mon. Not. Roy. Astron. Soc.*, 468:L68, 2017. 38

[178] D. Zeng. $d_\ell(z)$ and BAO in the emergent gravity and the dark universe. 2017. 38

[179] K. Griest. Galactic microlensing as a method of detecting massive compact halo objects. *Astrophys. J.*, 366:412–421, January 1991. 39

[180] D. Pfenniger, F. Combes, and L. Martinet. Is dark matter in spiral galaxies cold gas? 1. Observational constraints and dynamical clues about galaxy evolution. *Astron. Astrophys.*, 285:79–83, 1994. 39

[181] F. De Paolis, G. Ingrosso, P. Jetzer, and M. Roncadelli. A Case for a baryonic dark halo. *Phys. Rev. Lett.*, 74:14–17, 1995. 39

[182] R. N. Henriksen and L. M. Widrow. Hydrogen clouds and the MACHO / EROS events. *Astrophys. J.*, 441:70, 1995. 39

[183] O. Gerhard and J. Silk. Baryonic dark halos: A Model with MACHOs and cold gas globules. *IAU Symp.*, 171:167, 1996. 39

[184] E. Witten. Cosmic Separation of Phases. *Phys. Rev.*, D30:272–285, 1984. 39

[185] Bryan W. Lynn. Liquid Phases in SU(3) Chiral Perturbation Theory ($SU3^{PT}_{\chi}$): Drops of Strange Chiral Nucleon Liquid ($S\chi NL$) and Ordinary Chiral Heavy Nuclear Liquid (χNL). 2010. 39

[186] B. W. Lynn, A. E. Nelson, and N. Tetradis. STRANGE BARYON MATTER. *Nucl. Phys.*, B345:186–209, 1990. 39

[187] A. De Rujula and S. L. Glashow. Nuclearites: A Novel Form of Cosmic Radiation. *Nature*, 312:734–737, 1984. 39

[188] E. Farhi and R. L. Jaffe. Strange Matter. *Phys. Rev.*, D30:2379, 1984. 39

[189] A. Kusenko and M. E. Shaposhnikov. Supersymmetric Q balls as dark matter. *Phys. Lett.*, B418:46–54, 1998. 39

[190] D. M. Jacobs, G. D. Starkman, and B. W. Lynn. Macro Dark Matter. *Mon. Not. Roy. Astron. Soc.*, 450(4):3418–3430, 2015. 39

[191] D. M. Jacobs, G. D. Starkman, and A. Weltman. Resonant bar detector constraints on macro dark matter. *Phys. Rev.*, D91(11):115023, 2015. 39

[192] D. Cyncynates, J. Chiel, J. Sidhu, and G. D. Starkman. Reconsidering seismological constraints on the available parameter space of macroscopic dark matter. *Phys. Rev.*, D95(6):063006, 2017. [Addendum: Phys. Rev.D95,no.12,129903(2017)]. 39

[193] G. Gelmini. TASI 2014 Lectures: The Hunt for Dark Matter. In *Theoretical Advanced Study Institute in Elementary Particle Physics: Journeys Through the Precision Frontier: Amplitudes for Colliders (TASI 2014) Boulder, Colorado, June 2-27, 2014*, 2015. 39

[194] B. Paczynski. Gravitational microlensing by the galactic halo. *Astrophys. J.*, 304:1–5, May 1986. 39

[195] J. J. Dalcanton et al. Observational limits on Omega in stars, brown dwarfs, and stellar remnants from gravitational microlensing. *Astrophys. J.*, 424:550–568, April 1994. 39

[196] C. Alcock et al. The MACHO project: Microlensing results from 5.7 years of LMC observations. *Astrophys. J.*, 542:281–307, 2000. 39

[197] P. Tisserand et al. Limits on the Macho Content of the Galactic Halo from the EROS-2 Survey of the Magellanic Clouds. *Astron. Astrophys.*, 469:387–404, 2007. 39

[198] R. A. Allsman et al. MACHO project limits on black hole dark matter in the 1-30 solar mass range. *Astrophys. J.*, 550:L169, 2001. 39

[199] C. Alcock et al. Direct detection of a microlens in the milky way. *Nature*, 414:617–619, 2001. 39

[200] K. Griest, A. M. Cieplak, and M. J. Lehner. New Limits on Primordial Black Hole Dark Matter from an Analysis of Kepler Source Microlensing Data. *Phys. Rev. Lett.*, 111(18):181302, 2013. 39

[201] K. Griest, A. M. Cieplak, and M. J. Lehner. Experimental Limits on Primordial Black Hole Dark Matter from the First 2 yr of Kepler Data. *Astrophys. J.*, 786(2):158, 2014. 39

[202] L. Wyrzykowski et al. The OGLE View of Microlensing towards the Magellanic Clouds. III. Ruling out sub-solar MACHOs with the OGLE-III LMC data. *Mon. Not. Roy. Astron. Soc.*, 413:493, 2011. 39

[203] L. Wyrzykowski et al. The OGLE View of Microlensing towards the Magellanic Clouds. IV. OGLE-III SMC Data and Final Conclusions on MACHOs. *Mon. Not. Roy. Astron. Soc.*, 416:2949, 2011. 39

[204] J. Yoo, J. Chaname, and A. Gould. The end of the MACHO era: limits on halo dark matter from stellar halo wide binaries. *Astrophys. J.*, 601:311–318, 2004. 39

[205] D. S. Graff and K. Freese. Analysis of a hubble space telescope search for red dwarfs: limits on baryonic matter in the galactic halo. *Astrophys. J.*, 456:L49, 1996. 39

[206] J. Najita, G. Tiede, and J. Carr. From stars to super-planets: the low-mass imf in the young cluster ic348. *Astrophys. J.*, 541:977–1003, 2000. 39

[207] K. Freese, B. Fields, and D. Graff. Limits on stellar objects as the dark matter of our halo: nonbaryonic dark matter seems to be required. *Nucl. Phys. Proc. Suppl.*, 80:0305, 2000. 39

[208] R. H. Cyburt, B. D. Fields, and K. A. Olive. Primordial nucleosynthesis in light of WMAP. *Phys. Lett.*, B567:227–234, 2003. 39

[209] A. Dar. Dark matter and big bang nucleosynthesis. *Astrophys. J.*, 449:550, 1995. [,21(1995)]. 39

[210] S. Burles and D. Tytler. The Deuterium abundance towards Q1937-1009. *Astrophys. J.*, 499:699, 1998. 39

[211] S. Burles and D. Tytler. The Deuterium abundance toward QSO 1009+2956. *Astrophys. J.*, 507:732–744, 1998. 39

[212] J. M. O'Meara et al. The Deuterium to hydrogen abundance ratio towards a fourth QSO: HS 0105 + 1619. *Astrophys. J.*, 552:718–730, 2001. 39

[213] M. Rauch et al. The Opacity of the Lyman alpha forest and implications for omega(baryon) and the ionizing background. *Astrophys. J.*, 489:7–20, 1997. 39

[214] M. Fukugita, C. J. Hogan, and P. J. E. Peebles. The Cosmic baryon budget. *Astrophys. J.*, 503:518, 1998. 40

[215] S. W. Hawking. Gravitationally collapsed objects of very low mass. *Mon. Not. Roy. Astron. Soc.*, 152:75, 1971. 40

[216] S. W. Hawking. Black Holes From Cosmic Strings. *Phys. Lett.*, B231:237–239, 1989. 40

[217] M. Crawford and D. N. Schramm. Spontaneous Generation of Density Perturbations in the Early Universe. *Nature*, 298:538–540, 1982. 40

[218] K. Jedamzik and J. C. Niemeyer. Primordial black hole formation during first order phase transitions. *Phys. Rev.*, D59:124014, 1999. 40

[219] B. J. Carr and J. E. Lidsey. Primordial black holes and generalized constraints on chaotic inflation. *Phys. Rev.*, D48:543–553, 1993. 40

[220] E. Erfani. Primordial Black Holes Formation from Particle Production during Inflation. *JCAP*, 1604(04):020, 2016. 40

[221] A. M. Green and K. A. Malik. Primordial black hole production due to preheating. *Phys. Rev.*, D64:021301, 2001. 40

[222] T. Suyama, T. Tanaka, B. Bassett, and H. Kudoh. Are black holes overproduced during preheating? *Phys. Rev.*, D71:063507, 2005. 40

[223] H. Niikura et al. Microlensing constraints on $10^{-10}M_{\odot}$-scale primordial black holes from high-cadence observation of M31 with Hyper Suprime-Cam. 2017. 40

[224] B. Carr, F. Kuhnel, and M. Sandstad. Primordial Black Holes as Dark Matter. *Phys. Rev.*, D94(8):083504, 2016. 40, 41

[225] A. M. Green. Microlensing and dynamical constraints on primordial black hole dark matter with an extended mass function. *Phys. Rev.*, D94(6):063530, 2016. 40, 41

[226] S. Clesse and J. Garcia-Bellido. The clustering of massive Primordial Black Holes as Dark Matter: measuring their mass distribution with Advanced LIGO. *Phys. Dark Univ.*, 10:002, 2016. 40

[227] J. C. Niemeyer and K. Jedamzik. Near-critical gravitational collapse and the initial mass function of primordial black holes. *Phys. Rev. Lett.*, 80:5481–5484, 1998. 41

[228] F. Kuhnel, C. Rampf, and M. Sandstad. Effects of Critical Collapse on Primordial Black-Hole Mass Spectra. *Eur. Phys. J.*, C76(2):93, 2016. 41

[229] B. P. Abbott et al. Observation of Gravitational Waves from a Binary Black Hole Merger. *Phys. Rev. Lett.*, 116(6):061102, 2016. 41

[230] C. Weinheimer. The Neutrino mass direct measurements. In *Neutrino telescopes. Proceedings, 10th International Workshop, Venice, Italy, March 11-14, 2003. Vol. 1+2*, pages 335–344, 2003. 41

[231] N. Palanque-Delabrouille et al. Neutrino masses and cosmology with Lyman-alpha forest power spectrum. *JCAP*, 1511(11):011, 2015. 41

[232] G. Steigman and M. S. Turner. Cosmological Constraints on the Properties of Weakly Interacting Massive Particles. *Nucl. Phys.*, B253:375–386, 1985. 42

[233] G. Jungman, M. Kamionkowski, and K. Griest. Supersymmetric dark matter. *Phys. Rept.*, 267:195–373, 1996. 42

[234] T. Appelquist, H. Cheng, and B. A. Dobrescu. Bounds on universal extra dimensions. *Phys. Rev.*, D64:035002, 2001. 42

[235] G. Gelmini and P. Gondolo. Neutralino with the right cold dark matter abundance in (almost) any supersymmetric model. *Phys. Rev.*, D74:023510, 2006. 42, 57, 94

[236] P. Gondolo and G. Gelmini. Cosmic abundances of stable particles: Improved analysis. *Nucl. Phys.*, B360:145–179, 1991. 42, 55, 60, 169, 170, 171

[237] D. Cline. A Brief Status of the Direct Search for WIMP Dark Matter. 2014. 42

[238] J. Conrad. Indirect Detection of WIMP Dark Matter: a compact review. In *Interplay between Particle and Astroparticle physics (IPA2014) London, United Kingdom, August 18-22, 2014*, 2014. 42

[239] J. Monroe and P. Fisher. Neutrino Backgrounds to Dark Matter Searches. *Phys. Rev.*, D76:033007, 2007. 42

[240] J. Jaeckel and A. Ringwald. The Low-Energy Frontier of Particle Physics. *Ann. Rev. Nucl. Part. Sci.*, 60:405–437, 2010. 42

[241] A. Ringwald. Axions and Axion-Like Particles. In *Proceedings, 49th Rencontres de Moriond on Electroweak Interactions and Unified Theories: La Thuile, Italy, March 15-22, 2014*, pages 223–230, 2014. 42, 43, 132

[242] J. Goldstone. Field Theories with Superconductor Solutions. *Nuovo Cim.*, 19:154–164, 1961. 42

[243] R. D. Peccei and H. R. Quinn. CP Conservation in the Presence of Instantons. *Phys. Rev. Lett.*, 38:1440–1443, 1977. 43, 106, 132

[244] R. D. Peccei and H. R. Quinn. Constraints Imposed by CP Conservation in the Presence of Instantons. *Phys. Rev.*, D16:1791–1797, 1977. 43, 106

[245] S. Weinberg. A New Light Boson? *Phys. Rev. Lett.*, 40:223–226, 1978. 43, 107, 132

[246] F. Wilczek. Problem of Strong P and T Invariance in the Presence of Instantons. *Phys. Rev. Lett.*, 40:279–282, 1978. 43, 107, 132

[247] G. G. Raffelt. *Stars as laboratories for fundamental physics*. Chicago, USA: Univ. Pr. (1996) 664 p, 1996. 43, 107, 122, 123

[248] G. G. Raffelt. Particle physics from stars. *Ann. Rev. Nucl. Part. Sci.*, 49:163–216, 1999. 43, 107

[249] G. G. Raffelt. Astrophysical axion bounds. *Lect. Notes Phys.*, 741:51–71, 2008. [,51(2006)]. 43, 107, 122

[250] J. Preskill, M. B. Wise, and F. Wilczek. Cosmology of the Invisible Axion. *Phys. Lett.*, B120:127–132, 1983. 43, 68, 107, 108, 167

[251] G. 't Hooft. Symmetry Breaking Through Bell-Jackiw Anomalies. *Phys. Rev. Lett.*, 37:8–11, 1976. 43, 106, 107, 126, 132

[252] G. 't Hooft. Computation of the Quantum Effects Due to a Four-Dimensional Pseudoparticle. *Phys. Rev.*, D14:3432–3450, 1976. [Erratum: Phys. Rev. D18,2199(1978)]. 43, 106, 107, 126, 132

[253] O. Wantz and E. P. S. Shellard. Axion Cosmology Revisited. *Phys. Rev.*, D82:123508, 2010. 43, 68, 108

[254] L. Visinelli and P. Gondolo. Axion cold dark matter in non-standard cosmologies. *Phys. Rev.*, D81:063508, 2010. 43, 68

[255] F. Wilczek. Axions and Family Symmetry Breaking. *Phys. Rev. Lett.*, 49:1549–1552, 1982. 43

[256] Y. Chikashige, R. N. Mohapatra, and R. D. Peccei. Are There Real Goldstone Bosons Associated with Broken Lepton Number? *Phys. Lett.*, B98:265–268, 1981. 43

[257] G. B. Gelmini and M. Roncadelli. Left-Handed Neutrino Mass Scale and Spontaneously Broken Lepton Number. *Phys. Lett.*, B99:411–415, 1981. 43

[258] P. Svrcek and E. Witten. Axions In String Theory. *JHEP*, 06:051, 2006. 43, 48, 132

[259] L.J. Hall, K. Jedamzik, J. March-Russell, et al. Freeze-In Production of FIMP Dark Matter. *JHEP*, 03:080, 2010. 43, 44, 58, 59, 65, 81

[260] J. McDonald. Thermally generated gauge singlet scalars as self interacting dark matter. *Phys. Rev. Lett.*, 88:091304, 2002. 43, 58, 65

[261] J. McDonald. Warm Dark Matter via Ultra-Violet Freeze-In: Reheating Temperature and Non-Thermal Distribution for Fermionic Higgs Portal Dark Matter. *JCAP*, 1608(08):035, 2016. 44, 65, 66

[262] L. Covi, H. Kim, J. E. Kim, and L. Roszkowski. Axinos as dark matter. *JHEP*, 05:033, 2001. 44

[263] K. J. Bae, K. Choi, and S. H. Im. Effective Interactions of Axion Supermultiplet and Thermal Production of Axino Dark Matter. *JHEP*, 08:065, 2011. 44

[264] G. F. Giudice, A. Riotto, and I. Tkachev. Thermal and nonthermal production of gravitinos in the early universe. *JHEP*, 11:036, 1999. 44

[265] K. Choi, K. Hwang, H. B. Kim, and T. Lee. Cosmological gravitino production in gauge mediated supersymmetry breaking models. *Phys. Lett.*, B467:211–217, 1999. 44

[266] Y. Fukuda et al. Evidence for oscillation of atmospheric neutrinos. *Phys. Rev. Lett.*, 81:1562–1567, 1998. 44

[267] Q. R. Ahmad et al. Measurement of the rate of $\nu_e + d \rightarrow p + p + e^-$ interactions produced by ^8B solar neutrinos at the Sudbury Neutrino Observatory. *Phys. Rev. Lett.*, 87:071301, 2001. 44

[268] M. C. Gonzalez-Garcia and M. Maltoni. Phenomenology with Massive Neutrinos. *Phys. Rept.*, 460:1–129, 2008. 44

[269] S. Dodelson and L. M. Widrow. Sterile-neutrinos as dark matter. *Phys. Rev. Lett.*, 72:17–20, 1994. 44, 67

[270] X. Shi and G. M. Fuller. A New dark matter candidate: Nonthermal sterile neutrinos. *Phys. Rev. Lett.*, 82:2832–2835, 1999. 44

[271] T. Asaka, M. Shaposhnikov, and A. Kusenko. Opening a new window for warm dark matter. *Phys. Lett.*, B638:401–406, 2006. 44

[272] A. Merle. keV sterile neutrino Dark Matter. In *Neutrino Oscillation Workshop (NOW 2016): International Workshop on Neutrino and Astroparticle Physics (NOW 2016) Otranto (Lecce), Italy, September 4-11, 2016*, 2017. 44

[273] M. W. Goodman and E. Witten. Detectability of Certain Dark Matter Candidates. *Phys. Rev.*, D31:3059, 1985. 45

[274] I. Wasserman. Possibility of Detecting Heavy Neutral Fermions in the Galaxy. *Phys. Rev.*, D33:2071–2078, 1986. 45

[275] A. K. Drukier, K. Freese, and D. N. Spergel. Detecting Cold Dark Matter Candidates. *Phys. Rev.*, D33:3495–3508, 1986. 45

[276] C. E. Aalseth et al. Cogent: A search for low-mass dark matter using p-type point contact germanium detectors. *Phys. Rev. D*, 88:012002, Jul 2013. 45

[277] R. Bernabei et al. DAMA/LIBRA results and perspectives. *Bled Workshops Phys.*, 17(2):1–7, 2016. 45

[278] G. Angloher et al. Results on light dark matter particles with a low-threshold CRESST-II detector. *Eur. Phys. J.*, C76(1):25, 2016. 45

[279] E. Aprile et al. Dark Matter Results from 225 Live Days of XENON100 Data. *Phys. Rev. Lett.*, 109:181301, 2012. 45

[280] D. S. Akerib et al. Results from a search for dark matter in the complete LUX exposure. *Phys. Rev. Lett.*, 118(2):021303, 2017. 45

[281] R. Agnese et al. New Results from the Search for Low-Mass Weakly Interacting Massive Particles with the CDMS Low Ionization Threshold Experiment. *Phys. Rev. Lett.*, 116(7):071301, 2016. 45

[282] A. Tan et al. Dark Matter Results from First 98.7 Days of Data from the PandaX-II Experiment. *Phys. Rev. Lett.*, 117(12):121303, 2016. 45

[283] T. Marrodn Undagoitia and L. Rauch. Dark matter direct-detection experiments. *J. Phys.*, G43(1):013001, 2016. 45, 47

[284] J. Liu, X. Chen, and X. Ji. Current status of direct dark matter detection experiments. *Nature Phys.*, 13:212–216, 2017. 45

[285] C. E. Aalseth et al. Results from a Search for Light-Mass Dark Matter with a P-type Point Contact Germanium Detector. *Phys. Rev. Lett.*, 106:131301, 2011. 45

[286] C. E. Aalseth et al. Search for an Annual Modulation in a P-type Point Contact Germanium Dark Matter Detector. *Phys. Rev. Lett.*, 107:141301, 2011. 45

[287] R. Bernabei et al. First results from DAMA/LIBRA and the combined results with DAMA/NaI. *Eur. Phys. J.*, C56:333–355, 2008. 45

[288] R. Bernabei et al. New results from DAMA/LIBRA. *Eur. Phys. J.*, C67:39–49, 2010. 45

[289] G. Angloher et al. Results from 730 kg days of the CRESST-II Dark Matter Search. *Eur. Phys. J.*, C72:1971, 2012. 45

[290] R. Agnese et al. Silicon Detector Dark Matter Results from the Final Exposure of CDMS II. *Phys. Rev. Lett.*, 111(25):251301, 2013. 45

[291] R. Agnese et al. Silicon detector results from the first five-tower run of CDMS II. *Phys. Rev.*, D88:031104, 2013. [Erratum: Phys. Rev.D88,no.5,059901(2013)]. 45

[292] M. Cirelli. Indirect Searches for Dark Matter: a status review. *Pramana*, 79:1021–1043, 2012. 45

[293] M. Cirelli. Status of Indirect (and Direct) Dark Matter searches. 2015. 45

[294] J. M. Gaskins. A review of indirect searches for particle dark matter. *Contemp. Phys.*, 57(4):496–525, 2016. 45

[295] S. Gentile. The Alpha Magnetic Spectrometer on the International Space Station. In *Proceedings, 28th International Cosmic Ray Conference (ICRC 2003): Tsukuba, Japan, July 31-August 7, 2003*, pages 2145–2148, 2003. 46

[296] W. B. Atwood et al. The Large Area Telescope on the Fermi Gamma-Ray Space Telescope Mission. *Astrphys. J.*, 697:1071–1102, June 2009. 46

[297] M. Kestel. Design and status of IceCube. *Nucl. Instrum. Meth.*, A535:139–142, 2004. 46

[298] V. Bonvicini et al. The pamela experiment in space. *Nuclear Instruments and Methods in Physics Research Section A: Accelerators, Spectrometers, Detectors and Associated Equipment*, 461(1-3):262–268, 2001. 8th Pisa Meeting on Advanced Detectors. 46

[299] H. Hofmann. The HESS project. In *International Symposium: The Universe Viewed in Gamma Rays Kashiwa, Chiba, Japan, September 25-28, 2002*, page T03, 2002. 46

[300] S. W. Barwick et al. Measurements of the cosmic ray positron fraction from 1-GeV to 50-GeV. *Astrophys. J.*, 482:L191–L194, 1997. 46, 73

[301] O. Adriani et al. PAMELA results on the cosmic-ray antiproton flux from 60 MeV to 180 GeV in kinetic energy. *Phys. Rev. Lett.*, 105:121101, 2010. 46, 74

[302] M. Aguilar et al. First Result from the Alpha Magnetic Spectrometer on the International Space Station: Precision Measurement of the Positron Fraction in Primary Cosmic Rays of 0.5–350 GeV. *Phys. Rev. Lett.*, 110:141102, 2013. 46, 73

[303] M. Aguilar et al. Cosmic-ray positron fraction measurement from 1 to 30-GeV with AMS-01. *Phys. Lett.*, B646:145–154, 2007. 46, 73

[304] M. Ackermann et al. Measurement of separate cosmic-ray electron and positron spectra with the Fermi Large Area Telescope. *Phys. Rev. Lett.*, 108:011103, 2012. 46, 73

[305] M. Ajello et al. Fermi-LAT Observations of High-Energy γ-Ray Emission Toward the Galactic Center. *Astrophys. J.*, 819(1):44, 2016. 46, 74

[306] M. G. Aartsen et al. Evidence for High-Energy Extraterrestrial Neutrinos at the IceCube Detector. *Science*, 342:1242856, 2013. 46, 75

[307] M. G. Aartsen et al. Observation of High-Energy Astrophysical Neutrinos in Three Years of IceCube Data. *Phys. Rev. Lett.*, 113:101101, 2014. 46, 75

[308] M. G. Aartsen et al. The IceCube Neutrino Observatory - Contributions to ICRC 2015 Part II: Atmospheric and Astrophysical Diffuse Neutrino Searches of All Flavors. In *Proceedings, 34th International Cosmic Ray Conference (ICRC 2015): The Hague, The Netherlands, July 30-August 6, 2015*, 2015. 46, 75

[309] E. Bulbul et al. Detection of An Unidentified Emission Line in the Stacked X-ray spectrum of Galaxy Clusters. *Astrophys. J.*, 789:13, 2014. 46

[310] A. Boyarsky, O. Ruchayskiy, D. Iakubovskyi, and J. Franse. Unidentified Line in X-Ray Spectra of the Andromeda Galaxy and Perseus Galaxy Cluster. *Phys. Rev. Lett.*, 113:251301, 2014. 46

[311] T. E. Jeltema and S. Profumo. Discovery of a 3.5 keV line in the Galactic Centre and a critical look at the origin of the line across astronomical targets. *Mon. Not. Roy. Astron. Soc.*, 450(2):2143–2152, 2015. 46

[312] D. Hooper, P. Blasi, and P. D. Serpico. Pulsars as the Sources of High Energy Cosmic Ray Positrons. *JCAP*, 0901:025, 2009. 46, 74

[313] M. Di Mauro et al. Interpretation of AMS-02 electrons and positrons data. *JCAP*, 1404:006, 2014. 46, 74

[314] D. Hooper, I. Cholis, T. Linden, and K. Fang. HAWC Observations Strongly Favor Pulsar Interpretations of the Cosmic-Ray Positron Excess. 2017. 46, 74

[315] M. Di Mauro. The origin of the Fermi-LAT γ-ray background. In *14th Marcel Grossmann Meeting on Recent Developments in Theoretical and Experimental General Relativity, Astrophysics, and Relativistic Field Theories (MG14) Rome, Italy, July 12-18, 2015*, 2016. 46, 74

[316] S. Profumo. An observable electron-positron anisotropy cannot be generated by dark matter. *JCAP*, 1502(02):043, 2015. 46, 74

[317] E. Carlson and S. Profumo. Cosmic Ray Protons in the Inner Galaxy and the Galactic Center Gamma-Ray Excess. *Phys. Rev.*, D90(2):023015, 2014. 46, 74

[318] J. Petrovic, P. D. Serpico, and G. Zaharijas. Galactic Center gamma-ray "excess" from an active past of the Galactic Centre? *JCAP*, 1410(10):052, 2014. 46, 74

[319] D. Gaggero et al. Towards a realistic astrophysical interpretation of the gamma-ray Galactic center excess. *JCAP*, 1512(12):056, 2015. 46, 74

[320] K. N. Abazajian. The Consistency of Fermi-LAT Observations of the Galactic Center with a Millisecond Pulsar Population in the Central Stellar Cluster. *JCAP*, 1103:010, 2011. 46, 74

[321] N. Mirabal. Dark matter vs. Pulsars: Catching the impostor. *Mon. Not. Roy. Astron. Soc.*, 436:2461, 2013. 46, 74

[322] R. Bartels, S. Krishnamurthy, and C. Weniger. Strong support for the millisecond pulsar origin of the Galactic center GeV excess. *Phys. Rev. Lett.*, 116(5):051102, 2016. 47, 74

[323] S. K. Lee et al. Evidence for Unresolved γ-Ray Point Sources in the Inner Galaxy. *Phys. Rev. Lett.*, 116(5):051103, 2016. 47, 74

[324] H. A. Clark, P. Scott, R. Trotta, and G. F. Lewis. Substructure considerations rule out dark matter interpretation of Fermi Galactic Center excess. 2016. 47, 74

[325] M. Ackermann et al. The spectrum of isotropic diffuse gamma-ray emission between 100 MeV and 820 GeV. *Astrophys. J.*, 799:86, 2015. 47, 74

[326] M. Ackermann et al. Dark matter constraints from observations of 25 Milky Way satellite galaxies with the Fermi Large Area Telescope. *Phys. Rev.*, D89:042001, 2014. 47, 74, 79

[327] A. J. R. Sanderson, T. J. Ponman, and E. O'Sullivan. A statistically-selected Chandra sample of 20 galaxy clusters. 1. Temperature and cooling time profiles. *Mon. Not. Roy. Astron. Soc.*, 372:1496–1508, 2006. 47, 74

[328] K. Belotsky, R. Budaev, A. Kirillov, and M. Laletin. Fermi-LAT kills dark matter interpretations of AMS-02 data. Or not? *JCAP*, 1701(01):021, 2017. 47, 74

[329] M. Laletin. A no-go theorem for the dark matter interpretation of the positron anomaly. In *18th Frascati Spring School "Bruno Touschek" in Nuclear, Subnuclear and Astroparticle Physics & 5th Young Researchers Workshop on Physics Challenges in the LHC Era Frascati, Rome, Italy, May 9-13, 2016*, 2016. 47, 74

[330] M. H. Chan. Indirect constraints on the dark matter interpretation of excess positrons seen by AMS-02. *Phys. Rev.*, D92:083504, 2015. 47, 74

[331] M. G. Aartsen et al. All-sky Search for Time-integrated Neutrino Emission from Astrophysical Sources with 7 yr of IceCube Data. *Astrophys. J.*, 835(2):151, 2017. 47, 75

[332] S. Adrian-Martinez et al. The First Combined Search for Neutrino Point-sources in the Southern Hemisphere With the Antares and Icecube Neutrino Telescopes. *Astrophys. J.*, 823(1):65, 2016. 47, 75

[333] M. G. Aartsen et al. Lowering IceCube's Energy Threshold for Point Source Searches in the Southern Sky. *Astrophys. J.*, 824(2):L28, 2016. 47, 75

[334] L. Evans and P. Bryant. LHC Machine. *JINST*, 3:S08001, 2008. 47

[335] B. Barish and J. E. Brau. The International Linear Collider. *Int. J. Mod. Phys.*, A28(27):1330039, 2013. 47

[336] O. Buchmueller, C. Doglioni, and L. Wang. Search for dark matter at colliders. *Nature Phys.*, 13:217–223, 2017. 47

[337] A. Shcherbakova. Search for dark matter with the ATLAS detector at the LHC. *IOP Conf. Series: J. of Phys.: Conf. Series*, 798:012100, 2017. 47

[338] M. Aaboud et al. Search for dark matter at $\sqrt{s} = 13$ TeV in final states containing an energetic photon and large missing transverse momentum with the ATLAS detector. *Eur. Phys. J.*, C77(6):393, 2017. 48

[339] P. Sikivie. Experimental Tests of the Invisible Axion. *Phys. Rev. Lett.*, 51:1415–1417, 1983. [Erratum: Phys. Rev. Lett.52,695(1984)]. 48

[340] P. Sikivie. Detection Rates for 'Invisible' Axion Searches. *Phys. Rev.*, D32:2988, 1985. [Erratum: Phys. Rev.D36,974(1987)]. 48

[341] L. Krauss, J. Moody, F. Wilczek, and D. E. Morris. Calculations for Cosmic Axion Detection. *Phys. Rev. Lett.*, 55:1797, 1985. 48

[342] D. B. Kaplan. Opening the Axion Window. *Nucl. Phys.*, B260:215–226, 1985. 48

[343] G. Grilli di Cortona, E. Hardy, J. Pardo Vega, and G. Villadoro. The QCD axion, precisely. *JHEP*, 01:034, 2016. 48, 122, 126

[344] S. J. Asztalos et al. Design and performance of the ADMX SQUID-based microwave receiver. *Nucl. Instrum. Meth.*, A656:39–44, 2011. 49

[345] P. W. Graham and S. Rajendran. New Observables for Direct Detection of Axion Dark Matter. *Phys. Rev.*, D88:035023, 2013. 49

[346] D. Budker et al. Proposal for a Cosmic Axion Spin Precession Experiment (CASPEr). *Phys. Rev.*, X4(2):021030, 2014. 49, 109, 130

[347] E. Arik et al. Probing eV-scale axions with CAST. *JCAP*, 0902:008, 2009. 49

[348] I. G. Irastorza et al. Towards a new generation axion helioscope. *JCAP*, 1106:013, 2011. 49

[349] R. Ballou et al. Latest Results of the OSQAR Photon Regeneration Experiment for Axion-Like Particle Search. In *Proceedings, 10th Patras Workshop on Axions, WIMPs and WISPs (AXION-WIMP 2014): Geneva, Switzerland, June 29-July 4, 2014*, pages 125–130, 2014. 49

[350] R. Bahre et al. Any light particle search II -Technical Design Report. *JINST*, 8:T09001, 2013. 49

[351] M. Betz et al. First results of the CERN Resonant Weakly Interacting sub-eV Particle Search (CROWS). *Phys. Rev.*, D88(7):075014, 2013. 50

[352] M. Goodsell, J. Jaeckel, J. Redondo, and A. Ringwald. Naturally Light Hidden Photons in LARGE Volume String Compactifications. *JHEP*, 11:027, 2009. 50

[353] A. E. Nelson and J. Scholtz. Dark Light, Dark Matter and the Misalignment Mechanism. *Phys. Rev.*, D84:103501, 2011. 50

[354] N. Woollett et al. Preliminary Results of the CASCADE Hidden Sector Photon Search. In *Proceedings, 11th Patras Workshop on Axions, WIMPs and WISPs (Axion-WIMP 2015): Zaragoza, Spain, June 22-26, 2015*, pages 179–182, 2015. 50

[355] G. Zavattini et al. Measuring the magnetic birefringence of vacuum: the PVLAS experiment. *Int. J. Mod. Phys.*, A27:1260017, 2012. 50

[356] B. Majorovits and J. Redondo. MADMAX: A new Dark Matter Axion Search using a Dielectric Haloscope. In *12th Patras Workshop on Axions,*

WIMPs and WISPs (AXION-WIMP 2016) Jeju Island, South Korea, June 20-24, 2016, 2016. 50

[357] T. Gherghetta, C. F. Kolda, and S. P. Martin. Flat directions in the scalar potential of the supersymmetric standard model. *Nucl. Phys.*, B468:37–58, 1996. 52

[358] B. de Carlos, J. A. Casas, F. Quevedo, and E. Roulet. Model independent properties and cosmological implications of the dilaton and moduli sectors of 4-d strings. *Phys. Lett.*, B318:447–456, 1993. 52

[359] K. Enqvist and A. Mazumdar. Cosmological consequences of MSSM flat directions. *Phys. Rept.*, 380:99–234, 2003. 52, 103, 108, 132

[360] Y. Shtanov, J. H. Traschen, and R. H. Brandenberger. Universe reheating after inflation. *Phys. Rev.*, D51:5438–5455, 1995. 52, 88

[361] L. Kofman, A. D. Linde, and A. A. Starobinsky. Reheating after inflation. *Phys. Rev. Lett.*, 73:3195–3198, 1994. 52, 88

[362] P. Adshead, J. T. Giblin, T. R. Scully, and E. I. Sfakianakis. Gauge-preheating and the end of axion inflation. *JCAP*, 1512(12):034, 2015. 52

[363] M. Srednicki, R. Watkins, and K. A. Olive. Calculations of Relic Densities in the Early Universe. *Nucl. Phys.*, B310:693, 1988. 55

[364] L. Kofman, A. D. Linde, and A. A. Starobinsky. Towards the theory of reheating after inflation. *Phys. Rev.*, D56:3258–3295, 1997. 57, 88, 138

[365] G. F. Giudice, E. W. Kolb, and A. Riotto. Largest temperature of the radiation era and its cosmological implications. *Phys. Rev.*, D64:023508, 2001. 57, 91, 95

[366] D. J. H. Chung, E. W. Kolb, and A. Riotto. Superheavy dark matter. *Phys. Rev.*, D59:023501, 1999. 57, 59

[367] D. J. H. Chung, E. W. Kolb, and A. Riotto. Production of massive particles during reheating. *Phys. Rev.*, D60:063504, 1999. 57, 58, 59, 75, 89, 91, 92, 115, 127

[368] R. Allahverdi, A. Ferrantelli, J. Garcia-Bellido, and A. Mazumdar. Non-perturbative production of matter and rapid thermalization after MSSM inflation. *Phys. Rev.*, D83:123507, 2011. 57, 114, 135

[369] N. Fornengo, A. Riotto, and S. Scopel. Supersymmetric dark matter and the reheating temperature of the universe. *Phys. Rev.*, D67:023514, 2003. 57

[370] J. L. Feng, A. Rajaraman, and F. Takayama. Superweakly interacting massive particles. *Phys. Rev. Lett.*, 91:011302, 2003. 58

[371] R. Allahverdi and M. Drees. Production of massive stable particles in inflaton decay. *Phys. Rev. Lett.*, 89:091302, 2002. 58, 68

[372] R. Cowsik and J. McClelland. An Upper Limit on the Neutrino Rest Mass. *Phys. Rev. Lett.*, 29:669–670, 1972. 59, 63

[373] R. J. Scherrer and M. S. Turner. On the Relic, Cosmic Abundance of Stable Weakly Interacting Massive Particles. *Phys. Rev.*, D33:1585, 1986. [Erratum: Phys. Rev.D34,3263(1986)]. 59, 60

[374] M. Drees, M. Kakizaki, and S. Kulkarni. The Thermal Abundance of Semi-Relativistic Relics. *Phys. Rev.*, D80:043505, 2009. 59, 60, 64

[375] G. Bertone, D. Hooper, and J. Silk. Particle dark matter: Evidence, candidates and constraints. *Phys. Rept.*, 405:279–390, 2005. 60

[376] G. Steigman, B. Dasgupta, and J. F. Beacom. Precise Relic WIMP Abundance and its Impact on Searches for Dark Matter Annihilation. *Phys. Rev.*, D86:023506, 2012. 60, 61, 62

[377] M. Laine and Y. Schroder. Quark mass thresholds in QCD thermodynamics. *Phys. Rev.*, D73:085009, 2006. 61

[378] K. Griest and D. Seckel. Three exceptions in the calculation of relic abundances. *Phys. Rev.*, D43:3191–3203, 1991. 62

[379] J. R. Bond, G. Efstathiou, and J. Silk. Massive Neutrinos and the Large Scale Structure of the Universe. *Phys. Rev. Lett.*, 45:1980–1984, 1980. 64

[380] J. R. Bond and A. S. Szalay. The Collisionless Damping of Density Fluctuations in an Expanding Universe. *Astrophys. J.*, 274:443–468, 1983. 64

[381] J. Hamann and J. Hasenkamp. A new life for sterile neutrinos: resolving inconsistencies using hot dark matter. *JCAP*, 1310:044, 2013. 64

[382] K. M. Zurek. Multi-Component Dark Matter. *Phys. Rev.*, D79:115002, 2009. 64, 71, 102

[383] D. Feldman, Z. Liu, P. Nath, and G. Peim. Multicomponent Dark Matter in Supersymmetric Hidden Sector Extensions. *Phys. Rev.*, D81:095017, 2010. 64, 71, 102

[384] J. Hisano, K. Kohri, and M. M. Nojiri. Neutralino warm dark matter. *Phys. Lett.*, B505:169–176, 2001. 65

[385] G. Gelmini and C. E. Yaguna. Constraints on Minimal SUSY models with warm dark matter neutralinos. *Phys. Lett.*, B643:241–245, 2006. 65

[386] A. Boyarsky, J. Lesgourgues, O. Ruchayskiy, and M. Viel. Lyman-alpha constraints on warm and on warm-plus-cold dark matter models. *JCAP*, 0905:012, 2009. 65

[387] M. Blennow, E. Fernandez-Martinez, and B. Zaldivar. Freeze-in through portals. *JCAP*, 1401:003, 2014. 66

[388] A. H. Campos et al. Bounds on direct couplings of superheavy metastable particles to the inflaton field from ultrahigh-energy cosmic ray events. *Mod. Phys. Lett.*, A17:2179–2188, 2002. 68

[389] M. Kawasaki, K. Kohri, and N. Sugiyama. Cosmological constraints on late time entropy production. *Phys. Rev. Lett.*, 82:4168, 1999. 69

[390] S. Hannestad. What is the lowest possible reheating temperature? *Phys. Rev.*, D70:043506, 2004. 69

[391] F. Takahashi. Gravitino dark matter from inflaton decay. *Phys. Lett.*, B660:100–106, 2008. 70

[392] M. Fairbairn and J. Zupan. Dark matter with a late decaying dark partner. *JCAP*, 0907:001, 2009. 71

[393] K. Griest and M. Kamionkowski. Unitarity Limits on the Mass and Radius of Dark Matter Particles. *Phys. Rev. Lett.*, 64:615, 1990. 71, 80

[394] G. Mangano et al. Relic neutrino decoupling including flavor oscillations. *Nucl. Phys.*, B729:221–234, 2005. 72

[395] C. Boehm, M. J. Dolan, and C. McCabe. A Lower Bound on the Mass of Cold Thermal Dark Matter from Planck. *JCAP*, 1308:041, 2013. 72, 78

[396] K. M. Nollett and G. Steigman. BBN And The CMB Constrain Neutrino Coupled Light WIMPs. *Phys. Rev.*, D91(8):083505, 2015. 72, 78

[397] R. J. Wilkinson, A. C. Vincent, C. Boehm, and C. McCabe. Ruling out the light WIMP explanation of the galactic 511 keV line. *Phys. Rev.*, D94(10):103525, 2016. 72, 78

[398] C. Armendariz-Picon and J. T. Neelakanta. How Cold is Cold Dark Matter? *JCAP*, 1403:049, 2014. 72

[399] K. Jedamzik. Big bang nucleosynthesis constraints on hadronically and electromagnetically decaying relic neutral particles. *Phys. Rev.*, D74:103509, 2006. 73

[400] J. Hisano et al. Cosmic Rays from Dark Matter Annihilation and Big-Bang Nucleosynthesis. *Phys. Rev.*, D79:083522, 2009. 73

[401] B. Henning and H. Murayama. Constraints on Light Dark Matter from Big Bang Nucleosynthesis. 2012. 73, 79

[402] M. Kawasaki, K. Kohri, T. Moroi, and Y. Takaesu. Revisiting Big-Bang Nucleosynthesis Constraints on Dark-Matter Annihilation. *Phys. Lett.*, B751:246–250, 2015. 73

[403] M. Kawasaki, K. Nakayama, and T. Sekiguchi. CMB Constraint on Dark Matter Annihilation after Planck 2015. *Phys. Lett.*, B756:212–215, 2016. 73

[404] S. Galli, F. Iocco, G. Bertone, and A. Melchiorri. CMB constraints on Dark Matter models with large annihilation cross-section. *Phys. Rev.*, D80:023505, 2009. 73

[405] T. R. Slatyer, N. Padmanabhan, and D. P. Finkbeiner. CMB Constraints on WIMP Annihilation: Energy Absorption During the Recombination Epoch. *Phys. Rev.*, D80:043526, 2009. 73

[406] M. S. Madhavacheril, N. Sehgal, and T. R. Slatyer. Current Dark Matter Annihilation Constraints from CMB and Low-Redshift Data. *Phys. Rev.*, D89:103508, 2014. 73, 79

[407] G. Huetsi, A. Hektor, and M. Raidal. Constraints on leptonically annihilating Dark Matter from reionization and extragalactic gamma background. *Astron. Astrophys.*, 505:999–1005, 2009. 73

[408] M. Cirelli, F. Iocco, and P. Panci. Constraints on Dark Matter annihilations from reionization and heating of the intergalactic gas. *JCAP*, 0910:009, 2009. 73

[409] G. Hutsi, J. Chluba, A. Hektor, and M. Raidal. WMAP7 and future CMB constraints on annihilating dark matter: implications on GeV-scale WIMPs. *Astron. Astrophys.*, 535:A26, 2011. 73

[410] S. Galli, F Iocco, G. Bertone, and A. Melchiorri. Updated CMB constraints on Dark Matter annihilation cross-sections. *Phys. Rev.*, D84:027302, 2011. 73

[411] J. M. Cline and P. Scott. Dark Matter CMB Constraints and Likelihoods for Poor Particle Physicists. *JCAP*, 1303:044, 2013. [Erratum: JCAP1305,E01(2013)]. 73

[412] L. Bergstrom et al. New limits on dark matter annihilation from AMS cosmic ray positron data. *Phys. Rev. Lett.*, 111:171101, 2013. 74, 80

[413] L. A. Cavasonza et al. Constraints on leptophilic dark matter from the AMS-02 experiment. *Astrophys. J.*, 839(1):36, 2017. 74, 80

[414] M. Cirelli, M. Kadastik, M. Raidal, and A. Strumia. Model-independent implications of the e+-, anti-proton cosmic ray spectra on properties of Dark Matter. *Nucl. Phys.*, B813:1–21, 2009. [Addendum: Nucl. Phys.B873,530(2013)]. 74

[415] H. Jin, Y. Wu, and Y. Zhou. Implications of the first AMS-02 measurement for dark matter annihilation and decay. *JCAP*, 1311:026, 2013. 74

[416] P. S. B. Dev, D. K. Ghosh, N. Okada, and I. Saha. Neutrino Mass and Dark Matter in light of recent AMS-02 results. *Phys. Rev.*, D89:095001, 2014. 74

[417] I. Cholis and D. Hooper. Dark Matter and Pulsar Origins of the Rising Cosmic Ray Positron Fraction in Light of New Data From AMS. *Phys. Rev.*, D88:023013, 2013. 74

[418] D. Hooper, T. Linden, and P. Mertsch. What Does The PAMELA Antiproton Spectrum Tell Us About Dark Matter? *JCAP*, 1503(03):021, 2015. 74

[419] C. Evoli et al. Antiprotons from dark matter annihilation in the Galaxy: astrophysical uncertainties. *Phys. Rev.*, D85:123511, 2012. 74

[420] M. Cirelli and G. Giesen. Antiprotons from Dark Matter: Current constraints and future sensitivities. *JCAP*, 1304:015, 2013. 74, 79

[421] M. Cirelli et al. Antiproton constraints on the GeV gamma-ray excess: a comprehensive analysis. *JCAP*, 1412(12):045, 2014. 74

[422] O. Adriani et al. A new measurement of the antiproton-to-proton flux ratio up to 100 GeV in the cosmic radiation. *Phys. Rev. Lett.*, 102:051101, 2009. 74

[423] M. Ackermann et al. Search for gamma-ray spectral lines with the Fermi large area telescope and dark matter implications. *Phys. Rev.*, D88:082002, 2013. 74, 79

[424] M. Ackermann et al. Fermi LAT Search for Dark Matter in Gamma-ray Lines and the Inclusive Photon Spectrum. *Phys. Rev.*, D86:022002, 2012. 74

[425] A. Ibarra, S. L. Gehler, and M. Pato. Dark matter constraints from box-shaped gamma-ray features. *JCAP*, 1207:043, 2012. 74

[426] M. Ackermann et al. Constraints on the Galactic Halo Dark Matter from Fermi-LAT Diffuse Measurements. *Astrophys. J.*, 761:91, 2012. 74, 79

[427] M. Ackermann et al. Constraints on Dark Matter Annihilation in Clusters of Galaxies with the Fermi Large Area Telescope. *JCAP*, 1005:025, 2010. 74

[428] D. Hooper, C. Kelso, and F. S. Queiroz. Stringent and Robust Constraints on the Dark Matter Annihilation Cross Section From the Region of the Galactic Center. *Astropart. Phys.*, 46:55–70, 2013. 74, 79

[429] D. Hooper and T. Linden. On The Origin Of The Gamma Rays From The Galactic Center. *Phys. Rev.*, D84:123005, 2011. 74

[430] M. Kaplinghat, T. Linden, and H. Yu. Galactic Center Excess in γ Rays from Annihilation of Self-Interacting Dark Matter. *Phys. Rev. Lett.*, 114(21):211303, 2015. 74

[431] K. K. Boddy et al. Boxes, Boosts, and Energy Duality: Understanding the Galactic-Center Gamma-Ray Excess through Dynamical Dark Matter. *Phys. Rev.*, D95(5):055024, 2017. 74

[432] F. Calore, I. Cholis, C. McCabe, and C. Weniger. A Tale of Tails: Dark Matter Interpretations of the Fermi GeV Excess in Light of Background Model Systematics. *Phys. Rev.*, D91(6):063003, 2015. 74

[433] B. Lu and H. Zong. Leptophilic dark matter in Galactic Center excess. *Phys. Rev.*, D93(8):083504, 2016. [Addendum: Phys. Rev.D93,no.8,089910(2016)]. 74

[434] A. Abramowski et al. Search for a Dark Matter annihilation signal from the Galactic Center halo with H.E.S.S. *Phys. Rev. Lett.*, 106:161301, 2011. 74

[435] A. Abramowski et al. H.E.S.S. observations of the globular clusters NGC 6388 and M 15 and search for a Dark Matter signal. *Astrophys. J.*, 735:12, 2011. 74

[436] A. Abramowski et al. Search for Photon-Linelike Signatures from Dark Matter Annihilations with H.E.S.S. *Phys. Rev. Lett.*, 110:041301, 2013. 74, 79

[437] R. Abbasi et al. Search for Dark Matter from the Galactic Halo with the IceCube Neutrino Observatory. *Phys. Rev.*, D84:022004, 2011. 75, 80

[438] M. G. Aartsen et al. Multipole analysis of IceCube data to search for dark matter accumulated in the Galactic halo. *Eur. Phys. J.*, C75(99):20, 2015. 75, 80

[439] R. Abbasi et al. Search for Neutrinos from Annihilating Dark Matter in the Direction of the Galactic Center with the 40-String IceCube Neutrino Observatory. 2012. 75, 80

[440] M. G. Aartsen et al. Search for Dark Matter Annihilation in the Galactic Center with IceCube-79. *Eur. Phys. J.*, C75(10):492, 2015. 75, 80

[441] M. G. Aartsen et al. IceCube Search for Dark Matter Annihilation in nearby Galaxies and Galaxy Clusters. *Phys. Rev.*, D88:122001, 2013. 75, 80

[442] B. Feldstein, A. Kusenko, S. Matsumoto, and T. T. Yanagida. Neutrinos at IceCube from Heavy Decaying Dark Matter. *Phys. Rev.*, D88(1):015004, 2013. 75

[443] A. Esmaili and P. D. Serpico. Are IceCube neutrinos unveiling PeV-scale decaying dark matter? *JCAP*, 1311:054, 2013. 75

[444] Y. Ema, R. Jinno, and T. Moroi. Cosmic-Ray Neutrinos from the Decay of Long-Lived Particle and the Recent IceCube Result. *Phys. Lett.*, B733:120–125, 2014. 75

[445] C. Chen, P. S. B. Dev, and A. Soni. Standard model explanation of the ultrahigh energy neutrino events at IceCube. *Phys. Rev.*, D89(3):033012, 2014. 75

[446] V. Barger, J. Learned, and S. Pakvasa. IceCube PeV Cascade Events Initiated by Electron-Antineutrinos at Glashow Resonance. *Phys. Rev.*, D87(3):037302, 2013. 75

[447] K. Murase and J. F. Beacom. Constraining Very Heavy Dark Matter Using Diffuse Backgrounds of Neutrinos and Cascaded Gamma Rays. *JCAP*, 1210:043, 2012. 75, 80

[448] P. Gondolo et al. DarkSUSY: Computing supersymmetric dark matter properties numerically. *JCAP*, 0407:008, 2004. 76

[449] G. Belanger, F. Boudjema, A. Pukhov, and A. Semenov. MicrOMEGAs 2.0: A Program to calculate the relic density of dark matter in a generic model. *Comput. Phys. Commun.*, 176:367–382, 2007. 76

[450] M. Backovic, K. Kong, and M. McCaskey. MadDM v.1.0: Computation of Dark Matter Relic Abundance Using MadGraph5. *Physics of the Dark Universe*, 5-6:18–28, 2014. 76

[451] M. Ackermann et al. Updated search for spectral lines from Galactic dark matter interactions with pass 8 data from the Fermi Large Area Telescope. *Phys. Rev.*, D91(12):122002, 2015. 79

[452] H. Abdalla et al. H.E.S.S. Limits on Linelike Dark Matter Signatures in the 100 GeV to 2 TeV Energy Range Close to the Galactic Center. *Phys. Rev. Lett.*, 117(15):151302, 2016. 79

[453] D. S. Akerib et al. First results from the LUX dark matter experiment at the Sanford Underground Research Facility. *Phys. Rev. Lett.*, 112:091303, 2014. 80

[454] M. Szydagis. The Present and Future of Searching for Dark Matter with LUX and LZ. In *38th International Conference on High Energy Physics (ICHEP 2016) Chicago, IL, USA, August 03-10, 2016*, 2016. 80

[455] S. Chatrchyan et al. Search for dark matter and large extra dimensions in monojet events in *pp* collisions at $\sqrt{s} = 7$ TeV. *JHEP*, 09:094, 2012. 80

[456] G. Aad et al. Search for dark matter candidates and large extra dimensions in events with a jet and missing transverse momentum with the ATLAS detector. *JHEP*, 04:075, 2013. 80

[457] M. Aaboud et al. Search for new phenomena in final states with an energetic jet and large missing transverse momentum in *pp* collisions at $\sqrt{s} = 13$ TeV using the ATLAS detector. *Phys. Rev.*, D94(3):032005, 2016. 80

[458] S. Chatrchyan et al. Search for Dark Matter and Large Extra Dimensions in pp Collisions Yielding a Photon and Missing Transverse Energy. *Phys. Rev. Lett.*, 108:261803, 2012. 80

[459] G. Aad et al. Search for dark matter candidates and large extra dimensions in events with a photon and missing transverse momentum in *pp* collision data at $\sqrt{s} = 7$ TeV with the ATLAS detector. *Phys. Rev. Lett.*, 110(1):011802, 2013. 80

[460] M. Aaboud et al. Search for new phenomena in events with a photon and missing transverse momentum in *pp* collisions at $\sqrt{s} = 13$ TeV with the ATLAS detector. *JHEP*, 06:059, 2016. 80

[461] G. Aad et al. Search for new phenomena in dijet mass and angular distributions from pp collisions at $\sqrt{s} = 13$ TeV with the ATLAS detector. *Phys. Lett.*, B754:302–322, 2016. 80

[462] M. Aaboud et al. Search for dark matter produced in association with a hadronically decaying vector boson in pp collisions at $\sqrt{s} = 13$ TeV with the ATLAS detector. *Phys. Lett.*, B763:251–268, 2016. 80

[463] A. M. Sirunyan et al. Search for dark matter produced with an energetic jet or a hadronically decaying W or Z boson at sqrt(s) = 13 TeV. 2017. 80

[464] M. Aaboud et al. Search for dark matter in association with a Higgs boson decaying to b-quarks in pp collisions at $\sqrt{s} = 13$ TeV with the ATLAS detector. *Phys. Lett.*, B765:11–31, 2017. 80

[465] The ATLAS collaboration. Search for new phenomena in events with missing transverse momentum and a Higgs boson decaying to two photons in pp collisions at $\sqrt{s} = 13$ TeV with the ATLAS detector. 2016. 80

[466] M. Beltran, D. Hooper, E. W. Kolb, and Z. C. Krusberg. Deducing the nature of dark matter from direct and indirect detection experiments in the absence of collider signatures of new physics. *Phys. Rev.*, D80:043509, 2009. 81

[467] A. Boyarsky, O. Ruchayskiy, and M. Shaposhnikov. The Role of sterile neutrinos in cosmology and astrophysics. *Ann. Rev. Nucl. Part. Sci.*, 59:191–214, 2009. 81

[468] A. Merle. keV Neutrino Model Building. *Int. J. Mod. Phys.*, D22:1330020, 2013. 81

[469] D. Boyanovsky. Free streaming in mixed dark matter. *Phys. Rev.*, D77:023528, 2008. 81

[470] F. L. Bezrukov and M. Shaposhnikov. The Standard Model Higgs boson as the inflaton. *Phys. Lett.*, B659:703–706, 2008. 86

[471] G. F. Giudice, M. Peloso, A. Riotto, et al. Production of massive fermions at preheating and leptogenesis. *JHEP*, 08:014, 1999. 88

[472] P. B. Greene and L. Kofman. On the theory of fermionic preheating. *Phys. Rev.*, D62:123516, 2000. 88

[473] J. McDonald. Inflaton condensate fragmentation in hybrid inflation models. *Phys. Rev.*, D66:043525, 2002. 88

[474] K. Enqvist, S. Kasuya, and A. Mazumdar. Reheating as a surface effect. *Phys. Rev. Lett.*, 89:091301, 2002. 88

[475] S. Coleman and E. Weinberg. Radiative corrections as the origin of spontaneous symmetry breaking. *Phys. Rev.*, D7:1888–1910, March 1973. 88

[476] L. F. Abbott, E. Farhi, and M. B. Wise. Particle Production in the New Inflationary Cosmology. *Phys. Lett.*, B117:29, 1982. 88, 114, 119

[477] S. Davidson and S. Sarkar. Thermalization after inflation. *JHEP*, 11:012, 2000. 90

[478] A. Mazumdar and B. Zaldivar. Quantifying the reheating temperature of the universe. *Nucl. Phys.*, B886:312–327, 2014. 90

[479] M. Drewes. On finite density effects on cosmic reheating and moduli decay and implications for Dark Matter production. *JCAP*, 1411(11):020, 2014. 92, 96

[480] H. A. Weldon. Effective fermion masses of order gT in high-temperature gauge theories with exact chiral invariance. *Phys. Rev. D*, 26:2789–2796, November 1982. 92

[481] A. De Felice et al. Chaotic inflation in modified gravitational theories. *JCAP*, 1108:021, 2011. 97

[482] R. Kallosh, A. Linde, and D. Roest. Superconformal Inflationary α-Attractors. *JHEP*, 11:198, 2013. 97, 98

[483] A. A. Starobinsky. A New Type of Isotropic Cosmological Models Without Singularity. *Phys. Lett.*, B91:99–102, 1980. 97

[484] M. Ozkan, Y. Pang, and S. Tsujikawa. Planck constraints on inflation in auxiliary vector modified $f(R)$ theories. *Phys. Rev.*, D92(2):023530, 2015. 98

[485] H. Murayama, H. Suzuki, T. Yanagida, et al. Chaotic inflation and baryogenesis by right-handed sneutrinos. *Phys. Rev. Lett.*, 70:1912–1915, March 1993. 103

[486] S. Davidson, E. Nardi, and Y. Nir. Leptogenesis. *Phys. Rept.*, 466:105–177, 2008. 103, 167

[487] N. Cabibbo. Unitary Symmetry and Leptonic Decays. *Phys. Rev. Lett.*, 10:531–533, 1963. 648(1963). 106

[488] M. Kobayashi and T. Maskawa. CP Violation in the Renormalizable Theory of Weak Interaction. *Prog. Theor. Phys.*, 49:652–657, 1973. 106

[489] V. Baluni. CP Violating Effects in QCD. *Phys. Rev.*, D19:2227–2230, 1979. 106

[490] R. J. Crewther, P. Di Vecchia, G. Veneziano, and E. Witten. Chiral Estimate of the Electric Dipole Moment of the Neutron in Quantum Chromodynamics. *Phys. Lett.*, 88B:123, 1979. [Erratum: Phys. Lett.91B,487(1980)]. 106

[491] P. Cea and G. Nardulli. A Realistic Calculation of the Electric Dipole Moment of the Neutron Induced by Strong CP Violation. *Phys. Lett.*, B144:115–118, 1984. 106

[492] D. K. Hong, H. Kim, S. Siwach, and H. Yee. The Electric Dipole Moment of the Nucleons in Holographic QCD. *JHEP*, 11:036, 2007. 106

[493] J. Baron et al. Order of Magnitude Smaller Limit on the Electric Dipole Moment of the Electron. *Science*, 343:269–272, 2014. 106

[494] J. M. Pendlebury et al. Revised experimental upper limit on the electric dipole moment of the neutron. *Phys. Rev.*, D92(9):092003, 2015. 106

[495] J. Baron et al. Methods, Analysis, and the Treatment of Systematic Errors for the Electron Electric Dipole Moment Search in Thorium Monoxide. 2016. 106

[496] S. L. Adler. Axial vector vertex in spinor electrodynamics. *Phys. Rev.*, 177:2426–2438, 1969. 106

[497] W. A. Bardeen. Anomalous Ward identities in spinor field theories. *Phys. Rev.*, 184:1848–1857, 1969. 106

[498] C. Aubin et al. Light pseudoscalar decay constants, quark masses, and low energy constants from three-flavor lattice QCD. *Phys. Rev.*, D70:114501, 2004. 106

[499] F. Sanfilippo. Quark Masses from Lattice QCD. *PoS*, LATTICE2014:014, 2015. 106

[500] A. D. Linde. Axions in inflationary cosmology. *Phys. Lett.*, B259:38–47, 1991. 106, 108

[501] Y. Asano et al. Search for a Rare Decay Mode $K^+ \to \pi^+ \nu\bar{\nu}$ and Axion. *Phys. Lett.*, B107:159, 1981. [,411(1981)]. 107

[502] H. Cheng. The Strong CP Problem Revisited. *Phys. Rept.*, 158:1, 1988. 107, 123

[503] J. E. Kim. Light Pseudoscalars, Particle Physics and Cosmology. *Phys. Rept.*, 150:1–177, 1987. 107, 123

[504] J. E. Kim and G. Carosi. Axions and the Strong CP Problem. *Rev. Mod. Phys.*, 82:557–602, 2010. 107

[505] J. E. Kim. Weak Interaction Singlet and Strong CP Invariance. *Phys. Rev. Lett.*, 43:103, 1979. 107, 119, 173

[506] M. A. Shifman, A. I. Vainshtein, and V. I. Zakharov. Can Confinement Ensure Natural CP Invariance of Strong Interactions? *Nucl. Phys.*, B166:493–506, 1980. 107, 119, 173

[507] M. Dine, W. Fischler, and M. Srednicki. A Simple Solution to the Strong CP Problem with a Harmless Axion. *Phys. Lett.*, B104:199–202, 1981. 107, 119, 173

[508] A. R. Zhitnitsky. On Possible Suppression of the Axion Hadron Interactions. (In Russian). *Sov. J. Nucl. Phys.*, 31:260, 1980. [Yad. Fiz.31,497(1980)]. 107, 173

[509] L. F. Abbott and P. Sikivie. A Cosmological Bound on the Invisible Axion. *Phys. Lett.*, B120:133–136, 1983. 107, 167

[510] M. Dine and W. Fischler. The Not So Harmless Axion. *Phys. Lett.*, B120:137–141, 1983. 107, 167

[511] M. S. Turner. Cosmic and Local Mass Density of Invisible Axions. *Phys. Rev.*, D33:889–896, 1986. 108, 124, 125

[512] K. J. Bae, J. Huh, and J. E. Kim. Update of axion CDM energy. *JCAP*, 0809:005, 2008. 108

[513] Y. B. Zeldovich, I. Y. Kobzarev, and L. B. Okun. Cosmological Consequences of the Spontaneous Breakdown of Discrete Symmetry. *Zh. Eksp. Teor. Fiz.*, 67:3–11, 1974. [Sov. Phys. JETP40,1(1974)]. 108

[514] P. Sikivie. Of Axions, Domain Walls and the Early Universe. *Phys. Rev. Lett.*, 48:1156–1159, 1982. 108

[515] B. Holdom. Domain Walls. 1. Axion Models. *Phys. Rev.*, D27:332–338, 1983. 108

[516] T. Hiramatsu, M. Kawasaki, K. Saikawa, and T. Sekiguchi. Production of dark matter axions from collapse of string-wall systems. *Phys. Rev.*, D85:105020, 2012. [Erratum: Phys. Rev.D86,089902(2012)]. 108, 127

[517] M. Kawasaki, K. Saikawa, and T. Sekiguchi. Axion dark matter from topological defects. *Phys. Rev.*, D91(6):065014, 2015. 108, 127

[518] T. Hiramatsu, M. Kawasaki, K. Saikawa, and T. Sekiguchi. Axion cosmology with long-lived domain walls. *JCAP*, 1301:001, 2013. 108

[519] A. Ringwald and K. Saikawa. Axion dark matter in the post-inflationary Peccei-Quinn symmetry breaking scenario. *Phys. Rev.*, D93(8):085031, 2016. [Addendum: Phys. Rev.D94,no.4,049908(2016)]. 108

[520] M. Kawasaki, T. T. Yanagida, and K. Yoshino. Domain wall and isocurvature perturbation problems in axion models. *JCAP*, 1311:030, 2013. 108, 112, 127

[521] K. Harigaya, M. Ibe, M. Kawasaki, and T. T. Yanagida. Dynamics of Peccei-Quinn Breaking Field after Inflation and Axion Isocurvature Perturbations. *JCAP*, 1511(11):003, 2015. 109, 110, 112, 125

[522] J. Kearney, N. Orlofsky, and A. Pierce. High-Scale Axions without Isocurvature from Inflationary Dynamics. *Phys. Rev.*, D93(9):095026, 2016. 109

[523] M. Kawasaki, K. Nakayama, and M. Senami. Cosmological implications of supersymmetric axion models. *JCAP*, 0803:009, 2008. 109

[524] M. Cicoli, J. P. Conlon, and F. Quevedo. Dark radiation in LARGE volume models. *Phys. Rev.*, D87(4):043520, 2013. 109, 132, 145

[525] M. Cicoli and A. Mazumdar. Reheating for Closed String Inflation. *JCAP*, 1009(09):025, 2010. 109, 132

[526] K. Harigaya, M. Ibe, M. Kawasaki, and T. T. Yanagida. Non-Gaussianity from Attractor Curvaton. *Phys. Rev.*, D87(6):063514, 2013. 111

[527] P. B. Greene, L. Kofman, A. D. Linde, and A. A. Starobinsky. Structure of resonance in preheating after inflation. *Phys. Rev.*, D56:6175–6192, 1997. 113

[528] R. Allahverdi, K. Enqvist, J. Garcia-Bellido, and A. Mazumdar. Gauge invariant MSSM inflaton. *Phys. Rev. Lett.*, 97:191304, 2006. 114

[529] P. Graf and F. D. Steffen. Thermal axion production in the primordial quark-gluon plasma. *Phys. Rev.*, D83:075011, 2011. 114

[530] A. Salvio, A. Strumia, and W. Xue. Thermal axion production. *JCAP*, 1401:011, 2014. 114, 115, 116

[531] E. Masso, F. Rota, and G. Zsembinszki. On axion thermalization in the early universe. *Phys. Rev.*, D66:023004, 2002. 114, 115, 116

[532] M. L. Bellac. *Thermal Field Theory.* Cambridge University Press, 2011. 115

[533] S. Weinberg. Goldstone Bosons as Fractional Cosmic Neutrinos. *Phys. Rev. Lett.*, 110(24):241301, 2013. 116

[534] M. Kaplinghat. Dark matter from early decays. *Phys. Rev.*, D72:063510, 2005. 118

[535] P. B. Greene and L. Kofman. Preheating of fermions. *Phys. Lett.*, B448:6–12, 1999. 119

[536] R. R. Volkas, A. J. Davies, and G. C. Joshi. Naturalness of the invisible axion model. *Phys. Lett.*, B215:133–138, 1988. 120, 175

[537] D. I. Podolsky, G. N. Felder, L. Kofman, and M. Peloso. Equation of state and beginning of thermalization after preheating. *Phys. Rev.*, D73:023501, 2006. 120

[538] A. Burrows, M. S. Turner, and R. P. Brinkmann. Axions and SN 1987a. *Phys. Rev.*, D39:1020, 1989. 123

[539] J. Engel, D. Seckel, and A. C. Hayes. Emission and detectability of hadronic axions from SN1987A. *Phys. Rev. Lett.*, 65:960–963, 1990. 123

[540] G. G. Raffelt. Core Mass at the Helium Flash From Observations and a New Bound on Neutrino Electromagnetic Properties. *Astrophys. J.*, 365:559, 1990. 123

[541] A. Ayala et al. Revisiting the bound on axion-photon coupling from Globular Clusters. *Phys. Rev. Lett.*, 113(19):191302, 2014. 123

[542] N. Viaux et al. Neutrino and axion bounds from the globular cluster M5 (NGC 5904). *Phys. Rev. Lett.*, 111:231301, 2013. 123

[543] M. M. Miller Bertolami, B. E. Melendez, L. G. Althaus, and J. Isern. Revisiting the axion bounds from the Galactic white dwarf luminosity function. *JCAP*, 1410(10):069, 2014. 123

[544] M. Archidiacono et al. Axion hot dark matter bounds after Planck. *JCAP*, 1310:020, 2013. 124

[545] R. Penrose. Gravitational collapse: The role of general relativity. *Riv. Nuovo Cim.*, 1:252–276, 1969. [Gen. Rel. Grav.34,1141(2002)]. 125

[546] T. J. M. Zouros and D. M. Eardley. Instabilities of massive scalar perturbations of a rotating black hole. *Annals Phys.*, 118:139–155, 1979. 125

[547] A. Arvanitaki, S. Dimopoulos, S. Dubovsky, N. Kaloper, and J. March-Russell. String Axiverse. *Phys. Rev.*, D81:123530, 2010. 125

[548] A. Arvanitaki, M. Baryakhtar, and X. Huang. Discovering the QCD Axion with Black Holes and Gravitational Waves. *Phys. Rev.*, D91(8):084011, 2015. 125

[549] M. Kawasaki, T. Moroi, and T. Yanagida. Can decaying particles raise the upper bound on the Peccei-Quinn scale? *Phys. Lett.*, B383:313–316, 1996. 130

[550] A. R. Liddle, A. Mazumdar, and F. E. Schunck. Assisted inflation. *Phys. Rev.*, D58:061301, 1998. 131

[551] M. Dine, N. Seiberg, X. G. Wen, and E. Witten. Nonperturbative Effects on the String World Sheet. *Nucl. Phys.*, B278:769–789, 1986. 132

[552] K. Becker, M. Becker, and A. Strominger. Five-branes, membranes and nonperturbative string theory. *Nucl. Phys.*, B456:130–152, 1995. 132

[553] T. Higaki and F. Takahashi. Dark Radiation and Dark Matter in Large Volume Compactifications. *JHEP*, 11:125, 2012. 132

[554] J. R. Bond, L. Kofman, S. Prokushkin, and P. M. Vaudrevange. Roulette inflation with Kahler moduli and their axions. *Phys. Rev.*, D75:123511, 2007. 132

[555] A. A. Starobinsky and J. Yokoyama. Density fluctuations in Brans-Dicke inflation. In *Proceedings, Workshop on General Relativity and Gravitation (JGRG4): Kyoto, Japan, November 28-December 1, 1994*, page 381, 1994. 132

[556] A. A. Starobinsky, S. Tsujikawa, and J. Yokoyama. Cosmological perturbations from multifield inflation in generalized Einstein theories. *Nucl. Phys.*, B610:383–410, 2001. 132

[557] M. Fairbairn, R. Hogan, and D. J. E. Marsh. Unifying inflation and dark matter with the Peccei-Quinn field: observable axions and observable tensors. *Phys. Rev.*, D91(2):023509, 2015. 132

[558] P. Arias et al. WISPy Cold Dark Matter. *JCAP*, 1206:013, 2012. 133

[559] B. A. Bassett, D. I. Kaiser, and R. Maartens. General relativistic preheating after inflation. *Phys. Lett.*, B455:84–89, 1999. 133

[560] F. Finelli and R. H. Brandenberger. Parametric amplification of gravitational fluctuations during reheating. *Phys. Rev. Lett.*, 82:1362–1365, 1999. 133

[561] B. A. Bassett and F. Viniegra. Massless metric preheating. *Phys. Rev.*, D62:043507, 2000. 133

[562] K. Enqvist et al. Non-Gaussianity from instant and tachyonic preheating. *JCAP*, 0503:010, 2005. 133

[563] K. Enqvist, A. Jokinen, A. Mazumdar, T. Multamaki, and A. Vaihkonen. Non-Gaussianity from preheating. *Phys. Rev. Lett.*, 94:161301, 2005. 133

[564] A. Linde, S. Mooij, and E. Pajer. Gauge field production in supergravity inflation: Local non-Gaussianity and primordial black holes. *Phys. Rev.*, D87(10):103506, 2013. 133

[565] A. Mazumdar and S. Qutub. Nonperturbative overproduction of axionlike particles via derivative interactions. *Phys. Rev.*, D93(4):043502, 2016. 134

[566] W. Magnus and S. Winkler. *Hill's equation*. John Wiley and Sons, New York, 1966. 138

[567] K. M. Urwin and F. M. Arscott. Theory of the Whittaker-Hill Equation. In *Proceedings of the Royal Society of Edinburgh*, number 69, pages 28–44, 1970. 138

[568] E. T. Whittaker and G. N. Watson. *course of modern analysis*. Cambrigde University Press, Cambridge, 1962. 138

[569] N. W. McLachlan. *Theory and Applications of Mathieu Functions*. Oxford Univ. Press, Clarendon, 1947. 138, 142

[570] C. M. Bender and S. A. Orszag. *Advanced Mathematical Methods for Scientists and Engineers*. McGraw-Hill, 1978. 138

[571] J. Lachapelle and R. H. Brandenberger. Preheating with Non-Standard Kinetic Term. *JCAP*, 0904:020, 2009. 139

[572] M. Abramowitz and I. A. Stegun. *Handbook of Mathematical Functions with Formulas, Graphs, and Mathematical Tables*. National Bureau of Standard, U.S. Government Printing Office, 1972. 141

[573] J. F. Dufaux et al. Preheating with trilinear interactions: Tachyonic resonance. *JCAP*, 0607:006, 2006. 141

[574] J. Bernstein. *Kinetic theory in the expanding Universe*. Cambridge University Press, Cambridge, U.K., 1988. 165, 166

[575] C. Cercignani and G. M. Kremer. *The relativistic Boltzmann equation: theory and applications*. Springer, Basel AG, 2002. 165

[576] K. Petraki and R. R. Volkas. Review of asymmetric dark matter. *Int. J. Mod. Phys.*, A28:1330028, 2013. 167

[577] P. Fox, A. Pierce, and S. D. Thomas. Probing a QCD string axion with precision cosmological measurements. 2004. 167

[578] M. A. Luty. Baryogenesis via leptogenesis. *Phys. Rev.*, D45:455–465, 1992. 169